



Politecnico di Milano
Space Mission Analysis and Design
Course (A.Y. 2019/2020)

FINAL REPORT
MARS-PENGUIN MISSION



**MARS SOUTH POLE EXPLORATION AND
GEYSERS IN-SITU INVESTIGATION**

Professor: Michèle Lavagna

Authors:

Andrea Boni	(928441)	andrea1.boni@mail.polimi.it
Nicola Boscolo Fiore	(910552)	nicola.boscolo@mail.polimi.it
Elisa De Astis	(922433)	elisa.deastis@mail.polimi.it
Vahid Nateghi	(916833)	vahid.nateghi@mail.polimi.it
Maria Francesca Palermo	(920959)	mariafrancesca.palermo@mail.polimi.it
Luca Pascali	(920396)	lucamaria.pascali@mail.polimi.it
Claudio Pedrazzini	(928510)	claudio.pedrazzini@mail.polimi.it
Massimo Piazza	(919920)	massimo.piazza@mail.polimi.it
Lorenzo Pisani	(920419)	lorenzo.pisani@mail.polimi.it
Sabrina Saban	(926949)	sabrina.saban@mail.polimi.it
Francesco Ventre	(915640)	francesco.ventre@mail.polimi.it

July 21, 2020

Team members and roles

Team member	Team role
Andrea Boni	Thermal Control
Nicola Boscolo Fiore	EPS, OBDH, Thermal Control
Elisa De Astis	Propulsion
Vahid Nateghi	ADCS
Maria Francesca Palermo	Robotics
Luca Pascali	EDL
Claudio Pedrazzini	Cost and Risks, Programmatic, AIVT
Massimo Piazza	TMTC
Lorenzo Pisani	Configuration
Sabrina Saban	Structure
Francesco Ventre	Mission Analysis

Contents

1	Introduction	1
2	Mission Environment Analysis	2
2.1	Landing site	2
2.2	Geysers	3
2.3	General aspects	4
2.4	Criticalities and opportunities	6
3	State of the Art	8
3.1	Missions to Mars	8
3.1.1	Past missions	9
3.1.2	Future missions	9
3.2	Lessons learnt	9
4	Mission Architecture	11
4.1	Possible architectures	11
4.1.1	Space segment	11
4.1.2	Mars segment	11
4.2	Preliminary selection process	12
4.3	Payload (P/L)	15
4.4	Auxiliary aerial vehicle	16
4.4.1	Glider	17
4.4.2	Helicopter	17
4.4.3	Hexacopter	18
4.4.4	Aerial vehicle selection	19
4.5	Final architecture selection	19
4.5.1	Planetary Protection and Cleanliness and Contamination Control	19
5	Preliminary Mission Definition	21
5.1	Phases, timeline and ConOps	21
5.2	Tasks	23
5.3	Modes	25
6	Launchers	27
6.1	Constraints from mission to launchers	27
6.2	Potential launchers	27

7	Mission Analysis	29
7.1	Introduction	29
7.2	Trajectory trade-off	29
7.2.1	Preliminary trajectory	29
7.2.2	B-Plane Targeting	31
7.2.3	Optimisation	32
7.3	Final Trajectory	32
7.3.1	Geocentric	32
7.3.2	Interplanetary	33
7.3.3	Areocentric	34
7.4	Conclusions	34
8	Attitude Determination and Control	35
8.1	Introduction	35
8.2	Mission modes	35
8.3	Environment	35
8.3.1	Solar Radiation Pressure	36
8.4	Hardware	36
8.4.1	Sensors	36
8.4.2	Actuators	37
8.5	Software	38
8.5.1	Attitude estimation	38
8.5.2	Attitude Control	39
8.5.3	Attitude Control Architecture	39
8.5.4	Controller	39
8.5.5	Thrusters architecture	40
8.6	Simulation	41
8.6.1	De-tumbling	41
8.6.2	Slew	41
8.6.3	Further analysis	42
8.7	Entry, Descent and Landing	43
9	EDL	44
9.1	Introduction	44
9.2	Phases	44
9.2.1	Entry	44
9.2.2	Parachute deployment	45
9.2.3	Landing	45
9.3	Model Description	47
9.3.1	Entry model	47
9.3.2	Thermal analysis	48
9.3.3	Parachute model	49
9.3.4	Landing procedure selection and modelling	51
9.3.5	Montecarlo Analysis	52

9.3.6	Wind effect	54
9.3.7	GNC preliminary definition	54
9.4	Conclusion	54
10	Propulsion Subsystem	55
10.1	Propulsion in interplanetary missions	55
10.2	Preliminary analysis	55
10.2.1	Space segment	55
10.2.2	Mars segment	55
10.2.3	Requirements to be satisfied	56
10.3	Chemical solution preliminary architecture definition	56
10.3.1	Preliminary sizing	56
10.3.2	Possible architecture configurations	57
10.4	Electrical solution preliminary study and trade-off	58
10.5	Final configuration	58
10.5.1	Cruise stage	58
10.5.2	Landing stage	60
10.6	Effects on other subsystems	63
11	Telemetry and Telecommand	64
11.1	Introduction	64
11.1.1	Communication phases	64
11.2	Cruise	64
11.2.1	Earth's atmospheric attenuation	65
11.2.2	HGA sizing	66
11.2.3	Safe mode communication	69
11.2.4	Mass & power budget	69
11.3	Entry, Descent and Landing	70
11.3.1	Optimal phasing performance	70
11.4	Surface operations	71
11.4.1	Proximity antennas	72
11.4.2	Return link	72
11.4.3	Forward link	74
11.4.4	Mass & power budget	74
11.4.5	Solar conjunctions	74
12	On Board Data Handling	75
12.1	Introduction	75
12.2	Requirements	75
12.3	Functionalities	75
12.3.1	Autonomous Navigation	75
12.4	Architecture	76
12.5	Effects, inputs and constraints	77

13	Electric Power Subsystem	80
13.1	Introduction	80
13.2	Power budget breakdown	80
13.3	Possible power sources	82
13.3.1	Power Generation	82
13.3.2	Power Storage	83
13.4	Sizing	84
13.5	EPS architecture	85
13.6	Effects, inputs and constraints	85
14	Thermal Control Subsystem	87
14.1	Introduction	87
14.2	Effects, inputs and constraints	87
14.3	Cruise	88
14.4	EDL	89
14.5	Rover	90
15	Robotics	91
15.1	Introduction	91
15.1.1	Functionalities and requirements	91
15.2	Rover locomotion system	92
15.2.1	Travel path	92
15.2.2	Rover sizing and design	92
15.3	Sub-glacial lake region sampling	97
15.3.1	Sampling instrument selection	97
15.3.2	Reference drills	98
15.3.3	MARS-PENGUIN drill: Rico	100
15.4	Geysers ejecta sampling	101
15.4.1	Phenomenon observation and sample selection	101
15.4.2	Sampling instrument selection	101
15.4.3	MARS-PENGUIN robotic arm: Soldato	101
15.5	Sample handling and analysis	103
15.6	Modes and Timelines	104
16	Configuration	106
16.1	Introduction	106
16.2	Rover	106
16.3	Descend Module	107
16.4	Cruise Stage	107
16.5	Overall Configuration and Launcher Interface	108

16.6	Separation mechanisms	108
17	Structures	110
17.1	Introduction	110
17.2	Launch Phase	110
17.2.1	Requirements	110
17.2.2	Cruise stage	111
17.2.3	Entry Capsule	112
17.3	EDL phase	113
17.4	Separations	113
18	Helicopter preliminary design	114
18.1	Introduction	114
18.2	Power and Energy System	114
18.2.1	Solar Panel and Batteries	114
18.3	Thermal subsystem	114
18.4	Communication subsystem	115
18.5	Preliminary Design	116
19	Project Management	118
19.1	Introduction	118
19.2	Power budget	118
19.3	Mass budget	118
19.4	Assembly, Integration, Verification and Test	120
19.4.1	Models and Tests	120
19.5	Risk and Cost	121
19.5.1	Risk Management	121
19.5.2	Cost Analysis	122
20	Conclusion	125
A	Appendix	126
A.1	Names selection	126
A.2	Mass statistical estimation	127
A.3	ADCS	130
A.3.1	Disturbances	130
A.3.2	De-tumbling	130
A.4	EDL	131
A.4.1	Past Missions overview	131
A.4.2	Deceleration profile	131
A.4.3	Wind velocity	132

A.5	Propulsion subsystem architectures	133
A.6	TMTC	134
A.6.1	Communication modes	134
A.6.2	State of the art & available facilities	134
A.6.3	Earth's atmospheric attenuation (ITU models)	136
A.6.4	Safe mode communication	138
A.6.5	EDL	138
A.6.6	Surface operations	139
A.7	Robotics	142
A.7.1	Skipper Locomotion system	142
A.8	Configuration	144
A.8.1	Bridles Spool Mechanism	144
A.9	Structure	145
A.9.1	Materials selected	145
A.10	Project Management	146
	References	156

List of Figures

2.1	<i>Sub-glacial lake region and closer geysers.</i>	2
2.2	<i>The nearest thin geyser, centred approximately at 189.217° E and 80.687° S. HiRISE image: ESP_056553_0990 was acquired at $L_s = 233.8^\circ$ with 49.2 cm/px.</i>	4
2.3	<i>Temperature range (a) and annual pressure evolution at local noon (b) throughout a martian year at 81°S 193°E.</i>	4
2.4	<i>(a) Elevation of the Sun at 81°S 193°E in a martian year; Solar flux to the region of interest during a sol.</i>	5
2.5	<i>The map shows the thickness of the SPLD of Mars. Credits: NASA/JPL/ASI/ESA/University of Rome/MOLA Science Team/USGS</i>	6
2.6	<i>Latitudinal profiles of elevation change (Δh) over the course of the MGS mapping mission and martian seasons (solar longitude L_s) in south polar regions</i>	6
4.1	<i>Preliminary architecture tree</i>	12
4.2	<i>Hopper trajectory simulation</i>	15
4.3	<i>Payload positioning inside the main ground vehicle.</i>	17
5.1	<i>Timeline of the mission. The seasons are relative to the southern hemisphere.</i>	21
5.2	<i>ConOps from transfer to disposal of each segment.</i>	23
5.3	<i>Mission tasks</i>	24
6.1	<i>Launchers' performance profiles, obtained from [26],[27] and [28].</i>	27
7.1	<i>Trajectory trade-off process</i>	29
7.2	<i>Porkchop plot for Earth-Mars transfers (2024-2030)</i>	30
7.3	<i>Optimisation process flow</i>	32
7.4	<i>Geocentric trajectory</i>	33
7.5	<i>Heliocentric trajectory in J2000 frame</i>	33
7.6	<i>Areocentric trajectory</i>	34
8.1	<i>Cruise stage sensors</i>	36
8.2	<i>Thrusters' configuration</i>	37
8.3	<i>Thrusters' configuration optimisation</i>	38
8.4	<i>Attitude estimation error using a Cubature Kalman filter</i>	38
8.5	<i>(a) Euler angles and (b) angular velocity vector during control window during the three days after launch</i>	41
8.6	<i>(a) Required and real control torque and (b) thrust of each thruster for the first day slew manoeuvre</i>	42
8.7	<i>Entry capsule reaction control system</i>	43
8.8	<i>The behaviour of the RCSs and the entry capsule during spin-up</i>	43
9.1	<i>Viking-heritage 70° sphere-cone aeroshells</i>	44
9.2	<i>Viking-derived parachute systems</i>	44
9.3	<i>Ballistic and Lifting Entry Configurations</i>	45
9.4	<i>Mars Pathfinder EDL</i>	45
9.5	<i>Skycrane final landing phases</i>	46
9.6	<i>-12° EFPA trajectory</i>	48
9.7	<i>-12° EFPA velocity profile</i>	48
9.8	<i>Previous missions velocity profiles</i>	48
9.9	<i>Trend of the heat flux at the stagnation point</i>	49
9.10	<i>Trend of the wall temperature at the stagnation point</i>	49
9.11	<i>Model of the parachute capsule system</i>	50
9.12	<i>Parachute angle of attack</i>	50
9.13	<i>Capsule angle of attack</i>	50
9.14	<i>Parachute phase and heatshield trajectory</i>	51

9.15 Skycrane phase and backshell trajectory	52
9.16 Uncertainty model for each iteration	53
9.17 -12° EFPA landing ellipse	54
10.1 Possible configurations	57
10.2 Tank parameter variations during cruise	60
10.3 Skycrane propulsion system configuration	60
10.4 Thrust allocation among thrusters during landing	62
10.5 Tank parameter variations during landing	63
11.1 Earth-SC range and Sun-Earth-Probe angle over the trajectory	65
11.2 World attenuation map at 8450 MHz	65
11.3 Atmospheric attenuation exceeded for 1% of an average year at ESTRACK sites	66
11.4 Polar radiation pattern ($Az = 0^\circ$) of the HGA	67
11.5 Downlink data rate variation over the cruise	68
11.6 Maximum safe mode telemetry rate, parametrised by the off-boresight angle	69
11.7 EDL coverage performance corresponding to MRO's optimal phasing	71
11.8 Coverage map of the landing site	72
11.9 Return data rate as a function of elevation	73
11.10 Data return performance depending on orbiter pass ground track	73
11.11 Sun-Earth-Mars angle over a decade	74
12.1 Simplified, real time visualisation of Autonomous Navigation	76
12.2 Artist concept showing the primary driving information of Skipper in Roving Mode	76
12.3 The OBDH subsystem architecture	77
13.1 Power breakdown of Skipper	82
13.2 MMRTG	83
13.3 ASRG	83
13.4 Mars Penguin mission EPS architecture	86
14.1 Heat fluxes during the interplanetary leg	88
14.2 Temperatures for the cruise stage nodes	88
14.3 Temperatures for the EDL phase	89
14.4 Heat fluxes on Mars	90
14.5 Temperatures for Skipper's nodes	90
15.1 Travel path from the centre of the sub-glacial lake (point A) to the closest spider site (point B).	92
15.2 Elevation profile of the path.	92
15.3 Travel period	92
15.4 Wheel sinkage z as a function of wheel diameter, nominal width, slope angle and number of wheels.	93
15.5 Drawbar Pull developed by a single rigid wheel, as function of wheel diameter and width, in absence of grousers and with $h = 1$ cm grousers. The first row of graphs refers to a 4-wheel configuration, while the second row refers to a 6-wheel rover.	94
15.6 Total motion resistance R_{tot} , Soil Thrust H and Drawbar Pull DP developed by a single rigid wheel with 1 cm grousers, as functions of wheel diameter and width, considering a 6-wheel configuration.	95
15.7 CAD model of the Skipper's rocker-bogie suspension.	97
15.8 Possible sampling tools.	98
15.9 Referece drills.	99
15.10 Possible configuration for the drill Rico.	100
15.11 Possible geyser ejecta sampling instruments.	101
15.12 Soldato in different positions.	102
15.13 Preliminary FEM analysis of the upper arm.	103
15.14 Skipper Sample Handling and Distribution System	104
15.15 Lake region sampling timeline.	105
15.16 Geyser analysis timeline.	105

16.1 Rover Skipper preliminary design with payload positions	106
16.2 Release mechanism of the helicopter	107
16.3 Descend module preliminary design	108
16.4 Cruise stage and overall configuration	108
16.5 Launcher configuration	109
16.6 Separation mechanisms: a) cruise stage-entry capsule, b) entry capsule-heat shield, c) entry capsule - sky crane, d-e) sky crane- rover.	109
17.1 Overall configuration in the fairing with axis.	110
17.2 Primary structure model.	111
17.3 Stress field of the primary structure.	111
17.4 Preliminary FEM analysis of the upper arm.	112
17.5 Strain field under the maximum deceleration arising during the EDL phase.	113
17.6 Buckling representation for the two cases.	113
18.1 The Kowalski helicopter.	114
18.2 Temperatures for the helicopter nodes.	115
18.3 Radiation pattern of the helicopter antenna	116
18.4 Diagonal solar flux and horizontal solar flux arriving at 81°S.	116
18.5 Elevation of the Sun at the beginning of the Southern Spring.	116
18.6 Evolution of the energy at the BoL of the batteries.	117
18.7 Evolution of the energy at the EoL of the batteries.	117
18.8 Helicopter ConOps.	117
19.1 Power budget in Cruise.	118
19.2 Power budget in EDL.	118
19.3 Skipper's Power budget.	118
19.5 Mass division of each subsystem for segment.	119
19.6 Mass variations in relation with the timeline.	120
A.1 The Penguins of "Madagascar", in the order from the left side: Soldato, Kowalski, Skipper, Rico.	126
A.2 Regression lines	127
A.3 Disturbance torque applied during few hours	130
A.4 Angular velocity during the de-tumbling mode	130
A.5 -12° EFPA deceleration profile	131
A.6 Wind velocity profile	132
A.7 Cruise propulsion system schematic architecture	133
A.8 Landing propulsion system schematic architecture	133
A.9 Atmospheric attenuation components: gaseous, rain, clouds, scintillation	137
A.10 Radiation pattern of the LGP	138
A.11 MRO coverage in correspondence of the optimal phasing	138
A.12 Radiation pattern of the BUHF antenna	139
A.13 RUHF antenna pattern	139
A.14 MRO's ground track over 66 orbits	140
A.15 OUGH radiation pattern	140
A.16 Data return profile during 6 consecutive orbiter passes	141
A.17 Forward link performance depending on orbiter pass	141
A.18 Compaction Resistance R_c for a 6 rigid wheels configuration as a function of wheel diameter and tire width.	142
A.19 Skipper configurations with 4 and 6 wheels.	143
A.20 Displacement field of one side of the rocker-bogie suspension obtained from static analysis.	143
A.21 Bridles unroll mechanism.	144
A.22 S-curve of the mission with the beginning of each phase.	147
A.23 Gantt chart of the MARS-PENGUIN mission	147
A.24 WBS of the Space System	148
A.25 WBS of the Spacecraft	148

A.26 <i>WBS of the Spacecraft Bus</i>	148
A.27 <i>WBS of the Payload</i>	149
A.28 <i>WBS of the Ground Segment</i>	149
A.29 <i>Product Tree of the mission</i>	150
A.30 <i>Product Tree of the Flight Segment</i>	150
A.31 <i>Product Tree of the Platform</i>	150
A.32 <i>Product Tree of the rover Skipper</i>	151
A.33 <i>Product Tree of the helicopter Kowalski</i>	151

List of Tables

2.1	Classification of Martian dust storms	7
2.2	Table of the criticalities and opportunities identified per each environmental aspect	7
3.1	Past and future missions of interest	8
4.1	Weights in the criteria matrix	12
4.2	Criteria Matrix	13
4.3	Velocity and travelling distance	13
4.4	Payload characteristics.	16
4.5	Gliders data.[17] [18] [19] [20]	17
4.6	Mars helicopters proposed by NASA.[22]	18
4.7	MARS-PENGUIN helicopter design parameters	18
4.8	Proposed Mars hexacopters. [22] [23]	18
4.9	Criteria matrix for aerial vehicle	19
5.1	Mission phases	22
5.2	Mission modes	25
5.3	Possible modes during the mission	26
6.2	Past and future (*) launchers of interest for MARS-PENGUIN mission. (Mass, C3 and cost are indicative for a general Mars mission wherever never done)	28
7.1	2026 trajectory data	30
7.2	2028 trajectory data	30
7.3	Targeting - Initial data	31
7.4	Targeting - Departure hyperbola data	31
7.5	Targeting - Data at Earth SOI	32
7.6	Targeting - Data at Mars closest approach	32
7.7	Optimised parameters	32
7.8	Departure hyperbola data	33
7.9	Heliocentric trajectory data (Keplerian elements at departure, EclipJ2000 frame)	33
7.10	Arrival trajectory data	34
8.1	Required accuracy for ADCS modes	35
8.2	Disturbances present in mission phases	36
8.3	Thruster specification	37
8.4	Criteria weights for the cost function of thrusters' optimisation	37
8.5	Optimised angles for the thrusters' installation	38
8.7	The most promising attitude control architectures	39
8.8	De-tumbling mode's controller gains	39
8.9	Communication mode's controller gains	40
8.10	Thruster firing for controlling each axes	40
9.1	Entry vehicle characteristics	47
9.2	Heatshield c_D	47
9.3	-12° EFPA Parachute deployment	47
9.4	Thermal environment EDL using SLA561v as TPS	49
9.5	Parachute pendulum model characteristics	50
9.6	Parachute pendulum model aeroshell separation and thrusted landing initial conditions	50
9.7	Thrusts and times for the powered landing phase and sky crane impact distance	52
9.8	Considered Uncertainties	53

10.1 Performances required to a chemical propulsion system	56
10.2 Mass and volume estimated budgets divided per phase (margined)	57
10.3 Chemical-Electric trade-off for cruise stage propulsion system	58
10.4 Cruise stage components and characteristics	59
10.5 Landing stage components and characteristics	61
10.6 Highest power requirements	63
11.1 Return link budget analysis during cruise	68
11.2 Forward link budget analysis during cruise	69
11.3 Mass and power breakdown of the cruise stage's TMTTC subsystem	70
11.4 Priority of coverage quality during EDL	70
11.5 Telemetry parameters	70
11.6 Visibility statistics of MRO	71
11.7 Maximum data volume return exploiting a limited number of passes	74
11.8 Mass and power breakdown of the rover's TMTTC subsystem	74
12.1 Computational resources requested by the skycrane	78
12.2 Computational resources requested by Skipper	79
13.1 Power breakdown for each stage and mode in Watts.	81
13.2 Summary of consumption by each mode.	81
13.3 MMRTG and ASRG parameters comparison.	83
13.4 EPS sizing. Batteries capacity required.	84
13.5 Battery parameters.	84
13.6 Subsystems power distribution	85
14.1 Temperature ranges for cruise stage parts and components	88
14.2 Temperature ranges for EDL stage parts and components	89
14.3 Temperature ranges for rover parts and components	90
15.1 Summary of the expected trafficability of 4-wheel and 6-wheel configurations with rigid suspension on flat terrain. For the input power: drivetrain efficiency: 0.7, motor efficiency: 0.8, drive electronics efficiency: 0.85.	95
15.2 Properties of materials for wheels.	96
15.3 Properties of the materials for the suspension.	97
15.4 Criteria Matrix for sampling tool.	98
15.5 Drill parameters and performance	99
15.6 Sampling modes (in blue) and submodes(in white).	104
16.1 Materials and masses of the different structural components (without margins).	109
16.2 Separation springs characteristics: a) cruise stage-entry capsule, b) entry capsule-heat shield.	109
17.1 Loading factors of the worst cases related to lateral and axial directions.	110
17.2 Results of the multi-nodes analysis under QSL.	111
17.3 Results of the structural analysis on the entry capsule.	112
17.4 Results of the entry capsule under the maximum deceleration arising during the EDL phase.	113
17.5 Results for the separation cases.	113
18.1 Temperature ranges for helicopter parts and components	115
18.2 Helicopter's communication performance	116
19.1 Division of the mass for each segment.	119
19.2 Tests done for each model.	120
19.3 Risk Matrix	121
19.4 MARS-PENGUIN risk analysis and mitigation action	123
19.5 Division of the total cost of the mission.	124

A.1	Results from the preliminary analysis on the mass.	128
A.2	Division of the masses for the possible architectures.	129
A.3	Mass breakdown for each architectures.	129
A.4	EDL parameters of past missions.	131
A.5	Communication modes	134
A.6	Key characteristics of the current Mars relay network	135
A.7	Performance characteristics of the ESTRACK deep space ground stations	136
A.8	Properties of the material used for the multinodes analysis.	145
A.10	Severity Index categorisation.	146
A.11	Likelihood Index categorisation.	146

Acronyms

AC	Attitude Control
ACS	Attitude Control System
ADCS	Attitude Determination & Control System
AIVT	Assembly, Integration, Verification and Test
ASRG	Advanced Stirling Radioisotope Generator
BCH	Bose–Chaudhuri–Hocquenghem
BER	Bit Error Rate
BLF	Buckling Load Factor
BoL	Beginning of Life
BPSK	Binary Phase-Shift Keying
BUHF	Backshell Ultra High Frequency
C&CC	Cleanliness and Contamination Control
CCSDS	Consultative Committee for Space Data Systems
CER	Cost Estimating Relationship
CG	Centre of Gravity
CoDR	Conceptual Design Review
CONF	Configuration System
ConOps	Concept of Operations
COSPAR	Committee on Space Research
DGB	Disk Gap Band
DoF	Degrees of Freedom
DOR	Differential One-way Ranging
DSA	Deep Space Antenna
DSN	Deep Space Network
ECSS	European Cooperation for Space Standardisation
EDL	Entry, Descent and Landing
EFPA	Entry Flight Path Angle
EIRP	Emitted Isotropically Radiated Power
EM	Engineering Model
EoL	End-of-Life
EPS	Electric Power Subsystem
ESA	European Space Agency
FBC	Faster-Better-Cheaper principles
FDIR	Fault Detection, Isolation and Recovery
FEA	Finite Element Analysis
FEM	Finite Elements Method
FM	Flight Model
FOSY	Factor of Safety for Yield Strength

FOV	Field of View
GNC	Guidance, Navigation & Control
GS	Ground Station
GTO	Geostationary Transfer Orbit
HGA	High Gain Antenna
HiRISE	High Resolution Imaging Science Experiment
HPBW	Half-Power Beamwidth
IDA	Instrument Deployment Arm
IMU	Inertial Measurement Unit
IPS	Instructions per second
ITU	International Telecommunication Union
JPL	Jet Propulsion Laboratory
LDPC	Low-Density Parity Check
LEO	Low Earth Orbit
LEOP	Launch and Early Orbit Phase
LGA	Low Gain Antenna
LGP	Low Gain Patch
LHC	Left Hand Circular
LI	Likelihood Index
LM	Launch Mass
LoS	Line of Sight
LVA	Launch Vehicle Adapter
MA	Mission Analysis
MARSIS	Mars Advanced Radar for Subsurface and Ionosphere Sounding
MAVEN	Mars Atmosphere and Volatile Evolution
MCD	Mars Climate Database
MER	Mars Exploration Rover
MGH	Mars Geyser Hopper
MGS	Mars Global Surveyor
MIB	Minimum Impulse Bit
MMH	Monomethyl Hydrazine
MoM	Measure of Merit
MPF	Mars Pathfinder
MPL	Mars Polar Lander
MRO	Mars Reconnaissance Orbiter
MSL	Mars Science Laboratory
NAIF	Navigation and Ancillary Information Facility
NASA	National Aeronautics and Space Administration
NREL	National Renewable Energy Laboratory
NTO	Nitrogen Tetroxide

NVM	Non-volatile memory
OBDH	On-board Data Handling
OUHF	Orbiter Ultra High Frequency
P/L	Payload
PCEC	Project Cost Estimating Capability
PD	Proportional-Derivative
PM	Project Management
PP	Planetary Protection
PPU	Power Processing Unit
PROP	Propulsion
PS	Propulsion System
PWM	Pulse-Width Modulator
QM	Qualification Model
QPSK	Quadrature Phase-Shift Keying
QSL	Quasi Static Load
RA	Robotic Arm
RAM	Random-access memory
RBT	Robotics
RCS	Reaction Control System
RDA	Radar Doppler Altimeter
RHC	Rigt Hand Circular
RHU	Radioisotope Heater Units
RI	Risk Index
RLS	Raman Laser Spectrometer
ROD	Review-of-design
RTG	Radioisotope Thermoelectric Generator
RTOS	RealTime Operating System
RUHF	Rover Ultra High Frequency
S/C	spacecraft
SA	Solar Array
SI	Severity Index
SLAM	Simultaneous Localisation and Mapping
SM	Safety Margin
SNR	Signal-to-Noise Ratio
SOI	Sphere of Influence
SPLD	South Polar Layered Deposits
SPRC	South Polar Residual Cap
SRP	Solar Radiation Pressure
SS	Sun-Synchronous
SSI	Surface Stereo Imager
SSPA	Solid-State Power Amplifier
STM	Structural and Thermal Model

STR	Structural System
TBD	To Be Defined
TCM	Trajectory Correction Manoeuvre
TCS	Thermal Control Subsystem
TGO	Trace Gas Orbiter
TMTC	Telemetry & Telecommand
TOF	time of flight
TPS	Thermal Protection System
TRL	Technology Readiness Level
TTCP	Telemetry Tracking and Command Processor
TWTA	Traveling-Wave Tube Amplifier
UHF	Ultra-High Frequency
WBS	Work Breakdown Structure
X-DST	X-band Deep Space Transponder

1. Introduction

The success of a space mission coincides with the accomplishment of its objectives. This could be achieved only by defining proper requirements in the Phase-A of the mission design.

Such requirements must be defined on the basis of several aspects, apart from the pure objectives of the mission itself. Considerations about the operational environment, the lessons learnt from previous similar missions and the readiness in technology level are needed to achieve deep comprehension of the opportunities and criticalities that could determine the success of the quest.

For this scope, in this report the aforementioned aspects related to the MARS-PENGUIN mission are detailed.

MARS-PENGUIN is a mission to visit the Southern Polar Cap of Mars with three main objectives:

- Deepen the knowledge about the seasonal evolution of southern polar caps on Mars;
- Perform in-situ analyses to characterise the region above the sub-glacial lake discovered in the south pole region, and study its interaction with the Martian atmosphere;
- Conduct in-situ prospecting to understand the geyser-like eruption phenomena.

The design will answer to these objectives, but to define the **Measure of Merit (MoM)**, the performance for these objectives needs to be defined.

In the next chapters all the subsystems necessary for the mission will be defined and sized so as to ensure the feasibility of the mission.

2. Mission Environment Analysis

2.1 Landing site

The selection of the landing site for MARS-PENGUIN mission is strictly constrained by its objectives. Indeed, the mission shall sample the geysers ejecta and the sub-glacial lake region, that was discovered by **MARSIS**, an instrument on the Mars Express orbiter [1].

For this delicate operation, two possible strategies have been considered: landing in the lake area and then move to the closest geyser site or vice versa.

In order to grant a safe landing, the following requirements for the site have been selected:

- be a planar region (slopes no steeper than 10°)
- be bare of cliffs or jagged peaks
- have a low density of rocks of relevant sizes

Based on the listed requirements and the following considerations, the option of landing firstly in the lake region has been selected.

First of all, the main goal of the mission is to analyse the lake region, while the geyser investigation is a secondary objective. Therefore, it would be better to reach the lake site firstly, since some fails may occur during the transfer geysers-lake, leading to a failure.

Besides, the lake region is very flat, while in the geyser site the presence of more irregularities is foreseen because of these explosive phenomena. Moreover, a geyser eruption may occur during landing. Of course, it may be possible to land a bit far from the geyser area, but still this region presents more uncertainties and this additional distance should be covered by the ground vehicle.

An analysis of the landing region has shown that there will not be issues with big slopes, big rocks and great amount of dust. This has been confirmed from the albedo spectrum studies carried out in the South pole region, that indicate a predominant presence of material with high thermal inertia, excluding a high quantity of dust [2].

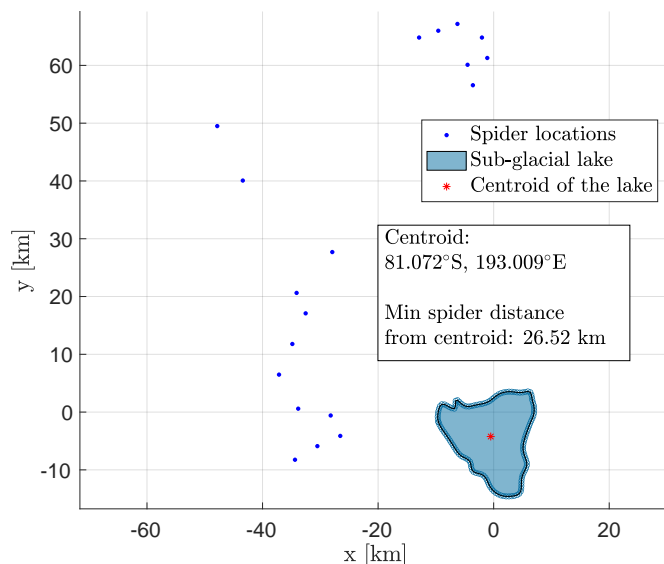


Figure 2.1: Sub-glacial lake region and closer geysers.

Given the choice to land firstly in the lake region, an analysis of the images taken by MARSIS has been carried out, to find out the closest geyser sites.

For this study, the lake geometry has been reconstructed by means of the [3] software, which allows to perform data points extraction from images. The image of the lake was taken from [1].

Using Haversine formula (Equation 2.1), the distance between the centroid of the lake and the nearest spider site has been computed as 26.52 km.

$$d = R_{\text{planet}} \cdot \arctan 2(\sqrt{a}, \sqrt{1-a}) \quad \text{where} \quad a = \sin^2\left(\frac{\Delta_{\text{lat}}}{2}\right) + \cos(\text{lat}_0) \cos(\text{lat}_{\text{spid}}) \sin^2\left(\frac{\Delta_{\text{lon}}}{2}\right) \quad (2.1)$$

From the analysis, it has emerged that any point within the lake's area (that extends for 191.8 km²), will be at a distance lower than 30 km from at least one spider (Figure 2.1).

2.2 Geysers

For almost two decades, since their identifications the geyser phenomena and the subsequent formation of the araineform terrains (denoted also spiders) have been studied. One of the main objectives of the MARS-PENGUIN mission is to deepen the knowledge of the geyser phenomenon as well as to confirm the studies done so far.

Geysers are seasonal events occurring in the early of southern spring. They form in the *cryptic* region of the South pole. Due to the condition of the latter, part of the ice condenses into the form of slab which is composed of larger grained solid CO₂ (polycrystalline ice), that is mostly transparent to visible light and opaque to the thermal infrared spectrum [4]. The layer of CO₂ ice performs a self-cleaning activity becoming transparent as the dust particles embedded in it migrate to the ground as a consequence of heating by solar radiation. Thus, when on ground these are heated up by the solar radiation, the basal sublimation at the bottom of the slab starts with a fast increase of pressure between the ice and the ground [5]. The gas enters and pressurises the porous substrate, until it increases leading to the slab's ruptures in its weakest point and so to gas jetting activity. Therefore, the gas escapes from substrate, entraining material at the substrate-free space boundary that produces the spiders [4]. The entrained material is lifted through the forced opening in the ice, forming an atmospheric plume. Material in this plume can be transported downwind before settling on the surface, forming fan-shaped deposits [6].

The nearest geyser

The condition of the presence of geyser in a region, consequently the formation of the spiders and their shapes, it depends on the soil's permeability, cohesion and porosity. The nearest geyser sites to the sub-glacial lake have various thin araineform terrains, shown in Figure 2.2. These are characterised with rough central pits which usually have irregular shapes and radially organised dendritic troughs. They sometimes are connected by troughs which make it hard to count and to distinguish them. Generally thin spiders have an extension that goes to 50 to 500 m, maximum trough width of 3 to 7 m and depth ranging from 0.6 to 2 m. Under the consideration of [7], the nearest spider's shape is characterised by an underlying soil that has:

- Low permeability such that restricts the gas flow causing a faster rise of local pressure. Sufficient pressure could be accumulated over a shorter distance to initiate gas jetting. Thus, it possibly leads to reduced spacing of spiders;
- High porosity of the substrate indicates higher capacity for containing sublimating CO₂ gas;
- High cohesion overlying soil determines the thin spider shapes with long dendritic structures.

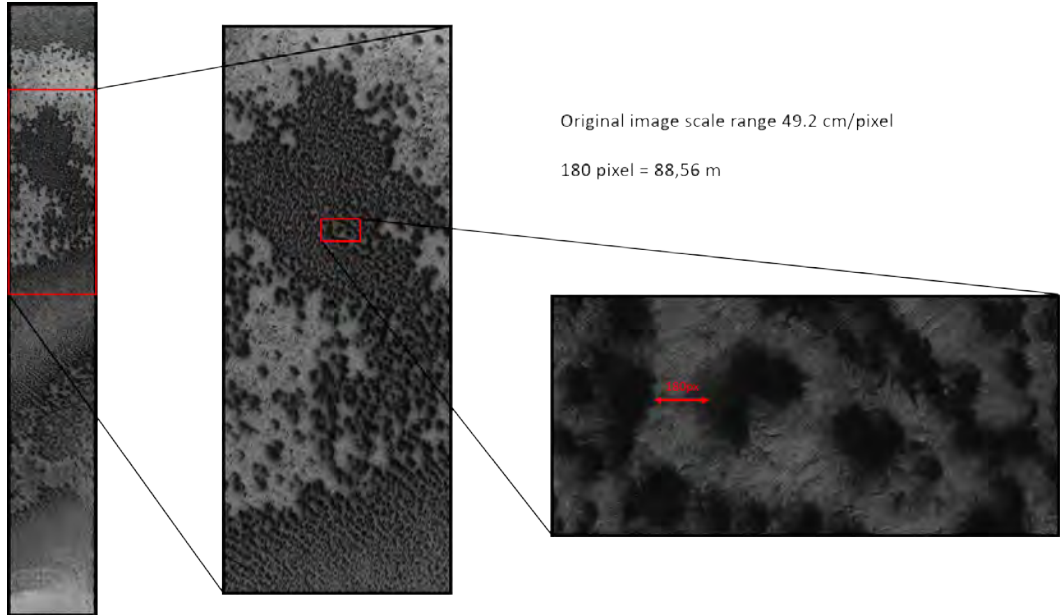


Figure 2.2: The nearest thin geyser, centred approximately at 189.217° E and 80.687° S. HiRISE image: ESP_056553_0990 was acquired at $L_s = 233.8^\circ$ with 49.2 cm/px.

2.3 General aspects

Temperature

The average temperature in time at the location of interest is about 140 K during winter and 210 K during summer, but to retrieve the evolution of temperature throughout a year, the Mars Climate Database (MCD) v5.3 is adopted. As explained in [8], an interpolation method to provide a global data coverage is used. In Figure 2.3a, the maximum and the minimum temperature of the region of interest is shown. It is worth mentioning that the non-smooth results are caused by the interpolation process.

Pressure

The same analysis has been computed for the pressure, as done for temperature based on the MCD, as shown in Figure 2.3b. It is worth noting that the pressure varies during a sol, but this aspect is not significant to be taken in account.

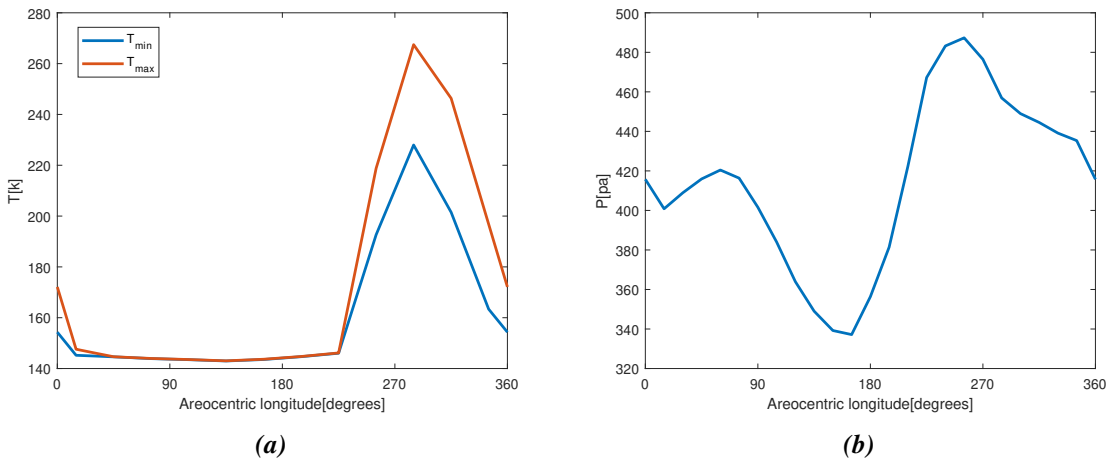


Figure 2.3: Temperature range (a) and annual pressure evolution at local noon (b) throughout a martian year at 81° S 193° E.

Solar Radiation

Mars is tilted of an angle of 25° , therefore the planet has different seasons. The landing site of the MARS-PENGUIN mission is at polar latitudes, which means that it is possible to go from periods where there is no Sun light (during southern winter) to periods where the Sun never goes below the horizon (during southern summer). The elevation of the Sun at $193^\circ\text{E}, 81^\circ\text{S}$, through a martian year is found thanks to the NASA tool Mars Trek [9]. The results are shown in Figure 2.4a.

The elevation of the Sun can influence also the variation of solar radiation on the Martian surface, which is influenced also by the varying Sun-Mars distance and the opacity of the Martian atmosphere (the amount of atmospheric dust is a relevant element to be considered). Based on the MCD, the solar flux to the region of the interest is shown in Figure 2.4b throughout a sol for four representative days regarding the season solstices.

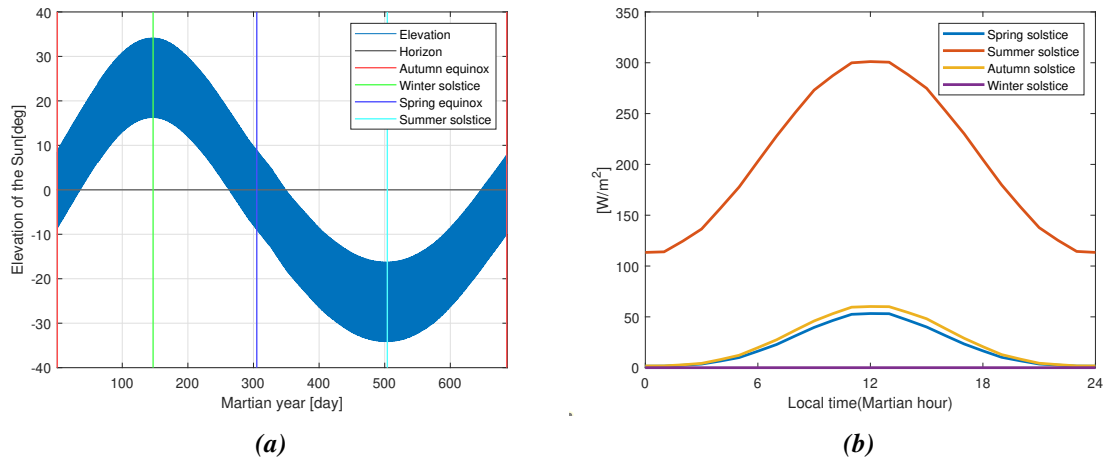


Figure 2.4: (a) Elevation of the Sun at 81°S 193°E in a martian year; Solar flux to the region of interest during a sol.

Events which can affect the amount of solar radiation arriving at the surface are eclipses. Mars has two irregularly shaped moons called Phobos and Deimos, which are both smaller than 25 km in diameter. The inclination of the two orbits is very small: respectively 1.1° and 2.4° . Due to the little dimensions and inclinations, the two moons do not reduce the radiation arriving to the MARS-PENGUIN site.

South Polar Cap

Mars South pole's CO_2 inventory can be divided into buried ice deposits and two broad surface ice caps, the temporary seasonal cap and the permanent South Polar Residual Cap (SPRC).

The buried deposits are located below the South Polar Layered Deposits (SPLD) and are comprised mostly of bands of dust and water ice in addition to the buried subsurface CO_2 ice reservoirs. A map of the SPLD thickness is shown in Figure 2.5.

The seasonal cap is a temporary CO_2 ice sheet that extends from the pole to latitudes as far north as -50° , and has a thickness between 0.9 to 2.5 m [10], which implies in an increment of the altitude depending on the latitude, as shown in Figure 2.6 [11].

Dust Storms

A frequent feature of the Mars surface and atmospheric environment is the presence of dust storms. One measure of the intensity of a Martian dust storm is its optical depth τ , which is a measure of the attenuation of a beam of sunlight as it passes through the entire (dust-obscured) atmosphere. If a dust storm τ value exceeds about one, the surface would still receive daytime sunlight through the hazy dust layer(s), but a surface based observer would be unable to see a clearly-defined edge to the apparent disk of the Sun through the "overcast" [12].

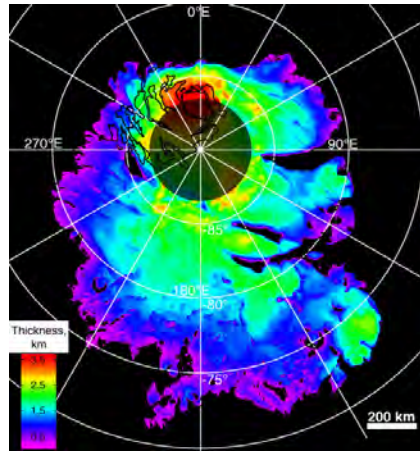


Figure 2.5: The map shows the thickness of the SPLD of Mars. Credits: NASA/JPL/ASI/ESA/University of Rome/MOLA Science Team/USGS

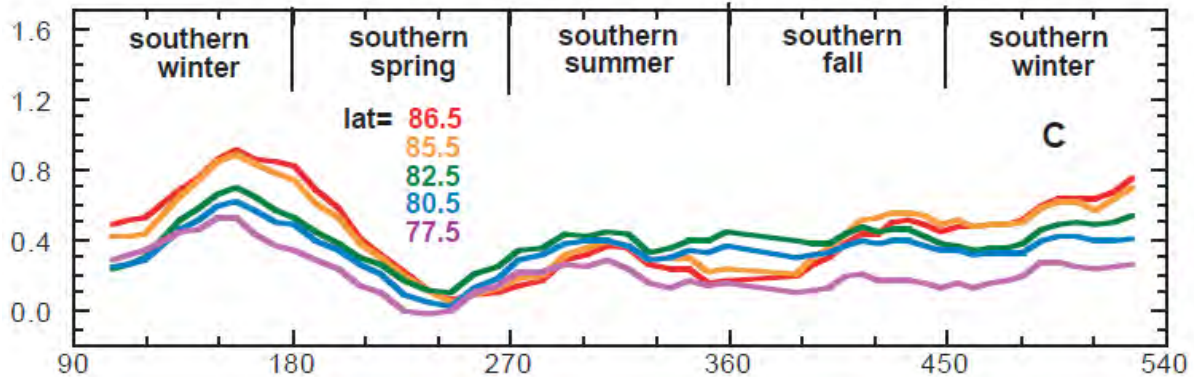


Figure 2.6: Latitudinal profiles of elevation change (Δh) over the course of the MGS mapping mission and martian seasons (solar longitude L_s) in south polar regions

Dust storms tend to occur near planetary perihelion. Since perihelion nearly coincides with the southern summer solstice, the resulting intense summertime radiation triggers dust storms that may last for several months. At such time, the optical depth can approach a value of five or more, adequate to obscure all surface features as seen from space or to make the Sun invisible from the surface.

Global storms over the years do not occur with any regularity [13] and, after a storm, normal conditions resume in 50 to 100 days. The likelihood of a dust storm occurring at a given Mars landing site on a given date cannot be made with any more accuracy than a prediction of a storm for a specific location and time on Earth.

Dust storms significantly affect surface temperature. Since dust blocks incoming sunlight, it lowers average temperature and significantly lowers maximum temperature. Dust also blocks outgoing thermal infrared radiation from the surface and raises minimum surface air temperature.

Below in Table 2.1 are presented the types of dust storm.

2.4 Criticalities and opportunities

From the bibliographic review on the environmental aspects related to MARS-PENGUIN mission, some considerations arise about the chances to be taken and critical points that will have to be faced during the design process. The results of the discussion are summarised in Table 2.2.

2. Mission Environment Analysis

MARS-PENGUIN

Type	Range for latitude of origin [°]	Season of origin (L_S [°])	Typical duration (Earth days)	Typical extent [km]	Other remarks
Local	+70 to -75	All	4-10	100	No rapid expansion
Type A	+50 to -60	$192 < L_S < 310$	70	2500	Expansion east-west
Type AB	-20 to -60	205	90	20000	Circle globe
Type B	-20 to -60	$250 < L_S < 310$	100	Global	Cover globe

Table 2.1: Classification of Martian dust storms

Aspect	Opportunities	Criticalities
Surface	Possibility to observe directly the evolution of a geyser phenomenon. Possibility to understand if the composition of the soil is affected by the presence of a sub-glacial lake.	Geyser phenomena occur only in spring. Extreme conditions: low temperatures and Sun a few degrees above the horizon. The mean chemical composition of the soil could cause a low corrosion effect on materials. Physical properties of the soil could create problems to both sampling and movement on the surface. The ice can melt/sublimate while taking samples of it.
Atmospheric	Possibility to study the seasonal ice.	The extremely thin atmosphere makes it difficult to softly land an object on Mars' surface. The rover will have to withstand dust storms, which may also cause a considerable reduction in terms of solar radiation available for powering the helicopter and the possibility of wear of mechanisms. The rover will have to survive in martian winter.
Illumination	Possibility to understand if moving during the martian night is efficient or not.	The south pole will be in dark for about half of the Mars orbit revolution.
Radiation	Possibility to exploit solar radiation as a power source for the helicopter.	The solar radiation reaching the Martian south pole is in general pretty low, in particular during southern winter time.

Table 2.2: Table of the criticalities and opportunities identified per each environmental aspect

3. State of the Art

3.1 Missions to Mars

Since the beginning of space exploration, Mars is the place in the Solar System in which most missions have been attempted (excluding the Moon). The first ones started at the beginning of the 60s, but it was necessary to wait until 1965 for the first successful mission, when the American spacecraft Mariner 4 completed a flyby of the planet. Some of the missions to Mars have accomplished their objectives and have obtained positive results, as the rover Curiosity which is still operational, whereas others failed. Moreover, there are missions that will begin in just a few months, and others under development for the near future.

Among the past missions, only those that could be useful as baseline for MARS-PENGUIN mission were chosen. The selected ones are reported in Table 3.1 in chronological order.

Mission	Focus
Viking 1 & 2 (1975)	Orbiter and lander incremented the knowledge of Mars, especially its atmosphere. Use of retro-rockets for landing.
Mars Pathfinder - Sojourner (1994)	First rover on another Planet. Use of airbags for landing.
Mars 96 (1996)	Orbiter, two small surface stations and two penetrators to analyse the inner surface and the atmosphere.
MGS (1996)	Orbiter that performed important studies on the topography, morphology and meteorology.
MPL - Deep Space 2 (1999)	The lander carries on-board two micro-probes to land near the south pole.
2001 Mars Odyssey (2001)	Orbiter still operating, served as a communications relay for rovers.
MER - Spirit & Opportunity (2003)	Two rovers, both has exceeded their operating planned time. Opportunity performed the longest distance driven by any off-Earth wheeled vehicle.
Mars Express - Beagle 2 (2003)	Orbiter and a lander. The first discovered a sub-glacial lake near the southern polar ice cap.
MRO (2005)	Orbiter still operating. It is used to examine potential landing sites for future surface missions and to provide a high-data-rate communications relay for other missions.
Phoenix (2008)	First successful landing in a martian polar region.
MSL - Curiosity (2011)	Massive rover to analyse atmosphere composition and soil, using a drill. Aerodynamic entry using a capsule, parachutes and a sky crane.
MGH (2016)	Should have investigated the geysers found in the south pole.
ExoMars - TGO (2016)	Orbiter and EDL demonstrator. The orbiter is used to analyse the atmosphere composition and as a relay.
InSight-MarCo (2018)	Couple of relay CubeSats with a lander. The latter is equipped with a RA to position the scientific P/L to its relative place on ground.
Mars 2020 - Perseverance (2020)	Rover that will seek signs of ancient life and collect rock and soil samples for possible return to Earth. Almost a twin of Curiosity.
ExoMars 2022 (2022)	Kazachock lander and Rosalind Franklin rover will seek for organic material.

Table 3.1: Past and future missions of interest

In the following sections, a deeper explanation of particularly relevant missions for MARS-PENGUIN is reported.

3.1.1 Past missions

Among all past missions on Mars, the closest ones to MARS-PENGUIN in terms of objectives are [MPL](#) and [MGH](#).

Mars Polar Lander (MPL) - Deep Space 2

MPL would have been the first-ever spacecraft to land on a polar region of the Red Planet, particularly at the South Pole, but contact was lost with both the Mars Polar Lander after the [EDL](#) phase. Designed to dig for water ice on Mars with a RA, one of its primary science objectives was to conduct a visual survey of polar caps, largely unknown dome of ice and dust, characterise the mineralogical makeup of the layered terrain, study the soil and climate of Planum Australe and test new technologies on behalf of future science missions.

Mars Geyser Hopper (MGH)

The Mars Geyser Hopper is a mission concept with the objective to investigate the springtime carbon-dioxide geysers found in regions around the South Pole of Mars. Its design is based on the Phoenix heritage systems and approach, but uses a single [ASRG](#) as the power source, rather than twin solar arrays, and it is designed to last over a one-year stay on the South Pole. The spacecraft will land at a target landing area near the South Pole of Mars, and thanks to its ability to “hop”, after a summertime landing, it will re-position itself close to a geyser site and wait through the winter until the first sunlight of spring to witness first-hand the geyser phenomenon [14].

It had a March 1, 2016 launch date requirement, but before this date [NASA](#) cancelled Lockheed Martin’s [ASRG](#) development contract for economic reasons, due to NASA’s planetary science budget cut, and up to this day only the project remains.

3.1.2 Future missions

There are several future missions that aim to study Mars in greater depth. In particular, two missions have been selected because of the high number of elements in common with MARS-PENGUIN: Mars 2020 by [NASA](#) and ExoMars 2022 by [ESA](#) and Roscosmos.

Mars 2020 - Perseverance rover and Mars Helicopter

The mission consists in bringing a rover, Perseverance, and an helicopter to the surface of Mars. The rover, which is very similar to Curiosity, has to search for any sign of ancient life on the Red Planet and has a drill in order to collect samples of rocks and soil. The helicopter instead is just a technology demonstration. The mission also provides opportunities to gather knowledge and demonstrate technologies that address the challenges of future human expeditions to Mars.

ExoMars 2022 - Kazachock and Rosalind Franklin

ExoMars (Exobiology on Mars) is an astrobiology programme by the European Space Agency (ESA) and the Russian Space Agency Roscosmos. This is the second part of the programme and it is planned to be launched in 2022 and it shares the same objectives as ExoMars 2016. It will be the first mission to combine the capability to move across the surface and to study Mars at depth, using the Kazachok lander that will deliver the Rosalind Franklin rover on the surface. The primary objective is to land the rover at a site with high potential for finding well-preserved organic material, particularly from the very early history of the planet.

3.2 Lessons learnt

Based on the analyses of the relevant aspects of past missions, some lessons learnt and design strategies have been here collected to be used as a baseline for the MARS-PENGUIN mission design.

Technological solutions & performance

- Power source: [SA](#), [RTG](#), [ASRG](#), lithium batteries, NiH₂ batteries.
- Landing parachute, airbags, propulsive landing (retro-rockets).
- Aerodynamic reentry: sky-crane landing, spin-stab during cruise, liquid cooling.
- Sampling methods: free ranging rover, robotic arm, penetrator, drill, mole, hopper.

Critical aspects

There are several critical aspects that caused the failure of some missions to Mars:

- dust storm could cause problem in the instrumentation and reduce the sun light reaching the solar panels;

- during the [EDL](#) if the landing system does not work properly, the lander/rover could crash on the Martian surface;
- choosing the landing site where to land depending on the soil morphology and on the season of the year.

Sizing criteria

The sizing of a space mission includes research activity, scientific conception, spacecraft and equipment design and development, selection of contractors, development costs, launch capability, costs, mission operations, data analysis and dissemination of scientific results. A very common technique to run all the trade-offs is called [Faster-Better-Cheaper principles \(FBC\)](#). The main idea is to increase the scientific return on a given investment [15]. Generally, the following considerations should be taken into account:

- some phenomena require large equipment in order to be observed;
- the payload dimensions and quantity limit the minimum size of the vehicle;
- the maximum size of the probe is limited by the launcher capabilities;
- the costs and risks depend on the size of the vehicle;
- low [TRL](#) solutions higher overall risks.

Operation strategy

The climate conditions are a relevant topic regarding the operational environment of Mars, as analysed in chapter 2. The choice of the season in which the mission is carried out is very important, especially regarding the poles.

For what concerns the operational configuration, it can be noted that most missions that involve the use of a rover often include the use of an orbiter, and not only a lander. Since the [EDL](#) phase is one of the most critical phases, in case of failure the mission can still fulfil some scientific requirements with the working orbiter.

Level of autonomy

All spacecrafts must be given a high degree of autonomy due to their low-bandwidth and high-latency communication channels to Earth. In the following are described some examples of the already mission studied:

Sojourner rover first spacecraft to autonomously drive on another planet. Sojourner operated in a semi-autonomous mode, with periodic communication with Earth via the Pathfinder lander.

MER both Spirit and Opportunity had driven many miles lasting well past their projected three-month lifetime and expected distances travelled.

MSL the rover Curiosity has four pairs of black and white navigation cameras. They are used for autonomous hazard avoidance during rover drives and for safe positioning of the robotic arm on rocks and soils.

Mars2020 In the Perseverance rover engineers have added a “simple planner” to the flight software. This allows more effective and autonomous use of electrical power and other rover resources.

Failures, losses

Among many missions sent to Mars through the years some of them failed. The major reasons are: software errors, management errors, lack of time or funding and the absence of data of the Mars environment. Another cause, happened in Beagle 2, is the failure in the solar panels deployment, which has obscured the spacecraft’s communications antenna.

4. Mission Architecture

Introduction

Considering the objectives of the mission it becomes understandable how both criticalities described in detail in section 2.4 and lessons learnt from the state of the art of technology (section 3.2) affect and constrain the design of the mission.

Indeed, the harsh environment of the Martian South Pole, which has not been successfully explored yet, represents a very important aspect to be considered. Moreover, many challenges are represented by the selection of the proper technology that would allow the achievement of these mission objectives, never accomplished before, such as in-situ sampling of geysers ejecta on Mars.

For sure a driving aspect is represented by the choice of the system that will operate on the surface of the planet. Indeed, the decision to use one or more landers or rovers will strongly affect the design of the whole mission.

Last but not less important, landing on Mars is a very critical aspect and no European mission has ever accomplished successfully this task so far. The Martian environment is really influential in this phase.

4.1 Possible architectures

An overview of possible mission architectures that may be suitable for the MARS-PENGUIN mission are presented in this chapter, along with the main advantages and disadvantages of each solution, based on the already-existing strategies presented in chapter 3 and on the environmental criticalities highlighted in chapter 2.

4.1.1 Space segment

In the space segment are analysed the different options which will be taken into consideration in the criteria matrix for the launch and for the orbiter around Mars.

Number of launches

Planning two launches can be useful since it would imply to split the amount of mass which is sent towards Mars, especially if the payload has a high mass. On the other hand, using one launcher can be more efficient from the cost view point. Moreover this last option has a lower complexity and a higher reliability. The launch window for Mars is every ~ 2 years, which can be a problem in case there are two launches: if there is a delay, the second lift-off can be moved some years after the first one.

Purpose-built orbiter or not

Exploiting an already present orbiter around Mars can be an advantage from different points of view: the total cost of the mission can be reduced, the launch mass is lower and the complexity is decreased. However having a purpose-built orbiter can be useful in terms of reliability and science data return which could help the Mars segment during its lifetime (i.e. the orbiter could provide assistance during its navigation of the in-situ segment on Mars). The possibility of having a temporary orbiter -performing scientific analyses staying in orbit for a certain period before landing- has been declined since the main mission objectives do not include specific imaging from orbit and there is no need to better localise the landing site because it is already accurately defined from the mission requirements. The most important functions of the orbiter are related to telecommunications and navigation, and both cannot be performed by a temporary orbiter.

4.1.2 Mars segment

For the Mars segment three different vehicles have been considered: a rover, a hopper or a lander.

The choices of using a rover or a hopper guarantee a very good scientific return and an average result according to all the other criteria.

The use of a lander is the cheapest, lightest and simplest option. But in this case the scientific return is compromised by the impossibility of movement: a moving a part would be required to reach the geysers, so another vehicle is necessary in this case.

For these reasons the option of the lander has been discarded if not supported by a second movable vehicle.

Therefore, the possibilities analysed in the final trade-off are: a rover, a hopper, or two vehicles (one of those would be a lander).

4.2 Preliminary selection process

In order to select the best architecture in a complex model, among the methods in decision analytic, a criteria matrix has been adopted.

Firstly, the most relevant criteria for the mission are selected and weighted to see how each of them contribute in the cost function. Then, a comparison between the options is carried out with respect to each criterion. In the comparison, each option is scored from 1 to 5 with the higher the better consideration.

In Table 4.1 are reported the weights defined for the different criteria. The MARS-PENGUIN mission is the first mission that is going to analyse the Mars' south ice cap and geysers (past interrupted mission excluded), so it is reasonable to consider the majority of the concern of the project to be the amount of scientific data the mission can provide. The second and the third most crucial aspects for a Mars mission are respectively the reliability and the complexity. Moreover, minimise the power needed and the mass to launch is more relevant than the cost of the mission, since this is a pioneer mission for these objectives and the customer's major concern is the success of it and meeting the objectives rather than limiting the cost.

	Cost	Mass	Power	Complexity	Reliability	Science return
Weight [%]	8	13	15	19	20	25

Table 4.1: Weights in the criteria matrix

In Figure 4.1 the architecture tree is presented.

Given the distance between the sub-glacial lake and the nearest geyser site (~ 30 km), the possibility to exploit two different vehicles that could land in different positions of the Martian surface has been also considered. Some branches have been deleted before being analysed with the criteria matrix, since it is not feasible to launch in a single launch three different segments and it would not make any sense to use two launches to put a single vehicle into orbit.

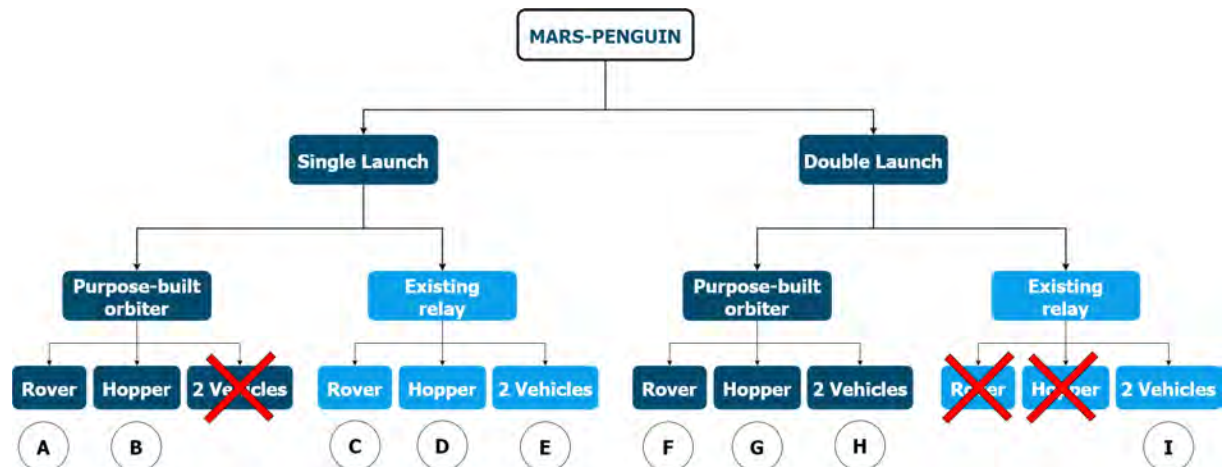


Figure 4.1: Preliminary architecture tree

The criteria matrix is reported in Table 4.2, and the two best architectures that minimise the cost function are highlighted with a yellow colour.

Considerations about the two best architectures

Both the two best alternatives do not involve the use of a purpose-built orbiter but they rely on an existing one. This choice does not limit the achievement of the MARS-PENGUIN mission objectives, as they are focused on ground operations. Telecommunications and navigation can be carried out using another orbiter, and even if this choice involves a cost for the use of a structure that may not be an ESA mission, it is still not comparable to the cost that

Architecture	Cost	Mass	Power	Complexity	Reliability	Science return	Result
	8%	13%	15%	19%	20%	25%	
A	3	3	2	3	3	4	2.97
B	3	2	3	3	3	3	2.87
C	5	4	4	5	2	3	3.62
D	5	3	5	4	2	2	3.20
E	3	1	2	2	4	4	2.85
F	2	5	2	2	4	3	3.04
G	2	4	2	2	4	3	2.91
H	2	3	1	1	5	5	3.06
I	2	4	2	1	4	4	2.97

Table 4.2: Criteria Matrix

would have been necessary for the construction of a new orbiter. Furthermore, the considerable amount of mass saved allows an heavier Mars segment.

In the following are reported some features and considerations about the two selected architectures. It must be considered that the current state of the art of Mars ground missions does not contain any type of vehicle capable of covering a distance of several tens of kilometres in a reasonably short time, therefore both the selected options would be pioneers for achieving this objective: in the case of the rover, it will have to be a long range rover while the hopper will be a ballistic hopper.

Even though these possibilities have been selected, they still have some drawbacks that has to be properly paid attention to. The Pros and Cons of the architectures are listed.

C - Long Range Rover

In order to have a rover able to cover the distance from the lake landing site to the geyser location some considerations must be done together with some calculations to assess the feasibility of the requirements to be achieved.

In Table 4.3 are reported speed-related data for different Martian rovers. It has to be noted that the velocity values are referred to commanded rover movements (ground-assisted), and that the time reported is the operating time, not the effective travelling time.

Rover	Max speed	Operating time	Max distance/day	Power	Mass
	[km/h]	[hours/day]	[m]	[W]	[kg]
Perseverance	0.152	4 h	600	110, RTG	1025
Rosalind Franklin	0.07	4 h	100-500	1200, SA	310
Curiosity	0.14	1 h 25'	200	110, RTG	899
Opportunity	0.18	4 h	177.5	300, SA	180
Spirit	0.18	4 h	124	300, SA	180

Table 4.3: Velocity and travelling distance

The distance to be travelled from the centre of the lake to the geysers' site resulted to be 26.52 km (see section 2.1). For a preliminary computation of the time needed to reach the location of interest, it was considered a worst case scenario, with a landing on the farthest point of the lake with respect to nearest geyser's location, of 27.8 km.

At this distance, a margin of 40% was added to take into account the non-rectilinear trajectory due to obstacles to avoid and impracticability of the terrain, computational errors, necessity of moving from the initially identified point to acquire better imaging of the phenomenon and other possible unconsidered setbacks, resulting in 38.92 km to cover. The rover has been supposed to travel with no interruptions for 3 h/day at a speed of 0.1216 km/h (20% less with respect to Perseverance's peak velocity of 0.152 km/h). With simple computations it has been found that the time to arrive to the geysers is 85 days, almost 3 terrestrial months.

Even if it could seem a short time, there are some considerations that strongly limit the long-range roving:

- Locomotion system design
- Operational limitations in terms of energy required (batteries to be re-charged)
- Processing capabilities of electronic equipment on-board
- Safety factors and operational robustness uncertainties
- Necessity of frequent contact with Earth
- Difficulty in mapping the terrain due to South pole perennial shadows during winter

If the option of using a long-range rover will be pursued, all these problems should be faced and overcame. In order to design a rover able to cover such a long distance in a relatively short time (3-4 months at maximum), the most challenging issue will be the design of an autonomous navigation system. This should not need frequent communication with Earth and be sufficiently autonomous to cover significant distances without stopping. The best solution would be having a rover able to travel 1 to 2 km each day and to compare orbital images with its own perceived ones. This way, the planning of the path would be easier and the travelling time will be reduced a lot. Another thing that should be taken into consideration is the fact that the region between the lake and the geysers is covered by CO₂ ice in the southern winter season and this can cause wheel slip problems, as well as the fact that in winter the solar illumination of the polar region is very poor. In order to simplify the operations, the rover should travel in a period of the year when the ice is melted and there are no illumination problems.

Pros:

- enhances mobility
- more reliable vehicle with respect to a hopper
- possibility of re-positioning after the landing and close to the geysers

Cons:

- long time requested to reach the geysers compared to a hopper
- complexity concerning the autonomous navigation system
- the rover could remain stuck in the Martian soil
- problems travelling in winter

D - Ballistic Hopper

The possibility of a fully controlled hovering motion, between the sub-glacial lake and the nearest geyser site, has been excluded due to the considerable distance to cover that would hence result in substantial gravity losses. The strategy here proposed consists in launching the hopper into a ballistic trajectory, taking advantage of the full available performance of its thrusters, let it move along an inertial trajectory with **RCS** control and eventually perform a landing burn once in the proximity of the geyser site.

This will clearly result in a less accurate landing location after the first hop, compared to a fully controlled trajectory. It should nonetheless be highlighted that lower accuracy of the landing position after the first hop is not expected to compromise the mission, given that the aim of the first hop is not to target a specific geyser but rather to approach the region so as to observe the ejecta at a safety distance and identify their exact locations. After the eruption, the hopper will be able to move closer to the location of the phenomenon by means of a short fully controlled second hop, which can be extremely precise.

In order to verify the feasibility of this configuration a 2DoF trajectory simulation has been carried out, so as to evaluate the propellant mass fraction that would be required in order to perform both the **EDL** burn⁽¹⁾ and the first hop.⁽²⁾ For simulating the landing at the lake site, the initial conditions reported in [16] have been taken as a reference, namely: $y_0 = 1.6$ km, $u_0 = 65$ m/s, $v_0 = -35$ m/s. In a worst case scenario in which the landing location after **EDL** is at the farthest point on the border of the lake from the spider site, this would translate into a ~ 30 km range of the trajectory. A propellant mass margin of 33.5% has been considered.

It has to be highlighted that for this preliminary study it was not accounted for:

- re-positioning burn in the event of landing outside the lake
- burn to perform the 2nd precise-positioning hop

Propulsive landing on Mars is usually performed by means of multiple monopropellant hydrazine thrusters. After the investigation of several off-the-shelf components, it was concluded that the desired performance level would result in an excessive mass of the monopropellant thrusters. For this reason, the possibility of using storable hypergolic bi-propellants has been explored. Indeed, the configuration chosen for the simulation makes use of

⁽¹⁾i.e. prior to the first touchdown on Mars

⁽²⁾during which the biggest deal of propulsive resources are depleted

12 Aerojet Rocketdyne R-42 thrusters (MMH/NTO). They are characterised by a specific impulse $I_{sp} = 305$ s, a steady-state thrust $T = 890$ N per engine and a valve power of 46 W. In particular, they have been chosen for the high thrust-to-weight ratio, given a mass of only 4.53 kg per thruster.

The estimated dry mass of the whole hopper (419 kg), which has been obtained through a statistical fitting. The resulting trajectory can be found in Figure 4.2. As it can be noted, the 30 km range is covered and the hopper lands with ideally zero vertical and horizontal velocity, both at the lake and at the geyser site. This corresponds to an estimated burned propellant mass of 164 kg and an additional 57.4 kg margin (i.e. an overall propellant mass fraction of 52.8%).

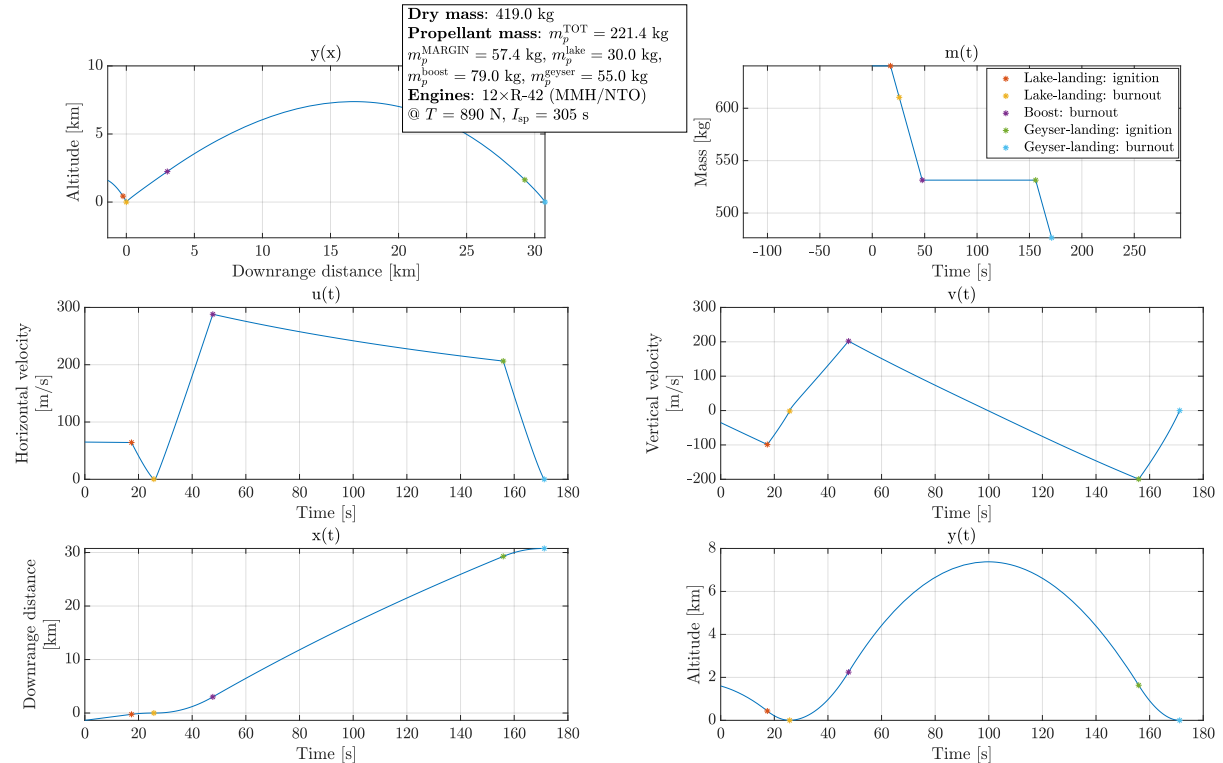


Figure 4.2: Hopper trajectory simulation

Pros:

- relatively low wet mass (640.4 kg), that would easily fit in a European launcher
- lower power requirements compared to a rover
- short travel time to reach the geyser site
- the same thrusters used for EDL are employed for moving on the surface of Mars and there is no need of a skycrane

Cons:

- lower mobility compared to a rover
- higher shocks and risks during the travel from the lake to the geyser site, compared to a rover
- need of high landing accuracy, unless substantial propellant margins are considered, to be able performing a re-positioning hop after EDL

4.3 Payload (P/L)

An overview of the given Payload (P/L) to mount on the vehicle is reported in Table 4.4 with their main characteristics. To be noted that the architectures derived consist in one vehicle to perform the sub-glacial lake and geyser analysis, therefore all the P/L are accounted inside the vehicle, as shown in Figure 4.3.

Instrument	Target	Mass [kg]	Power [W]	Purpose
1. Mass Spectrometer and Gas Chromatography for Organics	General	11.5	65	Analyse samples: Search for organic compounds investigating solid crushed samples only and characterise the molecular structures of it.
2. Raman Laser Spectrometer	General	4	30	Analyse environment: Provide geological and mineralogical information by identifying mineral phases produced by water-related processes.
3. Surface Stereo Imager	General	1.8	3	Identify sites of interest: Provide high-resolution, stereo, panoramic images. Generate range maps in support of digging operations.
4. Infrared Spectrometer	General	1.8	14	Identify potential sites: Study the mineralogical and petrographic composition of the surface near the rover.
5. Alpha Particle X-ray Spectrometer	General	0.64	1.4	Analyse environment: Identify the elemental chemistry of rocks and soils by measuring material's respond to X-rays and alpha particles.
6. Environmental Analyser	General	5.5	17	Analyse environment: Characterise the dust size and morphology, as well as surface weather.
7. Sounding Radar	Lake	0.4	20	Identify sites of interest: Determine the 3D geological context and could detect potential buried hazards that might jeopardise drilling activities.
8. Neutral Ice Subsurface	Lake	1.7	5	Identify sites of interest: Determine hydrogen content which is present as grain adsorbed water, water ice, or in hydrated minerals in the soil.
9. Dust Flux Monitor	Geyser	1.8	1.8	Collect and analyse: Used to provide real-time flux measurements of large particles, monitor the dust environment.

Table 4.4: Payload characteristics.

4.4 Auxiliary aerial vehicle

In order to support the main vehicle in its navigation and, also, to analyse better the geysers, the possibility of having a second innovative aerial vehicle has been considered. This vehicle would have some purposes in the mission such as helping the rover/hopper in its navigation in the geysers region, helping the rover in its path planning toward the geysers and help the rover/hopper in doing the analysis in the geysers region by taking images from different perspectives.

The presence of this vehicle could be justified, also, by the absence of a purpose-built orbiter in the MARS-PENGUIN mission. Indeed, the launch mass is reduced considerably and, so, it is possible to introduce a second vehicle in the mission.

Moreover, this innovative vehicle could also be a new type of technology demonstration on Mars, that might be important for future missions.

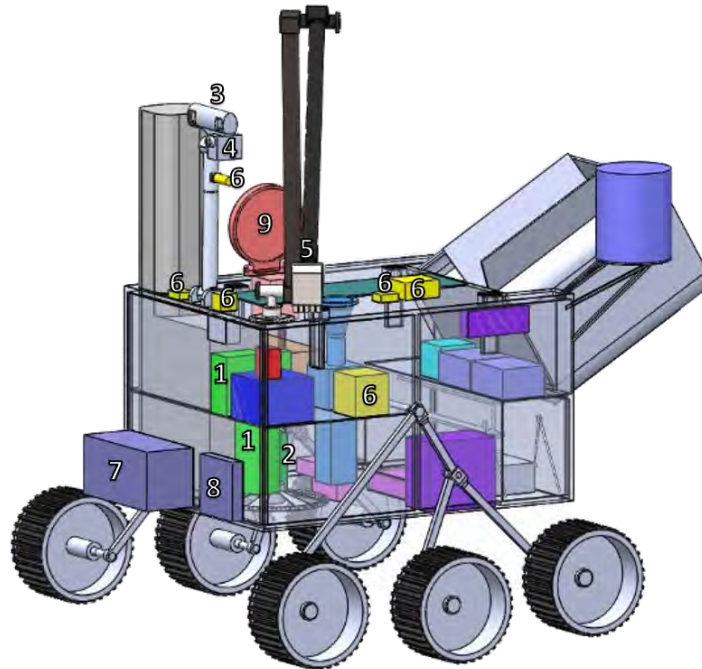


Figure 4.3: Payload positioning inside the main ground vehicle.

The three main solutions that have been analysed are reported in the following sections and are: a glider, a helicopter and a hexacopter.

4.4.1 Glider

A possible strategy that has been considered for supporting the navigation of the main vehicle is the deployment of a glider during the EDL phase. Indeed, the aircraft could glide from the landing site region of the lake towards the closer geyser site and take aerial images at high resolution.

During the years, many studies have been carried out (also considering powered planes). In particular, three interesting solutions for MARS-PENGUIN mission are reported below in Table 4.5.

Plane	Mass [kg]	Wingspan [m]	P/L [kg]	Range [km]	Endurance [min]
Mars Sailplane	5+19	3-6	0.4	70	15-20 or more
Prandtl-m	<1.5	0.6		32	10
Sky-Sailor	2.5	3.2	0.5	long-term	long-term

Table 4.5: Gliders data.[17] [18] [19] [20]

Pros:

- lightweight
- low power consumption
- cover high distances
- can exploit wind to fly longer

Cons:

- highly influenced by wind
- need of autonomous control
- image resolution dependent on flight velocity
- one shot
- folding or inflating mechanism

4.4.2 Helicopter

Another solution to provide the information supporting the main vehicle is a helicopter. This helicopter can be designed to fly in a low altitude to take images of the path of the rover toward the geysers. These high resolution images of the surface help the rover not only to have a priori knowledge of the terrain resulting in less stops and

higher velocity of the rover, but also to locate the geysers' region more precisely. The provided information can be sent to Earth through the orbiter or the rover itself to be analysed comprehensively.

The Mars Helicopter, Ingenuity, [21] designed by NASA through MARS 2020 program is defined as the baseline for MARS-PENGUIN mission. Although Mars Helicopter did not fly on Mars yet, a second generation of Mars helicopters [22] have been already proposed by NASA and have been considered here as well. The design parameters of these two helicopters are reported in Table 4.6.

	Gross mass [kg]	P/L mass [kg]	Power[kW]	Range [km]	Hover time [min]
Ingenuity	1.8	0	0.36	0.18 or	1.5
Advanced Mars Helicopter	4.6	1.3	0.88	2	2

Table 4.6: Mars helicopters proposed by NASA.[22]

Regarding the performance, a trade-off between range and endurance is being done for the two designs. Since Ingenuity has not flown on Mars yet and also since the performance of the Advanced Helicopter is predicted and is not tested and well-proved, a relatively high margin of 40% is considered to lower the performance of the MARS-PENGUIN helicopter.

The operational point in terms of range and hover time will be selected based on the mission performance of the main vehicle.

According to the sun radiation variation with respect to latitude and time of the year, the MARS-PENGUIN helicopter may face a different radiation with respect to the other two. This problem might be solved by modifying the mission performance of the helicopter to have enough time to recharge the batteries. This modification can be applied once the mission timeline is defined.

Considering the same P/L as Advanced Helicopter design, the first approximation of the MARS-PENGUIN helicopter design parameters can be listed as in Table 4.7.

Gross weight [kg]	P/L [kg]	Power[kW]	Range [km]	Endurance [min]	Batteries [A·h]
4.6	1.3	0.88	1	1	46

Table 4.7: MARS-PENGUIN helicopter design parameters

Pros:

- high image resolution in low altitude
- high operational lifetime
- capability to re-tune the mission from Earth

Cons:

- sensitivity of the mission to navigation of the helicopter
- occupying a space inside the rover/hopper

4.4.3 Hexacopter

The last solution which was taken into account to help the main vehicle during its journey from the sub-glacial lake to the geysers location is the hexacopter.

As for the helicopter, the hexacopter can fly at lower altitudes than the glider and take high resolution images. Three interesting solutions are reported in Table 4.8.

	Gross mass [kg]	P/L mass [kg]	Power[kW]
Mars Science Helicopter	17.66	2-8	3.31
6Xsol#6	6.52	0.7	1.079
6Xsol#14	6.52	0.7	1.175

Table 4.8: Proposed Mars hexacopters. [22] [23]

The pros and cons of this configuration are the same as the helicopter and can be found in section 4.4.2. Moreover the hexacopter has an advantage more: the length of the blades is lower. Thanks to that, there is not the risk to reach 1 Ma at the tip of the rotors. On the other hand, this configuration requires much more power than the helicopter.

4.4.4 Aerial vehicle selection

Three proposed vehicles are presented to show that all of them could be feasible and applicable for the MARS-PENGUIN mission. To select one, a criteria matrix has been set up to weight different criteria (Table 4.9).

Aerial vehicle	TRL 17%	Mass 32%	Power 20%	Complexity 8%	Reliability 10%	Science return 13%	Result
Helicopter	3	5	2	2	3	5	3.54
Glider	2	3	5	4	3	2	3.1
Hexacopter (Multi rotor)	1	4	1	1	4	5	2.78

Table 4.9: Criteria matrix for aerial vehicle

TRL is introduced here as a new effective criterion to consider the fact that the aerial vehicle must not limit the launch time because it is not a core part of the mission. The highest weight was given to mass indicating that this auxiliary vehicle should not affect the rest of the mission in terms of mass constraint.

As indicated in Table 4.9, the most promising aerial vehicle for MARS-PENGUIN mission is a helicopter.

4.5 Final architecture selection

Both the choices of the ground vehicle type are feasible, since they could be designed in order to be capable to cover such a large distance.

To satisfy the objectives of MARS-PENGUIN mission the proposed vehicle is a rover, that will be called “Skipper” (see appendix A.1 for the name meaning). The choice is motivated by the superiority of a rover over a hopper with regard to the crucial parameters for the MARS-PENGUIN mission: scientific return and reliability. Although the power needed and the final mass budget -accounting for the Entry Capsule, Sky crane and Cruise Module- would be higher, the need to have a vehicle capable of achieving the objectives with a wide margin of movement and the importance of the reliability has led to this choice.

The preliminary mass obtained for this architecture has been obtained from a statistical analysis, which is explained in section A.2. Therefore, the total mass obtained is 2281 kg.

In addition, the mission will also include a secondary aerial vehicle, given its high contribution in terms of demonstration and scientific return. This choice is also made possible by the absence of an orbiter and the resulting savings in mass.

The aerial vehicle will be a helicopter called “Kowalski”. It is considered that the helicopter is placed inside the rover and it is detached when the rover reaches geysers location.

4.5.1 Planetary Protection and Cleanliness and Contamination Control

Missions to Mars must cope with stringent Planetary Protection (PP) as well as Cleanliness and Contamination Control (C&CC) requirements, in order to minimise cross-contamination between Earth and Mars. The European Cooperation for Space Standardisation (ECSS) defined some requirements, reported in the ECSS-U-ST-20C document, according to the COSPAR’s planetary protection policy [24].

MARS-PENGUIN mission belongs to the Category IVb of this policy, which includes surface missions to a target body for which there is significant scientific interest relative to the process of chemical evolution and the origins of life and for which scientific opinion provides a significant chance that contamination by a spacecraft can compromise future investigations. The b section is for missions with life detection investigations.

Since the on board scientific instruments are characterised by an extremely high sensitivity, even a tiny amount of organics could interfere with their measurements. Therefore, it is essential to avoid chemical-physical interferences

that could result in a “false positive” (a compound carried from Earth is misinterpreted as from Martian origin) or even a “false negative” (a terrestrial contaminant acts to suppress the detection of a Martian species).

The landed system shall minimise the biological contamination of the planet surface, in order to preserve its pristine conditions and to avoid the detection of any form of life carried from Earth.

The **C&CC** discipline pertains to prevent any molecular and particulate organic contamination, to avoid false positives during life detection and to guarantee the nominal performances of all contamination sensitive items until the end of mission.

The main drivers of the PP and **C&CC** for MARS-PENGUIN mission are:

- Avoid contamination that can influence on scientific payloads (Mass Spectrometer, RLS) performances (losses of system signal and degradation of the signal to noise ratio)
- Avoid contamination propagation to other instruments or Scientific Laboratory.
- Protect Mars environment from terrestrial biological contamination.

MARS-PENGUIN could use the contamination control approach that Thales Alenia Space Italia (TAS-I) promoted for ExoMars mission, since also this mission is classified as IVb in **COSPAR** categories [25]. It is a Screening Outgassing Test Campaign to identify, among all the contaminants potentially outgassed from the **S/C** materials, the chemical compounds which could interfere with life detection experiments, during the on ground integration and testing activities, the cruise to the planet and the operational phase on Mars.

5. Preliminary Mission Definition

In order to have a good foundation for the following preliminary design for each subsystem, the mission phases are reported in the following sections, together with their relative tasks and modes.

5.1 Phases, timeline and ConOps

To better understand the evolution in time of MARS-PENGUIN mission, a sketch in terms of elapsed months is shown in Figure 5.1.

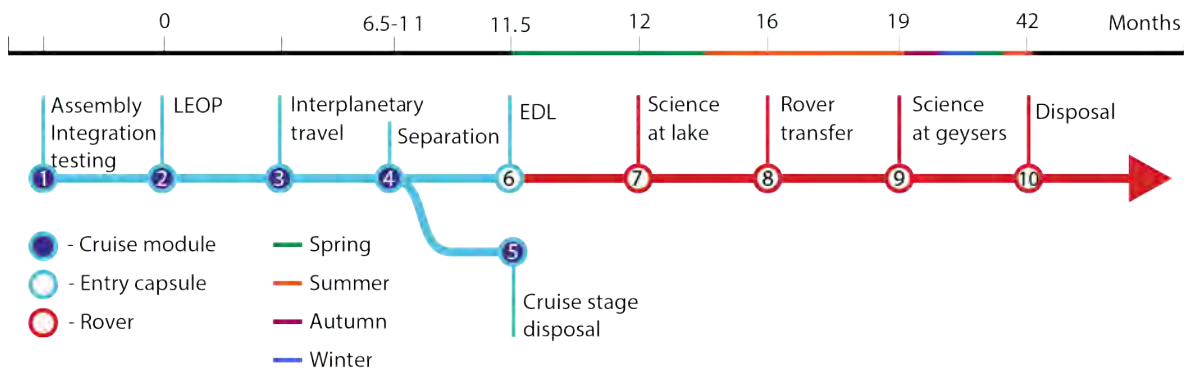


Figure 5.1: Timeline of the mission. The seasons are relative to the southern hemisphere.

It can be noticed that the mission is divided into space and ground segments. The space segment plays its role when the spacecraft is released into the interplanetary trajectory. The ground segment only starts after the separation from the cruise stage, or once the descent measures are started.

The following Table 5.1 shows all the mission phases, with a short description.

Phase	Description
Assembly, integration and testing	<i>Project integration and test:</i> During this phase all the system is tested by performing functional and environmental testing. A full system verification is provided. <i>Launch Integration:</i> here the integration phase can be repeated in a launch-integrated configuration.
LEOP	<i>Launch:</i> from the launch countdown, until orbit injection. During the launcher ascension the spacecraft should remain "silent". Obviously, the power supply, data handling and thermal control systems must be active at some level during all phases and the whole mission duration. The main drivers are to withstand vibration and acceleration loads present into the path of the launcher through the Earth atmosphere. A strong ambient pressure decompression takes place. <i>Deployment:</i> After detachment from the launcher the spacecraft should be brought in operational mode by activating the the corresponding subsystems. Then detumbling and a telemetry exchange sequence must be performed. As a final step a trajectory correction may be executed if needed. The spacecraft will be subjected to radiation coming from sun and space during the whole mission. It is important to maintain required attitude for communication and propulsive manoeuvres. Critical events like antenna deployment will take place.

continued on the next page

Interplanetary travel	After LEOP the spacecraft is travelling on its way to Mars. Only telemetry exchange and trajectory corrections will occur. The major difficulties linked to the space environment are space and solar radiation, and thermal control.
Separation	Here the separation of the ground segment from the cruise stage takes place. A final TCM could happen before separation. The drivers are the reliability of the separation technique and the proper functioning of the separated segments.
EDL	The ground vehicle must be safely deployed to the Martian surface without sustaining any damage. All possible solutions include the deployment of parachutes after the velocity of the capsule has been partially slowed down by means of friction (the presence of an heat shield is crucial). The final descend might be performed by means of a sky crane or retrorockets and airbags. This phase will be monitored on Earth by the communication of the descent module with a relay orbiter around Mars.
Ground operations	<p><i>Science operations in lake region:</i> once the rover has landed, it can begin working as intended, once all the system checks have been performed. It will need to perform sample collection of the icy soil in at least 5 different locations in the sub-glacial lake region.</p> <p><i>Rover transfer:</i> a crucial part of the MARS-PENGUIN mission is the rover journey from the sub-glacial lake region to the geysers site. The transfer will be performed during summer in order to exploit the solar illumination for guidance and to have less harsh conditions in terms of temperature and CO₂ ice on the surface.</p> <p><i>Science operations at the geyser site:</i> once the geyser site has been reached, the rover should start taking images in order to observe any geyser explosion from a safe distance. Once the explosion is occurred, the rover shall get closer to the geyser to sample and analyse the ejecta particles.</p> <p><i>Non-nominal conditions:</i> the ground vehicle must be able to withstand non-nominal conditions, and also eventual failures. Custom-tailored modes are to be developed for these situations, in order not to compromise the mission, if not for a small period of time.</p>
Disposal	Disposal occurs at the end of the life cycle of the mission. It should provide a safe decommissioning of the ground vehicle, but also of the cruise stage and of other potential parts (sky crane, parachutes...) according to COSPAR's planetary protection policy [24].

Table 5.1: Mission phases

Based on the phases defined, here are reported the Concept of Operations (ConOps) of the overall mission shown in Figure 5.2.

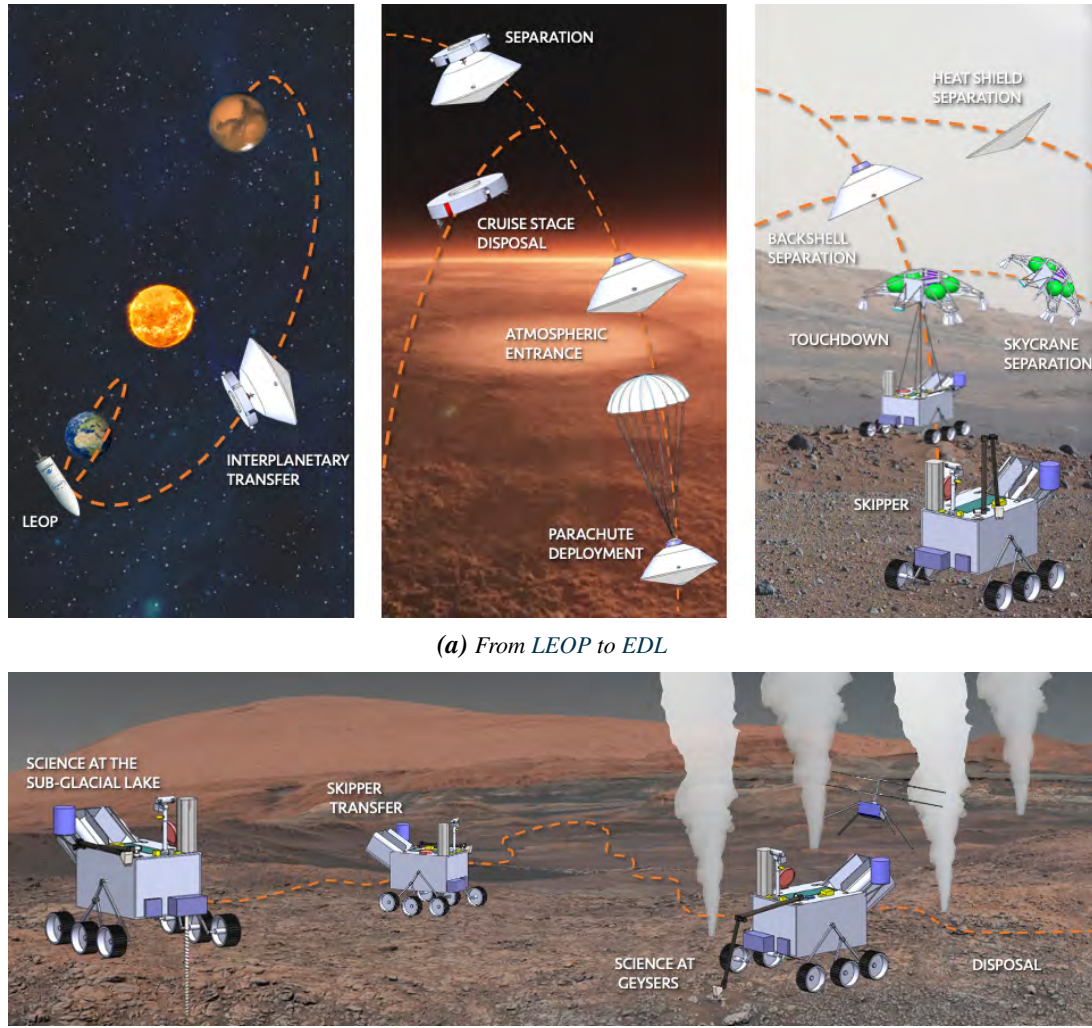


Figure 5.2: ConOps from transfer to disposal of each segment.

5.2 Tasks

After defining all the mission phases and a preliminary timeline, the step further is to define the various tasks for each single phase of the mission, as shown in fig. 5.3. These subdivisions help to break down all the functionalities the ground, the space segment and the spacecraft must have in order to facilitate the development of solutions to answer to each of these tasks.

5. Preliminary Mission Definition

MARS-PENGUIN

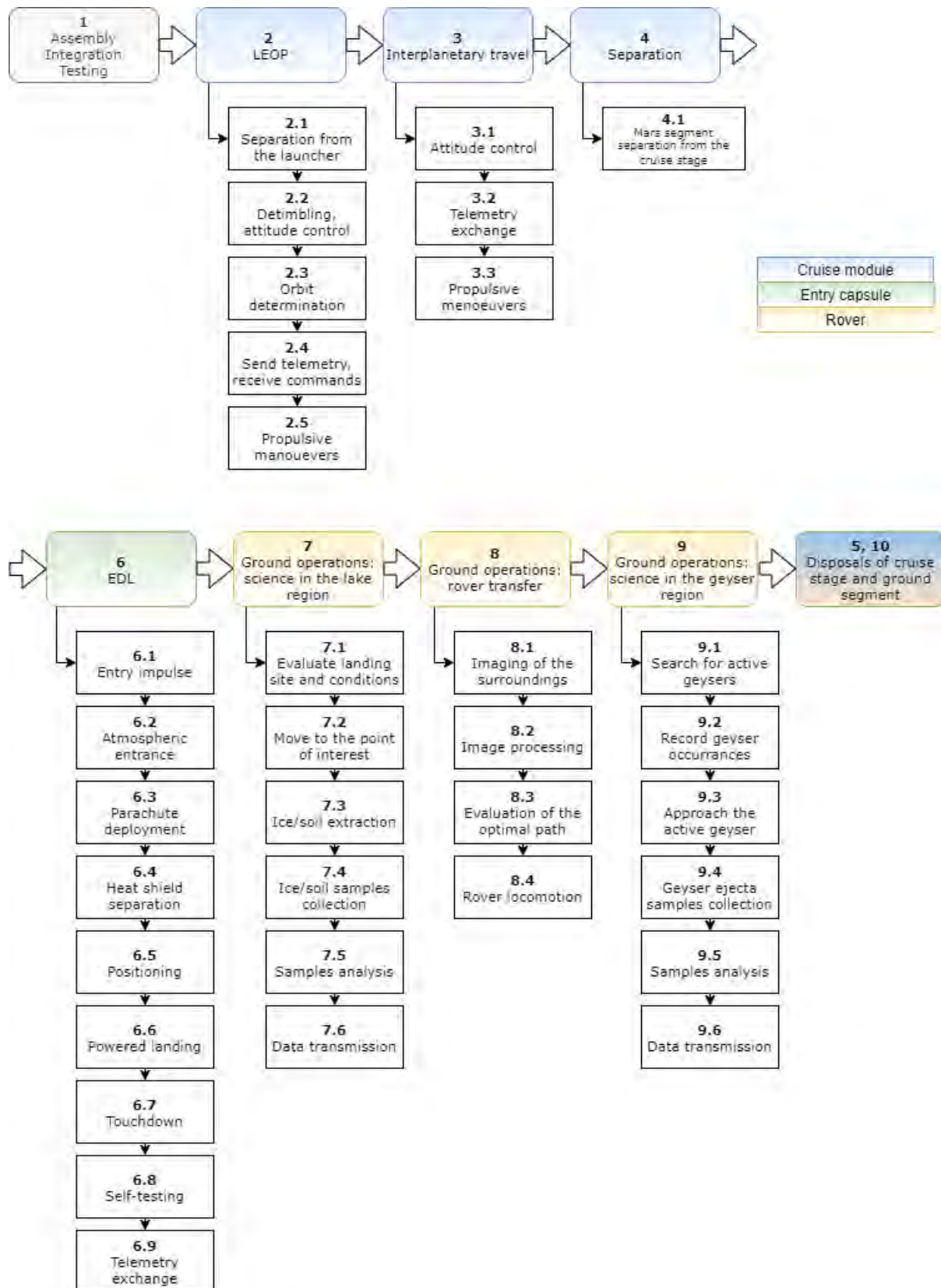


Figure 5.3: Mission tasks

5.3 Modes

Once the mission phases and tasks have been properly outlined, the modes of the mission have to be defined. These modes, which are shown in Table 5.2, should be seen as subroutines that have to be employed by the ground and space segment to overcome all the different scenarios that could occur in the mission, from simple tasks to non-nominal conditions.

Mode	Description	Active systems
SLP - Sleep mode	Spacecraft or rover are switched off, minimum power. TCS still active.	EPS-OBDH-TCS
STB - Standby mode	Active with minimum power, waiting for commands	EPS-OBDH-TCS
STE - Essential check mode	Diagnoses electrical equipment	EPS-OBDH-TCS-TMTC-P/L at minimum
STC - Complete check mode	Diagnoses all the subsystems	All systems at minimum
ATT - Attitude mode	Active during spacecraft attitude manoeuvres	ADCS-EPS-OBDH-TCS-PROP
PRP - Propulsive mode	Active during in-space manoeuvres	ADCS-EPS-OBDH-TCS-PROP
COM - Communication mode	Space and Mars segments use this mode to send or receive information	TMTC-OBDH-EPS-ADCS-TCS
LAN - EDL mode	Used in atmospheric entry to perform autonomous descent	ADCS-PROP-EPS-OBDH-TCS-TMTC
SWU - Software update mode	Active while the software is updating	EPS-OBDH-TCS
SAF - Safe mode	Decreases the impact of active faults shutting down all the systems at risk and works on solutions to the faults	EPS-OBDH-TMTC + other not at risk systems
MAN - Manual mode	Operations in non-nominal conditions	EPS-OBDH-TMTC + other systems manual
RNA - Rover navigation mode	The rover analyses the environment with cameras and other instruments and processes the data to define an optimal path	EPS-OBDH-TCS-RBT-P/L
ROV - Roving mode	Moving on the Martian surface	EPS-OBDH-TCS-RBT-P/L
LRS - Lake region sampling mode	Perform sampling of the soil in the lake region	EPS-OBDH-TCS-RBT-RBT
LRA - Lake region analysis mode	Perform analysis of the soil samples in the lake region	EPS-OBDH-TCS-RBT-RBT
GRS - Geyser region sampling mode	Perform sampling of the geyser ejecta particles	EPS-OBDH-TCS-RBT-RBT
GRA - Geyser region analysis mode	Perform analysis of the samples geyser ejecta particles	EPS-OBDH-TCS-RBT-PL

Table 5.2: Mission modes

Once all these modes have been defined, we can associate one or more of them to each phase of the mission as shown in Table 5.3, in order to have a more general idea of what is happening at every step of the mission.

Phase	Possible modes
LEOP	SLP - COM - ATT - PRP - SAF - STE
Interplanetary travel	COM - ATT - PRP - SAF
Separation	COM - MAN - ATT - PRP - SAF
EDL	LAN - COM - ATT - PRP - STE/STC - SAF
Ground oper.: lake	SLP - STB - COM - ROV - GOB - LRS - LRA - SAF - MAN - SWU - RNA
Ground oper.: transfer	STB - COM - ROV - SAF - MAN - SWU - RNA
Ground oper.: geysers	SLP - STB - COM - ROV - GRS - GRA - SAF - MAN - SWU - RNA
Disposal	SLP - STB

Table 5.3: Possible modes during the mission

6. Launchers

6.1 Constraints from mission to launchers

Different kinds of constraints come from the mission definition to the launcher that will put the spacecraft into orbit. All of them must be taken into considerations when selecting the launcher.

An important constraint for the selection of the launcher is the total mass that has to be stored in its fairing. As mentioned in section 4.5, the choice of suitable total masses in the preliminary mass budget is directly linked to the launchable mass of the launchers. The launchable mass is based on data coming from manuals and past missions. From a fitting of these values, the graph in Figure 6.1 is obtained.

This way, if C_3 is known, the launchable mass can be retrieved.

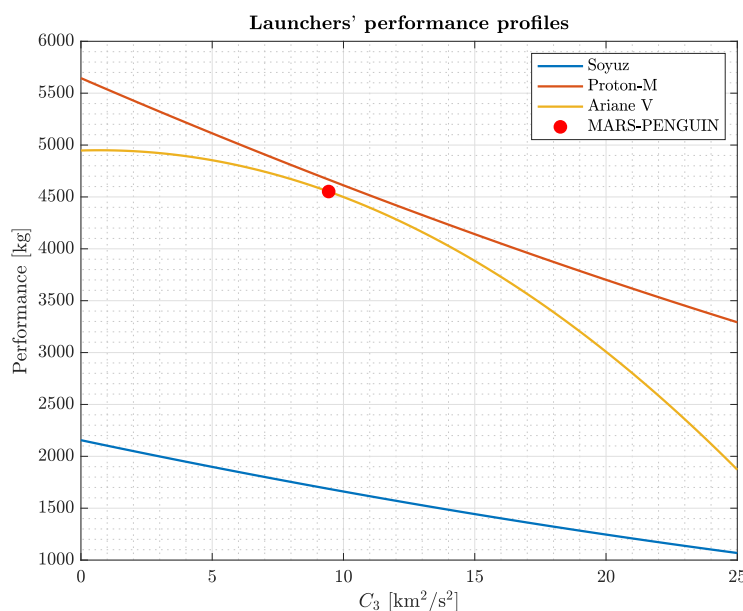


Figure 6.1: Launchers' performance profiles, obtained from [26],[27] and [28].

6.2 Potential launchers

The families of launchers needed for a mission to Mars with exploration objectives are the medium-lift and the heavy-lift launch vehicles. The latter can provide higher performance and, as a result, higher costs, but they are able to launch between 20000 kg and 50000 kg in LEO. Obviously, if the payload needs to be put directly into an interplanetary transfer orbit instead of a LEO, it must be significantly lower in mass. In Table 6.2 are reported the still-operational launchers used in the past for these kind of missions and the ones under development that could be available when MARS-PENGUIN mission will be launched (after 2024) together with related significant features.

Launcher	Agency/ Country of origin	Launch base	Launchable mass [kg]	C3 [km^2/s^2]	Cost launch	per	Mission (year)
Ariane 5 ECA	ESA	Kourou	2100	12.1	150 (2015)	M€	-
Ariane 62 (*)	ESA	Kourou	780	10.5	75 M€		from 2020
Ariane 64 (*)	ESA	Kourou	2100	12.1	90 M€		from 2020
Proton-M / Breeze-M	ESA & Roscosmos	Baikonur	4332 - 1800	13.78	65 M€		ExoMars (2016-2022)
Soyuz-2	Russia	Baikonur, Plesetsk, Vostochny, Kourou	780	10.5	80 M\$		-
Angara A5 / Breeze-M (*)	Russia	Plesetsk, Vos- tochny	5400 (into GTO)	-	90-105 (2016)	M\$	from 2021
Atlas V	NASA	Vandenberg/Ca Canaveral	694 - 1050	-	110 (2016)	M\$	InSight (2018), Mars 2020

Table 6.2: Past and future (*) launchers of interest for MARS-PENGUIN mission. (Mass, C3 and cost are indicative for a general Mars mission wherever never done)

From these analyses it can be deduced that Ariane 5 and the future Ariane 64 are compatible with MARS-PENGUIN mission constraints in terms of launchable mass and reachable transfer orbit. From section 7.2 analysis a C3 of 9.43 km/s has been derived, therefore a launchable mass of 4550 kg has been obtained considering Ariane 5. Moreover, the nice to have requirement of remaining inside Europe jurisdiction is fulfilled with the use of these launchers. If it would not be possible to launch with these vehicles due to unavailability of the platforms in the needed launch windows, Russian (Angara A5 with Breeze-M upper stage) or American (Atlas V) launchers could be taken into considerations. Also Proton-M combined with Breeze-M upper stage, that has already been involved in Mars missions with ExoMars programme, could satisfy MARS-PENGUIN requests. However, this launcher is of Russian property and it was used as a consequence of ESA and Roscosmos collaboration for those two missions.

7. Mission Analysis

7.1 Introduction

In this chapter are presented the Mission Analysis results for the MARS-PENGUIN mission.

In section 7.2 the trade-off process that led to the final trajectory is discussed and characterised.

Section 7.3 presents the trajectory of the MARS-PENGUIN mission, obtained through an optimisation process.

Finally, in section 7.4 are reported the conclusions of this analysis and addressed the future developments.

7.2 Trajectory trade-off

The process of trade-off is schematised in Figure 7.1.

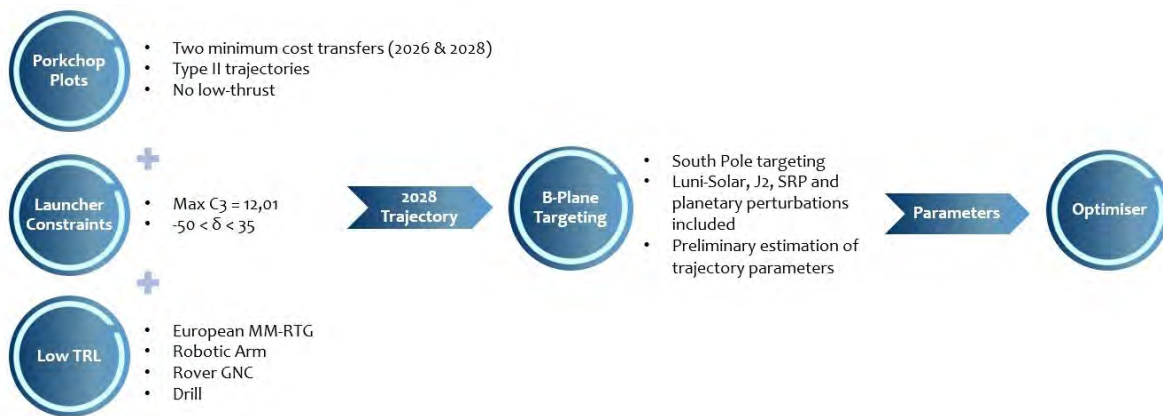


Figure 7.1: Trajectory trade-off process

Each step of the trade-off is specialised in the following subsections, however here it is presented a general overview of the process.

To compute a preliminary trajectory it has been plotted a porkchop to assess the Mars mission ΔV cost with departure dates between 2024 and 2030. Taking in account the low TRL of some hardware and software to be employed, it has been decided to depart as late as possible. Gathering also the constraints coming from the launcher it has been proceeded targeting the B-plane to fly-by Mars passing through the South Pole zone. Trajectory data retrieved from this computation have been used to feed an optimiser (specialised in subsection 7.2.3) to obtain the final trajectory.

7.2.1 Preliminary trajectory

To find the launch windows for the transfer to Mars, an analysis of the porkchop plot over the range 2024-2030 has been performed. The plot is shown in Figure 7.2. The result has been confirmed to be compliant with the ones from Trajectory Browser of NASA AMES and from [29].

It can be noticed the repetition of the pattern every 2.2 years (synodic period of the Earth-Mars system). Each pattern is composed of a two lobe structure: the upper lobe represents type II trajectories ($\theta > 180^\circ$) while the lower one represents type I trajectories ($\theta < 180^\circ$).

Porkchop outcome was of two minima in correspondence of November 2026 and 2028, respectively Two dates, corresponding to the local minimum ΔV in 2026 and 2028 (grey dot and square in Figure 7.2) have been chosen as a first guess for the following analyses.

Data of the two trajectories are shown in tables 7.1 and 7.2

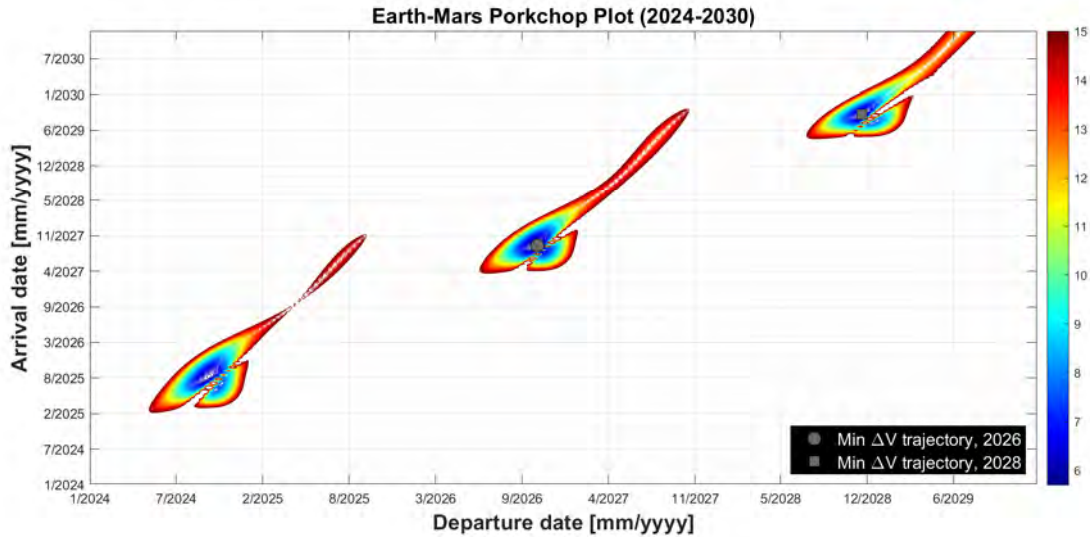


Figure 7.2: Porkchop plot for Earth-Mars transfers (2024-2030)

Parameter	Value
ΔV	5.6124 km/s
ΔV_{dep}	3.0427 km/s
ΔV_{arr}	2.5697 km/s
Departure Date	1/11/2026
Arrival Date	6/09/2027
TOF	310 days

Table 7.1: 2026 trajectory data

Parameter	Value
ΔV	5.9925 km/s
ΔV_{dep}	3.0234 km/s
ΔV_{arr}	2.9692 km/s
Departure Date	19/11/2028
Arrival Date	15/09/2029
TOF	300 days

Table 7.2: 2028 trajectory data

Both trajectories resulted to be of type II, with a similar TOF and slightly different ΔV s. From tables 7.1 and 7.2 it is apparent that the magnitude of the departure ΔV is around 3 km/s in the best case. This kind of change in velocity can be obtained using chemical thrusters. However, the propellant needed to perform such manoeuvre will be a too consistent percentage of the spacecraft mass, leading to the inconvenience of this solution. Therefore, a direct injection to the hyperbolic escape trajectory, to be performed by the launcher, has been considered for the MARS-PENGUIN mission.

In recent years, low-thrust transfers have increasingly attracted interest because of their long-lasting and propellant-saving features. Therefore, the possibility of exploiting a **low thrust trajectory** has been considered. It shall be noticed that this approach has never been used for transfers to Mars, although it has been widely studied.

The challenges related to low-thrust transfers are connected with the long **time of flight (TOF)** and with the multiple solutions of the feasible trajectory. Regarding Earth-Mars transfers, typical TOF retrieved from the analysis carried out in [30] lie in the range 600 to 1000 days.

As stated before, MARS-PENGUIN spacecraft will be injected on a hyperbolic orbit by the launcher, so it has been considered useless to exploit the electric propulsion capabilities only to perform TCMs. Other disadvantages that have been considered for low thrust option are the additional weight of the motor and the need of a separate power supply (see section 10.4 and chapter 13).

Moreover, based on the low TRL of some components, such as a European MM-RTG and an improved Rover GNC system, a the trajectory with departure in 2026 has been discarded. The choice of the 2028 trajectory meets the preferable condition of absence of CO₂ ice on the surface at arrival, a condition that verifies during Mars South Pole spring.

Summarising, the MARS-PENGUIN spacecraft will be directly injected into an hyperbolic trajectory by the launcher. The goal will be to target an entry point at the Martian atmosphere and land safely in the lake region.

7.2.2 B-Plane Targeting

To obtain accurate parameters to set the boundary conditions of the optimisation process, it has been chosen to target the B-Plane.

The algorithm firstly solves for the minimum ΔV using a patched-conic, two body, Lambert solution for the transfer trajectory from Earth to Mars. Using this solution as an initial guess, the second part implements a simple shooting method that attempts to optimise the characteristics of the geocentric injection hyperbola while numerically integrating the spacecraft's geocentric and heliocentric equations of motion and targeting to components of the B-plane relative to Mars. The script optimises the overall ΔV .

The spacecraft motion within the Earth's SOI includes the Earth's J_2 oblate gravity effect and the point mass perturbations of the Sun and Moon. The heliocentric equations of motion include the point-mass gravity of the Sun and the third-body perturbation of the first seven planets of the solar system.

The interplanetary injection has been supposed to occur impulsively from a circular parking orbit, with an altitude of 200 km.

Coordinates of the Sun, Moon and planets have been computed using the DE421 JPL ephemeris.

As mentioned before, dates retrieved from the porkchop computation have been employed for this routine.

Parameter	Value	Units
Departure Date	19/11/2028 (± 30)	days
Arrival Date	15/09/2029 (± 15)	days
$\underline{\mathbf{B}} \cdot \underline{\mathbf{T}}$	0	km
$\underline{\mathbf{B}} \cdot \underline{\mathbf{R}}$	6908	km

Table 7.3: Targeting - Initial data

In particular, the departure date 19/11/2028 has been set as initial guess and allowed to vary within a symmetric interval of 60 days. The arrival date, which shall preferably fall in the spring interval, has been set to 15/09/2029 and allowed to vary on a symmetric interval of 30 days. The value of the \mathbf{B} vector has been set in order to target an altitude above Mars of 150 km, a limit value retrieved by a preliminary EDL analysis.

The complete settings are reported in table 7.3.

LEOP The spacecraft's orbital motion has been modeled with respect to the Earth J2000 coordinate system and third body perturbation of Sun and Moon have been included.

Main objective of the analysis for the early orbit phase has been to obtain the departure hyperbola characteristics, reported in table 7.4. The ΔV required for the insertion in the hyperbolic trajectory is reported just for the sake of completeness, since the MARS-PENGUIN spacecraft shall be injected directly on a hyperbolic path by the launcher.

Thus, a more interesting parameters to look at, are the C_3 and the declination of the escape trajectory (δ). Comparing the obtained quantities with the ones retrieved from chapter 6, it is apparent that both the identified launchers (Ariane V and Ariane 64) will be capable to achieve the required values.

Cruise trajectory has been computed taking into account the point-mass gravity of the Sun and the third-body perturbation of the first seven planets of the solar system. Keplerian elements here reported are given with respect to the Ecliptic J2000 reference system. The results for the cruise trajectory obtained are reported in table 7.5.

Areocentric trajectory characteristics are summarised in table 7.6.

The altitude of closest approach resulted to be 200 km. The velocity at the periapsis of the hyperbola, instead, 5.7172 km/s. This value is compatible with the range expected for a correct atmospheric entry (5 to 7 km/s). The computed trajectory will require 302 days to be covered.

Parameter	Value	Units
Departure Date	26/11/2028	
C_3	9.075	km^2/s^2
Asymptote α	182.48	$^\circ$
Asymptote δ	27.83	$^\circ$
ΔV	3.63	km/s

Table 7.4: Targeting - Departure hyperbola data

Parameter	Value	Units
a	1.855×10^8	km
e	0.207	
i	24.69	°
ω	69.42	°
Ω	5.13	°
θ	350.88	°

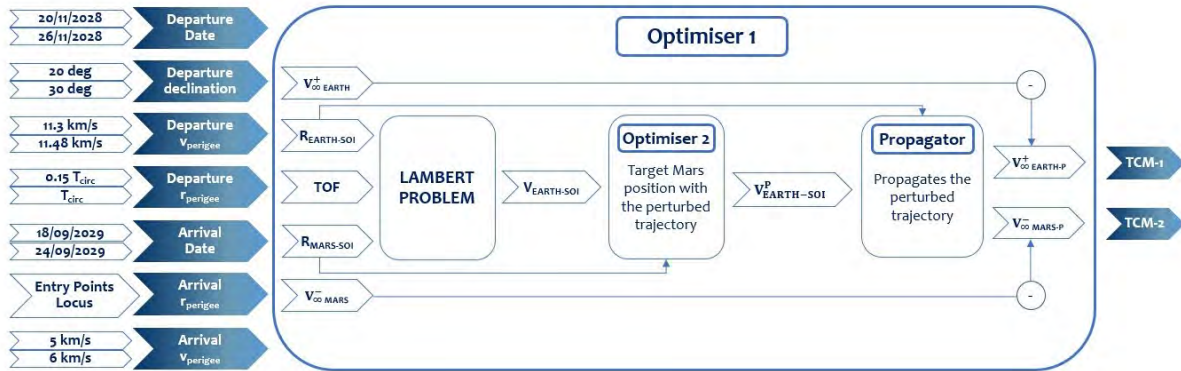
Table 7.5: Targeting - Data at Earth SOI

Parameter	Value	Units
Arrival Date	21/09/2029	
TOF	302	days
v_p	5.717	km/s
r_p	3590	km
Asymptote α	144.9	°
Asymptote δ	-29.66	°

Table 7.6: Targeting - Data at Mars closest approach

7.2.3 Optimisation

The final trajectory has been designed connecting the outgoing hyperbola at Earth SOI with the incoming hyperbola at Mars SOI through a simple Lambert arc. The arrival hyperbola has been obtained through a backward propagation starting from the entry interface point. Modeling details and results for the three legs are reported in section 7.3. Being a simple Lambert arc is not sufficient to account for the presence of perturbations (planetary and SRP), it has been implemented an optimiser whose structure is shown in Figure 7.3. It has been set in order to minimise the total ΔV for the TCMs needed to target the correct entry point at Mars SOI.

**Figure 7.3:** Optimisation process flow

The flow consists of a main routine fed with seven parameters allowed to vary through given boundaries (first column in Figure 7.3) compatibly with the launcher performance. Inside this box, the departure and arrival hyperbola are computed, giving the heliocentric departure and arrival position and velocities, as well as the time of flight. After few manipulations, a perturbed propagator finally leads to two velocities for the departure and arrival hyperbola which, compared with the ones computed from the initial parameters, give the TCM1 and TCM2. Those manoeuvres shall be performed, respectively after exiting Earth SOI and before entering Mars SOI.

With the obtained set of optimised parameters, reported in Table 7.7 the final trajectory has been computed.

7.3 Final Trajectory

7.3.1 Geocentric

Even if the launch phase planning is up to the launch provider, to have a preliminary estimation, it has been modeled taking in account a departure from a circular parking orbit at an altitude of 200 km. Such circular orbit has been supposed to start after the first stage separation, therefore from a point located at

Parameter	Value
Departure Date	23/11/2028 04:23:00
Departure δ	25.03 °
Departure v_{peri}	11.398 km/s
Departure r_{peri}	0.785 T_{circ}
Arrival Date	21/09/2029 11:19:25
Arrival v_{peri}	5.635 km/s
Arrival r_{peri}	from entry point locus

Table 7.7: Optimised parameters

north-east of the designed launch site, Kourou Space Center. From the optimisation, the inclination of such orbit resulted to be 25.23 degrees, while the coasting period 0.785 of the period (see Table 7.7).

After that time, the upper stage of the launcher has been supposed to inject the spacecraft on a hyperbolic trajectory with a C_3 of $9.436 \text{ km}^2/\text{s}^2$ and declination 25.03 degrees. The spacecraft reaches finally the Earth SOI after 3 days. J2 effect has been considered as the only perturbation acting on the S/C.

The data of the hyperbolic path and a sketch of the trajectory are reported in fig. 7.4 and table 7.8.

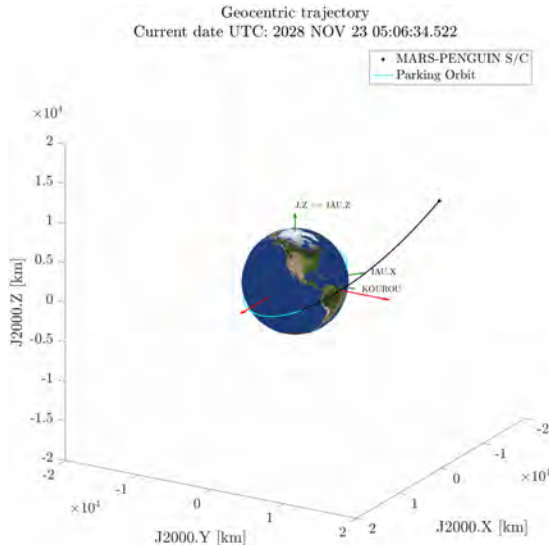


Figure 7.4: Geocentric trajectory

Parameter	Value	Units
UTC Date	23/11/2028 03:58:00	
a	-46170	km
e	1.142	
i	25.03	°
ω	331.7	°
Ω	62.63	°
θ	0	°
C_3	9.436	km^2/s^2
Asymptote α	187.63	°
Asymptote δ	25.03	°

Table 7.8: Departure hyperbola data

7.3.2 Interplanetary

The overall trajectory has been modeled in the Earth J2000 reference frame. However, the heliocentric trajectory is here reported in the Ecliptic reference frame at J2000 for the sake of clarity. For this leg, both SRP and first 7 planets perturbations have been included in the propagation.

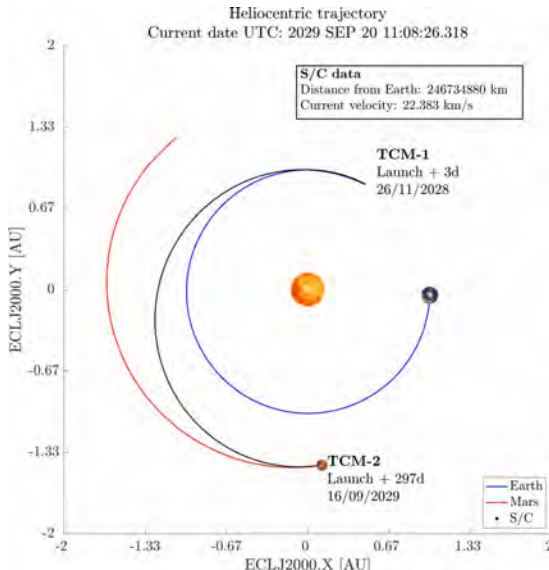


Figure 7.5: Heliocentric trajectory in J2000 frame

Parameter	Value
a	$1.845 \times 10^8 \text{ km}$
e	0.207
i	24.69°
ω	331.7 °
Ω	4.52 °
θ	344.26 °
TOF	297 days

Table 7.9: Heliocentric trajectory data (Keplerian elements at departure, EclipticJ2000 frame)

The spacecraft will depart from the Earth SOI on 26/11/2028 and will arrive at Mars after 297 days of cruise, on 19/09/2028 at a distance of 244 million kilometers from Earth. During the cruise it will perform two TCMs. The first will take place at the exit of Earth SOI and will require 25 m/s, while the second one will correct the trajectory before entering Mars SOI with a 63.5 m/s burn.

Heliocentric path data and plot are reported in fig. 7.5 and table 7.9

7.3.3 Areocentric

As stated before, the arrival hyperbola has been computed through a backward propagation process, starting from the entry interface point of interest. The optimal point has been identified among the ones of a circular cap at an altitude of 125 km from the Mars surface and at a distance from the lake (measured on the Mars surface) of 473.5 km. Both values have been given by the EDL team.

In the simulation, the rotation of Mars has been accounted for, whereas its gravity has been modeled through spherical harmonics up to the second order. The axis of the Equatorial reference frame (IAU Mars) have been retrieved at each epoch from the .pcm files provided by the NASA's Navigation and Ancillary Information Facility (NAIF). Also, the motion of the two natural satellites of Mars, Phobos and Deimos have been included using the NAIF ephemeris.

Concerning artificial satellites motion, MAVEN and MRO have been taken in account since they are the two candidates to serve as a relay for the communications. In particular, MAVEN trajectory has been extracted from NAIF files, while MRO one has been propagated manually.

In Figure 7.6 it is shown the trajectory of the S/C in proximity of Mars. It can be noticed that, about 15 minutes before the arrival at the entry interface, the aeroshell separates from the cruise stage along a direction parallel to the entry one with a relative velocity of 5 m/s.

The optimal arrival point is reached by the aeroshell on 21/09/2029 with a velocity of 5.75 km/s and a flight path angle of -12 degrees, as required for an optimal EDL phase.

The cruise stage enters Mars' atmosphere about 1 second after the aeroshell with a slightly lower velocity. The entry path of both S/C components is detailed chapter 9.

Data of the arrival trajectory are summarised in Table 7.10.

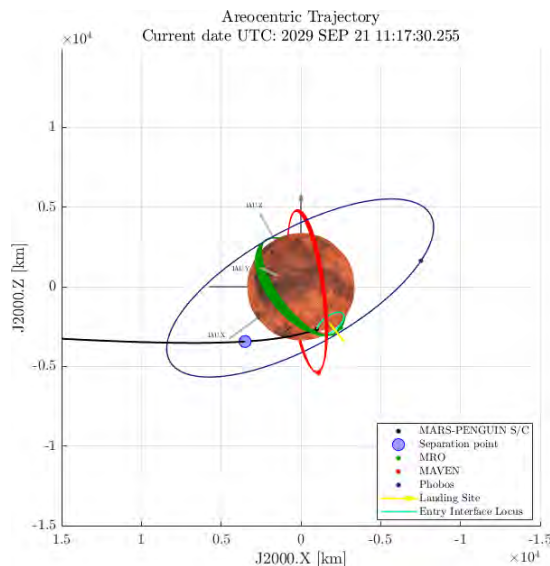


Figure 7.6: Areocentric trajectory

Parameter	Value	Units
UTC Date	21/09/2029 11:19:25	
a	-4907 km	km
e	1.687	
i	50.38	°
ω	300.34	°
Ω	191.56	°
θ	338.8	°
v_{EI}	5.749	km/s
Asymptote α	187.747	°
Asymptote δ	4.603	°

Table 7.10: Arrival trajectory data

7.4 Conclusions

In this chapter the main features of the MARS-PENGUIN mission trajectory have been presented. The S/C will depart in November 2028 and complete its journey in 303 days, arriving at Mars during the Southern Pole spring in September 2029. During cruise phase, two TCMs will be performed to correct the trajectory and target the entry interface point at Mars.

It shall be noticed that, to improve the presented results, an uncertainty analysis shall be performed. Moreover, the presence of the two artificial satellites shall be assessed at the arrival time to guarantee telecommunication capabilities.

8. Attitude Determination and Control

8.1 Introduction

The Attitude Determination and Control Subsystem (ADCS) for the MARS-PENGUIN mission is defined to guarantee the desired orientation of the S/C for different tasks of the mission such as TCMs and communication pointing.

In the following chapter, the analysis and the design of both the space segment (cruise stage) and the entry capsule during EDL phase are addressed.

8.2 Mission modes

According to the ADCS requirement and also other requirements coming from related subsystems such as TMTC, various modes can be defined as explained in the following.

De-tumbling: this mode begins after the launch to bring the S/C to rest within an acceptable angular velocity range.

Communication : the only frequent mode is the communication that occurs during the whole cruise phase. This mode aims to reach Earth line of sight in an acceptable range defined by TMTC subsystems.

TCM : it is inevitable not to have any trajectory correction manoeuvres. The MARS-PENGUIN mission considered a few manoeuvres for these corrections explained in Table 10.1. At this mode, the S/C orients itself to be able to perform the manoeuvres with respect to the position of engines.

Separation : in order to satisfy the separation constraints in terms of the attitude of the cruise module, a re-orienting is needed.

Safe mode : Since there is no solar panel, the safe mode means any failure in High Gain Antenna (HGA). In that case the S/C has to re-orient such that the Low Gain Antenna (LGA) will be in an acceptable range with respect to Earth line of sight.

Each of the mentioned modes require a certain accuracy based on the requirement's parent. Some of them are already defined but some needs more calculation before setting any requirement. In Table 8.1, some of the requirements are reported.

Mode	Accuracy
De-tumbling	$\omega_i < 0.01 \text{ deg /s}$
Communication	$\theta < 2 \text{ deg}$ $\omega_i < 0.01 \text{ deg /s}$

Table 8.1: Required accuracy for ADCS modes

Among the mentioned modes, de-tumbling and communication modes, as the highest priority are addressed in this chapter.

8.3 Environment

Before going through the sizing of the ADCS, it is needed to know which attitude disturbances are applied to the S/C during each phase of the mission. In Table 8.2, the disturbances for each phase are reported.

Since the main application of the ADCS of the mission is during the cruise, the only modelled disturbance is the solar radiation pressure as discussed in the following.

Phase	Disturbance
	SRP
LEOP	Gravity gradient Magnetic field
Cruise	SRP
Mars approach	SRP Gravity gradient

Table 8.2: Disturbances present in mission phases

8.3.1 Solar Radiation Pressure

Solar radiation pressure perturbation is a constant disturbance for the S/C attitude during the interplanetary trajectory. Regarding the final configuration elaborated on in section 16.4, the major contribution is caused by the entry capsule. For the sake of simplicity, the cruise stage has been considered as a cone and because of the position of centre of mass and the range of oscillation of the whole S/C, the other surfaces have been neglected. Furthermore, to consider other unmodelled disturbances, a random Gaussian disturbance with a zero mean and a standard deviation of 20% of the SRP has been augmented to the disturbances. The SRP formulation that has been adopted and the behaviour of the total disturbance for a day is shown in Figure A.3 in the appendix.

8.4 Hardware

8.4.1 Sensors

The selection of sensors to determine the attitude of the S/C has been carried on based on the environment of the mission. There are two sets of instruments for the cruise stage and the entry stage. The selection of the instruments has been done such that the sensors used for entry phase is applicable in the cruise phase considering the OBDH constraints in terms of sharing the data from entry vehicle to the cruise stage.

Cruise stage

The overall configuration of the sensors installed on the cruise stage is summarised in Figure 8.1.

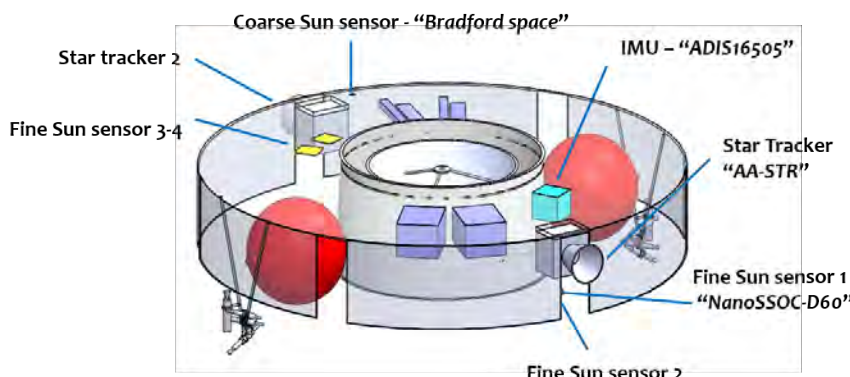


Figure 8.1: Cruise stage sensors

Note that the two star trackers and also sun sensors 1 and 3 are pointing radially while sun sensors 2 and 4 are pointing vertically (downward). It will be explained in section 8.5.1 how the sensors are going to be used to provide the full attitude of the S/C.

Entry capsule

Regarding the entry capsule a *LN-200s IMU* has been considered to provide the angular rates of the capsule. To obtain the altitude and the velocity of the sky crane, a Radar-Doppler-Altimeter(**RDA**) that is a combination of antennas in different orientations has been proposed to design.

8.4.2 Actuators

The selection of actuators highly depends on the accuracy needed for each mode. The only frequent mode is the communication mode. Considering the thrusters present to perform the **TCMs** as will be explained in section 10.3 and also due to the fact that there is no solar panel to be pointed toward the Sun, it is decided to use the same propulsion system used for **TCMs**, for the attitude manoeuvres. In Figure 8.2, the configuration of the thrusters is depicted. Note that with the proposed configuration, it is possible to fully control the spacecraft with even less than 12 thrusters.

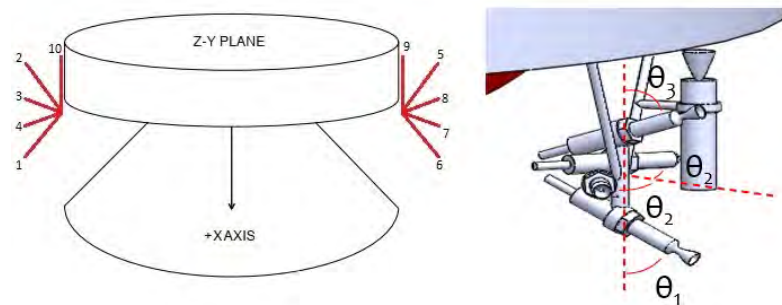


Figure 8.2: Thrusters' configuration

Notice that two vertical thrusters are not used for the attitude manoeuvres and will be explained in chapter 10. Considering the maximum size of the control moments needed to perform the manoeuvres, it is decided to use 1 N thrusters. In Table 8.3, the specification of the thrusters are reported.

Name	Thrust	MIB
MR-103J	0.19 to 1.13 N	0.0133 N s

Table 8.3: Thruster specification

Thrusters configuration optimisation

To choose a best set of angles for the thrusters installations a multivariable optimisation has been adopted. The two criteria that the problem optimised with respect to are the propellant used for the manoeuvres and the accuracy in achieving the desired control torque with the thrusters. For this optimisation, a linear weighting cost function has been established. In the table below, In the following figure the weight of each criterion are shown.

Criterion	Weight
Propellant consumption	40%
accuracy in provided moment	60%

Table 8.4: Criteria weights for the cost function of thrusters' optimisation

Based on some constraints that had to be satisfied in the optimising, the θ_3 has been set to be always 10 degrees higher than θ_1 . In Figure 8.3, the result is shown.

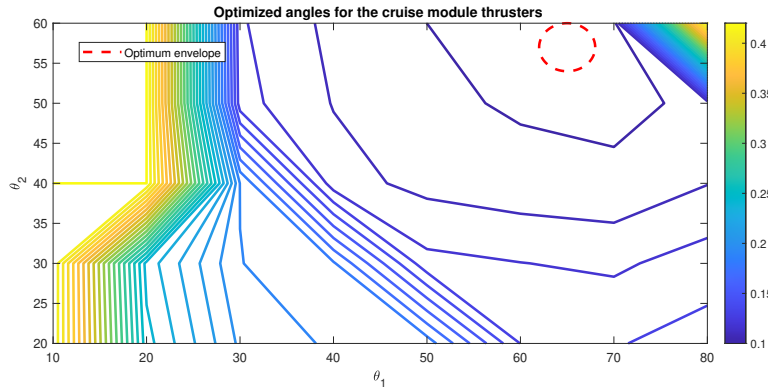


Figure 8.3: Thrusters' configuration optimisation

As noticed in the figure, an optimum envelope is chosen. The final angles are set as reported in Table 8.5.

Angle	Value[deg]
$[\theta_1, \theta_2, \theta_3]$	[60, 60, 70]

Table 8.5: Optimised angles for the thrusters' installation

8.5 Software

8.5.1 Attitude estimation

The first step is to estimate the attitude for which two observation vector are needed. Based on the pointing direction of sensors, since it may happen that the Sun stays in the FOV of the star tracker at specific attitudes(note that the star tracker does not work in this case), the two star trackers must be active always. Moreover, based on the designed heliocentric trajectory, at some point, Earth will be in the Sun line of sight, so the sun sensors cannot provide any observation vector. In that case, the output of both star trackers are needed to provide the full attitude of the S/C. To do this, a sensor fusion algorithm is required to be able to provide the estimation algorithm two preferably-perpendicular observation vectors at different attitudes.

By adopting a non-linear estimator called *Cubature Kalman Filter* as presented in [31], the attitude of the S/C can be retrieved. The error of estimation for a period of 50 s is shown in Figure 8.4.

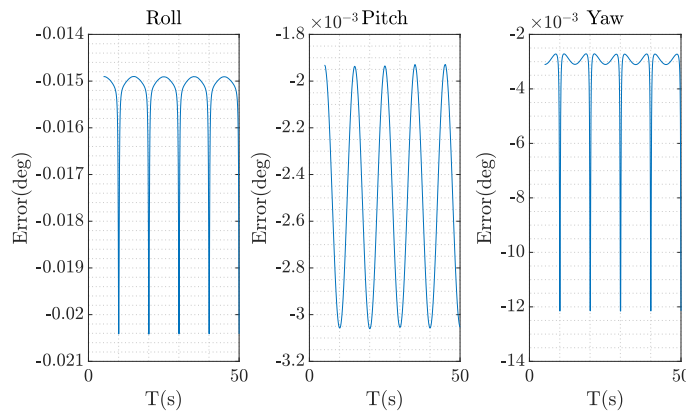


Figure 8.4: Attitude estimation error using a Cubature Kalman filter

To perform the mentioned estimation, a measurement vector at each time is needed.Based on the data-sheet of the sensors, the standard deviation of the selected star tracker is 0.005 deg while for the sun sensor is about 0.1 deg.

Moreover, it is assumed that the output of the rate gyro is also noisy and an angular random walk of $0.13 \text{ deg}/\sqrt{\text{h}}$ is augmented. It is worth mentioning that the result is achieved considering the observation vectors of a star tracker and a sun sensor. If the vectors come from the two star trackers, the result would be better due to better accuracy of the star tracker.

8.5.2 Attitude Control

Before going through the detail of the algorithms to control the attitude, it is worth mentioning that due to the fact that as the S/C goes farther than Earth, the time window needed to transfer the same volume of data must increased, the communication window is set by the longest period to be about 1 hour. As a result, it is considered that the S/C is controlled during the communication window and be free to rotate after that time window until the next communication session.

8.5.3 Attitude Control Architecture

To control the S/C attitude during the mission, various strategies has been analysed and as a result the two most promising methods are selected as shown in Table 8.7.

Method	Note
3-axis stabilised	Expensive in terms of propellant usage/Higher accuracy in pointing.
Spin stabilised	Cheaper in terms of propellant usage/ Robust with respect to the unmodelled disturbances.

Table 8.7: The most promising attitude control architectures

Spin stabilising method can be opted due to the fact that there are some disturbances that can not be modelled especially in the LEOP phase such as out-gassing and misalignment of the thrusters that can be rejected by spinning the S/C. Moreover, since the rotation of Earth line of sight is so small during the cruise, it would be a good idea to spin the S/C to avoid diverging the spacecraft attitude with even a small rate between two consecutive slew manoeuvres for the communication.

However, as a consequence of this spinning, the higher torque is needed to any orienting in the two non-spinning axes because of gyroscopic effect. Another problem can one brings about is that high accuracy pointing needed for a daily communication, makes the spinning worthless. As a result, based on the MARS-PENGUIN mission requirements, the 3-axis stabilisation has been chosen.

8.5.4 Controller

For each mode, a specific control law that based on the Lyapunov theorem is asymptotically stable is proposed to satisfy the ADCS requirements.

Detumbling mode For this mode, a simple de-tumbling augmented by a saturated term is adopted as in Equation 8.1.

$$u = -K_1 \bar{\omega} - K_2 \text{sign}(\bar{\omega}) \quad (8.1)$$

The control law proposed is a robust controller to disturbances that can be proved taking advantage of Lyapunov function if K_2 is an upper bound for the disturbances. The accuracy needed for the communication was reported in Table 8.1. A set of gains derived by trial and error is reported in Table 8.8.

Mode	K_1	K_2
De-tumbling	1.8	0.001

Table 8.8: De-tumbling mode's controller gains

Communication The pointing corresponding to communication are performed through a modified Proportional-Derivative (PD) controller. The pointing is toward Earth with respect to the position of the cruise stage and Earth during the trajectory. The position of the S/C is provided by the optimised interplanetary trajectory and Earth one is available from ephemeris of Earth provided by *DE421 JPL*. The control command is as shown in Equation 8.2.

$$u = -K_d J \bar{\omega} - 2K_p J q_{e,4} \bar{q}_e \quad (8.2)$$

in which \bar{q}_e is the multiplicative quaternion error, $\bar{\omega}$ is the angular velocity vector of the S/C measured by IMU and J is the inertia matrix of the S/C. The multiplicative quaternion error is derived by the quaternion representing the body frame and the quaternion related to the Earth line of sight frame. The calculation of q_e has been performed as reported in [32]. The set of gains has been selected as reported in Table 8.9.

Mode	K_p	K_d
Communication	0.0001	0.01

Table 8.9: Communication mode's controller gains

8.5.5 Thrusters architecture

As shown in Figure 8.2, the 8 thrusters have coupled contributions on the three axes. Firstly it is needed to find the *Transformation Configuration Matrix* to be able to perform the *Control Allocation* among the thrusters with respect to Equation 8.3.

$$\bar{u}_{control} = -[T]^+ \bar{u}_{ideal} \quad (8.3)$$

The transformation configuration matrix for the MARS-PENGUIN configuration is described in Equation 8.4.

$$T = \begin{bmatrix} 0 & 0 & S_\alpha r & -S_\alpha r & 0 & 0 & S_\alpha r & -S_\alpha r \\ 0 & 0 & -S_\alpha x_{cg} & S_\alpha x_{cg} & 0 & 0 & S_\alpha x_{cg} & -S_\alpha x_{cg} \\ S_\alpha x_{cg} + C_\theta r & -C_\theta r + S_\theta x_{cg} & C_\alpha x_{cg} & C_\alpha x_{cg} & C_\theta r - S_\theta x_{cg} & -S_\theta x_{cg} - C_\theta r & -C_\alpha x_{cg} & -C_\alpha x_{cg} \end{bmatrix} \quad (8.4)$$

in which C_θ and S_θ are $\cos \theta$ and $\sin \theta$ respectively. Moreover, in Table 8.10, it is indicated which thrusters have to fire to have control on a favourite axis.

Axis	Firing thrusters
Roll	3-7 or 4-8
Pitch	3-4-7-8
Yaw	1-5 or 2-6

Table 8.10: Thruster firing for controlling each axes

To obtain the thrust allocated for each thruster, a fast pseudo inverse approach[33] is adopted. Afterwards, a simplified Pulse-Width Modulator (PWM) [34] is used to retrieve the Δt_{on} as reported in Equation 8.5 and subsequently the control torque $u_{on/off}$ for each thruster.

$$\Delta t_{on} = \frac{u_{control} \Delta t}{F} \quad (8.5)$$

In which F is the nominal thrust and Δt is the sampling time.

8.6 Simulation

To simulate the system, the initial attitude and angular velocity is set by a random function considering a upper bound for the angular velocity. The attitude Euler equations and quaternion kinematics are integrating via an ODE function in MatLab through whole interplanetary trajectory. Firstly, the code starts the *de-tumbling* phase and as soon as the angular velocity falls below the threshold defined in Table 8.1, it switches to the next mode which is the communication mode.

8.6.1 De-tumbling

The S/C has been designed to be de-tumbled after a harsh separation from the launcher. As can be seen in Figure A.4 in the appendix, the cruise stage is de-tumbled in less than hour by consuming about 350 g of propellant.

8.6.2 Slew

For the communication mode of the simulation, a window of about 1 h is considered to reach the desired attitude. It is assumed that since at the beginning and end of the cruise it is more needed to communicate with Earth, for the 10 first and 10 last days of the transfer the S/C communicates once a day while for the mid cruise, once a week is sufficient.

In Figure 8.5, the Euler angles and the angular velocities of the S/C during the control window for the first three days are shown.

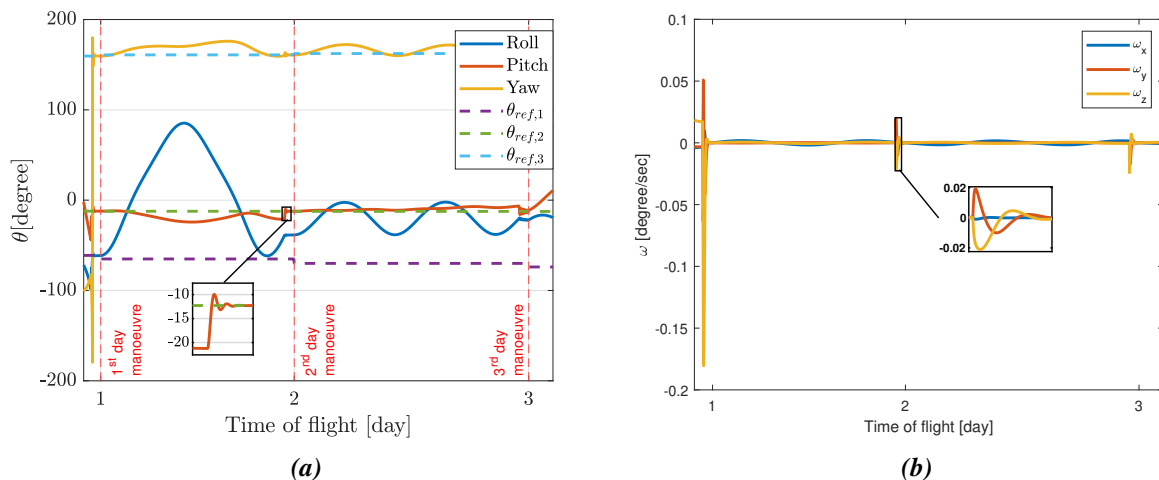


Figure 8.5: (a) Euler angles and (b) angular velocity vector during control window during the three days after launch

As shown above, *Roll* channel oscillates with a higher amplitude with respect to the others and does not follow its desired. The reason is that *Roll* angle is defined around the axis that is the same as Earth line of sight. Since the rotation around the Earth line of sight does not make an issue for the communication performance, in the desired Euler angles, the *Roll* angle is supposed as zero.

The ideal control effort as explained in Equation 8.2 and also the control torque produced by the thrusters for the first day manoeuvre are shown in Figure 8.6a.

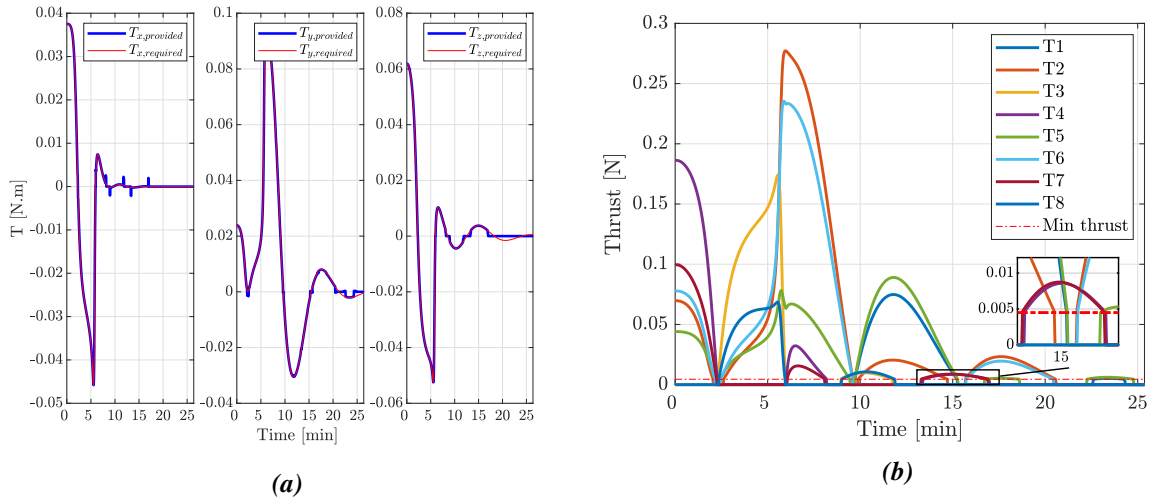


Figure 8.6: (a) Required and real control torque and (b) thrust of each thruster for the first day slew manoeuvre

According to the torques reported above, it is clear that the desired and the actual torque are not identical as the desire control torque gets close to zero. It happens because of MIB of the selected thrusters. This is also noticeable in Figure 8.6b when the thrust of each thruster is retrieved.

As a preliminary analysis that had been explained in the last report, the propellant used for the ADCS manoeuvres was about 12 kg. However, after a further analysis, considering the thrust profile of each thrusters during the manoeuvres, it is obtained that considering a 20% margin, an amount of 6 kg of propellant is sufficient.

8.6.3 Further analysis

As one understood so far, the S/C is free to rotate and diverge when no communication is carrying out. Two other approach can be adopted. Firstly, another control mode can be defined not to allow the S/C to diverge a lot. Thus, whenever the spacecraft exceeds a TBD range, the control becomes active to keep the spacecraft in the defined range. Alternatively, the spacecraft can be free to rotate but the communication time during a day can free to be chosen in real time. Thus, the control and consequently the communication process start whenever the S/C gets close to the desired point.

8.7 Entry, Descent and Landing

The last job of ADCS design, is to control the attitude the entry capsule during the first phase of EDL as will be explained in section 9.2. Before going through the active control, it is worth mentioning that the capsule has been designed such that the centre of pressure is behind the centre of mass to have a stable system. In case of uncertainties either externally like the wind or internally like the misalignment of centre of mass with respect to the symmetric axis, a trade-off between 3-axis stabilisation and spin stabilising to control the entry has been studied. The most promising method as explained in the last report is spinning the capsule. To do so, it is considered that the cruise stage provide the preset spin rate before separation. To have the control on the spin rate to keep the rate, two clusters of thrusters mounted on the back-shell as shown in Figure 8.7 such that the thrust vector provides a torque in the symmetric axis.

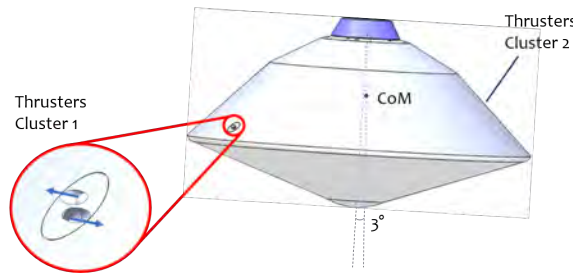


Figure 8.7: Entry capsule reaction control system

To design for the worst case, the performance of the RCS has been analysed assuming that the capsule is going to gain the preset spin rate starting from the stationary state and considering a 3 deg misalignment of the CG as shown in Figure 8.7.

In Figure 8.8, it is shown that the capsule spins-up to a preset 2 rpm in less than 20 s. One can notice how accurate the thrusters can provide the requested torques.

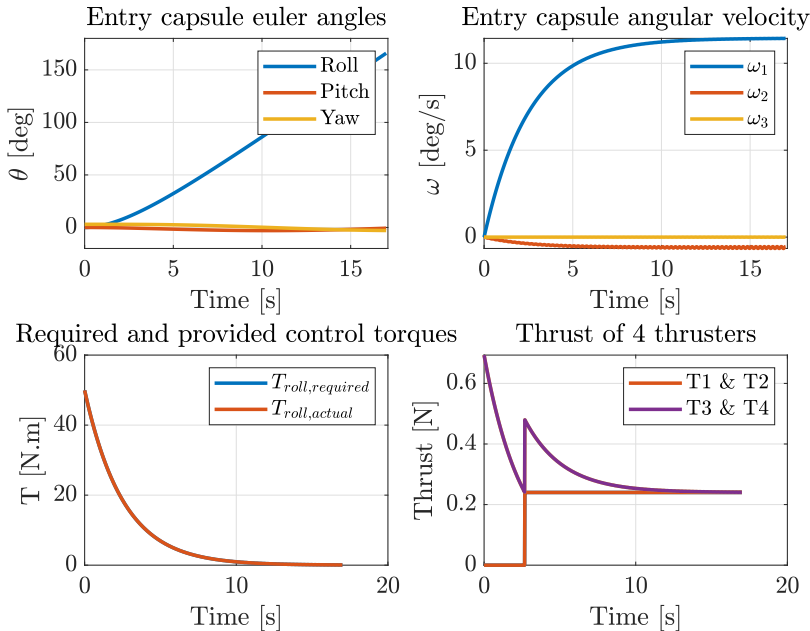


Figure 8.8: The behaviour of the RCSs and the entry capsule during spin-up

9. EDL

9.1 Introduction

The EDL phase is one of the most critical phases of the whole mission since it is the one that has to safely deliver the rover to the Martian soil. This task can be achieved both by a direct entry or by an entry from a parking orbit. In general, the EDL can be divided in three main phases:

- Entry
- Parachute deployment
- Landing

Before starting the description of these phases some analysis have been done looking at previous missions in order to understand the strategies and the technology used. A brief description of the main features of these mission is represented in appendix Table A.4. The crucial devices resulted to be the aeroshell (heat shield) and the parachute represented in Figure 9.1 and Figure 9.2.

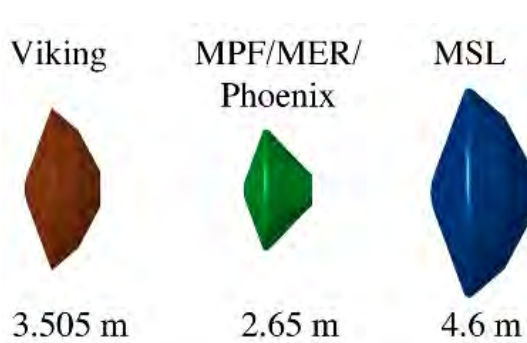


Figure 9.1: Viking-heritage 70° sphere-cone aeroshells

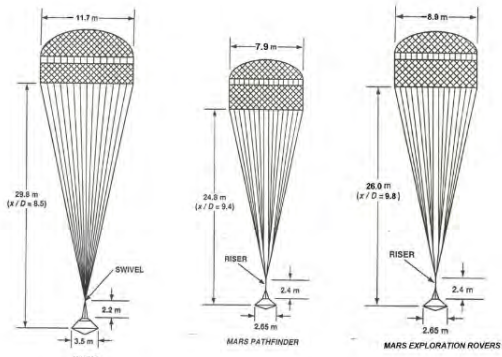


Figure 9.2: Viking-derived parachute systems

In general the kind of aeroshell used is the 70° sphere cone shape with a SLA-561V TPS (density of $\rho = 264.3 \text{ kg/m}^3$) that grants an hypersonic c_D of around 1.68 and has a diameter that ranges from 2.5 to a maximum of 4.5 m, whereas regarding the parachute the selected one is the Disk Gap Band (DGB) that grants a c_D of around 0.65 with a diameter that ranges from 14 to 19.7 m [35]. Another important aspect is the value of the ballistic coefficient β that can be evaluated as $\beta = m/(c_D \cdot A)$. In fact, the lower it is the better it would be in terms of higher altitude for the parachute deployment. Of course it is not always possible to keep this value low due to constraints in terms of mass and dimension. For this reason, a possible solution could be to exploit the small amount of lift generated by the aeroshell in order to still be able to deploy the parachute at a good altitude as done in the case of Curiosity. In the end, another crucial element is the Entry Flight Path Angle (EFPA) that influences the whole trajectory as well as the uncertainty of the final landing position.

9.2 Phases

9.2.1 Entry

Regarding the entry there are mainly two possible solutions: Ballistic Entry or Lifting Entry [36] (Figure 9.3). In a Ballistic Entry, the Centre of Gravity (CG) of the capsule is aligned with its axis of symmetry, which results in a zero angle of attack and thus a zero lift force. On the other hand, in a Lifting Entry the CG is displaced away from the capsule axis of symmetry, which causes it to trim with an angle of attack and thus generate a Lift force. In a Lifting Entry architecture, a Reaction Control System (RCS) is required to control the direction of the Lift vector. In a Ballistic Entry the vehicle is usually spin stabilised but the overall manoeuvre is still less precise since it is more difficult to correct possible errors.

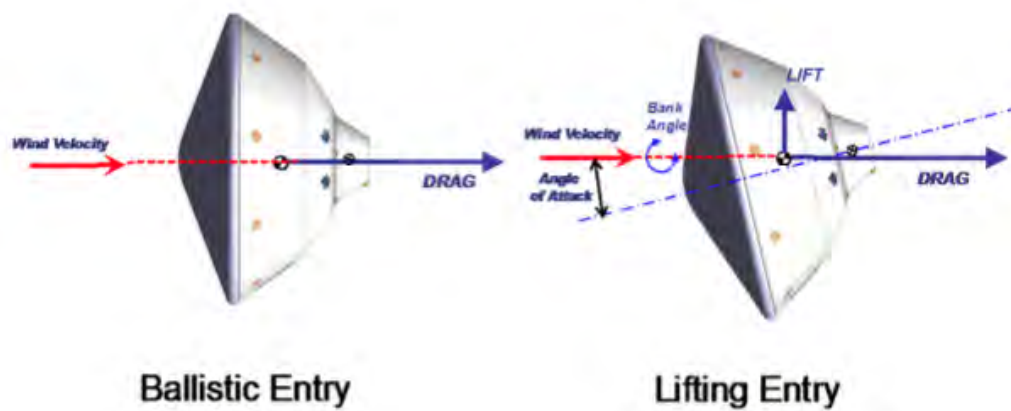


Figure 9.3: Ballistic and Lifting Entry Configurations

9.2.2 Parachute deployment

If no other systems are employed for slowing down the vehicle apart from the heat shield, it is possible to see that the touchdown velocity would be around some hundreds of m/s. For this reason a parachute is needed in order to bring the vehicle in the subsonic regime at a certain altitude. The Disk Gap Band parachute is usually deployed between Mach 2.1 and 1.4 with a dynamic pressure in the range 780 to 350 Pa [35]. The parachute is important since it brings stability and also allows a positive separation of the aeroshell once a Mach number of 0.8 is reached. As it is possible to see also from Table A.4 in appendix, typical values for the parachute deployment altitude are around 5 to 10 km. The parachute remains operative till the next phase.

9.2.3 Landing

The final landing phase usually starts at 1.5 to 2 km from the surface. The main objective of this final phase is to reduce the velocity range in order to have acceptable values at touchdown and deliver the rover to the surface. At the beginning of this stage, the separation of the backshell together with the parachute is performed and the propulsive system starts working in order to have the velocity needed by the selected touchdown solution.

In general there are mainly three options:

- Airbags (used in MER and MPF)
- Breakable Legs (used in Viking and Exomars Schiapparelli)
- SkyCrane (used in MSL)

Airbags and Breakable Legs

The airbag solution was the one selected by both the MPF and MER missions while the legs option was used in many cases such as Viking and Exomars Schiapparelli missions. Both the approaches consist in having a propulsion system attached on the backshell that ignites after the separation of the rover that still remains connected to the described structure thanks to a bridle (of around 20 m length and 7 kg mass) as shown in Figure 9.4. In this way the rover is taken to the correct velocity and altitude

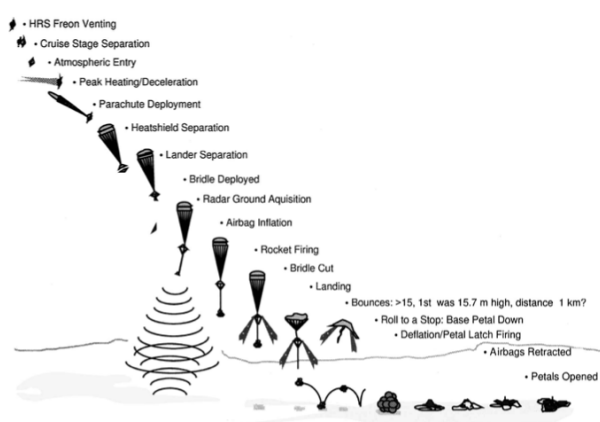


Figure 9.4: Mars Pathfinder EDL

needed for the airbag or breakable legs and then definitely separated from the backshell that flies away in order to

land at a safe distance from the rover itself. Furthermore in this way the plume of the propulsive system is unlikely to pollute too much the surroundings or to raise dangerous hazards from the ground. For the airbags the accepted maximum touchdown velocities are 26 m/s vertical and 16 m/s horizontal whereas for the legs they are around 3.5 m/s vertical and <1 m/s horizontal [35]. In the airbag option the rover is usually dropped from a 20 m altitude from the soil.

SkyCrane

This approach was used for the first time by the MSL mission. It can be divided in four phases [36] as shown in Figure 9.5.

The following phases are reported and described through the values used for the MSL [36] but still they are useful to understand the working principles of this kind of entry and find possible boundaries in terms of altitude and velocities of each kind of manoeuvre that shall be considered for the MARS PENGUIN mission. The Powered

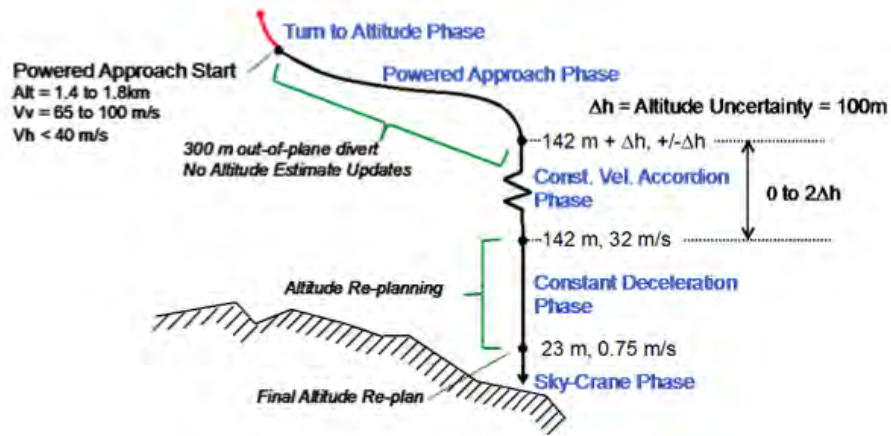


Figure 9.5: Skycrane final landing phases

Approach phase objective is to bring to zero the horizontal velocity, reduce the descent velocity to 32 m/s, align the lander attitude with the vertical, and perform a 300 m divert manoeuvre to avoid the parachute/backshell from recontacting with the lander. The Constant Velocity Accordion phase allocates altitude margin as an “accordion” to compensate for the altitude measurement error introduced at the beginning of Powered Approach. During the Constant Deceleration phase the vertical velocity of the lander is brought down to the 0.75 m/s touchdown velocity, while continuing to follow a vertical profile (i.e. zero horizontal velocity). During this phase, there is also a reference trajectory re-planning capability used to adjust for minor changes in the altitude knowledge.

The SkyCrane phase starts at an altitude of 23 m, with the lander already at the right ground relative velocity required for touchdown: 0.75 m/s vertical velocity and 0 m/s horizontal velocity. Since there is no need for large deceleration during this phase, usually some engines are throttled down to keep the remaining ones at a throttle level comfortably higher than the minimum allowed. The throttle-down occurs at the start of the SkyCrane phase and around 2.5 s are allocated for the transients to subside before proceeding with Rover Separation that happens thanks to a 7.5 m bridle similarly to what done also in the previous solution at an altitude of approximately 20 m. During this phase GNC keeps the vehicle controlled and descending with the same velocity profile, even in the presence of the large transients caused by the Rover separation. Finally the SkyCrane itself can have surface imaging and compare the obtained data with on-board maps for better landing and avoid possible rocks. Once the rover is on the soil it is detached and the SkyCrane performs a fly-away manoeuvre in order to impact at a safe distance of around 600 m away from the rover.

9.3 Model Description

Comparing with data from previous missions the aeroshell and parachute drag coefficients have been selected to develop the analysis. The direct entry was selected since the MARS PENGUIN mission does not have an orbiter and a ballistic kind of entry was analysed at first in order to understand the feasibility of using this simpler method both in terms of landing effectiveness and precision. The mass is evaluated as a sum of all the masses involved, whose values are taken from the analysis developed for the subsystems involved in the entry vehicle. The Thermal Protection System (TPS) mass has been evaluated from a loop of preliminary thermal analysis described in subsection 9.3.2 and also the dimensions of the parachute and the aeroshell have been selected after a loop of evaluations starting from typical values in order to get good performance compromises. From these dimensions it is possible

to evaluate the masses of the parachute and the relative mortar [37] [38] to finally develop the final entry mass. All these final characteristics are reported in Table 9.1, where the entry velocity is the outcome of the mission analysis subsystem and the skycrane is the landing method selected, as it will be later explained in subsection 9.3.4. The masses are not only structural but they consider all the other systems implied such as sensors, propellant, etc and are all margined as described in section 19.3. What it is possible to immediately notice is the low value of the ballistic coefficient that in our case is good since the landing site has an elevation around 2.7 km.

Entry mass	1043.1 kg
Entry altitude	125 km
Entry velocity	5.749 km/s
Aeroshell hyper-sonic c_D	1.68
Aeroshell D	3.85 m
Ballistic coefficient	54 kg/m ²
Parachute c_D	0.65
Parachute D	16 m

Table 9.1: Entry vehicle characteristics

9.3.1 Entry model

In order to model the entry a code has been implemented in Matlab considering the entry vehicle as a point mass entering in a ballistic way and performing a 2D trajectory. The heatshield c_D has been modelled as varying with the mach number starting from the hyper-sonic value to then decrease with different linear variations in order to reach the values reported in Table 9.2 [39], that are the same of MER. Actually the entry phase ends with the parachute deployment that happens before the reach of a subsonic velocity but in any case the same model of the aeroshell drag coefficient behaviours will be used for the next phases.

c_D	1.68	1.23	1.12	1.05	1.01
Mach	>50	0.9	0.75	0.55	<0.3

Table 9.2: Heatshield c_D

EFPA	-12°
Parachute deployment altitude	6.147 km
Parachute deployment dynamic pressure	752 Pa
Parachute deployment Mach number	1.51

Table 9.3: -12° EFPA Parachute deployment

The atmosphere density has been modelled thanks to an exponential law [40]. The results of these calculations have been obtained in correspondence of an EFPA of -12°, whose choice will be lately explained in subsection 9.3.5. As it is possible to see from Figure 9.6 also the trajectory of the cruise stage has been modelled as well using as initial conditions the ones coming from the mission analysis subsystem and considering a c_D equal to 2 which is the typical value for spacecraft like structures. The result shows that the cruise stage lands at a safe distance from the rover.

The results reported in Table 9.3 show the feasibility of having a ballistic direct entry since the parachute deployment happens at good altitudes within the needed ranges of Mach and dynamic pressure and the obtained overall velocity trend is comparable with the ones of previous missions as shown by Figure 9.7 and Figure 9.8, suggesting acceptable heat flux trends as well. During this phase also the maximum value of axial deceleration is experienced with a value of 13.58 g that will be analysed in section 17.3.

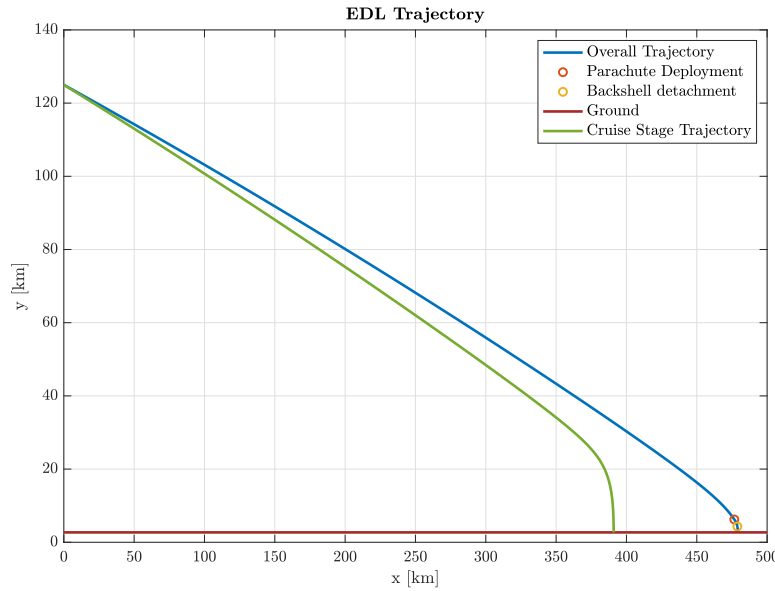


Figure 9.6: -12° EFPA trajectory

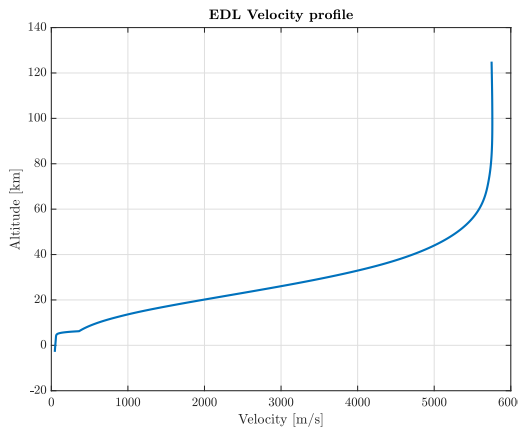


Figure 9.7: -12° EFPA velocity profile

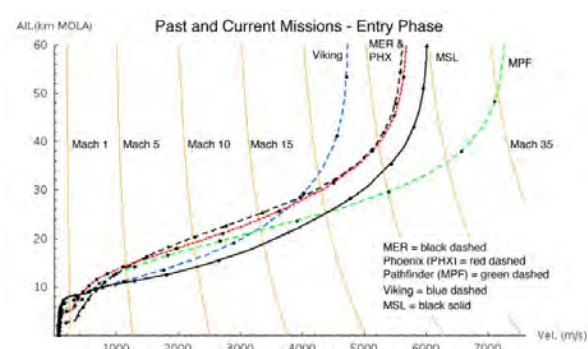


Figure 9.8: Previous missions velocity profiles

9.3.2 Thermal analysis

Starting from the density and velocity profiles obtained from the entry model analysis in subsection 9.3.1 and considering the geometrical characteristics of the heatshield, it is possible to obtain the heat flux at the stagnation point using the Sutton-Graves formula [38]. The result represented in Figure 9.9 shows that the obtained value is comparable to the one of other missions [35]. The peak value is around 48 W/cm^2 and the total heat results to be 1930 J/cm^2 . Thanks to this value the selection of SLA561V can be confirmed as the TPS material with the characteristics described in Table 9.4. Starting from these data the wall temperature is at first estimated thanks to the Allan-Eggers equation that equals the stagnation heat flux to the radiation flux considering the heatshield as a grey body:

$$T_w = \left(\frac{q_s}{\varepsilon \sigma} \right)^{1/4}$$

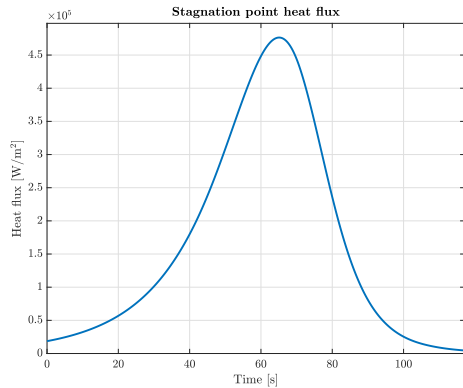


Figure 9.9: Trend of the heat flux at the stagnation point

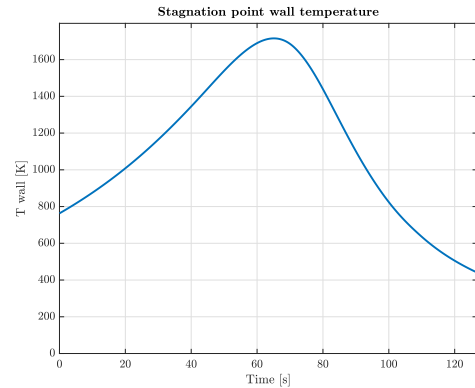


Figure 9.10: Trend of the wall temperature at the stagnation point

The result is shown in Figure 9.10.

Then the TPS thickness is estimated as the summation of the ablated thickness and the insulation one applying two different simplified models. Regarding the ablation, a conservative thickness regression rate has been estimated with the following steady state ablation formula

$$t < \frac{q_{cw}}{q_{abl} \rho}$$

[38] where q_{abl} is the heat of ablation and q_{cw} is the cold wall heat flux evaluated as

$$q_{cw} = \varepsilon \sigma (T_w^4 - T_{surr}^4)$$

where T_{surr} is the surrounding temperature.

Regarding the insulation thickness the general conduction equation shall be solved. In this case an analytical solution considering a semi infinite slab with constant surface temperature has been used [41] :

$$T(x,t) = \text{erf}(x/2\sqrt{t\alpha})(T_i - T_s) + T_s$$

where T_s is the surface temperature and T_i the initial one. Selecting the surface temperature as the highest wall temperature obtained during the whole trajectory and an initial temperature of 0 K it has been found the value of $x(t)$ for which a temperature of 250 °C, that represents a typical value on the cold side of the insulator, is obtained. Then the maximum value of depth $x(t)$ is selected as the insulation thickness. Finally the total TPS thickness is obtained and the correspondent mass is evaluated as reported in Table 9.4.

Thermal environment EDL using SLA561v as TPS

m_{TPS} [kg]	35.9
$t_{ablation}$ [cm]	0.15
$t_{insulation}$ [cm]	1.02
t_{TPS} [cm]	1.17
Q_{max} [J/cm²]	$1.93 \cdot 10^3$
q_{max} [J/cm² · s]	47.64
T_{max}^w [K]	1715.6
c_P^{TPS} [J/kgK]	1256
k_{TPS} [W/mK]	0.05477
ρ_{TPS} [kg/m³]	264.3
α_{TPS} [m²/s]	$1.65 \cdot 10^{-8}$
ε_{TPS}	0.97

Table 9.4: Thermal environment EDL using SLA561v as TPS

9.3.3 Parachute model

In order to better understand the dynamics of the parachute and capsule system, a model has been developed considering the whole as a double pendulum like system as represented in Figure 9.11.

The capsule and the parachute are modelled as two point masses linked through a mass-less beam with a hinge located at a distance of 2 m from the capsule and 37 m (evaluated as described in [42]) from the parachute.

These distances represent the relative positions of the centres of mass with respect to the hinge. To better represent the reality, a rotational spring has been added in correspondence of the hinge to simulate the resistance to rotation opposed by the material of the suspension lines of the parachute that are usually made of Kevlar. To model this spring, the same relations between the nominal parachute diameter and the suspension line diameter D_s and Kevlar elastic module considered for MSL have been used [43]. Then the number of suspension lines for the MARS PENGUIN parachute n has been found through a proportion with respect to the number used for MER and an equivalent diameter $D = n \cdot D_s$ has been evaluated. Finally, using this equivalent diameter, the rotational constant has been calculated as:

$$I = \pi \cdot D^4 / 64 \quad [\text{m}^2] \quad \text{Circular section inertia}$$

$$k = EI/l \quad [\text{Nm/rad}] \quad \text{Cantilever beam rot. stiffness}$$

The evaluated characteristics are reported in Table 9.5. Thus, implementing this model, the angle of attack of the capsule and the parachute as well as their motion after the parachute deployment have been evaluated as represented by Figure 9.12 and Figure 9.13.

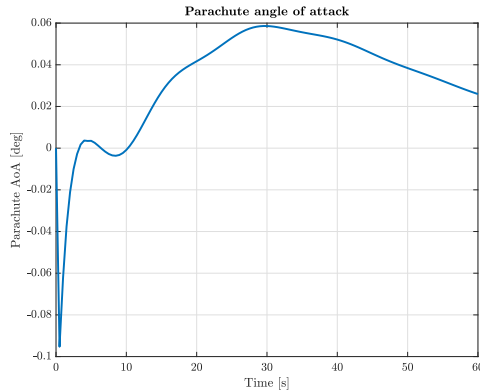


Figure 9.12: Parachute angle of attack

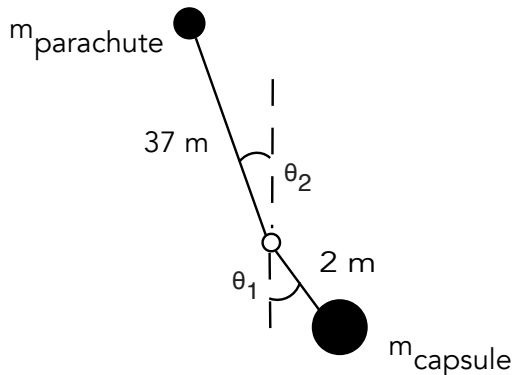


Figure 9.11: Model of the parachute capsule system

Parachute pendulum model characteristics

k_{kevlar}	$5.30 \cdot 10^5 \text{ N} \cdot \text{m/rad}$
E_{kevlar}	12.9 GPa
suspension line D [cm]	0.32 cm
number of suspension lines	55

Table 9.5: Parachute pendulum model characteristics

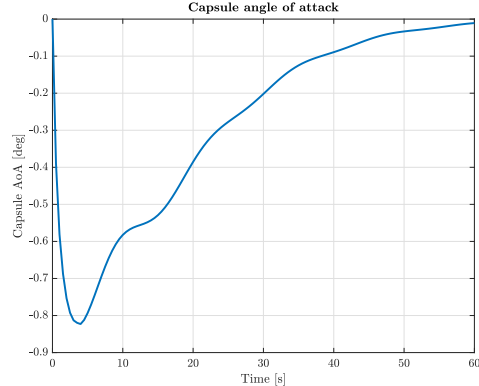


Figure 9.13: Capsule angle of attack

The results show a stable movement of both the parachute and the capsule that after an initial rotation reaching angles of attack lower than 1° immediately after the deployment, realign to the velocity direction during the following trajectory. To initialise this model the values obtained by the entry model trajectory evaluation at the parachute deployment altitude have been used.

Finally from this model it is possible to determine in a more accurate way the aeroshell separation altitude as well as the velocities obtained at an altitude of 4.3 km (around 1.6 km from the soil), that is the position where the backshell detaches and the final thrusted landing phase starts.

Aeroshell separation altitude	5.773 km
Horizontal velocity at 4.3 km	24.5 m/s
Fall vertical velocity at 4.3 km	-59.4 m/s

Table 9.6: Parachute pendulum model aeroshell separation and thrusted landing initial conditions

As shown in Figure 9.14 also the trajectory of the heatshield after its separation has been modelled as well using as

initial conditions the ones coming from the described model at the altitude reported in Table 9.6, considering also an additional 2 m/s of deltaV due to the release mechanism. The change of drag and mass of the capsule after the aeroshell detachment has been considered as well modelling the drag coefficient after the deployment as the one of a disk with a diameter equal to the one of the capsule ($c_D = 1.12$).

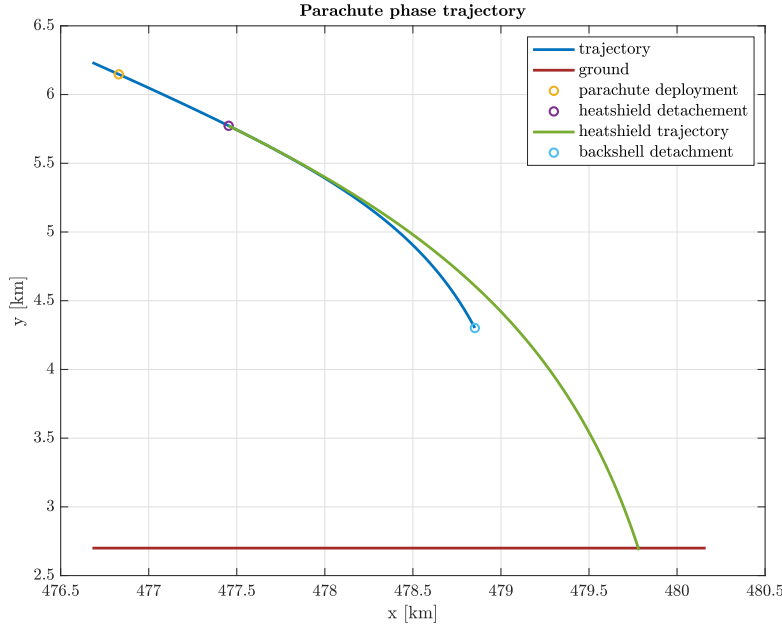


Figure 9.14: Parachute phase and heatshield trajectory

9.3.4 Landing procedure selection and modelling

The velocities at the end of the parachute phase show the feasibility of all landing solutions presented since they respect the ranges reported in subsection 9.2.3 for the skycrane utilisation and are low enough to be reduced to the needed ones for the other landing options through a proper propulsion system. In the end the skycrane configuration was selected due to its higher reliability with respect to the other options even though, through a preliminary analysis, it seems to be the one with the highest value of required mass. However, the possibility of performing rock avoidance and having a low landing velocity were considered significantly important for the safety of the rover and so the success of the mission since SKIPPER should report the lowest possible damages due to the landing phase. For the landing phase a model that simulates the phases described for the skycrane utilisation has been implemented. Starting from the values obtained by the parachute model at 1.6 km from the surface (4.3 km of altitude) reported in Table 9.6, the landing phase has been divided in 4 main phases:

1. Deceleration of the vertical velocity to 32 m/s and of the horizontal velocity to 0 m/s in the altitude range 1600 to 145 m from the surface.
2. Deceleration to a vertical velocity <1 m/s in the altitude range 145 to 25 m from the surface.
3. Constant velocity descent and rover release
4. Fly away of the skycrane

When the first phase starts the backshell and the heat-shield have been already removed and the only remained masses are the one of the rover, deployed along a 8 m long bridle during the third phase, and of the skycrane.

The drag coefficient of the skycrane has been considered to be equal to 2, which is a typical value for spacecraft-like structures.

To understand the needed values of vertical and horizontal thrusts during the first phase a shooting method has been used whereas for the thrusts of the other phases a loop calculation has been applied to find the optimal values to reach the needed velocity and altitude boundaries. The mass has been considered as time dependent thanks to the use of a function of the mass flow rate given by the propulsive subsystem analysis that has been included in the model. The results of this overall phase, considering a varying mass with respect to time and the new drag due to the skycrane shape (different from the one of the capsule), are reported in Table 9.7 and Figure 9.15.

Powered Landing Phase			
Phase	$Thrust_y$ [N]	$Thrust_x$ [N]	t_b [s]
1	2830.5	432	32.28
2	5228.5	0	7.6
3	1506.5	0	35.66
4	2230.6	500	11.42
	t_b^{13}		75.54 s
	t_b^{tot}		86.96 s
	skycrane impact distance		626 m

Table 9.7: Thrusts and times for the powered landing phase and skycrane impact distance

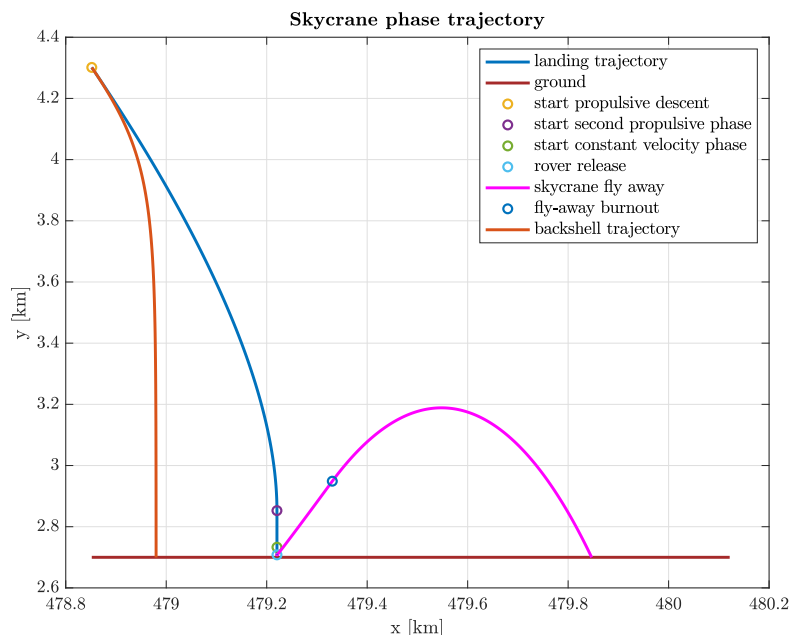


Figure 9.15: Skycrane phase and backshell trajectory

From these results it is possible to see that the obtained trajectory respects all the imposed boundaries and the skycrane impacts the soil at a distance of 626 m away from the rover.

It has to be said that the final thrust considered are all constant apart the one relative to the third phase, since it is the phase in which a constant descending velocity is needed, for which the value reported in Table 9.7 is the mean one. Furthermore, as it is possible to notice from Figure 9.15, the trajectory of the backshell once detached has been evaluated as well and added to the model using as initial conditions the one at Table 9.6 (the same used for the skycrane).

9.3.5 Montecarlo Analysis

Some calculations have been done as well in order to understand the uncertainty on the final landing position. For this purpose a Montecarlo simulation has been performed on Matlab considering the dynamic model previously described for the entry phase extended to the 3D case, since now also possible lateral deviations have to be considered, with some additions in order to model the trajectory up to reach the surface. The parachute

deployment has been modelled as an increment of drag according to the selected parachute characteristics.

The change of drag and mass of the capsule after the aeroshell detachment has been modelled as previously described in subsection 9.3.3. Since the final range is not affected significantly by the last landing phase it has been chosen not to include a specific model for it in order to keep the code as light and fast as possible to perform the Montecarlo analysis.

A gaussian distribution of 3σ of the parameters listed in Table 9.8 [44] was considered with an exception for the density that was considered as having an uniform distribution. For each iteration starting from the obtained value from the altitude uncertainty a sphere of position uncertainty was created, considering the deviation in x and y direction having the same distribution, and propagated in order to get the outcome from all the possible directions of deviation on the initial position. Regarding the velocity, for each iteration the obtained values of EFPA and heading angle deviations were considered as creating an ellipse of uncertainty relative to the initial velocity vector direction in order to consider all the possibilities of deviation. The described procedure can be better understood by looking Figure 9.16. The results reported in Figure 9.17 show the landing ellipse with -12° of EFPA with the respective Crossrange and Downrange uncertainties of $3\sigma_{\text{downrange}} = 9.48 \text{ km}$ and $3\sigma_{\text{crossrange}} = 3.22 \text{ km}$. These values show the compatibility with the landing site, whose largest dimension is around 20 km. Furthermore it has to be considered that the landed rover, in case of landing a little aside from the lake, could cover that distance in an acceptable time. While developing these analysis it has been verified that, as expected, the higher is the EFPA the lower is the range error. However, this will cause the parachute deployment altitude to be lower, which could be a problem in the case of having a landing site at relatively high elevations as it happens in the case of the MARS-PENGUIN mission (MOLA = 2.7km). For this reason, an EFPA of -12° has been eventually selected as a good compromise.

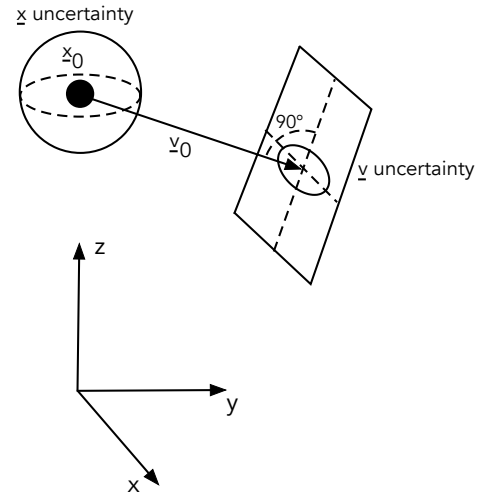


Figure 9.16: Uncertainty model for each iteration

Variable	3σ uncertainty
h	1 km
v	5 m/s
EFPA	0.1°
Heading angle	0.5°
density	10%
parachute deployment dynamic pressure	50 Pa

Table 9.8: Considered Uncertainties

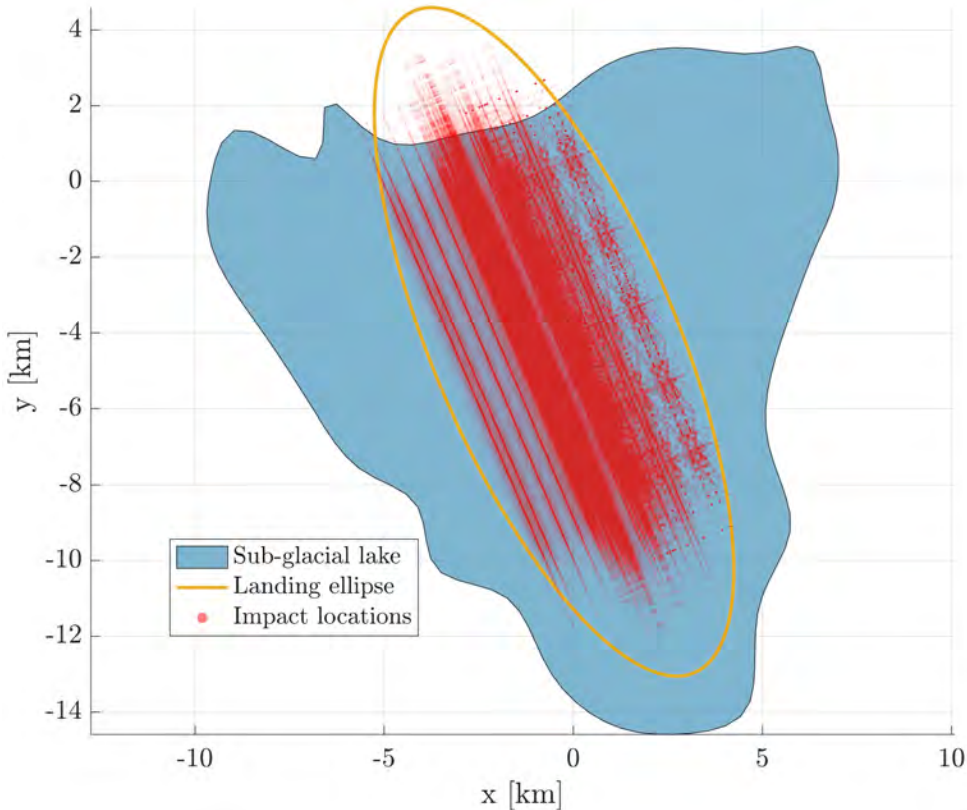


Figure 9.17: -12° EFPA landing ellipse

9.3.6 Wind effect

The horizontal wind velocity effect has been modelled as well in this simulation, with the trend at the time and location of MARS PENGUIN arrival [45] as the one reported in appendix Figure A.6. Using the same dynamic model described for the Montecarlo analysis and considering a mean value across the altitude of the wind velocity of 93.81 m/s as it acts creating a lateral drag force, it comes out a maximum lateral deviation of 337.3 m that is a deviation that can be corrected thanks to the skycrane propulsive system.

9.3.7 GNC preliminary definition

Regarding the GNC the used sensor are mainly two: IMU and Radar Doppler Altimeter. During the entry phase, that goes from the entry up to the parachute deployment and lasts 137.6 s, only IMU is used. During the parachute phase, that lasts 26 s, IMU is used up to the heatshield detachment and after that also the radar attached to the skycrane starts to be employed in order to get better measurements. For the last skycrane phase that lasts 114.94 s both the sensors keep working. The output of those sensors are sent to a Navigation filter that outputs the current state of the system and enables the whole GNC system to work properly identifying the exact points where the critical operations like parachute deployment, heatshield detachment, etc shall take place.

9.4 Conclusion

The described EDL allows the MARS-PENGUIN MISSION to deliver the rover safely at the Mars surface with a landing ellipse compatible with the subsurface lake that has to be investigated. Of course what has been presented is still a preliminary analysis and further computations with more refined models shall be done for the future development of the mission itself as some problems underestimated in this modelling may arise. For instance, in case of an incompatibility of the landing ellipse with respect to the landing site coming from further studies in more advanced phases of development, a lifting and 3 axis controlled entry could be considered to overcome this bottleneck. Also the GNC system has to be better defined in terms of algorithm and software development. However, the results showed in this chapter still demonstrate the feasibility of performing a successful EDL with the main features described in previous sections.

10. Propulsion Subsystem

10.1 Propulsion in interplanetary missions

The propulsion subsystem is crucial for the overall success of the mission since it is the one that provides the thrust needed for the different required manoeuvres in cruise and during [EDL](#) phase. Depending on the kind of manoeuvres, and so on the overall amount of energy required, two kind of propulsion systems can be distinguished: primary and secondary.

Concerning the first one, it is involved in all the most demanding activities of its related segment:

- [Trajectory Correction Manoeuvre \(TCM\)](#) in cruise
- Retrorockets firing during the landing

Regarding the secondary propulsion system, it is involved in low energy but still important manoeuvres such as:

- Collision avoidance manoeuvres
- Attitude control

So depending on the kind of manoeuvres that each segment has to perform in the different phases of the mission, there are some solutions that could be more suitable with respect to others. For this reason, the trade-off shall be done considering the pros and cons of adopting each propulsion technology as well as the drivers of the mission.

10.2 Preliminary analysis

10.2.1 Space segment

To achieve the goals of the mission, the launched segment must be able to perform all the necessary manoeuvres to arrive at Mars and land on it satisfying all the requirements coming from [EDL](#) analysis. For this reason, it must be provided with both a primary and secondary propulsion system. Chemical and electrical solutions are taken under consideration for the trade-off that will lead to the final architecture definition.

Primary propulsion system

Looking in the past, almost all of the Mars exploration missions used liquid mono or bipropellant chemical engines for the primary propulsion system. The well proven technology, the guarantee of a relatively fast travel and the possibility of performing instantaneous manoeuvres are what makes the chemical an attractive choice. Nevertheless, the low specific impulse means a higher propellant mass to transport and the design of tanks, feeding systems and valves implied in the utilisation of liquid propellant it is still a challenging task with high complexity and cost. On the other hand, electric propulsion, grants lower propellant mass but needs more massive components and constraints relative to the required power should be considered too.

Secondary propulsion system

For what concerns the secondary propulsion system, it shall be active whenever the primary propulsion system is working in order to correct the small momentum generated by the misalignment between the high thrust direction and the position of the spacecraft centre of mass. Furthermore, it answers the need of controlling the attitude of the spacecraft during cruise and entry in Martian atmosphere. These manoeuvres require lower levels of thrust with respect to the ones cited in the previous section.

The choice has still to be done between electric and chemical propulsion. For the low thrust requested, monopropellant or cold gas thrusters could represent a good choice thanks to their reliability and simplicity with respect to the bipropellant one and they were used in previous missions. The difference in terms of specific impulse remains with respect to the more efficient electric engines. The issues listed before for an electric primary propulsion can be applied to this case too.

10.2.2 Mars segment

Regarding the Mars segment what it is usually needed is a primary propulsion system to be used during the landing phase. Since for this application having high thrust is fundamental to effectively slow down the fall velocity during the last phase of the landing, only chemical engines can be considered. In particular, liquid ones were used for the benefits of having throttability during this critical phase. The propellant more largely used for this purpose is hydrazine, that grants high performance and reliability.

Considerations regarding the disposition of the thrusters on the cruise and landing stages must be done. This is because, using a distributed number of engines with respect to having just a main single one could be very useful to better control the attitude while landing with the same propulsive system. Also the number of tanks and their distribution are fundamental since they strongly influence the position of the centre of mass.

10.2.3 Requirements to be satisfied

From the considerations made in the previous sections and the Δv budget breakdown obtained in mission analysis, some requirements were set regarding the propulsion subsystem in terms of performances during the different phases in which it is involved. In Table 10.1 are reported the amount of Δv required for each manoeuvre and its duration in the case of chemical propulsion. The TCMs are performed to correct the trajectory right after the exit from Earth SOI and before entering Mars' one (REF MA). The mass of propellant needed for each manoeuvre is computed inverting the Tsiolkovsky equation, assuming hydrazine as propellant with $I_s = 225$ s. Total impulses and thrust levels are consequently retrieved from their definitions when not specifically requested.

Manoeuvre	Δv [m/s]	Duration	Total Impulse [N · s]	Average Thrust [N]
TCM1	25	9' 57"	36076.86	60.41
TCM2	63.5	24' 25"	88490.08	60.41
EDL Phase 1	46.28	32.28"	93985.95	2863.30
EDL Phase 2	40.80	7.60"	41777.06	5288.50
EDL Phase 3	148.74	35.66"	53723.00	1506.53
EDL Phase 4	64.94	11.42"	89800	2285.98

Table 10.1: Performances required to a chemical propulsion system

10.3 Chemical solution preliminary architecture definition

For a preliminary definition of the architecture of the propulsion subsystem it was decided to proceed with a pressure-fed liquid monopropellant. The chosen propellant is hydrazine and the pressurisation system is a simple blowdown operating with helium gas. These choices allowed to have a first idea of the masses at stake, with a reliable system widely used for this kind of applications due to its high-performance and versatility.

10.3.1 Preliminary sizing

To begin with, masses and volumes of propellant and pressurising gas are computed. As already mentioned, the mass of propellant is obtained by means of Tsiolkovsky equation, with an additional margin on the Δv of 20%:

$$m_p = m_f \left(e^{\frac{\Delta v}{I_s g_0}} - 1 \right) = m_0 \left(1 - e^{-\frac{\Delta v}{I_s g_0}} \right)$$

A 30% margin is added to this propellant mass estimation for the preliminary sizing, in order to take into account extra-needs of propellant for not-yet defined manoeuvres.

The volume of propellant comes straight from the ratio between mass of propellant and its density, accounting for a 3% margin for the unusable propellant trapped in the tank and a 0.5% for loading uncertainties. The initial volume of pressurising gas to load is computed as following:

$$V_{gi} = \frac{V_{prop}}{B - 1}$$

where B is the blowdown ratio (ratio between initial and final pressure of the gas or between final and initial volume). The pressurant mass is then derived from the equation of state, adding a 20% margin:

$$m_g = \frac{P_g V_{gi}}{R_{He} T_i}$$

where P_g is the initial gas pressure inside the tank assumed to be $26 \cdot 10^5$ Pa, R_{He} is the specific gas constant equal to 2078.5 J/kg K and T_i is the temperature in the tank at loading equal to 293.15 K (20°C). The total volume needed

for the tank is obtained summing up the propellant and pressurant volumes to the volume of the diaphragm/bladder, set equal to 1% of the previously mentioned volumes:

$$V_{tank} = V_{prop} + V_{gas} + V_{diaph}$$

In table Table 10.2 the masses and volumes for each phase are reported.

Parameter	Cruise		Landing	Total
	TCM1	TCM2		
Mass of propellant [kg]	21.74	53.32	124.51	199.57
Mass of pressurant [kg]		0.135	0.224	0.359
Volume of propellant [L]	79.19		131.37	210.56
Volume of pressurant [L]		31.68	52.55	84.23
Volume of single tank [L]	111.98		185.76	297.74

Table 10.2: Mass and volume estimated budgets divided per phase (margined)

As it can be noticed, the volume required for one single tank is quite high, especially for the cruise phase, for this reason it will be necessary to split the amount of propellant and pressurising gas in different tanks.

10.3.2 Possible architecture configurations

To begin with, the configuration of the propulsion subsystem in terms of disposition of the components and connections depends a lot on the general configuration of the launched spacecraft and on the landing strategy. Three general configurations were identified and taken into consideration:

- a) Single propulsion system
- b) Two separate propulsion systems, landing with airbags
- c) Two separate propulsion systems, landing with skycrane

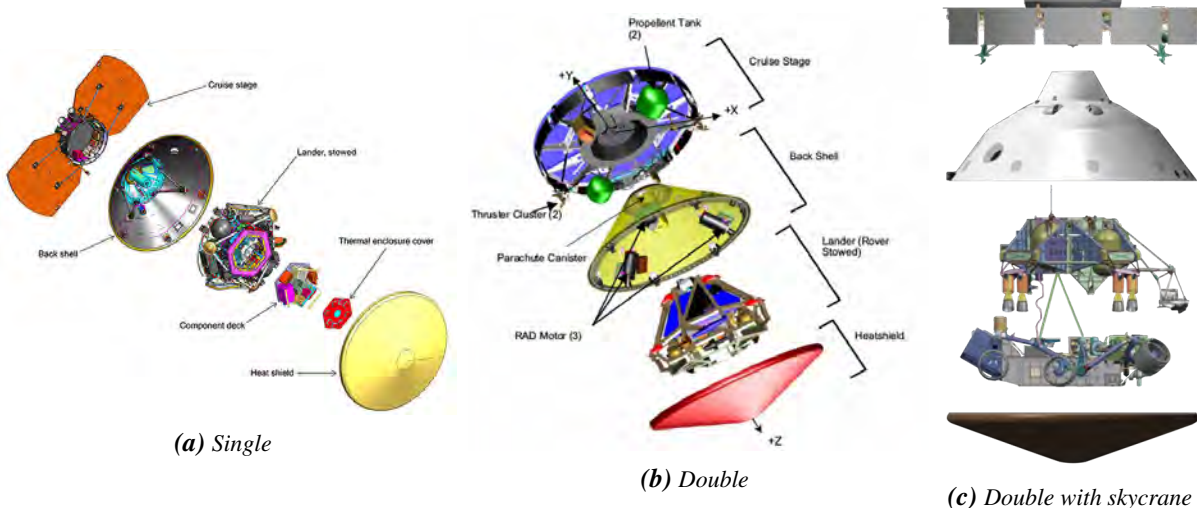


Figure 10.1: Possible configurations

The third alternative was chosen as final one, due to its better accuracy in landing and reliability. Indeed, the skycrane is equipped with a set of liquid engines that provide the high thrust required for landing safely the rover, eased down to the surface thanks to cables, and for pushing away the skycrane sufficiently far from the rover landing site. The cruise stage has clusters of liquid thrusters for primary and secondary propulsion, together with its own tanks and feeding lines.

10.4**Electrical solution preliminary study and trade-off**

Trade-off between chemical and electric propulsion system is done only for what concerns the cruise stage, since for the landing phase it is mandatory to have high and impulsive thrust that an electric engine cannot provide.

The gridded ion thruster and the Hall thruster were taken into consideration as electric alternatives. The Hall thruster has lower specific impulse, lower thrust efficiency, higher thrust density, lower specific power, wider angle ion plume, lower voltage, greater reliability than the gridded ion thruster.

To obtain a preliminary estimation for an electric propulsion system, some values were calculated after selecting some parameters from literature. The gridded ion engine is the QinetiQ T6 (Bepi Colombo) instead the hall engine mass is the Keldysh KM-45 engine. Gallium Arsenide (GaAs) cells (19% BoL efficiency) were chosen for SA. The propellant mass was computed knowing the Δv necessary for the TCMs with a 30% margin.

In Table 10.3 the comparison in terms of masses is shown. For chemical propulsion two possible architectures were given, one with European components and another one with American components, that resulted to be very similar in terms of mass. The I_s of an electric engine is much higher than the one of the chemical, this means lower propellant mass required but longer duration of the propulsive thrust. So the propellant mass is obviously higher in the chemical propulsion, but the dry mass of the electric system balances it out because it needs a PPU to increase the voltage for operating. In the case of the gridded ion thruster the required voltage is so high that just the mass of the PPU is higher than the whole dry mass of the chemical propulsion system. Moreover, the power demand is higher using electric propulsion and it must be taken into account that also solar panels will be needed, that will increase significantly the total mass of the cruise stage.

Final considerations on this trade-off will be discussed in chapter 13.

	Chemical		Electric	
	EU	US	Gridded	Hall
Dry mass [kg]	27.41	22.66	165.45	153.10
Propellant mass [kg]		75.06	13.22	23.27
Total mass [kg]	102.47	97.72	178.67	176.37

Table 10.3: Chemical-Electric trade-off for cruise stage propulsion system

10.5 Final configuration

The final configuration was chosen to be the one that granted lower mass and wider thrust applications in terms of throttleability, attitude control and stabilisation, both for cruise and landing stages. The margin on propellant was reduced to 20% and the one on pressurising gas to 10%, now that the architecture is defined, with a more precise component division for what concerns valves, catalytic beds and feeding system in general.

10.5.1 Cruise stage**Configuration**

The cruise stage propulsion system is composed by two clusters, each one with one MR-106L of 22 N thrust capability (primary propulsion) and four MR-103J thrusters of 1 N (secondary propulsion), all provided by Aerojet. The main engines are oriented in the axial direction of the cruise stage. For each manoeuvre the spacecraft will be re-oriented so that the thrust will have only an axial component. The secondary engine configuration allows to fully control the attitude of the cruise deck during all the interplanetary travel, with redundant thrusters for backup (detailed description in Section 8.4). The whole configuration is illustrated in Figure 8.2. Two rolling diaphragm tanks by MOOG, with 50.8 L capacity each, are completely filled with a total of 72.93 kg of propellant (Hydrazine) and 0.116 kg of pressurising gas (Helium). In terms of volumes they correspond to 74.34 L of Hydrazine and 27.26 L of Helium. Table 10.4 reports the components of the propulsion system. Its architecture decomposition is illustrated in Figure A.7 (Appendix A.5).

Component / Parameter	Material / Value	Quantity	Mass [kg]
MR-106L thrusters		2	1.18
Thrust range [N]	10 - 34		
Specific Impulse [s]	228 - 235		
Total Impulse [N · s]	561388		
Propellant mass flow rate [g/s]	4.1 - 14.0		
Feed pressure [bar]	5.9 - 27.6		
Chamber pressure [bar]	3.8 - 13.4		
MR-103J thrusters		8	2.96
Thrust range [N]	0.19 - 1.13		
Specific Impulse [s]	202 - 224		
Total Impulse [N · s]	183000		
Propellant mass flow rate [g/s]	0.09 - 0.5		
Feed pressure [bar]	4.8 - 21.3		
Chamber pressure [bar]	4.5 - 23.8		
Catalyst	Shell 405	10	
Heaters		10	
Feeding system			4.45
Valves		14	2.8
Lines			1.65
Rolling Diaphragm Tank	Aluminium Alloy	2	14.70
Diameter [cm]	46.228		
Volume [L]	50.8		
Dry mass			22.68
Propellant	Hydrazine		72.93
Pressurant	Helium		0.116
Total mass			96.73

Table 10.4: Cruise stage components and characteristics

Performances

The two TCMs, as previously said, occur respectively 3 days after launch and at the entrance of Mars SOI (-3 from landing). The first TCM consumes 17 kg of propellant for a 10-minute manoeuvre of 25 m/s Δv . The second one, more demanding, lasts for 24 minutes in order to achieve 63.5 m/s Δv using thrusters at full capability and burns more than 40 kg of propellant (more than 50% of the propellant on board). Final propellant mass in the tank is not zero because part of the remaining propellant is used for AC manoeuvres (5.8 kg), whilst the other part can be used for unplanned TCMs (complete variation in Figure 10.2a).

Pressure profile in the tanks is reported in Figure 10.2b. Since in a blowdown system the pressure in the tank gradually decreases while expelling propellant, it was verified that the feeding system could always provide the minimum feed pressure (5.9 bar) to the thruster accounting also for feeding and injection losses, in order to keep the thrusters working at nominal level.

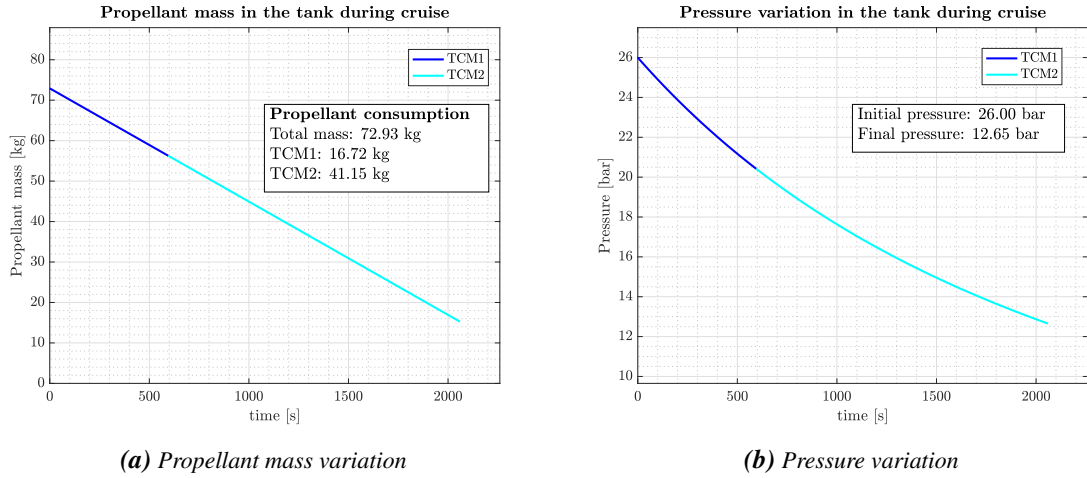


Figure 10.2: Tank parameter variations during cruise

10.5.2 Landing stage

Configuration

For landing, the propulsion system is centred in the skycrane were the tanks are placed, but a set of RCS thrusters is located also in the backshell. They are 4 MR-106L of 22 N, the same of the primary propulsion system of the cruise stage and are used for the beginning of EDL to stabilise the capsule when entering Mars' atmosphere. Twelve MR-104H throttling rocket engines, with 510 N nominal thrust but capable of reaching 554 N if used at maximum, are placed at the four corners of the skycrane structure. They will allow the skycrane to safely land Skipper on the surface. Four rolling diaphragm tanks (same of the cruise stage) will be filled completely with 145.85 kg of Hydrazine and 0.190 kg of Helium. The architecture components are reported in Table 10.5 and the schematics of the whole system is illustrated in Its architecture decomposition is illustrated in Figure A.8 (Appendix A.5). As also an horizontal component of thrust is needed in some phases of the landing, the two lateral thrusters of each cluster will be inclined of 20° in the XZ plane, whereas the central ones will be aligned with the vertical axis. With respect to the XY plane, the lateral thrusters will be inclined of 20° also in this direction, in order to have control on the y-axis too and counteract possible unexpected disturbances that could arise. The configuration is shown in Figure 10.3.

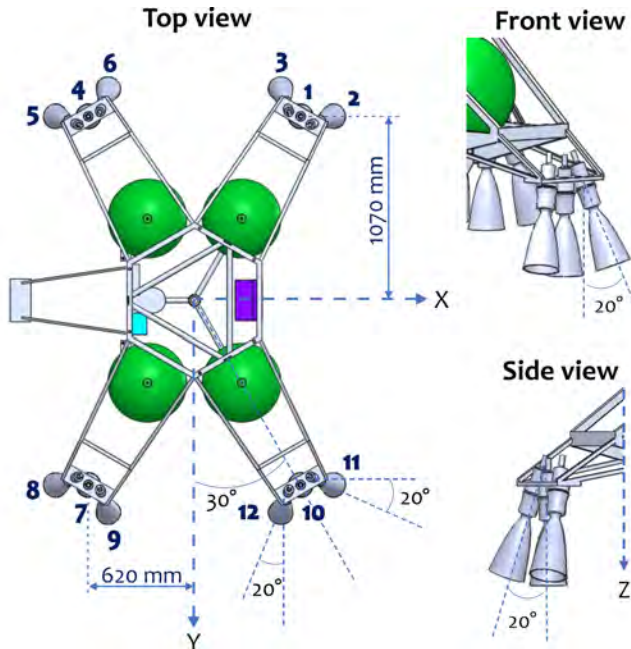


Figure 10.3: Skycrane propulsion system configuration

Component / Parameter	Material / Value	Quantity	Mass [kg]
MR-106L thrusters		4	2.36
Thrust range [N]	10 - 34		
Specific Impulse [s]	228 - 235		
Total Impulse [N · s]	561388		
Propellant mass flow rate [g/s]	4.1 - 14.0		
Feed pressure [bar]	5.9 - 27.6		
Chamber pressure [bar]	3.8 - 13.4		
MR-104H thrusters		12	28.8
Thrust range [N]	201 - 554.2		
Specific Impulse [s]	223 - 237		
Propellant mass flow rate [g/s]	90.8 - 249.5		
Feed pressure [bar]	6.9 - 28.9		
Chamber pressure [bar]	3.9 - 10.7		
Catalyst	Shell 405	16	
Heaters		16	
Feeding system			12.71
Valves		24	9.6
Lines			3.11
Rolling Diaphragm Tank	Aluminium Alloy	4	29.39
Diameter [cm]	46.228		
Volume [L]	50.8		
Dry mass			73.31
Propellant	Hydrazine		145.85
Pressurant	Helium		0.190
Total mass			219.35

Table 10.5: Landing stage components and characteristics

Performances

EDL is divided into four phases for what concerns the propulsive part (Section 9.2.3): Phase 1 reduces to zero the horizontal velocity and to 32 m/s the vertical one, Phase 2 drastically brakes the landing stage till 0.75 m/s, Phase 3 is a constant velocity descent while lowering the rover, Phase 4 is the skycrane final burn to fly away from the rover and land at least 600 m distant from it. The requested performance for the propulsive phase of the landing in terms of thrust and burning time is reported in Table 9.7.

For the calculations that will be performed from now on, a different reference system will be adopted, so, vertical thrust will be addressed as T_z and will have a minus sign, whilst the horizontal thrust will be T_y .

As explained before, there is a thrust component in y-direction in the first phase to reduce to zero the horizontal velocity and after that only vertical thrust is needed. In the end, for the fly-away of the skycrane thrust is needed both in y and z directions.

To allocate the requested thrust among the twelve thrusters, a constrained linear programming algorithm was used. It solves a classical linear system of the type:

$$Ax = b$$

with A : 24x24 matrix composed by two 12x12 identity matrixes, the first one with a minus sign

b : 24x1 vector with 12 zeros and 12 maximum values of thrust (510 N)

(in order to have positive thrust and to set the upper bound of thrust that each thruster is capable to give) imposing the constraint:

$$A_{eq}x \leq b_{eq}$$

with A_{eq} : 6x12 matrix containing forces and moments applied to each of the twelve thruster

b_{eq} : 6x1 vector with desired total thrust along the x,y and z directions and moments (zero in each direction)

$$A_{eq} = \begin{bmatrix} F_{x_1} & F_{x_2} & \dots & F_{x_{12}} \\ F_{y_1} & F_{y_2} & \dots & F_{y_{12}} \\ F_{z_1} & F_{z_2} & \dots & F_{z_{12}} \\ M_{x_1} & M_{x_2} & \dots & M_{x_{12}} \\ M_{y_1} & M_{y_2} & \dots & M_{y_{12}} \\ M_{z_1} & M_{z_2} & \dots & M_{z_{12}} \end{bmatrix} \quad b_{eq} = \begin{bmatrix} T_x \\ T_y \\ T_z \\ 0 \\ 0 \\ 0 \end{bmatrix}$$

Applying this algorithm to each of the four phases, the thrust required from each thruster was found. Obtained values are reported visually in Figure 10.4a divided per thrusters and phases. As it can be seen, only in Phase 2 all thrusters are fired simultaneously and not all of them use maximum thrust.

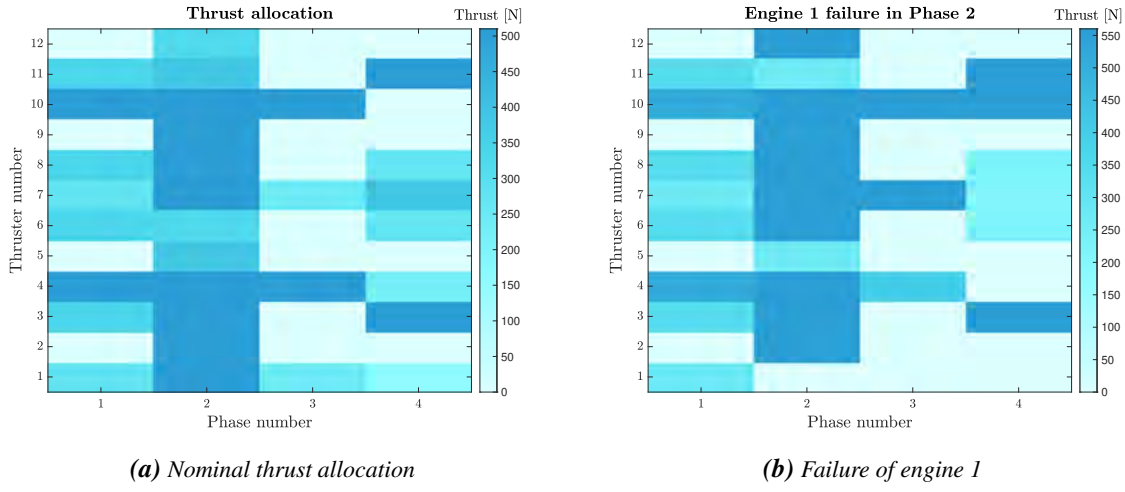


Figure 10.4: Thrust allocation among thrusters during landing

The system is robust with respect to not only the disturbances in x and y directions, but also to engine failures. Indeed, the system is able to provide the same thrust profile even loosing of a lateral or central thruster for case of one engine failure or loosing two central engines. In the case of failure the thrusters use the maximum thrust of 554 N. In Figure 10.4b the thrust allocation in case of failure of engine 1 (central engine) during Phase 2 is shown. This proves that the system can ensure a safe landing even in the worst case of one-engine failure, which is the loss of a central engine during the most demanding phase in terms of vertical thrust required.

From the values of thrust per thruster, mass flow rates are retrieved as:

$$\dot{m} = \frac{T}{I_s g_0}$$

Consequently, as the thrust and mass flow rates are assumed to be constant during each phase, the mass of propellant is computed as:

$$m_{prop} = \dot{m} \cdot t_b$$

In Figure 10.5a the propellant mass used for landing is represented, divided by phases. The most demanding in terms of propellant is the first phase, with more than 40 kg. A part of the propellant is used also from the RCS thrusters during entry (about 1 kg) but, as in the case of the cruise stage, not all the propellant is consumed since the tanks are filled with more than the required mass of propellant. This allows to have some reserves for unplanned manoeuvres.

Pressure variation profile (Figure 10.5b) shows that the pressure at the end of the landing is sufficient to guarantee the correct functioning of the thrusters (minimum feed pressure 6.9 bar), accounting for the pressure decrease intrinsic of the blowdown architecture and feeding and injection losses from the tank to the combustion chamber.

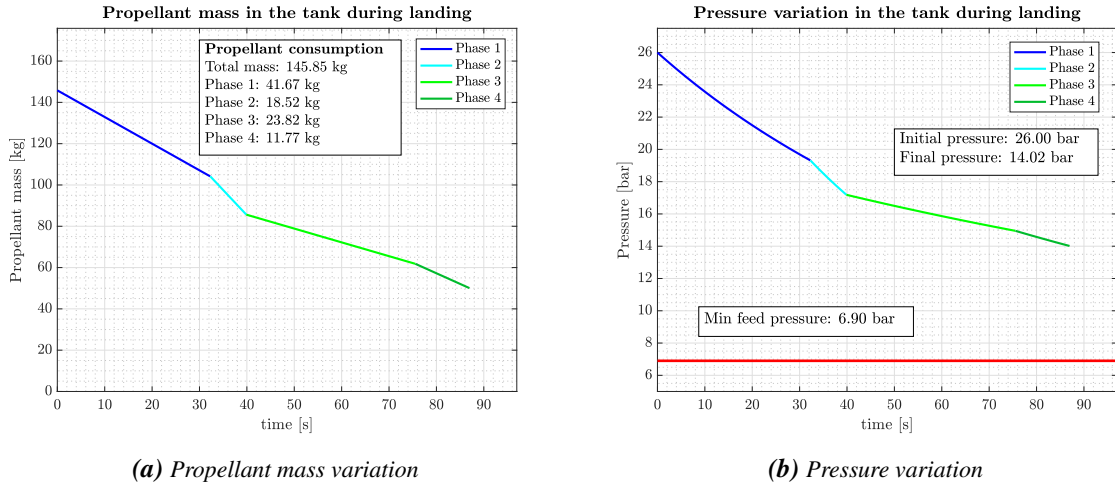


Figure 10.5: Tank parameter variations during landing

10.6 Effects on other subsystems

The propulsion subsystem affects other subsystems in terms of requests and constraints.

In terms of requests, the most affected subsystem is the **EPS**. Power demand of the propulsion subsystem comes mainly from the flow control valves, the catalytic bed heater and its valve. In the table below the maximum operating values for power needed from the thrusters are shown.

Component	Parameter	Value
MR-104H 510N valve	Max power	52 W @28 Vdc
MR-104H 510N catalytic bed	Max heater power	8.1 W per el @28 Vdc
MR-106L 22N valve	Max power	25.1 W @28 Vdc
	Max heater power	4 W @28 Vdc
MR-106L 22N catalytic bed	Max heater power	7.06 W @28 Vdc
MR-103J 1N valve	Max power	8.25 W @28 Vdc
	Max heater power	1.54 W @28 Vdc
MR-103J 1N catalytic bed	Max heater power	6.32 W @28 Vdc

Table 10.6: Highest power requirements

Also the **TCS** is required to satisfy some requirements for the propulsion subsystem. Indeed, catalytic beds require to be heated and kept at their nominal operating temperature, especially during the landing phase, when it is fundamental that thrusters work in their optimal conditions.

For what concerns the constraints, the propulsion subsystem drives the design of the skycrane configuration with its tanks and thrusters, in terms of dimensions and location, as it will be explained in Chapter 16.

11. Telemetry and Telecommand

11.1 Introduction

11.1.1 Communication phases

Communications with Earth during the mission can be divided into three main phases.

i) Cruise

Communication will take place by means of direct X-band links with ESTRACK's DSA antennas, using a parabolic HGA along with a 65 W TWTA. In off-nominal situations, two wide-beam LGAs (one for uplink, the other for downlink) will be available to provide low rate telemetry and telecommanding. The cruise phase will terminate upon separation of the cruise stage, prior to entering Mars' atmosphere.

ii) Entry, Descent and Landing (EDL)

From now on, communications with Earth will solely rely on UHF relay links, using initially a wraparound antenna on the backshell of the entry capsule and later switching to the Rover Ultra High Frequency antenna during terminal descent. The presence of at least one orbiter above the landing site will be necessary, in order to provide full real-time coverage of the event. A transmission of the telemetry after landing would not be accepted given that, in the event of failure, it would not be possible to assess its causes.

Despite the excellent coverage of polar regions, the certainty of the presence of an orbiter during the whole EDL is still not guaranteed. To address the issue, it might be possible to perform phasing adjustments (i.e. adjustments of the true anomaly) in order to optimise the timing of the orbiter overflight during EDL. The same procedure was used by MGS, during the landing of the Spirit rover.

iii) Surface operations

The Skipper rover of the MARS-PENGUIN mission will have no direct-to-Earth communication capability and will rely exclusively on UHF relay links.

The polar location of the landing site will on the one hand result in limited LoS with Earth, on the other hand it will further promote the use of a relay link. Indeed, orbiters are typically placed in near-polar orbits, which means they cross both polar regions once per orbit, thus resulting in increased contact frequency compared to lower latitudes.

Among the currently operating orbiters of the Mars relay network, MRO has been identified as the most suitable one. The performance of the two more recently launched orbiters (i.e. MAVEN and TGO) has been analysed and they have been ruled out due to their lower orbit inclination, which would be inconvenient in terms of coverage of the 81°S latitude of the landing site. In addition, it is estimated that MRO will have enough propellant to keep operating into the 2030s.

11.2 Cruise

The antenna sizing and the corresponding link budget analysis have been carried out, considering the trajectory reported in section 7.2. In addition, a detailed atmospheric modeling is also implemented in order to estimate the signal attenuation caused by the Earth's atmosphere.

As it can be seen from Figure 11.1 the Earth-S/C range will increase monotonically up to 1.62 AU upon arrival at Mars. In addition, from the trend of the Sun-Earth-Probe (SEP) angle, it can be concluded that no communication outages due to solar superior conjunctions will occur. Indeed, thanks to the uplink tests conducted by the NEAR S/C, it was possible to determine that at X-band practically no link degradation occurs as long as $\text{SEP} > 2.3^\circ$ (provided that no other significant solar transient events are taking place) [46]. Below 1.3° strong scintillation phenomena are expected to have severe consequences. It should also be underlined that the effects of Sun during inferior conjunctions were proved to be negligible.

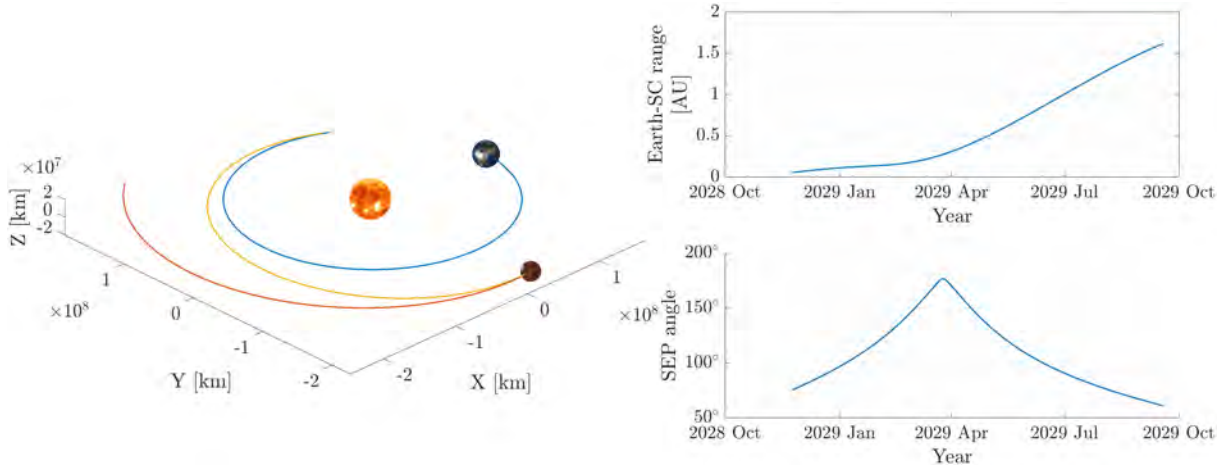


Figure 11.1: Earth-SC range and Sun-Earth-Probe angle over the trajectory

11.2.1 Earth's atmospheric attenuation

In the design of Earth-space links for communication systems, the effect of multiple sources of simultaneously occurring atmospheric attenuation must be considered. The overall attenuation represents the combined effect of 4 main components: atmospheric gases, rain, clouds, scintillation.

All these contributions depend on p , the probability that a given attenuation level is exceeded. The value $p = 1\%$ has been considered as an acceptable threshold for sizing our communication architecture.

The effect of varying elevation angle to the S/C, θ , is relevant: the lower θ , the higher the attenuation. In particular, it is assumed that a minimum elevation of 5° is required for establishing a link with the ESTRACK stations.

In other words, the sizing condition for designing the deep space link will be the attenuation level in correspondence of $\theta = 5^\circ$, that is exceeded for 1% of an average year at the most critical Earth station.

Prediction methods required for the design have been implemented according to International Telecommunication Union (ITU) recommendations outlined in [47]. Further modeling details are provided in subsection A.6.3.

The total attenuation map in Figure 11.2, obtained from the aforementioned models, has been computed in correspondence of our sizing conditions, i.e. 5° elevation and 99% weather. It can be clearly noticed that, besides being 120° apart, the three ESTRACK stations are all located in mid-latitude regions, which are favourable in terms of low atmospheric attenuation.

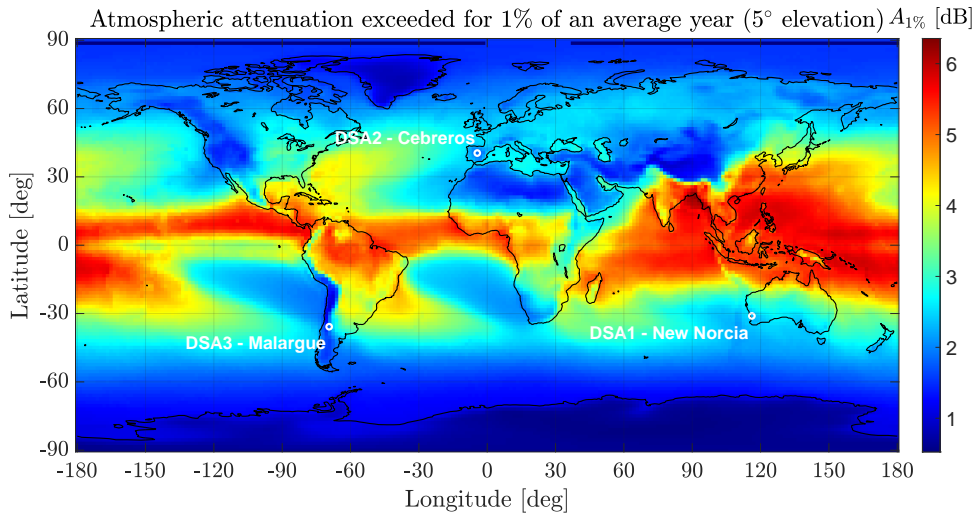


Figure 11.2: World attenuation map at 8450 MHz

Let us now focus on the three sites of interest, at which the total attenuation exceeded for 1% of an average year is plotted as a function of the elevation angle in Figure 11.3. It can be seen that the most critical GS is the one in New

Norcia (Australia), with a peak attenuation of 2.15 dB (return carrier). Such a value will be considered for sizing the deep space link.

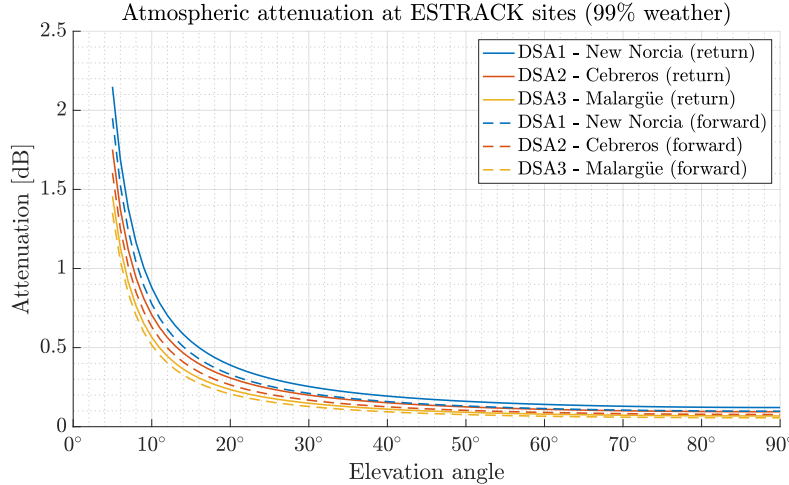


Figure 11.3: Atmospheric attenuation exceeded for 1% of an average year at ESTRACK sites

11.2.2 HGA sizing

The HGA sizing has been performed such as to guarantee a given minimum downlink/uplink data rate, assuming a 3 dB link margin, in the most critical condition (i.e. upon arrival at Mars, when range is maximum).

Each DSA is characterised by:

- $D_{DSA} = 35 \text{ m}$
- $\text{EIRP}_{DSA} = 138 \text{ dBm}$ (using X-band High Power Amplifiers)
- $(G/T)_{DSA} > 50.1 \text{ dB/K}$
- upper bound of total atmospheric attenuation: $A_{atm} = -2.15 \text{ dB}$
- assumed pointing accuracy: 0.1° ⁽¹⁾
- HPBW at X-band: 0.064°
- X uplink band: 7.145-7.235 GHz
- X downlink band: 8.4-8.5 GHz

For the return link, **BPSK** modulation with Viterbi-decoded convolutional coding will be employed, which is characterised by a constraint length $k = 7$ and a rate $r = 1/2$.⁽²⁾ Both **QPSK** and **BPSK** modulation could in principle be used with $(7, 1/2)$ convolutional coding, nevertheless ESTRACK stations are **TTCP** compliant, which means that between the two only **BPSK** is supported in remnant carrier mode [48]. The choice of **BPSK** modulation + Viterbi coding is mainly driven by the excellent **BER** performance and is indeed typical of deep space links, where clear limitations in terms of antenna size and power available to the space segment require to communicate successfully also in the event of low **SNR**. Reed-Solomon Viterbi decoding would actually allow even higher **BER** performance: it has not been chosen due to its higher complexity and given the fact that a sufficient downlink performance level would be achieved using $(7, 1/2)$ coding.

For the forward link **BPSK** modulation is still used, while as suggested by **CCSDS**, **BCH** $(63, 56)$ coding is preferred.

The quality of a digital communication link can be measured in terms of **Bit Error Rate (BER)**. The latter is directly related to the energy-per-bit to noise-power-density ratio, E_b/N_0 , by a relationship that depends on the specific coding and modulation techniques. In other words, once coding and modulation are fixed, it is possible to determine

⁽¹⁾in the ESTRACK handbook, the pointing accuracy is provided for all ground stations except DSAs; however, for all other stations the value is indeed in the order of 0.1°

⁽²⁾sometimes denoted as $(7, 1/2)$

the $(\frac{E_b}{N_0})_{\min}$ such as to guarantee a given BER_{\max} . The corresponding link budget equation may then be written as:

$$\begin{aligned}\frac{E_b}{N_0} &= \frac{B_n}{R_D} \cdot \text{SNR} \\ &= \frac{B_n}{R_D} \cdot \frac{P_{\text{TX}} G_{\text{TX}} L_{\text{TX}} \cdot G_{\text{RX}} / T_h L_{\text{RX}} \cdot A_{\text{atm}} L_{\text{FP}}}{K_b B_n}\end{aligned}$$

The design of the HGA has been carried out with the aid of Matlab's Antenna Toolbox. This led to the selection of a parabolic reflector with a diameter of 71 cm ($20\lambda_{\text{return}}$) and a focal length of 17.7 cm ($5\lambda_{\text{return}}$). The resulting far-field radiation pattern is reported in Figure 11.4.

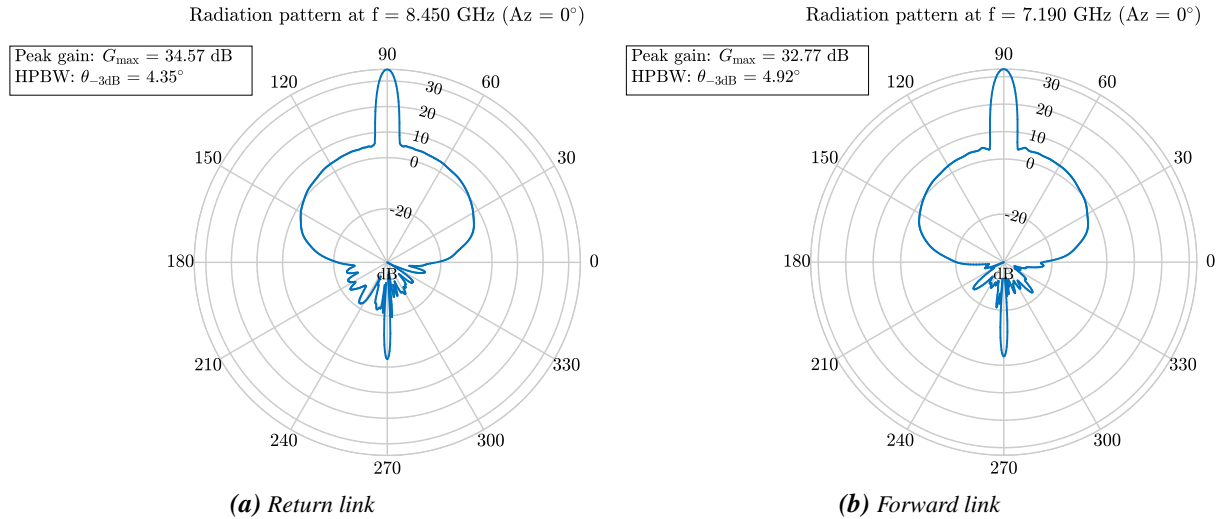


Figure 11.4: Polar radiation pattern ($Az = 0^\circ$) of the HGA

As expected, a slightly higher gain and lower HPBW is obtained for the return link, since a higher frequency band is allocated for the latter.

In addition to this, a desired pointing accuracy of at least $\pm 2^\circ$ has been assumed for link budget calculations.

Return link

The return link has been designed such as to achieve the following performance:

- min data rate guaranteed at the end of cruise: $R_D^{\min} = 8$ kbit/s
- max allowed error rate: $\text{BER}_{\max} = 10^{-5} \xrightarrow{[49]} (\frac{E_b}{N_0})_{\min} = 4.4$ dB

As a comparison, the cruise stage of the MSL mission was capable of guaranteeing a minimum downlink data rate of 7 kbit/s at the end of cruise [50], although it could benefit from 70 m parabolic reflectors of the DSN, which are double in size compared to those of ESTRACK's DSAs.

The link budget analysis corresponding to the end of cruise for the MARS-PENGUIN mission is reported in Table 11.1.

Return link parameters	[dB]
P_{HGA}	18.13
G_{HGA}	34.57
$L_{\text{point}}^{\text{HGA}}$	-2.54
L_{FP}	-278.71
A_{atm}	-2.15
$L_{\text{point}}^{\text{GS}}$	-0.29
$(G/T)_{\text{GS}}$	50.1
$1/K_b$	228.60
$1/R_D$	-36.99
$\frac{E_b}{N_0}$	10.72
$(E_b/N_0)_{\min}$	4.4
Link margin	6.32

Table 11.1: Return link budget analysis during cruise

In addition, the resulting maximum data rate variation over the course of the cruise is reported in Figure 11.5.

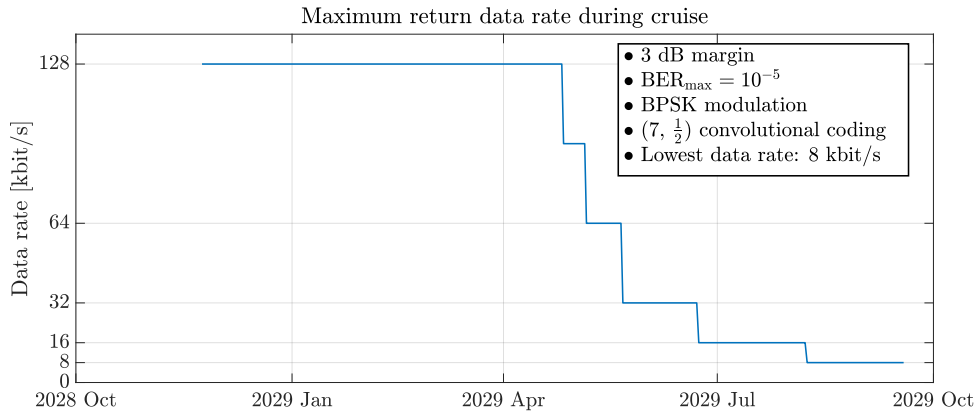


Figure 11.5: Downlink data rate variation over the cruise

Forward link

The forward link has been designed such as to achieve the following performance:

- data rate guaranteed throughout the whole cruise: $R_D^{\min} = 4 \text{ kbit/s}$
- max allowed error rate: $\text{BER}_{\max} = 10^{-6} \xrightarrow{[51]} \left(\frac{E_b}{N_0}\right)_{\min} = 11.0 \text{ dB}$

As a comparison, the cruise stage of the MSL mission was capable of guaranteeing a minimum uplink data rate of 0.5 kbit/s at the end of cruise and a maximum of 2 kbit/s [50], using 34 m reflectors only.

The link budget analysis corresponding to the end of cruise for the MARS-PENGUIN mission is reported in Table 11.2.

Forward link parameters	[dB]
EIRP _{GS}	108
$L_{\text{point}}^{\text{GS}}$	-0.29
A_{atm}	-2.15
L_{FP}	-277.31
$(G/T)_{\text{HGA}}$	13.70
$L_{\text{HGA}}^{\text{point}}$	-2.54
$1/K_b$	228.60
$1/R_D$	-32.00
E_b	29.15
N_0	
$(E_b/N_0)_{\min}$	11.0
Link margin	21.00

Table 11.2: Forward link budget analysis during cruise

11.2.3 Safe mode communication

Two separate microstrip Low Gain Patch (LGP) for TX/RX, fed by the same TWTA as the HGA, will be employed for safe mode communication. The latter will be automatically entered upon detection of off-nominal conditions, whenever the tight pointing requirements of the HGA can no longer be guaranteed.

The antenna pattern reported in [52] and depicted in Figure A.10 has been taken as a reference.

The resulting low rate telemetry data rate is provided in Figure 11.6. It can be seen that in correspondence of a very coarse pointing with an accuracy of $\pm 40^\circ$, an acceptable data rate ranging from 8 kbit/s to 8 bit/s is still guaranteed.

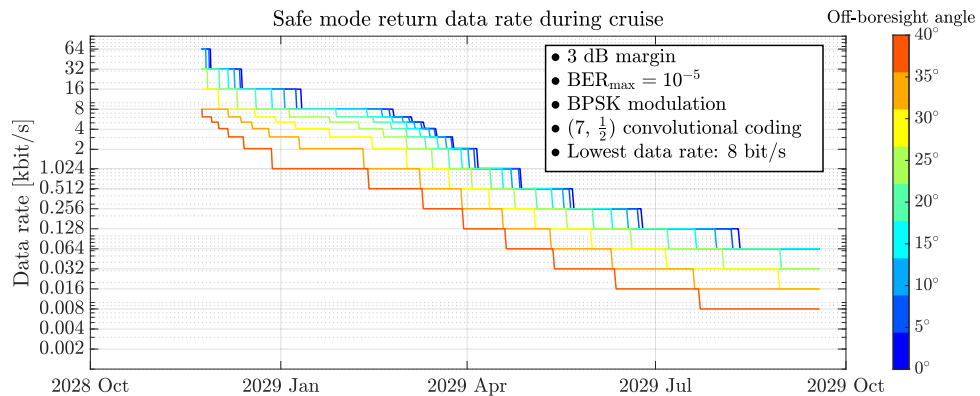


Figure 11.6: Maximum safe mode telemetry rate, parametrised by the off-boresight angle

11.2.4 Mass & power budget

The chosen X-band Deep Space Transponder (X-DST) is X²PND, produced by Thales Alenia Space. Its mass and input power⁽³⁾ are reported in [53]. The cruise stage will be equipped with two identical X-DSTs for redundancy. Mass and input power of the TWTA have been estimated by means of statistical fittings, expressed as a function of the RF input power of 65 W. The cruise stage will be equipped with two identical TWTAAs for redundancy.

The antenna mass has been estimated through a similar fitting law for parabolic reflectors,⁽⁴⁾ given as a quadratic function of the diameter [54].

In addition, RUAG Space's antenna pointing mechanism has been selected, which guarantees an azimuth/elevation

⁽³⁾assuming full duplex mode

⁽⁴⁾which also accounts for the mass of the antenna feed

pointing accuracy of 0.1° . Its mass and power demand are provided in [55]. The values obtained are reported in Table 11.3.

Component	Mass [kg]	Power [W]	Margin
X-DST ($\times 2$, i.e. redundant)	2×3.3	52	10%
TWTA ($\times 2$, i.e. redundant)	2×7.0	121	10%
HGA (including feed)	3.2	-	10%
HGA's pointing mechanism	9.0	6	10%
Total	32.8	173	
Total with margin	36.1	190.3	

Table 11.3: Mass and power breakdown of the cruise stage's TMTC subsystem

11.3 Entry, Descent and Landing

Antennas onboard the entry capsule will exclusively operate in transmit mode during EDL. Being the latter deemed an extremely critical phase, the presence of multiple orbiters above the landing site would be advisable. Communications will take place through UHF links to the Mars relay network, by means of the Electra-lite transceiver inside the rover and two different antennas.

- i) Wraparound antenna mounted on the backshell of the entry capsule (BUHF), whose radiation pattern [56] is depicted in Figure A.12a (the simplified pattern in Figure A.12b has actually been used in the EDL simulation). The BUHF antenna will be employed starting from cruise stage separation until backshell separation.
- ii) Quadrifilar helix antenna mounted on the rover (RUHF), whose radiation pattern is represented in Figure A.13. It will be used during terminal descent, i.e. from backshell separation until landing and for the remainder of the mission, whenever the rover will have to communicate with Earth.

11.3.1 Optimal phasing performance

As already mentioned, it is possible to ask to the owner of an orbiter to perform some small phasing adjustments prior to EDL. The optimal phasing of MRO has then been identified by maximizing a score that accounts for the average E_b/N_0 over each of the three main phases of EDL. These three phases are weighted based on a given priority in terms of coverage quality that we are willing to guarantee, as defined in Table 11.4.

Phase	Priority of coverage quality	R_D	32 kbit/s
Entry → Parachute deployment	20%	BER	10^{-7}
Parachute deployment → Backshell separation	35%	Modulation	BPSK
Backshell separation → Landing	45%		

Table 11.4: Priority of coverage quality during EDL

The resulting optimal phasing is reported in Figure A.11 and corresponds to $\overline{(E_b/N_0)}$ values⁽⁵⁾ of (34.48, 39.40, 38.34) dB. The performance parameters in Table 11.5 are guaranteed for the whole duration of EDL. In addition, the related E_b/N_0 profile is provided in the top plot of Figure 11.7.

MRO's UHF antenna, whose radiation pattern is given in Figure A.15, is typically nadir-pointing during nominal relay operations. However, the orbiter is capable of performing slew maneuvers to keep the antenna boresight aligned with the entry capsule during EDL. In this way, the link performance can be easily determined from the knowledge of the range to the orbiter and the angle between the OUHF boresight and the symmetry axis of the

⁽⁵⁾i.e. the integral average computed in the aforementioned time intervals

radiation pattern of EDL antennas. The latter, which is provided in the center plot of Figure 11.7, is computed as the difference: $|\text{flight path angle}| - (\text{orbiter elevation})$, according to the trajectory given in chapter 9. The gain discontinuity at E+173 s is due to switching from the BUHF to the RUHF antenna.

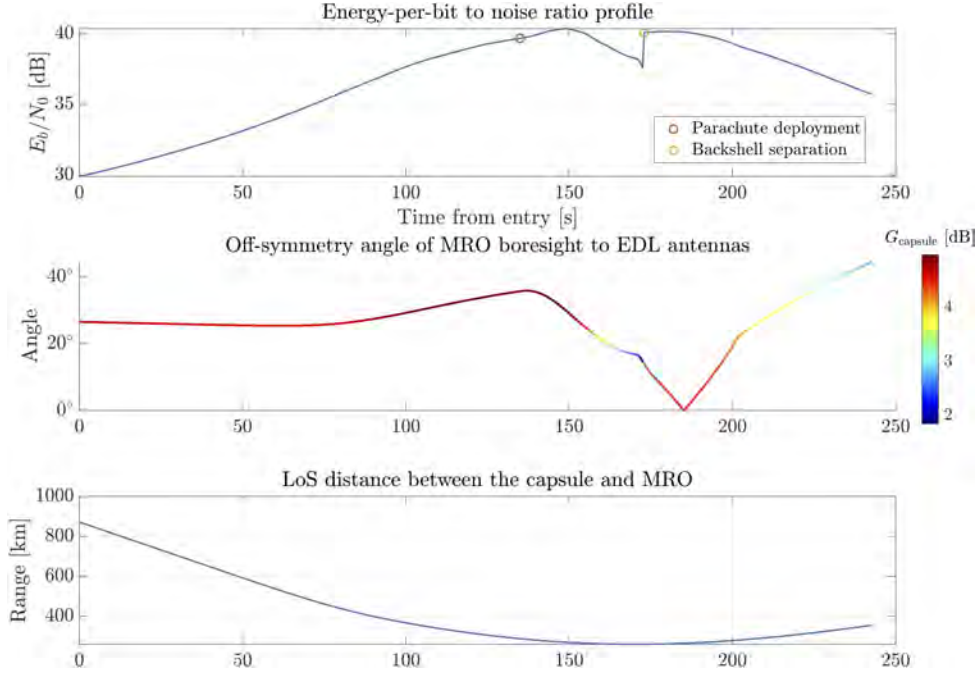


Figure 11.7: EDL coverage performance corresponding to MRO's optimal phasing

It can be immediately noticed that a huge link margin is present for the whole duration of EDL (> 24 dB). This is nevertheless reasonable, given the extreme criticality of such a phase, also considering the presence of relevant modeling uncertainties. Despite the considerable margin, a plasma blackout typically lasting 1 to 2 min is still expected to take place, caused by the formation of a plasma sheet around the entry capsule, in proximity of the peak heating event.

If a handshaking protocol were enabled, any corrupted data would be re-sent. However, in the context of EDL this is actually undesirable since, in the event of link dropouts, it may result in repeated re-sends of the same data at the expense of more recent telemetry. For these reasons, EDL communications will exclusively take place in one-way unreliable mode.

11.4 Surface operations

In this section, the data volumes that can be downlinked to Earth and uplinked to the Skipper rover during surface operations have been carefully evaluated.

The coverage provided by MRO along its nominal orbit [57] has been considered for a proximity link simulation over 5 sols. The ground track propagated for the corresponding time span can be found in Figure A.14.

In Figure 11.8 the coverage map of the landing site is depicted, which has been computed assuming a typical 10° elevation mask. MRO's ground track over 1 sol (i.e. 13 orbits) is also reported.

In addition the main visibility statistics of the orbiter from the landing site are given in Table 11.6.

Avg. visibility per sol	Avg. passes per sol	Avg. pass duration	Max gap time
1 h 38 m (6.6%)	13	7 m 24 s	1 h 48 m

Table 11.6: Visibility statistics of MRO

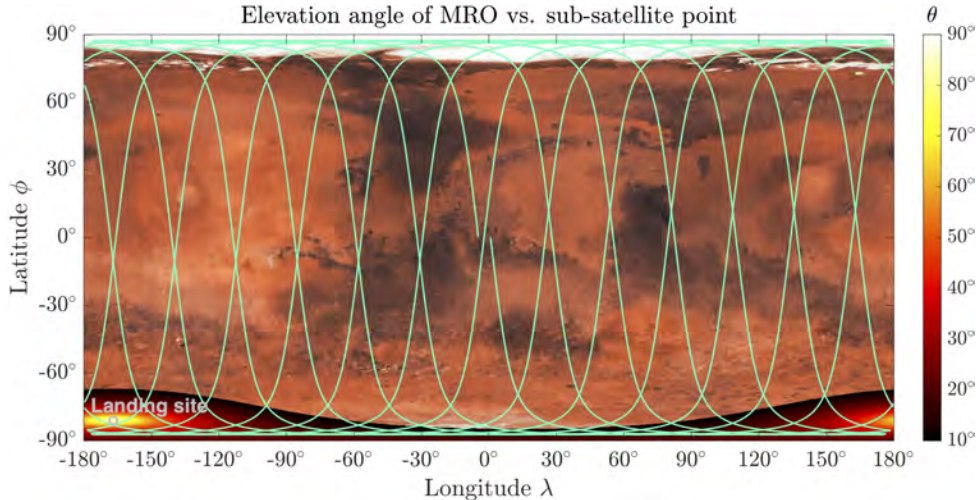


Figure 11.8: Coverage map of the landing site

11.4.1 Proximity antennas

For both TX/RX, BPSK modulation⁽⁶⁾ + (7, 1/2) convolutional coding have been chosen.

Orbiter antenna (OUHF)

MRO's Electra payload is provided with a UHF LGA antenna with 5.0 W RF output power in full duplex mode⁽⁷⁾ and the radiation pattern reported in Figure A.15 [57].

The data points corresponding to the aforementioned radiation pattern have been extracted from [57] using the WebPlotDigitizer software [3] and included in the simulation. The antenna is always nadir pointing and, for the sake of simplicity, the local vertical corresponding to the sub-satellite point has been assumed to be parallel to the nadir direction at the landing site, when computing the off-boresight angle.

Rover antenna (RUHF)

The rover will be equipped with the Electra-lite transceiver, which is a reduced-weight version of the payload onboard orbiters, delivering 8.5 W of RF output power.⁽⁸⁾ A quadrifilar helix antenna design has been chosen for the RUHF, given its extremely wide beam and acceptable gain even at very low elevation angles. The radiation pattern to be included in the simulation has been assumed from literature [58] and is reported in Figure A.13

11.4.2 Return link

The Electra payload features adaptive data rate, which allows it to adjust the data rate along any orbiter pass. In particular, as MRO approaches the nadir direction, the SNR tends to increase (i.e. higher data rates are allowed). Accounting for the fact that all powers of 2 in the range 2 to 2048 kbit/s are supported by the return link to MRO and considering a $\text{BER}_{\max} = 10^{-5}$ along with a 3 dB link margin, the dependence of the resulting maximum allowed data rate as a function of the orbiter elevation is depicted in Figure 11.9.

⁽⁶⁾which is the only kind supported by MRO's proximity link

⁽⁷⁾i.e. simultaneous TX/RX at different frequencies, while in half duplex mode the RF power would increase to 7.0 W

⁽⁸⁾it has actually been computed that 4.0 W would suffice to achieve the desirable return data volume, also thanks to the remarkable coverage of such a polar location; thus, the development of a lower power version of the Electra-lite standard transceiver would be desirable for the MARS-PENGUIN mission, whose design will nevertheless base on the currently available 8.5 W version

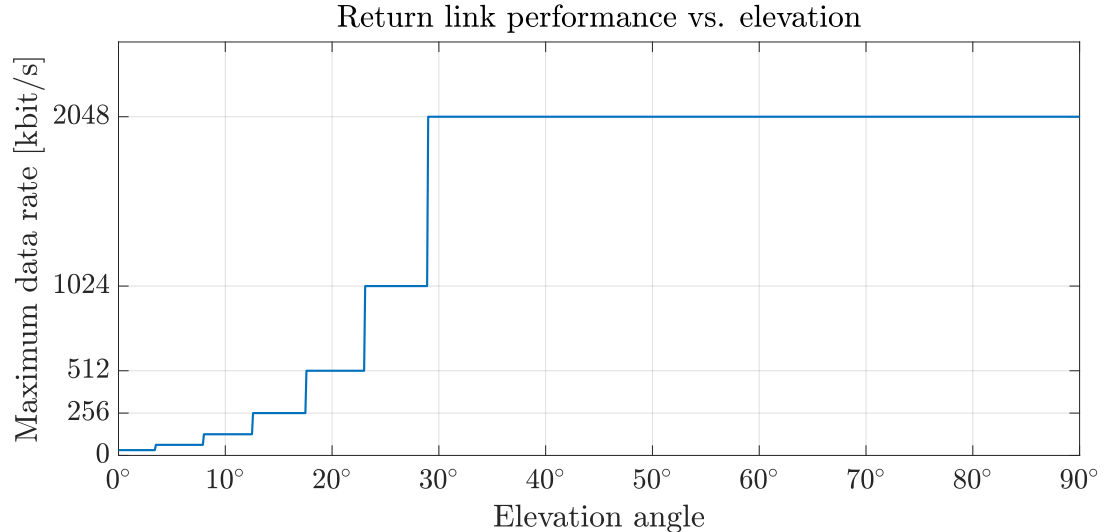


Figure 11.9: Return data rate as a function of elevation

We may at this point determine the data return profile by propagating MRO's orbit and considering the previous dependence. The result of the overall simulation is reported in Figure 11.10, while in Figure A.16 a sample of the data return profile over a few hours is provided.

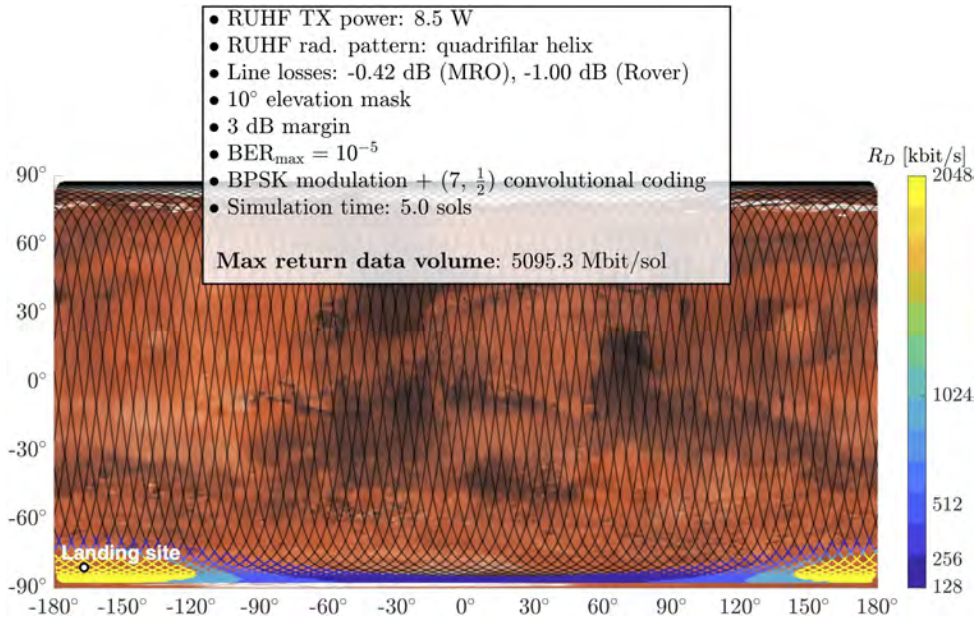


Figure 11.10: Data return performance depending on orbiter pass ground track

It has to be underlined that, although by assuming to exploit all pass opportunities a maximum data volume return of 5.1 Gb/sol would be achieved, such a value actually overshoots the maximum allocated space on Solid-State Recorders of up to 5 Gbit/day for all landed elements at Mars relying on MRO. In addition to this, in a more realistic scenario one would be able to relay data to an orbiter only during a limited portion of the day, since the rest would be devoted to science operations and/or roving.

Assuming to exploit just the N best successive pass opportunities during a given sol, the average performance reported in Table 11.7 is obtained.

Best N successive pass opportunities	Avg. return data volume [Mbit/sol]
2	1212.4
3	1696.1
4	2083.4

Table 11.7: Maximum data volume return exploiting a limited number of passes

11.4.3 Forward link

A simulation similar to the one presented in subsection 11.4.2 has been performed also for the forward link and its result can be found in Figure A.17.

11.4.4 Mass & power budget

Mass and input power of the Electra-lite transceiver are reported in [59]. The mass of the RUHF antenna is instead estimated by taking Curiosity's quadri-filar helix antenna as a reference [60], given its similar radiation pattern. The values obtained are reported in Table 11.8.

Component	Mass [kg]	Power [W]	Margin
Electra-lite transceiver ($\times 2$, i.e. redundant)	2×3.0	65	10%
RUHF LGA	0.55	-	10%
Total	6.55	65	
Total with margin	7.20	71.5	

Table 11.8: Mass and power breakdown of the rover's TMTCS subsystem

11.4.5 Solar conjunctions

As already explained in section 11.2, X-band⁽⁹⁾ outages caused by solar superior conjunctions occur whenever the Sun-Earth-Mars angle becomes lower than 2.3° .

Given the mission requirement of guaranteeing at least 30 months of operations on Mars, an 18 days long communication outage would hence take between May 17th and June 4th 2030, as it can be seen from Figure 11.11.

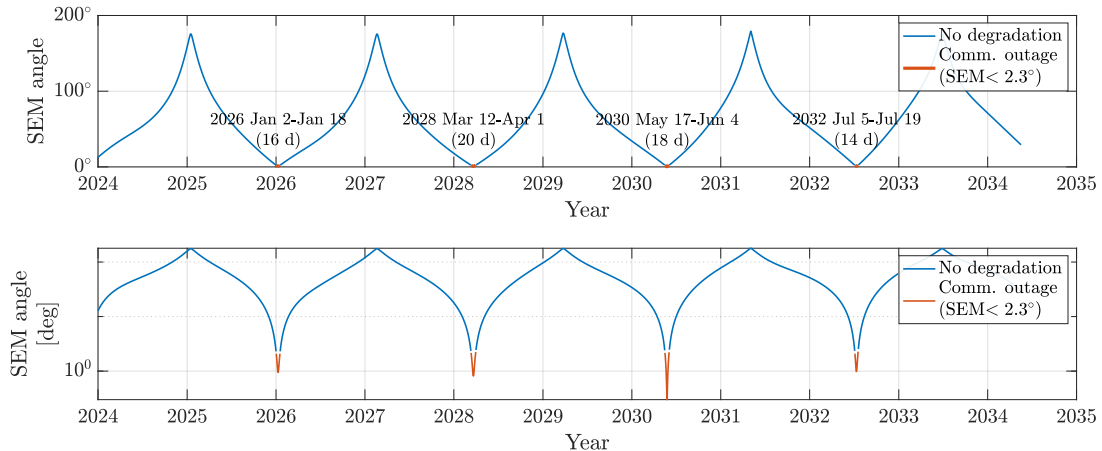


Figure 11.11: Sun-Earth-Mars angle over a decade

⁽⁹⁾MRO's deep space link to Earth makes use of X-band too

12. On Board Data Handling

12.1 Introduction

The On-board Data Handling (OBDH) system of the MARS-PENGUIN mission is dedicated to acquire, store, process, and transmit the data. The data could be scientific, generated by the payloads, or technical, generated by other subsystems. The data could have a time of life which should be handled in real life and therefore has different priorities. Technical data includes control commands sent to the subsystem, telemetry and health data received. Considering the above mentioned, to perform data handling procedures a RealTime Operating System (RTOS) should be implemented.

This chapter is dedicated to select the architecture and perform the sizing of the OBDH system. The computational resources identified will be throughput expressed in Instructions per second (IPS), Non-volatile memory (NVM) expressed in MB, and Random-access memory (RAM) in MB. As output, the OBDH will contribute to the overall Mass and Power budgets and constraints for other subsystems will be evaluated.

12.2 Requirements

To begin with, the overall mission requirements indicate that the OBDH must acquire, store, process, and transmit the data to all subsystems and payloads, to all stages during the whole mission. Secondly, the OBDH must withstand the harsh environment during cruise and operation on Mars surface. As discussed in Chapter 2, the OBDH must resist to 34.8 Rad present during the mission. The temperature ranges exceed the operational ranges of any OBDH system, therefore thermal control must be performed. As discussed in Chapter 9 the Sky-crane will perform a fly-away manoeuvre. It means that it shall have a separate Flight control unit.

12.3 Functionalities

Here the functions performed by the OBDH are described. The functions are discussed in reference to each subsystem. Table 12.1 and Table 12.2 show the computational resources needed by the stages.

- ADCS management. This function is to acquire the data from the star-trackers, sun sensors, three IMU. Process raw data and store it, if necessary. Other processes related to ADCS are: Kinematic Integration, Error determination, Precession Control, Ephemeris propagation and Orbit propagation. The actuation is performed by the propulsion subsystem.
- TMTTC management. The function is to exchange data with the Telemetry & Telecommand (TMTTC) subsystem to communicate it to Earth directly or via a relay satellite. The maximum data rate achieved is 2 MB/s.
- EPS, Propulsion, Robotics. Digital telemetry is received from each subsystem. The control of Electric Power Subsystem (EPS) is performed directly, while the Propulsion and Robotics subsystems are controlled by analog signals by means of the EPS. The EPS controls the voltage of the valves and switches the drivers of the stepper motors as requested by the OBDH subsystem.
- Payloads. The OBDH must control the payloads, collect data and store to send it during the nearest availability window to the mission control.
- FDIR and Diagnostics. Fault Detection, Isolation and Recovery (FDIR) function must be present to increase the fault tolerance of the system. The diagnostics information is constantly updated to have the full state of the mission.

12.3.1 Autonomous Navigation

As discussed, Skipper will perform an intensive drive from the lake region to the geyser location operation at least 4 hours per day. This could not be possible by classic rover tele-operation navigation, when the mission control completely controls each movement of the rover. A constant communication with Earth not only dramatically increases the power consumption (discussed in the following Chapter 13) but also introduces a reaction time lag which could be from 8 min to 44 min, as the data travels between the planets. Instead, an autonomous navigation technique must be used [61]. This type of navigation requires a preloaded terrain map and a set of sensors for

local hazards identification and vision-based localisation algorithms (Figure 12.1). Simultaneous Localisation and Mapping (SLAM) algorithms and machine learning will identify the current Skippers position.

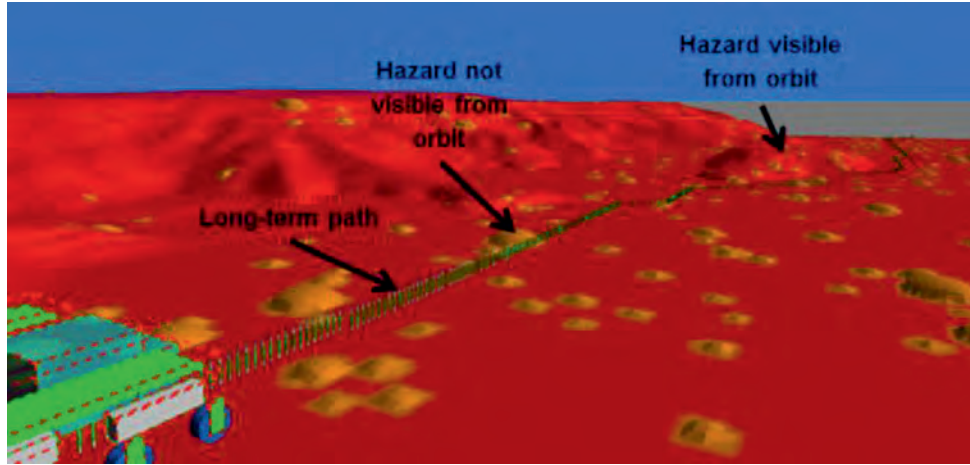


Figure 12.1: Simplified, real time visualisation of Autonomous Navigation

The topographic map of a region of 40x40 km with a resolution of 10 meters and 32 bits per cell occupies 64 MB of storage space.

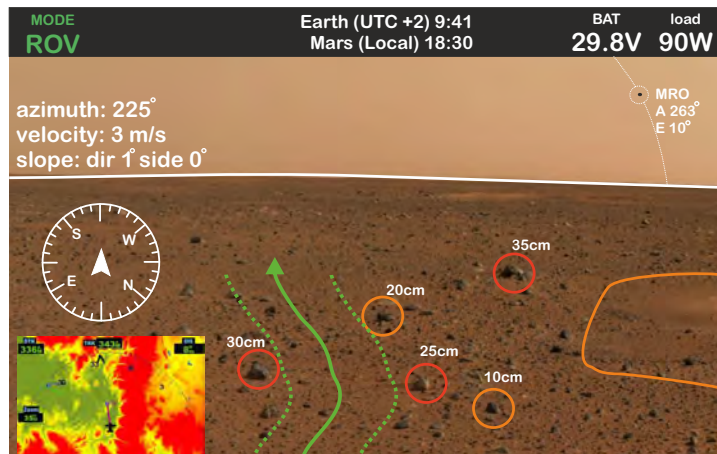


Figure 12.2: Artist concept showing the primary driving information of Skipper in Roving Mode

12.4 Architecture

As discussed before, the MARS PENGUIN mission is consisted of three stages: Cruise, Entry with sky-crane, and Skipper. The propulsion system along with attitude determination sensors is situated in the cruise stage. The Entry stage is consisted of an EPS regulator. Skipper has the payloads, the EPS, the TMTc, Robotics. Skipper and the Skycrane must have separate computers as the Skycrane shall has a simple autonomy for the flyaway manoeuvre. A suitable solution could be a computer based on GR740 Quad-Core LEON4 SPARC V8 Processor. It is equipped with PCI, SpaceWire, CAN, RS233, MIL-STD-1553, Ethernet, GPIO, SPI, JTAG interfaces [62]. It offers 700 MIPS. Despite the fact that its computational capabilities are excessive for our mission, it is power efficient and is equipped by many interface standards (needed by the selected sensors).

In addition, the computer should be equipped with 1.5MB of NVM for code, 24 MB of RAM and 2 GB of long term memory for scientific and technical data to be sent to Earth.

The Skycrane requires simple autonomy with resources reported in Table 12.1. Therefore, a simple flight control computer could be used. A suitable solution is ISIS On Board Computer which provides 80 MIPS of computational resources, 64MB of RAM and 2MB of ROM. It weights 100g and consumes less than 500mW [63]. Skipper's and Skycrane will exchange information via RS422 data bus. The Overall architecture is shown in Figure 12.3. The integration procedures will be performed via JTAG interfaces.

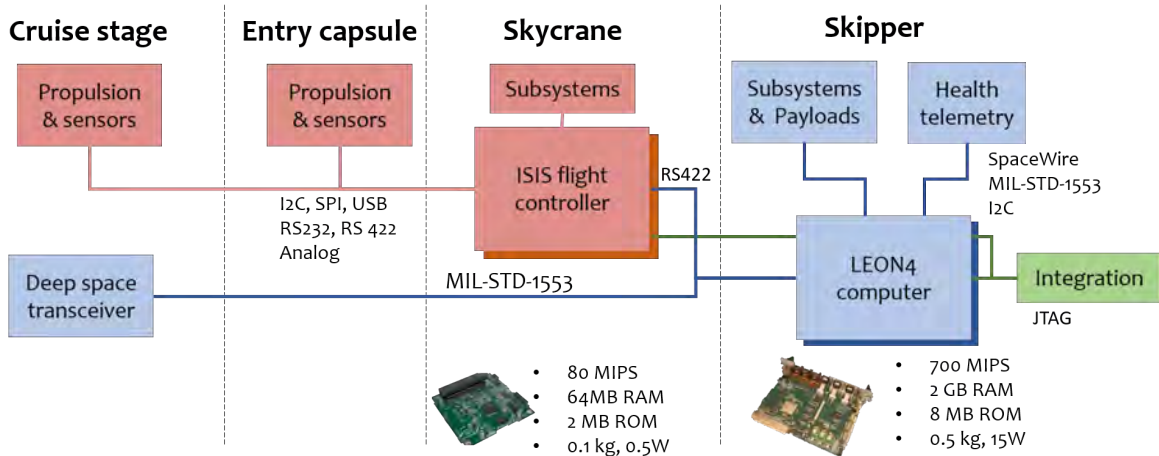


Figure 12.3: The OBDH subsystem architecture

12.5 Effects, inputs and constraints

As mentioned, the computers must be shielded from radiation. The operational temperature ranges must be respected by introducing heaters or similar devices. All equipment should have the interfaces available in LEON4. The power consumption is expected to be 15 W, while the mass is 1.5 kg.

Function	Pz on board	Size		Throughput	Execution
		Code [kwords]	Data [kwords]	[kIPS]	Frequency [Hz]
ADCS					
IMU	3	0.80	0.50	9.00	30.00
Star Tracker	2	2.00	15.00	2.00	0.01
Sun sensor	3	0.50	0.10	1.00	1.00
Kinematic Integration	1	2.00	0.20	15.00	10.00
Error determination	1	1.00	0.10	12.00	10.00
Precession Control	1	3.30	1.50	30.00	10.00
Thruster control	1	0.60	0.40	1.20	2.00
Ephemeris propagation	1	2.00	0.30	2.00	1.00
Orbit propagation	1	13.00	4.00	20.00	1.00
Simple autonomy	1	2.00	1.00	1.00	1.00
Fault detection					
Monitors	1	4.00	1.00	15.00	5.00
Fault correction	1	2.00	10.00	5.00	5.00
Other functions					
Power management	1	1.20	0.80	5.00	1.00
Thermal control	1	0.80	1.50	3.00	0.10
Kalman Filter	3	8.00	1.00	80.00	0.00
RTOS					
Executive	1	3.50	2.00	60.00	
Run-Time Kernel	1	8.00	4.00		
I/O Device handlers	1	2.00	7.00	0.05	
Built-in Test and Diagnostics	1	0.70	0.40	0.50	
Math utilities	1	1.20	0.20		
Subtotal [MB]		234.40	276.80	443.75	
Margin		400%	400%	400%	
Total [MB]		1172.00	1384.00	2218.75	

Table 12.1: Computational resources requested by the skycrane

Function	Pz on board	Size	Througput	Execution
		Code [kwords]	Data [kwords]	[Hz]
Communications				
Command processing	1	1.00	4.00	7.00
Telemetry processing	1	1.00	2.50	3.00
Payloads				
Surface stereo imager	1	1.00	400.00	100.00
X ray spectrometer	1	1.00	2.00	1.00
Infrared spectrometer	1	1.00	2.00	1.00
Mass spectrometer and GC for organics	1	1.00	2.00	1.00
Environmental Analyser	1	1.00	2.00	1.00
Sounding radar	1	1.00	100.00	1.00
Neutral ice subsurface	1	1.00	2.00	1.00
Dust flux monitor	1	1.00	2.00	1.00
Raman Laser Spectrometer	1	1.00	2.00	1.00
Robotics				
RA	1	10.00	10.00	10.00
Drill	1	10.00	10.00	10.00
Navigation				
Camera	6	5.00	100.00	200.00
Driving	1	10.00	10.00	10.00
Other functions				
Power management	1	1.20	0.80	5.00
Thermal control	1	0.80	1.50	3.00
Kalman Filter	3	8.00	1.00	80.00
RTOS				
Executive	1	3.50	2.00	60.00
Run-Time Kernel	1	8.00	4.00	
I/O Device handlers	1	2.00	7.00	0.05
Built-in Test and Diagnostics	1	0.70	0.40	0.50
Math utilities	1	1.20	0.20	
Subtotal [MB]		285.60	4677.60	1656.55
Margin		400%	400%	400%
Total [MB]		1428.00	23388.00	8282.75

Table 12.2: Computational resources requested by Skipper

13. Electric Power Subsystem

13.1 Introduction

The scope of this chapter is to characterise the Electric Power Subsystem (EPS) given operating conditions, functionalities and constraints. The Mars Penguin spacecraft consists of three stages: Cruise deck, Descent stage and the Rover named Skipper. The cruise deck carries the equipment necessary for the interplanetary flight such as: the antenna for deep space communication, propulsion system to perform the manoeuvres, an electric system and thermal control system and the attitude control reaction system. The propulsion system is supposed to be chemical because of reasons described in section 7.2 and in section 10.4. The Descent stage is needed for a controlled and safe **EDL**. It is consisted of an aerodynamic entry capsule and a soft landing system and is equipped by: **ADCS** with dedicated propulsive system, a propulsive system for the soft landing of Skipper, a mechanical system for soft landing and dedicated propulsors, **EPS** and **TCS**. Skipper is dedicated to carry the scientific mission and is equipped by a **Thermal Control Subsystem (TCS)**, **Electric Power Subsystem (EPS)**, **On-board Data Handling (OBDH)**, **Telemetry & Telecommand (TMTC)**, several mechanisms such as the wheels, robotic arm, a drill, and the scientific payload.

The major drivers for sizing and architecture definition of the **Electric Power Subsystem (EPS)** of the mission are:

1. the Rover should be able to operate below 80°S for at least 30 terrestrial months
2. be able to travel at least for 4 hours per sol

13.2 Power budget breakdown

This subsection describes the loads needed by the spacecraft during all mission phases for each stage. The objective is to identify peak and mean power consumption at each mode and stage, and their duration. This will be summed up for the sizing of the whole system.

As mentioned in section 5.3, 19 modes are used during the mission. Some of them are very close at the purpose point of view, therefore 11 of them were highlighted and analysed. The modes are: SLP - Sleep mode, STE - Self testing essential, STC - Self testing complete, ATT - Attitude mode, PRP - Propulsive mode, COM - Communication mode, STB - Standby mode, **EDL**, SAF - Safe mode, ROV - Roving mode and a general Science mode. The power breakdown is represented in Table 13.1. A margin of 12% is applied as all the components were successfully used in previous missions and have **TRL 9**.

It can be observed that ATT, PRP, EDL are the key modes in terms of power demand that will mostly affect the sizing process. Considering that they are used in Cruise and **EDL** and that the Rover consumption is much less, it is reasonable to introduce a separate power source for each stage with a possibility of sharing the generated power at different phases.

A summary of power demands at each mode is reported in Table 13.2. One can see the typical peak and average load and its duration. The minimal consumption in cruise phase is 58.80 W in Sleep mode and 40.34 W for Skipper. These are due to the proper functioning of the **TCS** and **OBDH** watchdog timers. The maximum load is achieved during **EDL** by the separation and parachute deployment systems while performing energetic attitude manoeuvres.

Stage	Margin	SLP - Sleep mode	STE - Self testing essential	STC - Self testing complete	ATT - Attitude mode	PRP - Propulsive mode	COM - Communication mode	STB - Standby mode	EDL	SAF - Safe mode	ROV - Roving mode	Science mode
Cruise		11.76	11.76	30.58		298.70	149.35	11.76		11.76		
TCS	12%	11.20	11.20	11.20		33.60						
EPS	12%	0.56	0.56	1.46		14.22		7.11	0.56	0.56		
TMTC	12%			1.12				142.24	11.20			11.20
PROP	12%			16.80		250.88						
EDL		11.76	11.76	41.16	318.70	318.70				1729.90		
TCS	12%	11.20	11.20	11.20	33.60	33.60				33.60		
ADCS	12%			11.20	119.84	119.84				119.84		
EPS	12%	0.56	0.56	1.96	15.18	15.18				82.38		
PROP	12%			16.80	150.08	150.08				150.08		
RBT	12%									1344.00		
Skipper		42.34	64.68	82.32	64.68	64.68	141.12	88.20	99.96	52.92	236.38	258.72
TCS	12%	39.20	39.20	39.20	39.20	39.20	39.20	39.20	39.20	39.20	39.20	39.20
EPS	12%	2.02	3.08	3.92	3.08	3.08	6.72	4.20	4.76	2.52	11.26	12.32
OBDH	12%	1.12	22.40	22.40	22.40	22.40	22.40	11.20	22.40	11.20	22.40	22.40
TMTC	12%			5.60			72.80	33.60	33.60			
RBT	12%			5.60							163.52	112.00
PL	12%			5.60								72.80

Table 13.1: Power breakdown for each stage and mode in Watts.

Stage	Phase	Pulse load [W]	Duration [min]	Continous load [W]	Duration [min]	Energy needed [Wh]	Energy by Bat [Wh]
SLP	Cruise			58.80			
	Mars			42.34			
STE	Cruise			88.20	10		
	Mars			64.68	10		
STC	Cruise			154.06	20	51.35	12.35
	Mars			82.32	20	27.44	
ATT	Cruise	383.38	10	160.46	60	197.61	80.61
PRP	Cruise	682.08	10	431.20	30	257.41	198.91
COM	Cruise	217.67	15	96.67	30	78.59	20.09
	Mars	141.12	15	78.32	30	54.86	
STB	Cruise			99.96			
	Mars			88.20			
EDL	EDL	1829.86	7	485.86	30	399.73	341.23
SAF	Cruise			64.68			
	Mars			52.92			
ROV	Mars	236.38	15	154.62	240	638.90	170.90
Science	Mars	185.92	60	146.72	180	479.36	128.36

Table 13.2: Summary of consumption by each mode.

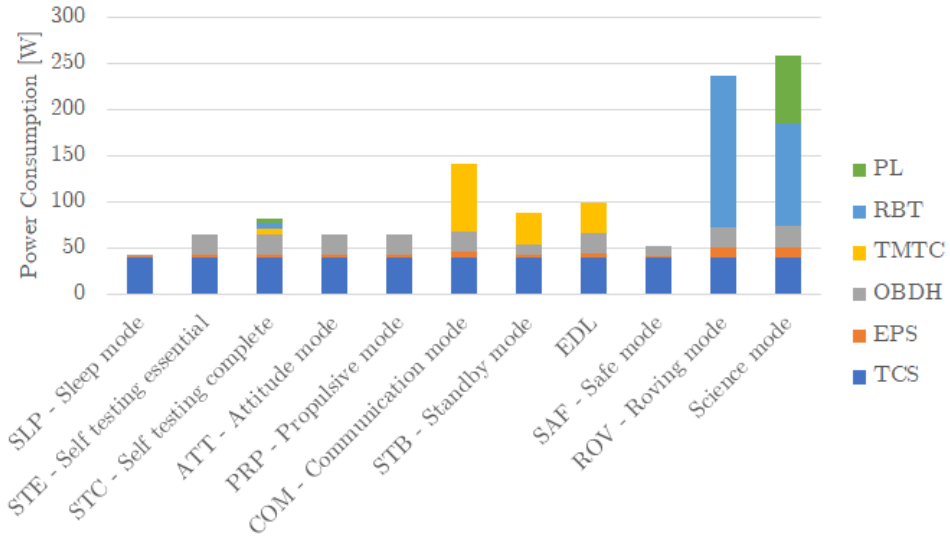


Figure 13.1: Power breakdown of Skipper.

13.3 Possible power sources

13.3.1 Power Generation

The possible power sources are Primary and Secondary Batteries, Solar Array (SA), Radioisotope Thermoelectric Generator (RTG). The primary power source selection application is described in [54]. It turns clear that the EDL stage should be powered by Primary batteries as the power source of the cruise deck will not be available after separation and Skipper requests lower loads. A lithium based primary battery could be considered in the analysis. Its advantage is storage time not achievable by Silver-zinc batteries. A value of 210 Wh/kg could be applied [54]. On the other hand the overall mass could be reduced by removing secondary batteries from the cruise stage and installing them in the descent stage (replacing its primary batteries). It could be beneficial to decrease overall mass budget.

The major constraint to pay attention to when sizing Skipper's power source is its operation duration on Mars. It is requested to operate at least for 30 terrestrial months which corresponds to slightly more than one Martian year. It means that Skipper must survive the Martian south winter and the polar night whose duration is about 300 terrestrial days. The application of SA would require another source that should provide the power of 40.34 W during this period. The energy consumed through this time is estimated to be 290,304 Wh using an electric heat source, and 14,400 Wh using a radioisotope heater unit. It is highly unlikely to achieve this values using any sort of chemical batteries within a reasonable mass budget.

Another option would be a radioisotope electric power generator widely used in Mars missions. It also could provide Skipper a significant part of thermal power. Two possible RTG models will be considered. The first is the multi-mission radioisotope thermoelectric generator (MMRTG) in Figure 13.2, produced under the jurisdiction of the United States Department of Energy's Office of Space and Defense Power Systems within the Office of Nuclear Energy and successfully used in MSL Curiosity rover and Perseverance rover to be launched in summer 2020 and other planned missions. The second possible solution is the advanced Stirling radioisotope generator (ASRG) in Figure 13.3, in development by ESA to be ready for flight in mid 2020. [64] Technical characteristics of the above mentioned RTGs are reported in Table 13.3.

Parameters	MMRTG	ASRG
General		
Dimensions [cm]	66x64x64	104x29x38
Mass [kg]	43	22
Thermal power at BOM [W]	1877	360
T_cold at BOM [°C]	210	80
Performance at BOM		
Mars Surface Elec Power [W]	123	140
Performance 3 years past BOM		
Mars Surface Elec Power [W]	117	133
TRL at launch	9	8

Table 13.3: MMRTG and ASRG parameters comparison.

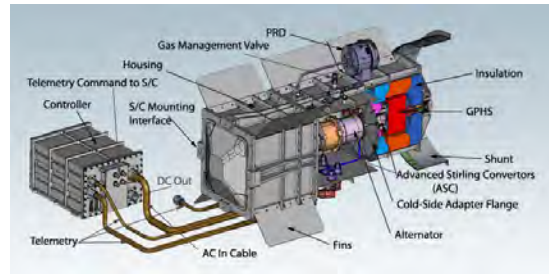
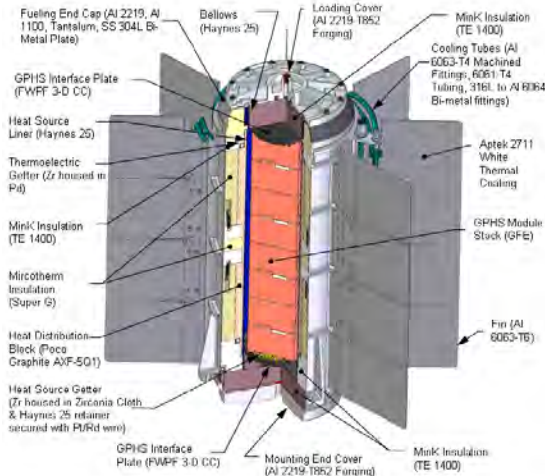


Figure 13.3: ASRG

Figure 13.2: MMRTG

The clear advantage of the MMRTG is its high TRL, while ASRG is still in development but promises to be ready for flight to the preliminary departure date (Nov 2028) and provides more electrical power with less mass. The cruise deck could use a fixed SA or the power source of the rover. A triple junction gallium-arsenide solar array will be considered for the sizing as a worst case [65]. It has an average performance (efficiency 19%) for multi-junction cells[54], has demonstrated its reliability during previous Mars missions. Its annual degradation ($d=3.75\%$) will not affect the analysis as the maximum cruise duration is estimated to be about one year. The aspect angle will be considered 45° as a worst case [65].

13.3.2 Power Storage

The spacecraft will need power storage to perform its mission. Lithium ions secondary batteries will be applied. A research was performed to identify optimal cell model in terms of energy and power density. The LP33330 cells manufactured by Eagle Pitcher technologies will be used. Each cell has 6 Ah of capacity at 3.33 V. As it will be discussed later in section 13.5 the main power bus will be kept at 30 V, therefore there will be 9 cells in series. The manufacturer guarantees a DOD of 100% at 2000 cycles, which corresponds to the cycles needed during the mission (considering one per day during cruise, two while operating in south polar day and one per day during polar night). The internal resistance is reported to be 1 mOhm and the mass of each cell is 0.222 kg [66].

13.4 Sizing

A trade-off could be performed to validate the presence of solar arrays on the cruise deck, but Table 13.4 clearly reports that the use of identical secondary batteries on Skipper and the descent stage will fulfill the mission power needs. The preferred RTG is ASRG as it is more lightweight and powerful than the MMRTG. But as it is not clear if it will be ready for flight at launch, the MMRTG will be considered. The results of the batteries capacity needed are represented below in Table 13.4.

Power generated [W]	Batteries energy [Wh]				Total
	RTG	Cruise	EDL	Mars	
117.00	-	170.32	170.90	341.23	

Table 13.4: EPS sizing. Batteries capacity required.

As the batteries do not require to have a great capacity, the energy density advantage of separate primary sources on the descent stage vanishes. The overall masses are: RTG 44 kg, Descent stage Secondary Battery 2.5 kg, Skipper battery 2.5 kg. Wiring and regulators 18 kg. Total mass is 67 kg.

The technical properties of the Li-on batteries are reported in Table 13.5.

Parameter	Value	Parameter	Value	Parameter	Value
Cell	LP33330	Voltage [V]	3.33	Mass tot [kg]	2.00
Type	Li-on	Energy [Wh]	19.98	Energy tot [Wh]	179.82
Mass [kg]	0.22	Series	9	Energy density [W/kg]	90.00
Current const [A]	24.00	Parallel	1	Power density [W/kg]	360.36
Current pulse [A]	48.00	Power const [W]	720.00	Resistance [Ohm]	0.001
Capacity [Ah]	6.00	Power pulse [W]	1440.00		

Table 13.5: Battery parameters.

13.5 EPS architecture

As discussed before, power sources are present on Skipper and Sky crane. It introduces a Power Regulation and control unit on each stage with a power source. Each PRCU is equipped by a source control unit (depending on the source) and a power conditioning and distribution unit. As mentioned before, the stages will share the Main power bus and complement each other in order to charge the battery or satisfy a high power demand. Shut-off switches are foreseen to disconnect the circuits before the separation of the stages. The Mars Penguin mission EPS architecture is presented in [Figure 13.4](#).

The main bus voltage is set to be 28-32 VDC as the total power is less than 2 kW. The bus will be regulated by the OBDH. Some equipment requires 100 VDC, therefore they will have a separate voltage converters. The RTG load controller will dissipate the exceeding power through a series of shunt stages situated on the RTG's cold plate. Each load has a designated shut-off switch. It is expected to have a separate small battery for the OBDH to power the clocks and drivers as their supply quality is highly essential.

Taking into account the above mentioned requirements a THERMA power control unit is selected. It has a modular architecture, so the two units could have dedicated functionalities. For example the Skipper unit will have a shunt regulator, while the Skycrane unit a pyro actuation and a propulsion control module. The common modules will be Battery Charge/discharge Regulation, Equipment Power Distribution, Heater PD, Command and Monitoring. The mass of each PCDU is 8.3 kg and each process 2.4 kW of power.

To sum up, the Main Bus regulation uses direct energy transfer, is regulated and distributed. Cabling is set to be 10% of the EPS system. The mass of the sources, storage regulation units and cabling is expected to be 51.5 kg and 67 kg for the whole Electric Power Subsystem (EPS). The duration of full battery charging process will be about 3 hours. All components are expected to be TRL9 besides the ASRG. Approximate power distribution shares are listed in [Table 13.6](#).

Subsystem	TCS	EPS	TMTC	PROP	ADCS	RBT	OBDH	PL
Share	26%	10%	4%	21%	3%	31%	4%	2%

Table 13.6: Subsystems power distribution

All metal components will be connected by conductive bypasses to keep all part with the same electric potential. As Skipper's potential before touchdown could vary a lot from Mars's one, a grounding mechanism will be foreseen.

13.6 Effects, inputs and constraints

As the mission will not be equipped by SA, no constraints are fixed for the Mission Analysis and Attitude Control. The nominal voltage of the sources should be close to the Main Bus voltage.

The RTG produces an elevated amount of heat so as the shunts, so a proper thermal control should be performed. The Li-ion batteries operating temperatures are in the range of 0-30 °C.

The RTG should be treated with high security standards at integration and launch. The selection of ASRG could move the launch to late 2020s as it could not be ready before.

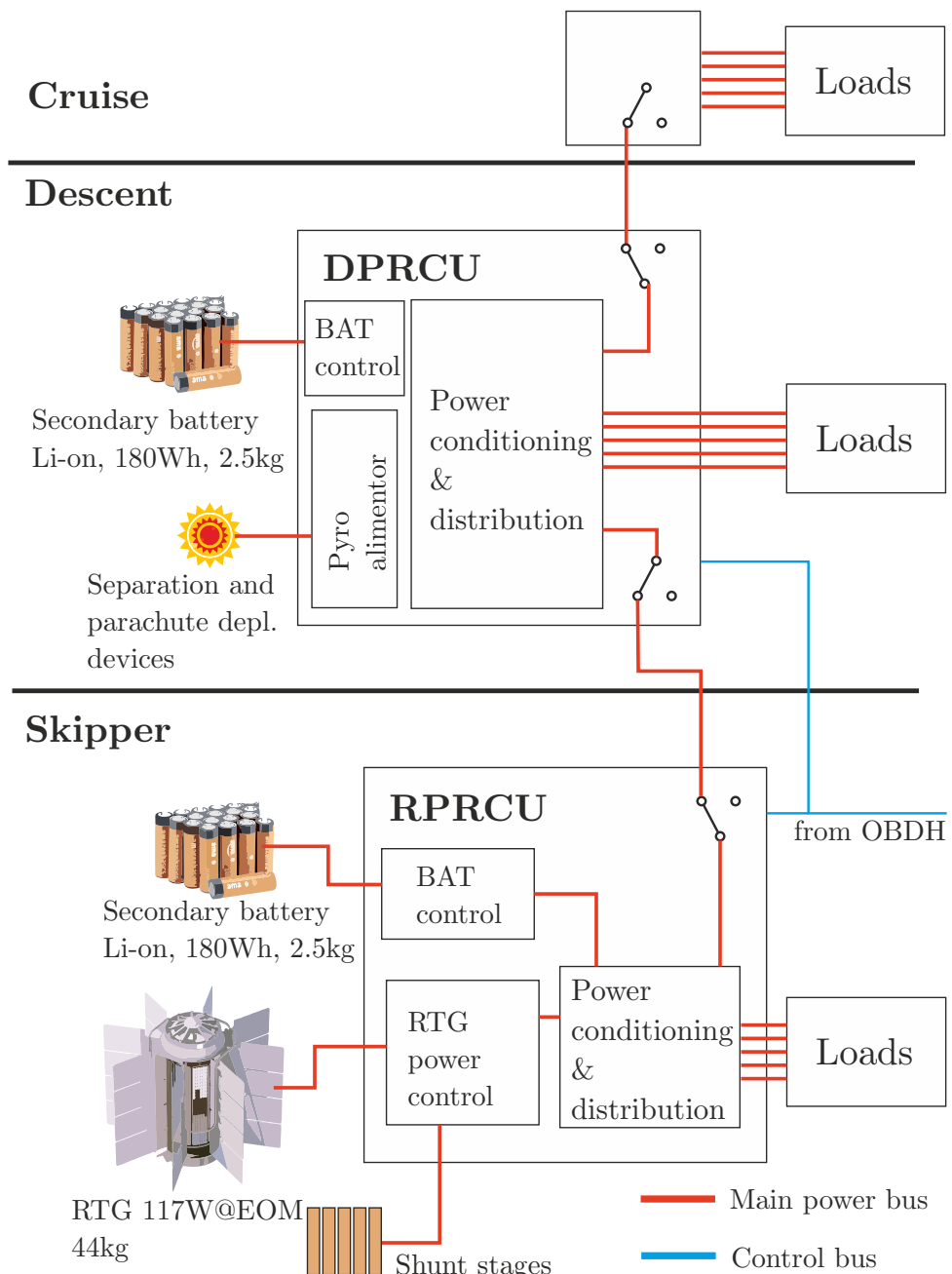


Figure 13.4: Mars Penguin mission EPS architecture.

14. Thermal Control Subsystem

14.1 Introduction

The MARS-PENGUIN mission needs a thermal control system that allows all the subsystems on board to work within a certain temperature range, in nominal conditions.

The thermal system will be strictly connected to all the subsystem present on board, as each of them could have a different temperature requirement, and different sensibility to change of temperatures. This will be taken into account once the thermal analysis will be done on a more complex level.

Some assumptions have been put in place for the thermal sizing and general understanding of the thermal problem, in particular:

- The analysis is performed in a steady-state environment (the total heat flux must be zero)
- Outer space is assumed to be at 0 K

There are four situations that have been considered separately, and a model has been developed for each one of them, in order to find the proper architecture that would allow each stage of the mission to operate as expected. The following stages or structures have been studied:

- The interplanetary leg
- The [EDL](#) phase
- The rover
- The helicopter

The last one will be presented in the chapter dedicated to the helicopter, [chapter 18](#). A brief overview of the work is hereby presented: first of all, hot and cold cases have been presented. Then a preliminary single node analysis has been performed, to get a "feel" for the problem, while keeping an eye on the temperature ranges for each component inside of the mission phase of choice. Once this has been done, more nodes are added to get a more precise analysis for each mission phase. In general, a passive solution will always be sought, and only afterwards active solutions will be employed, once it's been proven that the passive solutions alone will not be able to satisfy the given temperature ranges.

14.2 Effects, inputs and constraints

As will be discussed later the design of the [TCS](#) is mostly driven by other subsystems and the environment. The most part of the components require standard solutions, while the [RTG](#) need specific positioning to radiate generated heat. A part of it could be used to heat Skipper's inner compartment. The technology used for thermal control is well-studied and has high TRL, and therefore will not put at risk the launch date.

14.3 Cruise

The thermal analysis for the cruise stage has been developed starting from a simple 3 node analysis of the worst hot (after departure with maximum solar flux $q = 1360 \text{ W/m}^2$) and cold (before EDL when the solar flux is minimal $q = 590 \text{ W/m}^2$) cases that this stage of the mission will have to encounter.

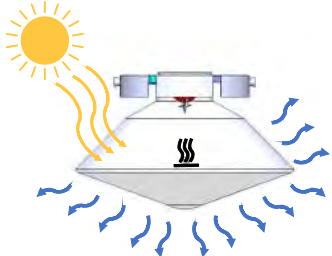


Figure 14.1: Heat fluxes during the interplanetary leg

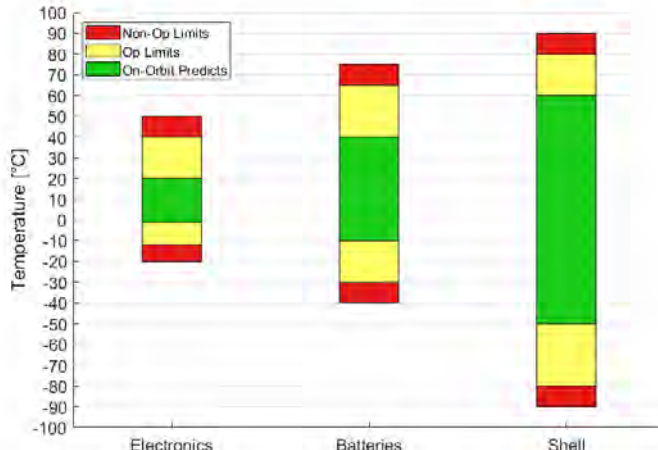


Figure 14.2: Temperatures for the cruise stage nodes

Then, the temperature limits are considered for the most sensitive and significant components of the spacecraft like: Electronics bay, Batteries, Shell. The operational limits are reported in Table 14.1 and filled green and yellow in Figure 14.2.

Data processor and power unit	Battery (Li-ion)	Power unit	Sensors	Antennas	Shell
Max T [°C]	+50	+75	+50	+50	+175
Min T [°C]	-20	-40	-20	-20	-130

Table 14.1: Temperature ranges for cruise stage parts and components

The shell node will be linked to the outside and to the other nodes. The sensors nodes and the batteries node will be linked to each other and to the shell node, but not to the outside. It means that the shell will have to withstand the biggest temperature variations, whereas the internal nodes will be protected from the outside conditions, allowing for smaller temperature gradients and variations.

The final architecture found makes use of white paint surface finish: namely S13GP : 6N/LO-1 with $\varepsilon = 0.90$ and $\alpha = 0.18$ which is enough to keep the temperatures within the limits. The interplanetary leg is long enough for a small amount of degradation to be considered. But this is actually a positive factor for the mission, as the absorbtivity will increase as the solar radiation will decrease, and the two effects will counteract each other.

As it's shown in Figure 14.2, the margins for this phases are quite large, as this phase is not very demanding, and the heat fluxes in play do not change as drastically as they would on other mission phases, like when the rover is deployed.

14.4 EDL

The thermal analysis for the EDL stage has been developed considering that the whole descent has similar heat fluxes during its whole duration. The only main difference being the friction, which relies on the speed and the composition of the atmosphere.

Then, the temperatures for each part or component of the EDL phase has to be evaluated, in order to decide which nodes to select for the thermal problem.

Data processor and power unit	Battery (Li-ion)	Power unit	Equipment	Antennas	Shell
Max T [°C]	+50	+75	+50	+50	+175
Min T [°C]	-20	-40	-20	-20	-90

Table 14.2: Temperature ranges for EDL stage parts and components

While looking at the Table 14.2, a net of 4 nodes has been employed to represent the most important components of the EDL phase: outside shell, equipment bay, batteries of the rover, processing of the Sky crane, the backshell. The shell node will be linked to the outside and to the other nodes. The nodes relative to the rover will be connected to the outside shell and to each other, and the backshell sensors node will only be connected to the outside shell node. The highest temperature that is allowed to the structure is 250°C, and this temperature is going to be considered as the temperature that the inner shell of the spacecraft has to deal with. The solution is to use a solar reflector. The surface finish is a white paint surface finish: namely S13GP : 6N/LO-1 with $\epsilon = 0.90$ and $\alpha = 0.18$. The structure is to be considered of aluminium honeycomb, which is able to keep the temperature low enough while having a low density, for a width of 1.7 cm.

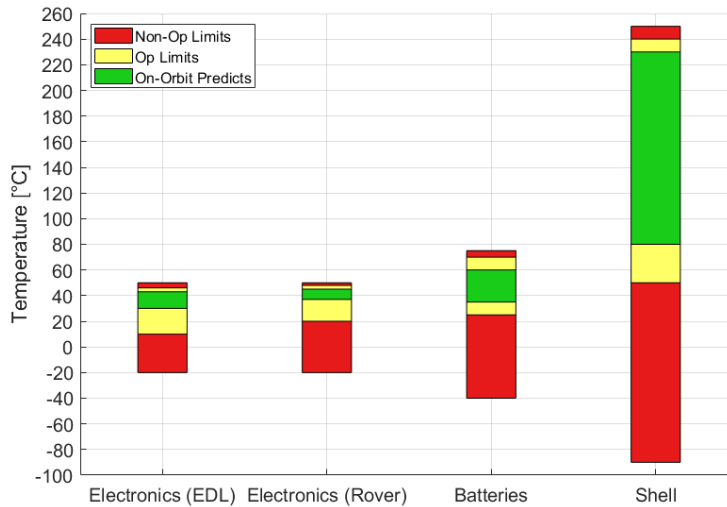


Figure 14.3: Temperatures for the EDL phase

The values of the temperatures are shown in Figure 14.3, and it can be seen how in this case the values of the temperature margins have all migrated to the upper parts of the graph. The upper margins are often very small, but since the EDL conditions do not change much throughout the whole process, it is an acceptable result.

14.5 Rover

The thermal analysis for the rover has been developed starting from an analysis of the worst hot and cold cases that this stage will have to encounter. The worst hot case for the rover happens while the power generation is maximum, as an example while the telecommunication mode is active, during Martian summer and in plain daylight, with still air (no wind). The worst cold case happens while the power generation is minimum, as an example while the rover is using a standby mode, during Martian winter and during nighttime, with wind. The flows can be observed in Figure 14.4.

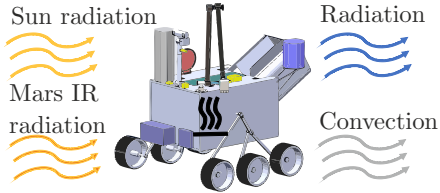


Figure 14.4: Heat fluxes on Mars

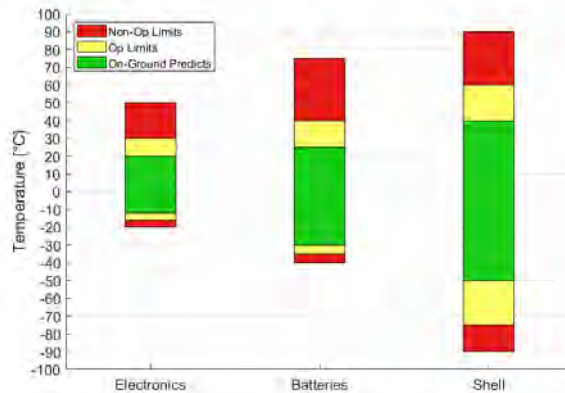


Figure 14.5: Temperatures for Skipper's nodes

Then the temperature ranges have been highlighted, in order to give a hint where to put the nodes for the thermal model (See Table 14.3). It must be noted that the sensors have different temperature requirements, but the temperature range that has been taken comes from the most sensible values between all the components (highest low limit, and lowest high limit).

Data processor and power unit	Battery (Li-ion)	Power unit	Equipment	Antennas	Shell	Wheels
Max T [°C]	+50	+50	+50	+175	+90	+120
Min T [°C]	-20	-40	-20	-130	-90	-70

Table 14.3: Temperature ranges for rover parts and components

Thanks to the table, the nodes can be placed on the most sensible parts of the rover in order to keep track of their temperatures: outside shell, sensors and data processor, batteries. The shell node will be connected to the two inner nodes (battery node and sensors node) and the outside, while the two inner nodes will only be connected to each other and the outside node (shell node), but not to the outside. The final architecture features 2 kW of power provided by radioactive means, which will then be transferred to the most sensible parts of the rover with 3 m of aluminium pipes filled with NH_3 . Along with this, a radiator of 0.2 m^2 has been added to the rover, and the surface finish is the silver paint Electrodag 503 with $\epsilon = 0.44$ and $\alpha = 0.37$. As it's shown in Figure 14.5, the margins for this phases are narrower close to the lower temperature boundaries, due to the fact that the worst cold case scenario will be the most demanding one for the thermal subsystem, due to its duration.

15. Robotics

15.1 Introduction

MARS-PENGUIN mission needs robotic payloads to meet its sampling objectives.

The robotic subsystems are mainly focused on:

- locomotion system of the rover;
- instrument for sampling the region above the sub-glacial lake;
- geysers sampling tool.

After having accurately defined the functionalities and the requirements for the components, and having defined the criteria for the assessment, different alternatives have been considered. The trade-off has been refined with sizing, and finally accomplished with the definition of the baseline for each goal.

15.1.1 Functionalities and requirements

The main functionalities and requirements for on-surface robotics are listed below.

Environmental related requirements

The rover and the instruments shall operate at:

- temperature range from 140 to 270 K
- pressure range from 340 to 490 Pa
- UV radiation wavelength range from 190 to 400 nm
- the solar flux range from about 0 to 300 W/m²
- gravitational acceleration of 3.728 m/s²
- polar latitude of 81°S

Rover

The rover shall:

- operate at least for 30 terrestrial months
- cover a distance of 50 km in less than 100 sol, during summer
- be able to move with a cruise speed of at least 0.1 m/s
- be able to travel for at least 4 hours per sol
- reach the cruise speed in at most 3 s (acceleration of almost 0.0333 m/s²)
- operate on slopes up to 20°
- have a step climbing capability such that it allows to overcome rocks with height of 1.5 of wheel diameter
- have a ground clearance of at least 30 cm

Lake region sampling

The instrument shall:

- work in summer/spring
- penetrate at least 1 m through the soil
- preserve possible traces of collected ice
- guarantee samples sterility
- transfer the material to the sample analysis system
- collect at least 5 different samples

Geyser analysis

The instrument shall:

- observe and record the phenomenon remotely
- guarantee samples sterility
- transfer the material to the sample analysis system
- collect at least 2 different samples

The instrument should:

- collect samples before and after the geyser occurrence

15.2 Rover locomotion system

15.2.1 Travel path

The travel path that Skipper shall cover from the centre of the lake to the closest geyser, is shown in red in Figure 15.1, while Figure 15.2 has been generated using the Mars Trek NASA tool [9] and reports the elevation profile of the path.

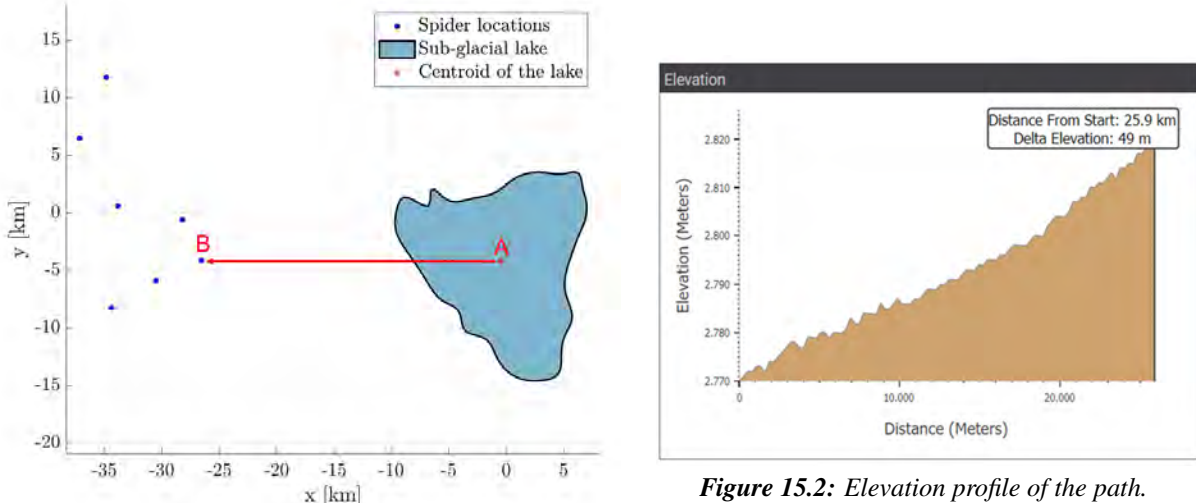


Figure 15.1: Travel path from the centre of the sub-glacial lake (point A) to the closest spider site (point B).

Figure 15.2: Elevation profile of the path.

Considering the elevation differences, the total distance to cover is ~ 26.5 km, while the Line-of-Sight distance is 25.97 km. This result is very close the value computed initially by the MARS-PENGUIN team in section 2.1, of 26.52 km.

Data were processed and the maximum slope is 0.75% (0.43°), while the average slope is 0.19% (0.12°). These very low values are consistent with the small total elevation difference of only of 49 m, over a 26 km travel. Given the lack of significant information on the type of soil in the region of interest, it will be modelled considering worst case scenario from the point of view of the locomotion system, i.e. as sandy loam with presence of rocks.

Figure 15.3 shows the time window available for Skipper's travel: the whole summer of the Martian South Pole. As it can be seen it lasts more than 7 terrestrial months, but considering 0.1 m/s as the average speed and travelling 4 hours per sol, the distance can be covered in only 35 sols.

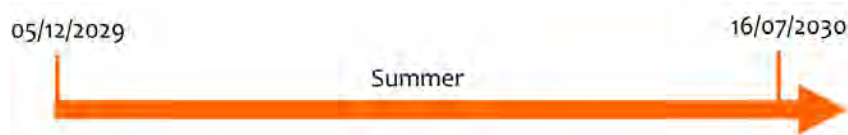


Figure 15.3: Travel period

15.2.2 Rover sizing and design

Wheel number and sizing

The wheel sizing will determine the traction capability of the rover. The real design of the wheel may complicate the calculation process so additional testing is preferable.

There are three general indices of performance to consider for the locomotion system design:

- Tractionability, which is a robot's ability to traverse soft soils or hard ground without loss of traction.
- Maneuverability, which addresses a robot's ability to navigate through an environment.
- Terrainability, which captures a robot's ability to negotiate terrain irregularities.

The trafficability aspect has been mainly considered at this stage of the design, and the Bekker's Theory proposed in [67] and the model used in [68] have been used.

An important role in wheel diameter selection is played by the ground clearance requirement, that was chosen to be at least 30 cm; for this reason all diameter values lower than 20 cm have been discarded. The cylindrical body for wheels was chosen for the calculations.

The first step in calculations is to determine the wheel sinkage, Equation 15.1.

$$z = \left(\frac{3W_w \cos \theta}{(3-n)(k_c + w k_\phi) \sqrt{d}} \right)^{\frac{2}{2n+1}} \quad (15.1)$$

Where:

W_w wheel load: mg/N , where N is the number of wheels

w wheel width

d wheel diameter

θ slope

The following coefficients depend on the wheel/soil interface properties and their values have been selected according to [69], considering the worst case scenario of dry sand:

$n = 1.1$ exponent of sinkage

$\phi = 31.9^\circ$ angle of internal friction

$k_c = 15.6 \text{ kPa/m}^{n+1}$ cohesive modulus

$k_\phi = 2407.4 \text{ kPa/m}^{n+2}$ frictional modulus

From Figure 15.4 it is evident that larger wheel diameters and widths result in lower sinkage.

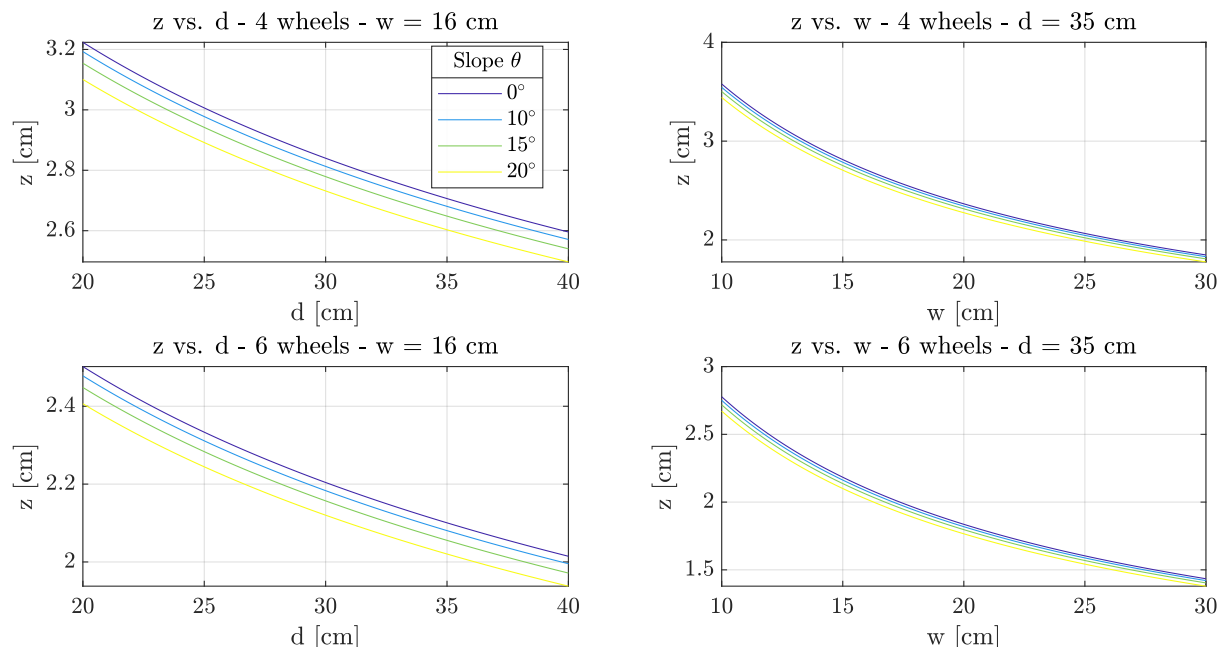


Figure 15.4: Wheel sinkage z as a function of wheel diameter, nominal width, slope angle and number of wheels.

The resistance that is created on the wheel is the sum of the following components:

- Compaction resistance, due to the soft soil compaction;
- Rolling resistance, due to the wheel slip;
- Gravitational resistance, which causes additional resistance when the rover is driving over the slopes;
- Bulldozing resistance, is caused by soil displacement to the sides, and is relevant only for wheel widths larger than 25 cm.

For the conceptual design, it has been assumed that the bulldozing resistance can be neglected. Formulas to compute all the other resistance contributes can be found in Appendix, subsection A.7.1.

The force that the soil creates if wheel is driven is the soil thrust, H , described by Equation 15.2 in absence of grousers.

$$H = (CA + W_w \tan \phi \cos \theta) \left[1 - \frac{K}{l} \left(1 - e^{\frac{sl}{K}} \right) \right] \quad (15.2)$$

Where:

$$l = d/2 \cdot \arccos(1 - 2z/d) \text{ length of the wheel contact path}$$

$$A = wl \text{ wheel contact area}$$

$$C = 251 \text{ Pa soil cohesion}$$

$$K = 0.03 \text{ m coefficient of soil slip (MER value)}$$

$$s = 0.3 \text{ wheel slip ratio}$$

The soil thrust increases significantly considering the presence of grousers of height h on the wheels and it is modelled according to [70], with Equation 15.3.

$$H = \left[wlC \left(1 + \frac{2h}{w} \right) N_g + W_w \tan \phi \left(1 + 0.64 \frac{h}{w} \arctan \frac{w}{h} \right) \right] \left[1 - \frac{K}{l} \left(1 - e^{\frac{sl}{K}} \right) \right] \quad (15.3)$$

Where $N_g = 19.7$, Terzaghi's coefficient of bearing capacity, function of ϕ .

Known as Drawbar Pull (DP), the difference between traction and motion resistance is a pivotal metric for robotic locomotion performance, because it expresses whether or not a robot can drive without loss of traction independently of how it is controlled. Configuration for trafficability should maximise soil thrust while minimising motion resistance. Maximising DP also improves the slope and obstacle climbing capabilities of a robot as well as its response to immobilisation.

$$DP = H - R_{\text{tot}} \quad (15.4)$$

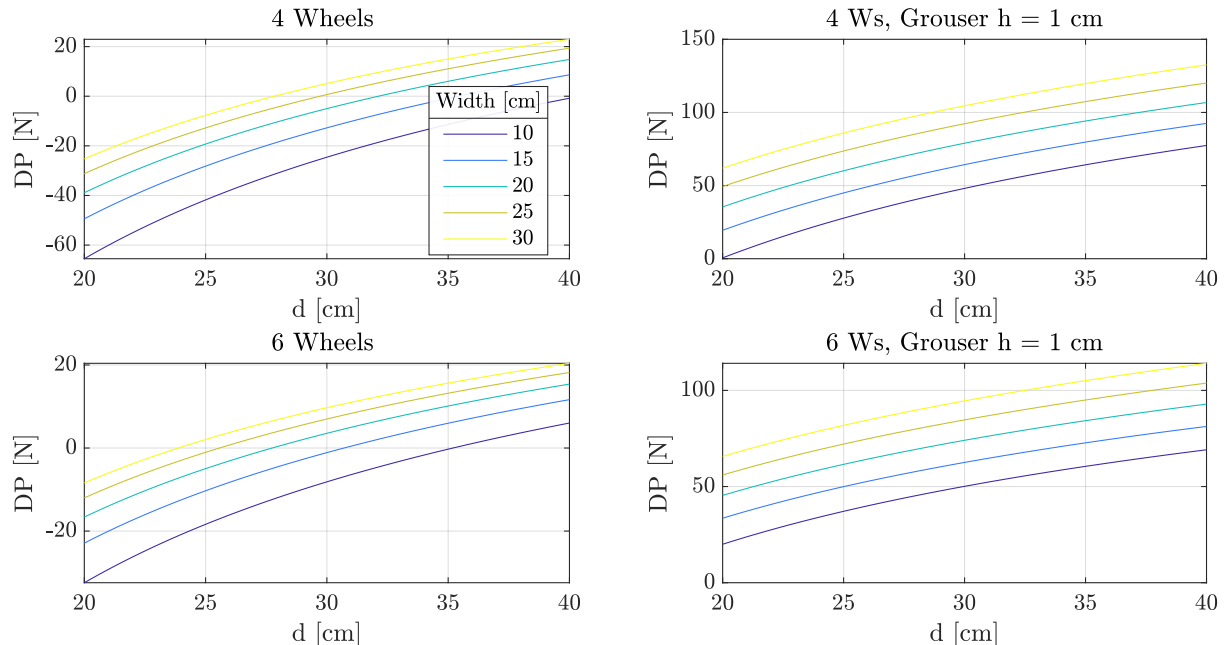


Figure 15.5: Drawbar Pull developed by a single rigid wheel, as function of wheel diameter and width, in absence of grousers and with $h = 1 \text{ cm}$ grousers. The first row of graphs refers to a 4-wheel configuration, while the second row refers to a 6-wheel rover.

The graphs in Figure 15.5 shows the Drawbar Pull dependence on wheels' diameter and width for different configurations. Obviously, the performance of the wheel increases with an increase in diameter and width. It has to be noticed how much DP increases by introducing 1 cm grousers on the wheels.

A comparison among the values of the total motion resistance, the soil thrust and the drawbar pull is shown in Figure 15.6.

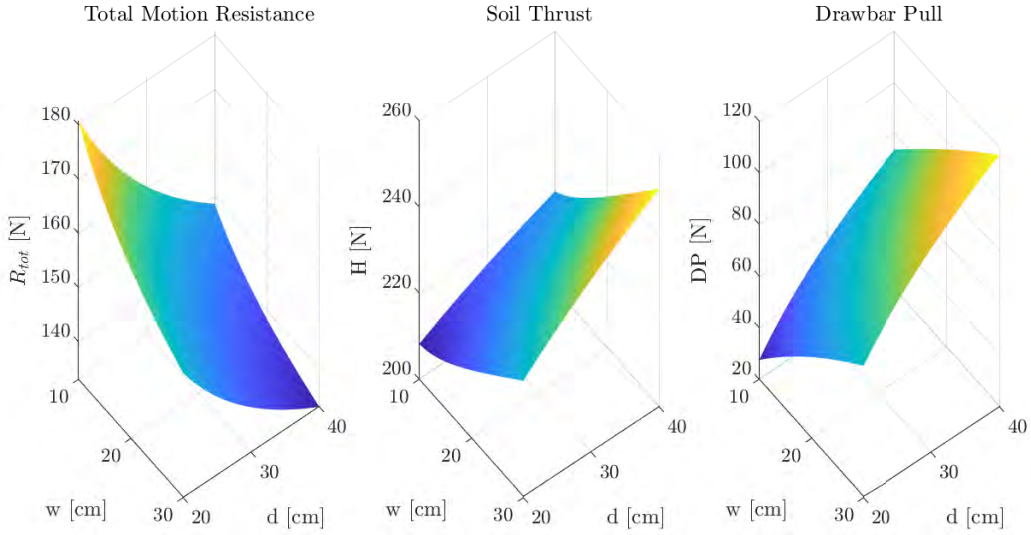


Figure 15.6: Total motion resistance R_{tot} , Soil Thrust H and Drawbar Pull DP developed by a single rigid wheel with 1 cm grousers, as functions of wheel diameter and width, considering a 6-wheel configuration.

The maximum slope that the rover can afford depends on the DP, Equation 15.5.

$$\theta_{\max} = \arctan \left(\frac{DP}{W_w} \right) \quad (15.5)$$

Finally, the configurations should minimise power expenditure P_w due to motion resistance, dependant on the drive torque T_w , described by Equation 15.6 ($\delta = 0$ for rigid wheel). This result is the output power, while the input power shall be computed accounting for the real efficiencies of the system.

$$T_w = R_{tot} \frac{d}{2} - \delta, \quad P_w = T_w \frac{2v}{d} \quad (15.6)$$

The main performance parameters are summarised in Table 15.1, comparing 4-wheel and 6-wheel configurations, with rigid suspension (worst-case choice), both considering 1 cm high grousers and only front wheels powered.

Performance metric	Symbol	Unit	4-Wheel	6-Wheel
			$d = 37 \text{ cm}, w = 25 \text{ cm}$	$d = 35 \text{ cm}, w = 16 \text{ cm}$
Rover Drawbar Pull	DP	N	~ 450	~ 450
Travelling speed	v	m/s	0.1	0.1
Sinkage	z	cm	2.03	2.10
Maximum slope	θ_{\max}	deg	13.60	13.60
Drawbar Pull/wheel	DP	N	112.73	75.09
Total Resistance/wheel	R_{tot}	N	221.87	150.42
Soil Thrust/wheel	H	N	334.60	225.52
Drive Torque/wheel	T_w	Nm	41.05	26.32
Drive Power/wheel (Outpt)	P_w^{out}	W	22.19	15.04
Drive Power/wheel (Input)	P_w^{in}	W	93.22	63.20
Total Drive Power	P^{in}	W	186.44	126.40

Table 15.1: Summary of the expected trafficability of 4-wheel and 6-wheel configurations with rigid suspension on flat terrain. For the input power: drivetrain efficiency: 0.7, motor efficiency: 0.8, drive electronics efficiency: 0.85.

The dimensions are selected in order to obtain the same value of the global drawbar pull, $DP \sim 450$ N, ensuring a sinkage value around $z = 2$ cm. The same travelling speed $v = 0.1$ m/s has been considered and the maximum negotiable slope, depending on the drawbar pull-weight-ratio, is the same since the wheel DP is the same. A sketch of the two configurations can be found in the Appendix, Figure A.19.

The 4-wheel rover is advantageous in terms of soil thrust, while the 6-wheel configuration leads to better results regarding all the other parameters: smaller dimensions, lower motion resistance and higher maximum slope and lower drive power. Considered that 6 wheels are also much more convenient in terms of manoeuvrability and overcoming obstacles, this configuration has been selected for Skipper.

Wheel material

A further design aspect to investigate regards in the selection of a suitable material for the wheels. Two main materials widely used in the aerospace field are considered: Aluminium alloy AL7075T6 and Titanium alloy Ti-6 Al-4V. The former has a high ductility and malleability, and it is characterised by a light weight; the latter instead is stronger with respect to the previous, it is highly corrosion-resistant and it also has very high bio-compatibility, although a high density. A statistical analysis is performed considering one wheel subject to a pressure on one side of a magnitude of 700 Pa and fixed to the face that is connected to the chassis. The properties considered to make the comparison are reported in Table 15.2, based on these the Titanium alloy is considered for its high corrosion-resistant and the mechanical properties obtained even though the components weights more.

Material	Total Mass [kg]	Yield Strength [N/m ²]	Max. Deformation [-]
Aluminium Alloy (AL7075T6)	10.44	5.05×10^8	2.58×10^{-3}
Titanium Alloy (Ti-6 Al-4V)	16.45	8.274×10^8	2.54×10^{-9}

Table 15.2: Properties of materials for wheels.

Suspension system

The suspension system chosen for Skipper is the rocker-bogie configuration, since a long travel has to be performed from the sub-glacial lake to the geyser sites. This type of configuration is the best one for optimal stability and control to traverse on uneven terrain for the following reasons [71]:

- it does not need for axles and springs, which are usually susceptible to dust accumulation in the Mars harsh environmental conditions;
- it allows the rover to travel over steps up to two times the wheel diameter;
- during the motion it maintains centre of gravity of entire vehicle: when one rocker moves upward then the other goes down through a differential mechanism that connects the left and right side rocker bogie assemblies, which helps to minimise the maximum or average ground pressure;
- each of the wheels is powered individually by its own DC-motor and the presence of the differential mechanism allows a balanced spreading of the load between wheels and motors;
- it allows each of the six wheels to remain in contact with the ground while it traverses over obstacles, helping to propel the vehicle over the terrain.

During the motion, in order to pass over obstacles, the rover must be geared down significantly to allow for enough torque to raise the mass of the robot. Consequently, this reduces overall speed. Then the front wheels are forced against the obstacle by the centre and rear wheels which generate maximum required torque. The rotation of the front wheel then lifts the front of the vehicle up and over the obstacle and obstacle overtaken. Those wheels which remain in the middle, is then pressed against the obstacle by the rear wheels and pulled against the obstacle by the front till the time it is lifted up and over. At last, the rear wheel is pulled over the obstacle by the front two wheels due to applying pull force [72].

The final design of the chassis is shown in Figure 15.7, and minimum and maximum distances between the wheels are reported.

Chassis material

Three typical aerospace materials have been considered for building Skipper's chassis:

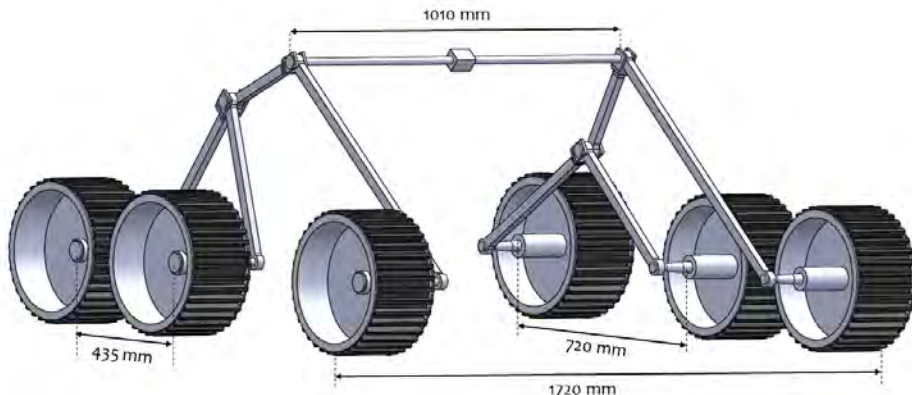


Figure 15.7: CAD model of the Skipper's rocker-bogie suspension.

- **Stainless Steel (SS304L)** due to its corrosion resistance and high ductility properties;
- **Aluminium Alloy (6061)** is a light weight material with good physical properties and great weldability; being one of the most common Aluminium alloys, it is easily available and cheap;
- **Titanium Alloy (Ti-6 Al-4V)** has a high strength-to-weight ratio and also provides exceptional bending and torsional capability, while minimising volume and mass.

The static analysis is performed on only one side of the chassis by applying loads with a magnitude of 1250 N on the ends of the link and fixing the pivot point. Comparing the properties of these materials, shown in Table 15.3, in terms of mass of the only suspension, yield strength and maximum deformation from a static analysis, a possible material for the chassis is chosen. From these analysis, the Aluminium Alloy has been chosen since it has a good compromise with strength and price, even though is the one that weights more.

Material	Total Mass [kg]	Yield Strength [MPa]	Max. Deformation [-]
Stainless Steel (SS304L)	21.72	206	9.30×10^{-7}
Aluminium Alloy (6061)	7.33	55.1	3.64×10^{-6}
Titanium Alloy (Ti-6 Al-4V)	12.03	827	2.37×10^{-6}

Table 15.3: Properties of the materials for the suspension.

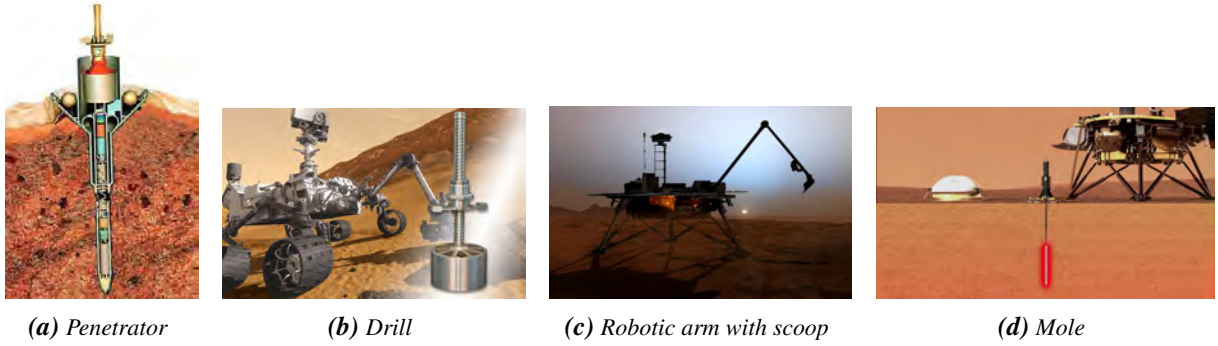
The displacement field obtained from this analysis can be found in Appendix, Figure A.20.

15.3 Sub-glacial lake region sampling

15.3.1 Sampling instrument selection

Skipper shall collect samples when it is above the sub-glacial lake, and the selection of the areas to penetrate will be made by the scientists who will have available, in addition to the orbital images, the SSI of the rover and the helicopter camera. Scientific payloads such as the Sounding Radar and the Neutral Ice Subsurface will be also used. The RLS will help to identify organic compounds and search for microbial life by identifying the mineral products and indicators of biologic activities. The Infrared Spectrometer studies instead the mineralogical and petrographic composition of the Martian surface in the vicinity of the rover, and in combination with the other remote sensing instruments, it will hence aid in the selection of potential targets for close-up investigations and digging sites.

It has to be noted that the region is covered by ice in winter while the ice melts in summer. The mission has been designed such that the landing is planned to be in spring and the rover will stay in the lake region until summer, hence the mandatory requirement for the instrument is the capability to penetrate the soil, to collect and to preserve

**Figure 15.8:** Possible sampling tools.

any ice (CO_2 or H_2O) that may be present underground.

In the initial stage of the analysis four types of sampling tool were taken into account: a penetrator, a drill, a mole-like instrument, and a robotic arm with a scoop. They are reported in Figure 15.8.

A surface penetrator is a scientific package usually released during the EDL phase in order to traverse some distance in a solid target using the kinetic energy of its arrival. The choice of this kind of instruments can be discarded since it would not be suitable to achieve the objective of collecting five samples from different positions.

The use of a robotic arm increases the degrees of freedom of the sampling instrument. Being the selected vehicle a rover, the great contribution of the robotic arm in terms of mobility is not necessary to achieve this goal; on the contrary, this tool has been discarded because it does not allow to dig deep, which is a fundamental aspect.

After these considerations, a criteria matrix (Table 15.4) has been used for the accomplishment of the trade-off between the two remaining options. For each alternative the first row reports some estimate values that justify the relative score in the second row (ranging from 1 to 5, “the higher the better”).

		Mass 20%	Power 20%	Complexity 10%	TRL 25%	Samples Quality 25%	Result
Drill	Approx. Value	21 kg	80 W	Low	8	High	3.45
	Score	2	2	4	4	5	
Mole	Approx. Value	3 kg	2 W	High	5	Low	3.35
	Score	4	5	3	2	3	

Table 15.4: Criteria Matrix for sampling tool.

ExoMars 2022 drill and InSight mole (HP³) have been taken as references for mass and power estimations. The TRL has been reported according to [73], and considering that drills have been already successfully used for several mission on Mars, while mole-like instruments for collecting underground material never succeeded in space environment: in fact, the Insight mole is not a sampling tool, it measures the planet’s “vital signs”: seismologic quantities, and temperatures. The PLUTO mole on Beagle 2 lander (Mars Express) was designed to collect a small volume of material but the mission failed.

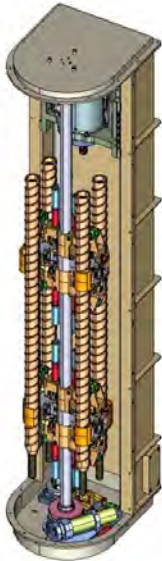
After this analysis the instrument selected for MARS-PENGUIN mission is a drill.

15.3.2 Reference drills

Three existing drills have been taken as a reference for MARS-PENGUIN drill: the first is the one designed for Rosalind Franklin (ExoMars), the second is TRIDENT, of ARTEMIS mission and the third is ProSEED, the drill of Luna-27 mission. The first one has been selected for its multistroke technology and since it is designed for Mars environment, the other two have been selected given their capacity to drill and sample the Moon’s icy soil, which is, from some points of view, similar to the Mars south pole terrain. The drills are shown in Figure 15.9 and their main characteristics are reported in Table 15.5. A description of the different sampling methods is given in the following paragraphs.

Drill	Mass	Power	Box length	Action type	TRL	Depth	Manufacturer
Rocky soil drill (Mars)							
ExoMars drill	21 kg	80 W	85 cm	rotary/translation	8	2 m	Leonardo
Icy soil drill (Moon)							
TRIDENT	16 kg	500 W	170 cm	rotary+percussive	6	1 m	Honeybee Robotics
ProSEED	20 kg	100 W	230 cm	rotary+percussive	6	1.2 m	Leonardo

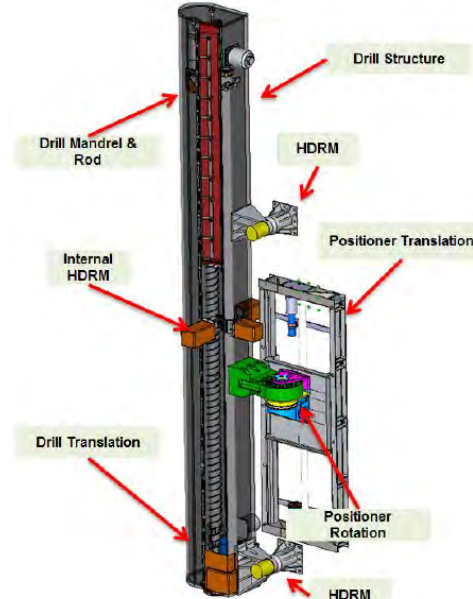
Table 15.5: Drill parameters and performance



(a) ExoMars 2022 drill, developed by ESA/ASI with Leonardo [74].



(b) TRIDENT, ARTEMIS mission, developed by Honeybee Robotics and NASA [75].



(c) ProSEED, Luna-27 mission, developed by Leonardo, ESA and Roscosmos [76].

Figure 15.9: Reference drills.

ExoMars

The ExoMars Drill Tool was designed to cope with sand and rocky materials that can be found in the Mars geology. It has the capability to create cores of material with a diameter of about 10 mm. In order to be able to collect sandy materials, a specific semi-spherical shuttering mechanism was designed.

TRIDENT

The goal of TRIDENT is to penetrate up to 1 meter depth, deliver cuttings to the surface and capture subsurface volatile rich sample for analysis. TRIDENT uses a sampling technique called “bite” sampling which is akin to peck drilling or pecking in machine shop terminology. The sample transfer from the auger to the scientific laboratory is made by a passive brushing system, designed to help remove regolith from the drill auger and direct it to an on board Oxygen & Volatile Extraction Node.

ProSEED

ProSEED is derived from that being developed for ExoMars and the SD2 drill flown on Rosetta’s Philae lander and it has been modified to account for the mission requirements and the expected properties of the lunar surface in polar regions.

ProSEED collects samples with two different methods for the Russian instrument and the European laboratory. The

Russian sample is stored inside an helicoidal chamber formed by protruding the sampling tool head. A deep groove helix exits from the drill tube. In this configuration the material is processed (unconsolidated) by the cutting bits, and then it is captured by the deep helix groove instead of getting to the tube auger that would bring the material to the surface. After filling the helix chamber, the drill bit can be replaced in the drilling configuration in order to secure the sample inside the augered-tube. In the center of the cutting bit it will be implemented another mechanism to acquire the european sample. This sampling operation is performed by raising the drill string by some millimetres (slightly more than the length of the push-tube) and then protruding the sampling-tube. Sample is then acquired by by roto-translation of the drill. Now the helix grove is filled with unconsolidated material and the push-tube filled with consolidated or unconsolidated (depending on the soil properties) sample, compatible with the ProSPA ovens design. For the sample discharge operations, the ProSPA sample will be delivered first, then the unconsolidated material will be discharged in the Russian robotic arm receptacle.

15.3.3 MARS-PENGUIN drill: Rico

It is crucial to study all the available information about the soil characteristics that the MARS-PENGUIN drill, called “Rico”, has to penetrate. The more spatially extensive part of the SPLD has a low albedo and a dustlike spectral signature, which raises the question of whether the dominant component of the SPLD as a whole is volatile (H_2O and/or CO_2) or dust.

The key unknowns were the densities of the crust, mantle, and SPLD and the topography along the crust/mantle interface (the Moho). The densities of the Martian crust and mantle were taken to be 2900 and 3500 kg/m³, respectively.

In [77] the SPLD density was iterated to find the best fit between the modeled and observed gravity, using MRO results. For the preferred case of zero flexure beneath the deposits, the result is a density of 1220 kg/m³. This value, taking into account surface spectral measurements, is most simply explained by water ice with a silicate dust content of 15%. This result can be compared with a dust content of 0 to 10% inferred from the dielectric loss tangent of the SPLD measured by MARSIS. It also supports an earlier inference based on laboratory measurements of rheological properties that the SPLD are mostly water ice rather than denser (1589 kg/m³) CO_2 ice.

Therefore Rico has to be designed as an icy soil drill and, based on the reference drills, the estimated mass and power (without margins), are 20 kg and 100 W. Rico shall be able to dig at least 1 m under the Martian surface, and the total length shall not exceed 1.30 m, in order to keep it in a vertical position inside the rover body. Considering these dimensions, multi-rod technology is not required. The box containing the drill must be able to move down from the body of the rover in order to use the entire length of the auger to drill the ground. The main baseline for the action type is ProSEED, that requires just 100 W of total input power for both the rotary and the percussive action. Further analysis will be performed about whether or not the percussive action is necessary.

Since the drill relies on technologies already tested in space but will be customised specifically for our needs, the TRL is 5. In Figure 15.10 a possible configuration for the drill auger and instrumentation is shown.

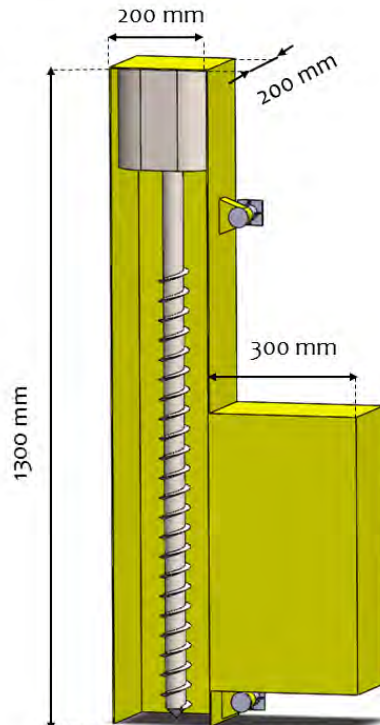


Figure 15.10: Possible configuration for the drill Rico.

15.4 Geysers ejecta sampling

15.4.1 Phenomenon observation and sample selection

Once in the Geyser region, the MARS-PENGUIN mission shall first of all observe the phenomenon of the eruptions and record it with the SSI on the Skipper rover, and the camera on Kowalski, the helicopter. A great useful aspect of this phase is the identification of the areas where the material has deposited on the surface for subsequent sampling. In case the geyser occurrence could not be observed, Skipper and Kowalski should look for the most significant areas to sample, focusing on possible darker spots with respect to the surrounding soil. Similarly to the lake sampling case, the location to sample will be selected by scientists using images from the orbiter and from ground, and especially by means of the scientific payloads mounted on the rover.

15.4.2 Sampling instrument selection

Five alternatives were initially considered for the geyser ejecta sampling: a Robotic Arm (RA) with a scoop, a folding reverse-umbrella-like collector, a deployable boom, an expendable mini-rover for approaching the ejection location and a sampling instrument on the helicopter Kowalski.

The deployable boom alternative, was considered as part of the umbrella one since their sampling methods could be considered similar.

The mini-rover option has been discarded. It may appear advantageous to deploy an expendable small vehicle from the lander to approach the geyser location, avoiding the risk to go close with the main vehicle, but such a small vehicle is requiring to be powered by its own battery, which would likely be insufficient to cover the back and forth travel. For these reasons, the mini-rover was not considered for further evaluation.

The last alternative of equipping Kowalski with a sampling instrument was discarded because of the large increase in mass and power required, which would have significantly reduced the flight time and the distance that can be covered.

The two final alternatives are sketched in Figure 15.11.

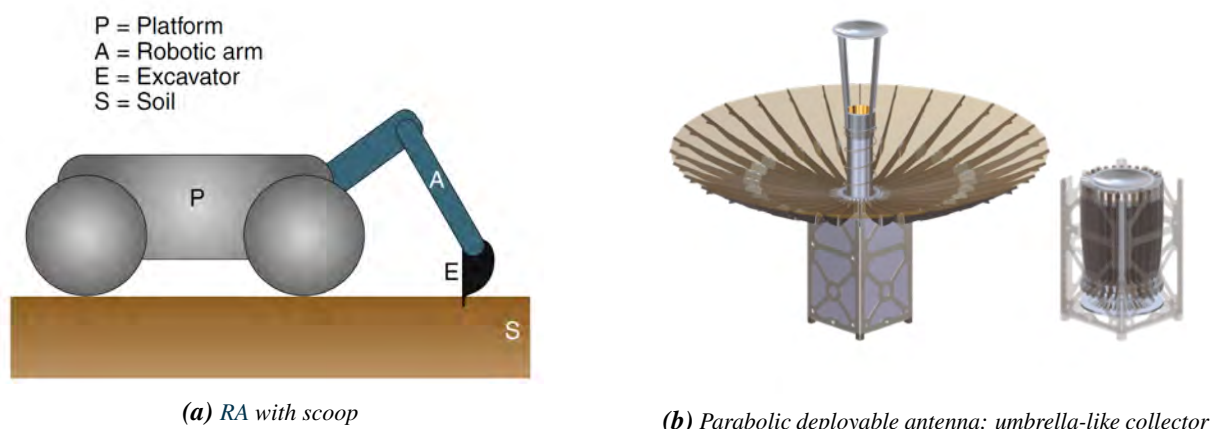


Figure 15.11: Possible geyser ejecta sampling instruments.

Without the need for quantitative analysis, a RA was selected for MARS-PENGUIN mission, because of the low TRL level of the umbrella collector and especially the high risks involved in approaching too close the geyser during the eruption. Moreover, there are lot of criticalities in collecting falling material, and even if it worked, there would be no chance to collect material from the ground before and after the eruption to compare them.

15.4.3 MARS-PENGUIN robotic arm: Soldato

The minimum number of Degrees of Freedom (DoF) that allow the instrument to dig the soil and then to bring the material to the scientific laboratory to be analysed is four, and the following joint combination has been selected:

1. shoulder yaw,
2. shoulder pitch,
3. elbow pitch,
4. wrist pitch.

The RA of Phoenix mission [78], the only one successful polar mission to Mars, with 4 DoF and a back-hoe design, can be considered as a first baseline for the MARS-PENGUIN RA, especially for the scoop design.

A possible prototype of the MARS-PENGUIN's RA, baptised "Soldato", is shown in Figure 15.12. The RA is composed by five parts: a base, the shoulder pitch joint, an upper arm, a forearm and a scoop. The upper arm and the forearm are both 0.9 m long and, extended to its limit, the arm can reach a point 2 m far from the base. The scoop capacity is 731.15 cm³. The instrument is also equipped with an X-Ray Spectrometer to select the optimal sampling site.



Figure 15.12: Soldato in different positions.

Actuators

Soldato is a 4-degree of freedom manipulator with a motorised joint actuator for each DOF. Referring to the actuators with the number of the relative DoF listed in the previous paragraph, actuators 1 and 2 share a common housing, actuators 1 and 3 share a common architecture of motor/planetary gearbox/harmonic gear/output bearing. A good baseline for Soldato's actuators is the Insight Instrument Deployment Arm (IDA), and it has the same 4 DoFs as well. It is essentially the same design as the robotic arm that assisted the MVACS experiment sent to Mars in 1998 as part of the MPL mission.

All actuators of IDA are driven by American Technology Consortium (ATC) motors with graphite brushes. These motors were selected following a period of testing in Martian atmospheric conditions. At the time of selection, brushed motors were preferred over brushless motors due to electrical simplicity and a history of usage at JPL, most notably on the Mars Pathfinder mission and its Sojourner rover. As a side-note, similar brushed motors were used once again for the 2003 MER and 2008 Phoenix missions. The motors are equipped with redundant thin-film heaters and a single bonded-on platinum resistance thermometer (PRT). The motors have iron core rotors with naturally occurring detent torque that provides joint-holding torque when the actuators are powered off [79].

Structure

In terms of material and structure IDA is a good baseline as well. The upper arm and forearm tubes are made of XN-70 and XN-80 carbon-fiber composite material with wall thicknesses of 0.8 mm and 1.1 mm, respectively. They are Ultra High Modulus materials, with a density of 2.17 g/cm³ and a tensile stress in the order of 1 GPa. End-fittings are thin-walled titanium and are bonded to the exterior of the composite tubes with Hysol EA 9309 adhesive. The original MPL arm used XN-70 for both tubes, but the forearm was redesigned for the Surveyor arm because of increased mid-span loading due to the addition of a 400-gram Mossbauer spectrometer mounted onto

the forearm. Redesign included thickening of the forearm tube wall from 0.8 mm to 1.1 mm and the substitution of XN-80 for XN-70 due to availability at the time. Tubes and end-fittings were tested under load throughout the mission temperature range (-105°C to 55°C) during development of the MPL arm.

Soldato's arms adopt similar design and the materials of IDA, it has been decided to use the same composite, XN-80, for both the two arm, since it guarantees good mechanical and structural properties.

The total weight of the RA without payloads is approximately 6 kg.

A preliminary FEM analysis has been performed on the upper arm, since this one is the most stressed, and the results in terms of stress and displacement are shown in Figure 15.13. A bending force of 500 N is considered and the maximum stress is one order of magnitude lower than the yield stress of the selected material (XN-80).

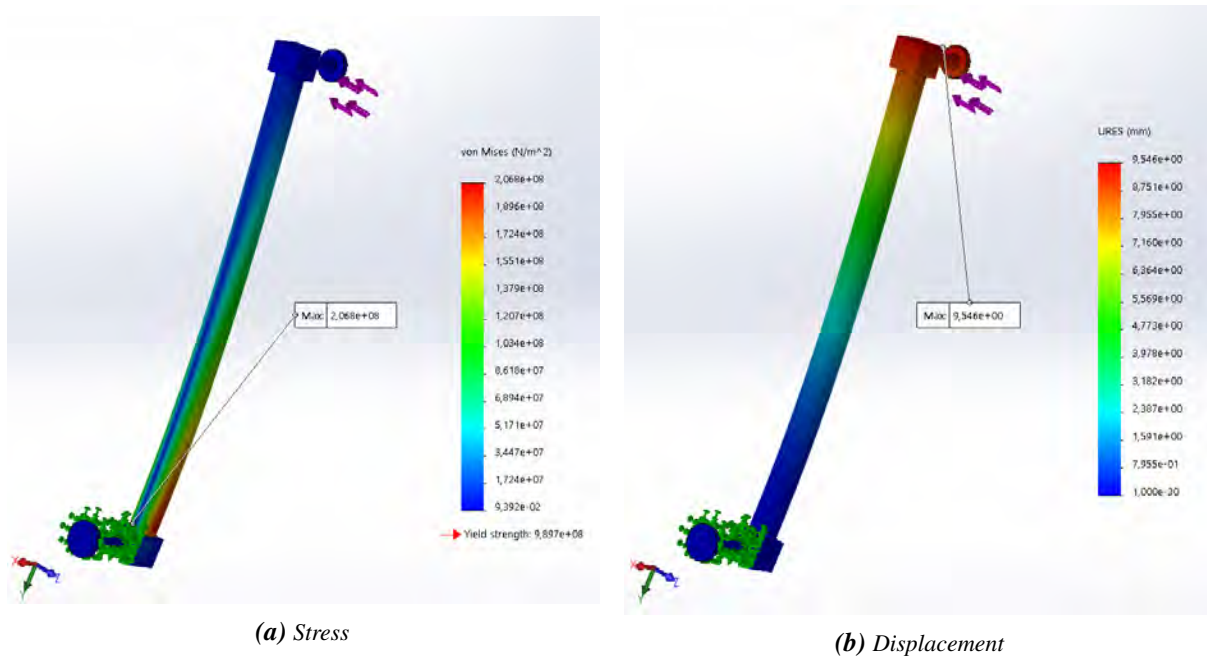


Figure 15.13: Preliminary FEM analysis of the upper arm.

15.5 Sample handling and analysis

Skipper is equipped with a sample analysis laboratory, which includes the Mass Spectrometer and the RLS for sample in-situ analyses. The rover will need a system for the material handling and transfer to the above mentioned laboratory. This will be the assembly of structures, mechanisms, containers and devices that allow transport and processing of the samples collected by the two sampling instruments.

The rover shall be provided with at least 10 containers to collect the material from the drill, in order to guarantee the 5 samples required with a certain margin.

Concerning the geyser sampling instead, after collecting the samples from the ground, the robotic arm shall place the material in a dedicated storage area in the rover from which the sample is transferred to the laboratory.

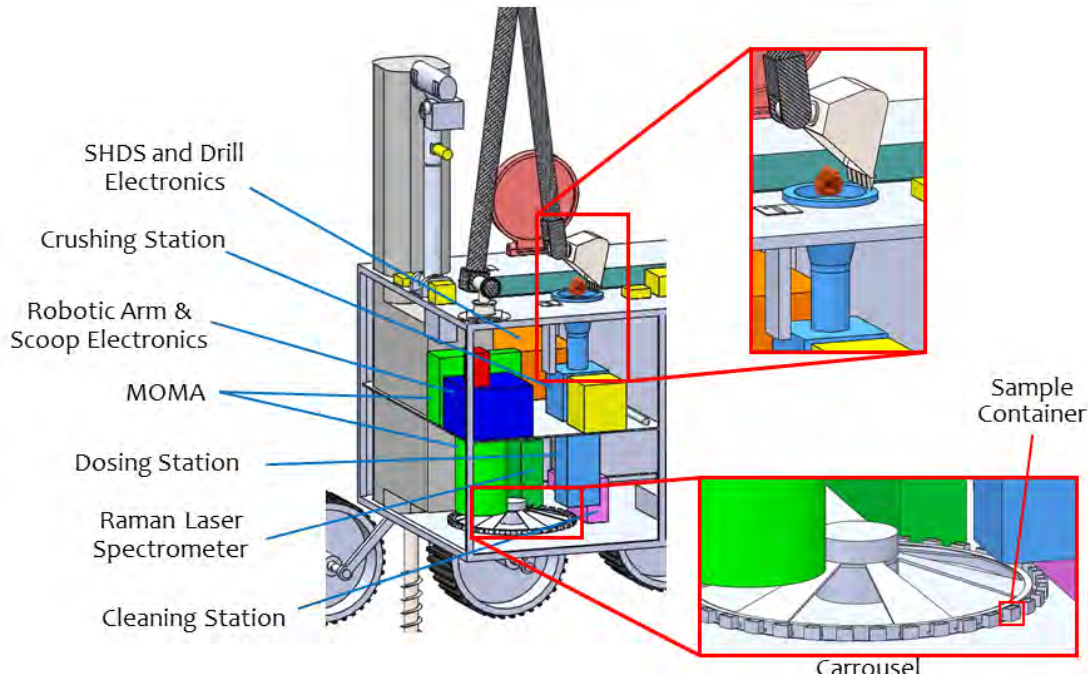


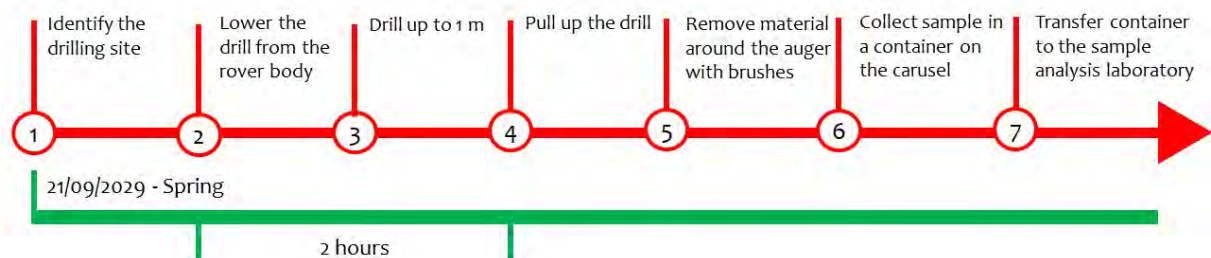
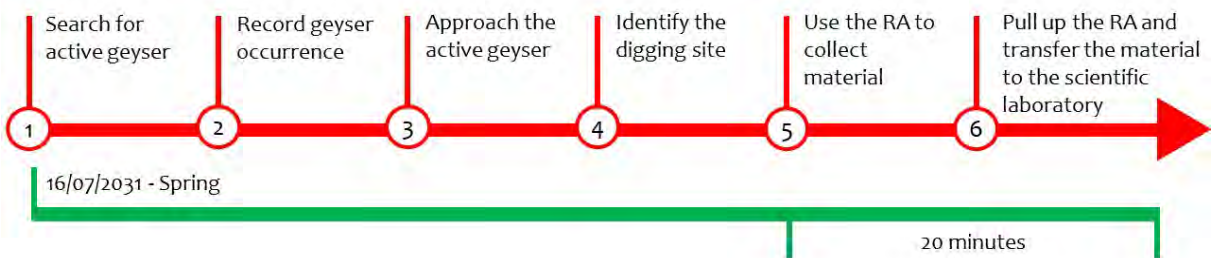
Figure 15.14: Skipper Sample Handling and Distribution System

15.6 Modes and Timelines

Sampling modes and submodes		Description
LRS	Lake region sampling mode	
DRL	Drilling mode	Perform sampling using the drill to penetrate the soil
LRA	Lake region analysis mode	
SPD	Sample preparation and distribution mode	Prepare and transfer samples to the scientific laboratory
SAA	Sample analysis mode	Perform sample analysis by making use of the scientific laboratory
GRS	Geyser region sampling mode	
ROA	Robotic Arm mode	Perform sampling of the geyser ejecta particles digging with the RA
GRA	Geyser region analysis mode	
GOB	Ground Observation mode	Observe and record significant martian areas or events (e.g. geyser phenomena)
SPD	Sample preparation and distribution mode	Prepare and transfer samples to the scientific laboratory
SAA	Sample analysis mode	Perform sample analysis by making use of the scientific laboratory

Table 15.6: Sampling modes (in blue) and submodes(in white).

In order to better understand the succession of the operations concerning sampling, two timelines related respectively to the lake region and the geyser region are shown in Figure 15.15 and Figure 15.16.

*Figure 15.15: Lake region sampling timeline.**Figure 15.16: Geyser analysis timeline.*

16. Configuration

16.1 Introduction

Mars-Penguin mission will be composed of several segments: the rover Skipper, the helicopter Kowalski (chapter 18), a descend module (entry capsule and sky crane) and the cruise stage.

The configuration of the different segments has been defined considering the payload requirements, in terms of positioning and dimensions, and the requirements from the other subsystems. For instance, electronics have been placed as close as possible to the instruments to reduce the length of cables.

The process of definition and sizing of the parts has started from Skipper and then moved to the other segments following an inverse flow with respect to the mission timeline.

The mechanisms of separation between the different segments have been analysed as well.

16.2 Rover

As explained above, the rover is the first element that has been analysed. Indeed, its dimensions strongly constrain the sizing of the descend module and of the all spacecraft.

The dimensions of the main box have been selected to be compliant with the studies on the chassis and on the wheels reported in chapter 15. The height of the box is a bit higher than usual to give more stability to the drill which is a very tall instrument.

Skipper has been divided into two main sections: a “scientific module” and a “service module”. In Figure 16.1, the rover Skipper is shown along with its dimensions and the positions of the different payloads and elements.

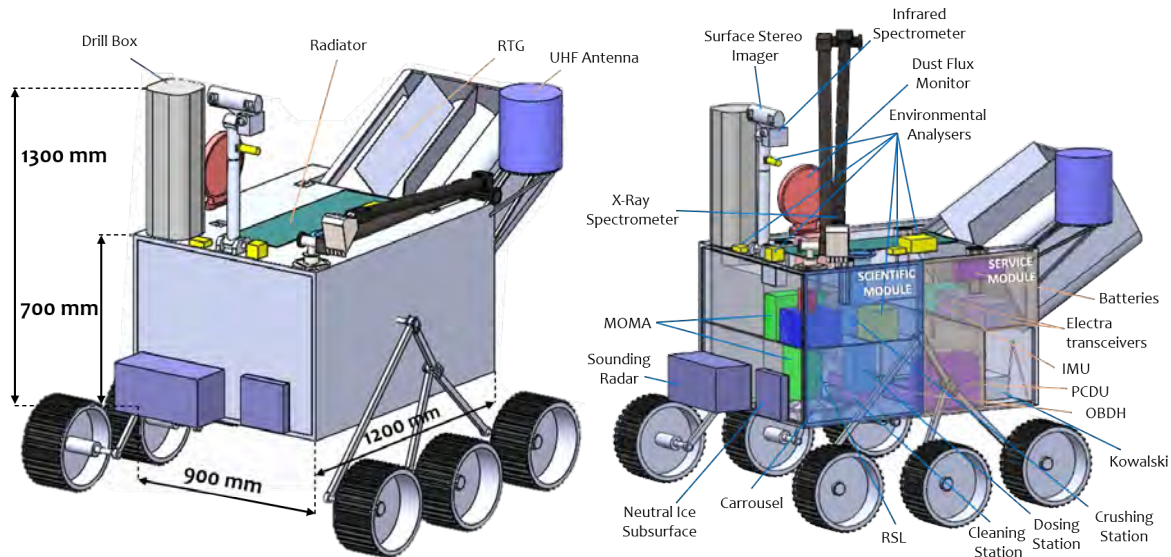


Figure 16.1: Rover Skipper preliminary design with payload positions.

Scientific Module

The scientific laboratory is characterised by two sections: an upper zone with the electronic boxes of the instruments and a bottom part, that will be an ultra clean zone, with the actual laboratory for samples handling and analyses. Two ways of sample handling have been considered: a linear or a circular pattern. The circular one with a carrousel that gathers and transports samples has been chosen for many reasons (Figure 15.14). This mechanism is the one usually used in space so it has a higher TRL, it is more compact and bidirectional.

Regarding the drill, the possibility of placing it outside the rover and having a mechanism to rotate it horizontally has been evaluated. However, given the large dimensions of it (1.3 m long) and its way of collecting samples with brushes, it was judged to be more efficient if placed directly close to the carrousel in a vertical position and inside

the rover to be more stable. The drill box will have a degree of freedom in the vertical direction, so that it can get closer to the ground.

The scoop will deliver its samples into a hole (that will be equipped with a closing mechanism) on the top of the rover. The samples in this case will be gathered in the crushing station, that will make the dimensions of the particles compatible with the requirements of the instruments, and then a dosing station will distribute samples to the collectors. Finally, a cleaning station has also been defined to properly clean the collectors from the previous samples.

Service Module

As already explained, the service module contains all the other elements necessary to support the scientific laboratory such as power, thermal control, on-board data system and telecommunication system.

The **RTG** is placed at the very back of the rover, in order to radiate the majority of its huge heat power in the external environment and not inside the rover. Instead of being horizontal, it is inclined of an angle of 60° for stability and mass distribution reasons. The other elements have been placed according to their specific requirements.

Helicopter Kowalski positioning and release mechanism

Kowalski will be released once the geyser site region has been reached by the rover Skipper. Therefore, the helicopter shall be stowed within the rover for the whole journey from the lake region and a release mechanism should be proposed. In order to fit inside the rover, its legs and blades will be folded. The blades will be put on one side.

The helicopter height is greater than the ground clearance, so it is not possible to release it directly below the rover. Therefore, the proposed solution is characterised by the release of part of the bottom and rear panels to let the helicopter deploy its legs, while still attached to the rover. Skipper would then release it and move away Figure 16.2.

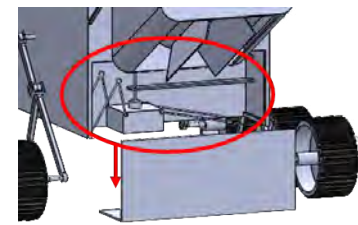


Figure 16.2: Release mechanism of the helicopter

16.3 Descend Module

The descend module is composed by two segments: the sky crane and the entry capsule.

Sky Crane

The central shape of the sky crane is hexagonal (Figure 16.3a). This shape is particularly good for this element since 4 sides will be elongated to provide support to the thrusters and the other two opposite sides will be placed in correspondence of the **RTG** and of the drill which are the highest parts of the rover. A fifth smaller arm is used to place a radar-Doppler altimeter, that will be crucial during the descend phase. The sky crane will be attached to the rover by means of four legs.

Entry Capsule

The entry capsule is composed by the heat shield and the backshell. Its preliminary design is shown in Figure 16.3b. Regarding the first one, as explained in chapter 9, the classical 70-degree half-angle sphere-cone shape used in almost all the other missions to Mars has been considered [80]. Its diameter has been set to 3.85 m according to the EDL analysis and its thickness has been defined by the thermal analysis (section 14.4).

For the backshell, a triconic shape design has been selected. This shape is useful to have a larger diameter on the top of the capsule to grant enough space for the sky crane, but without having to enlarge too much the maximum diameter of the entry capsule. Its dimensions have been evaluated with a structural analysis (section 17.2.3).

16.4 Cruise Stage

The design of the cruise stage is mainly based on the dimensions of the tanks, of the launcher adapter and of the **HGA**, which has been positioned at the centre.

As it is shown in Figure 16.4a, the two tanks have been placed symmetrically and close to the thrusters, to reduce the length of the pipes. The two clusters of thrusters and the instruments have been distributed according to the attitude control system requirements.

The lateral vertical panels protect the systems inside the cruise stage from the space environment, mostly from the thermal point of view. Some gaps between the panels are left for instruments and are used as a way of saving mass.

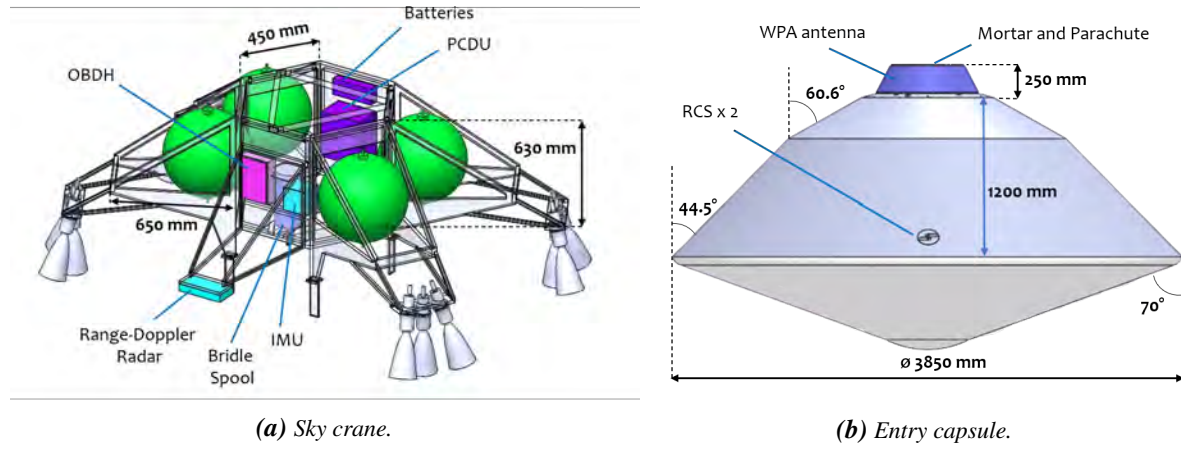


Figure 16.3: Descend module preliminary design.

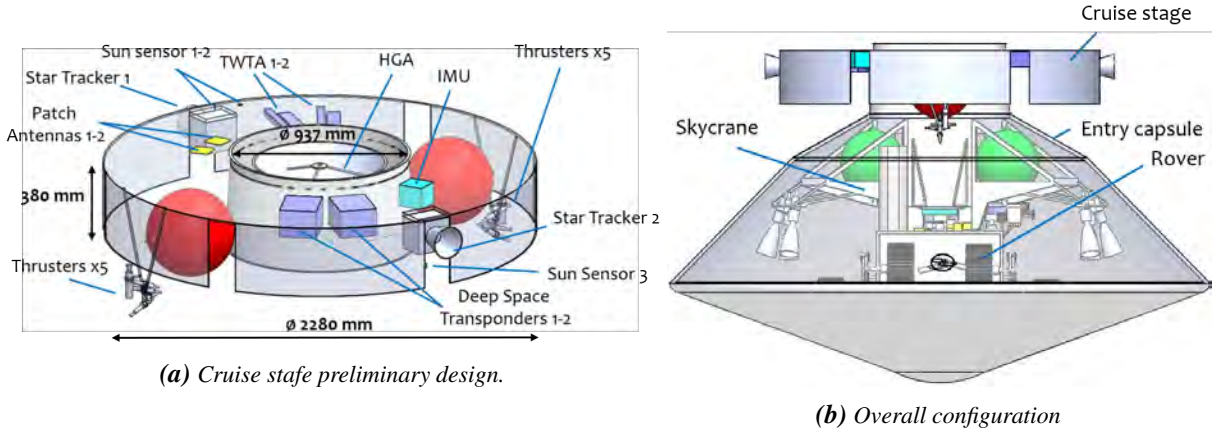


Figure 16.4: Cruise stage and overall configuration

16.5 Overall Configuration and Launcher Interface

In Figure 16.4b, is reported the overall configuration of the Mars-Penguin mission.

In the process of design of the different segments, the interface with the launcher has been taken into account. The dimensions of all the parts are compliant with the fairing of both the selected possible launchers Ariane 5 and 6, as it is shown in Figure 16.5. Moreover, the dimension of the top section of the cruise stage is compatible with the selected adapter, the PAS 937 mm (compatible with Ariane 5 and 6), which has been identified as the most suitable solution.

In Table 16.1, the masses of the different structures, computed from the definition of shape, dimensions and material according also to TCS and structural analyses, are reported.

For the evaluation of the moments of inertia, a simplified model, in which the mass of each part (cruise stage, backshell, heat shield, sky crane, rover box, wheels) was considered to be distributed homogeneously in its volume, has been used.

16.6 Separation mechanisms

During the EDL several separations will occur. Therefore, the interfaces between different segments have been studied along with some possible mechanisms of separation.

In Figure 16.6, a summary of the different mechanisms selected is depicted. In general, the separation nuts will be used to connect the different parts and to allow the separation. These elements will be sufficient in case of the entry capsule-sky crane and sky crane-rover separations, since the drag of the parachute and the thrusters of the sky crane will provide a sufficient relative acceleration between the parts. However, in the cases of cruise-entry capsule and



Figure 16.5: Launcher configuration

Component	Material	Mass [kg]
Rover body	Al 7075-T6 Al honeycomb	35
Rover wheels	Al 7075-T6	98.7
Rover chassis	Al 6061	7.3
Sky crane structure	Al 7075-T6	108.8
Cruise deck cylinder	Al 7075-T6	22.5
Cruise deck panels	Al honeycomb	16.3
Heat shield TPS	SLA-561V	35.9
Heat shield structure	Al honeycomb	96
Backshell	Al honeycomb	123.3

Table 16.1: Materials and masses of the different structural components (without margins).

backshell-heat shield, separation springs will be needed. Their characteristics have been studied with a dynamical model and are reported in Table 16.2.

Moreover, guide rails will be used in the capsule-sky crane and sky crane-rover separations in order ensure that the two bodies divide without recontact. In the second case, this is mainly done to protect the drill.

Just prior to the firing of the nuts, several pyro cutters will be fired to cut the electrical lines.

The rover will be delivered to the ground by means of four bridles that will be rolled up on a braked spool, as shown in Figure A.21.

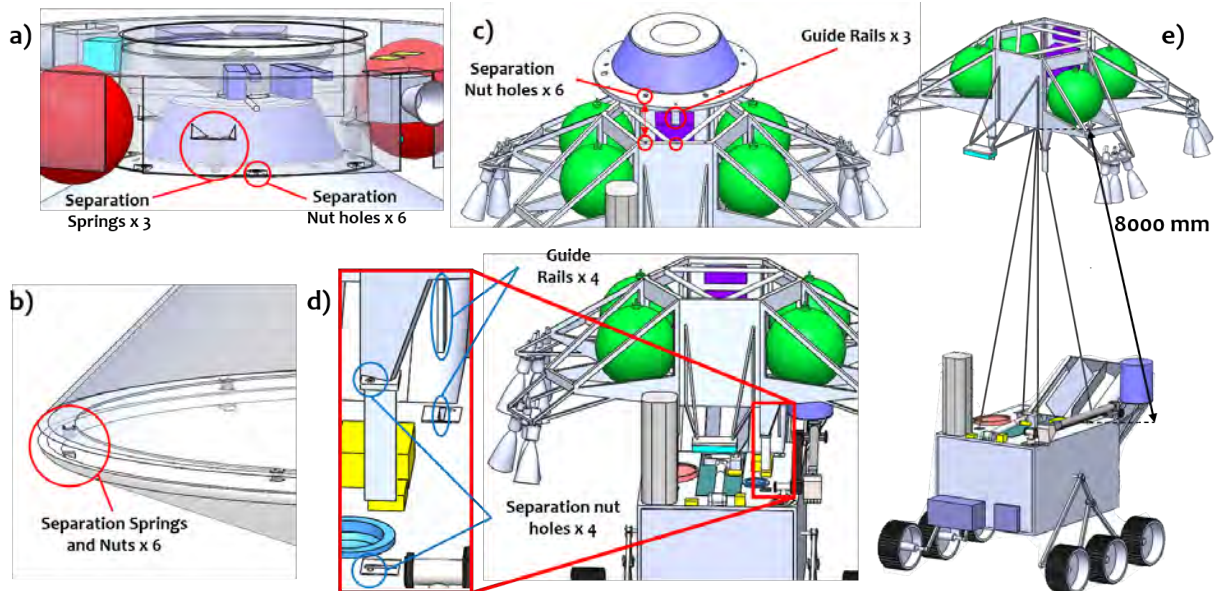


Figure 16.6: Separation mechanisms: a) cruise stage-entry capsule, b) entry capsule-heat shield, c) entry capsule - sky crane, d-e) sky crane- rover.

Separation Springs	Requested ΔV [m/s]	Number [-]	Spring Constant [N/mm]	Free Length [mm]	Δx_{max} [mm]
a)	5	3	196	180	80
b)	2	6	46	80	40

Table 16.2: Separation springs characteristics: a) cruise stage-entry capsule, b) entry capsule-heat shield.

17. Structures

17.1 Introduction

Structural analysis have been performed to size the two main segment of the MARS-PENGUIN mission, namely the primary structure of the cruise stage and the entry capsule, since they have to withstand different loading conditions through the overall mission. The most critical loading conditions among all the phases arise along the launch and the EDL.

In this chapter have been reported the structural analyses, explaining the assumptions made and the results based on a multi-nodes analysis for the two critical phases.

Before performing the analyses, the materials for the two bodies have been selected based on their mechanical properties and low density. So that the degrees of freedom coincides with the dimensions of the considered structures.

17.2 Launch Phase

The launch phase generally has been considered the most critical condition in terms of load acting on a satellite. From the simulation it arises being the driving condition for the design of both structures. To size them a FEA have been performed by studying the static and dynamic response, then also the buckling phenomenon. The structures have been sized under loading conditions obtained from Ariane V launcher's manual [81].

17.2.1 Requirements

From the Ariane V launcher's manual a requirement on the frequency has been imposed for which the structures shall have the natural frequency satisfying the following conditions:

- Lateral frequencies ≥ 10 Hz;
- Longitudinal frequencies ≥ 31 Hz.

In the design for safety reason, the frequency requirement considered for the modal analysis has been the longitudinal frequency, which is the more constraining between the two condition, then increased such that

$$f_{nat} - f_{con} \geq \frac{1}{2} f_{con} \Rightarrow f_{nat} \geq 46.5 \text{ Hz}$$

where f_{nat} is the natural frequency that is the first modes arising and f_{con} is the constraining frequency related to the longitudinal direction from the launcher manual.

Also the structures inside the fairing shall withstand the loads during the overall launch. Therefore, two worst cases related to the axial and lateral direction has been considered in order to identify which one has an higher impact on the structure. Along with the QSL, also the acoustic and sinusoidal loads have been studied and combined following [82]. Then, the loading factors identified are reported in Table 17.1 in which only two components have been reported because the structure is symmetric, and in Figure 17.1 is represented the reference system considered.

	X [g]	Y [g]
Lateral Worst case	3.62	10.98
Axial Worst case	14.72	3.6

Table 17.1: Loading factors of the worst cases related to lateral and axial directions.

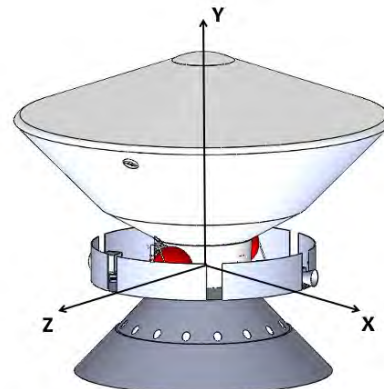


Figure 17.1: Overall configuration in the fairing with axis.

17.2.2 Cruise stage

The primary structure of the cruise stage have been analysed, since during the launch phase it is the component that has to withstand all the solicitation and supports appropriately the entry capsule in the fairing. In addition, the primary structure have been considered as the element that at one end is connected to Launch Vehicle Adapter (LVA) and the other to entry capsule. To design the structure, a simplified model have been considered with the following considerations:

- The primary structure have been considered as an hollow truncated cone;
- The entry capsule have been considered as a concentrated mass;
- The primary structure is fixed at the LVA end.

For the primary structure the material selected is the Aluminium 7075-T6 since it is commonly used in the aerospace industry and it is very high strength material used for highly stressed structural parts, its main properties are reported in appendix A.9.1. The degrees of freedom for the sizing for the FEA are the upper diameter related to the entry capsule end d_1 , the height h_1 and the thickness of the truncated cone $t = 4.5$ mm. The results of the sizing are reported in Figure 17.2.

In the following the static, dynamic behaviour and buckling analysis have been reported for the resulting primary structure.

Quasi Static Load (QSL)

The results obtained from the multi-nodes analysis are shown in Figure 17.3 and reported in Table 17.2. From the latter can be seen that the lateral solicitation has a higher impact on the structure based on the maximum von Mises strength, therefore it has been considered as the loading condition studied for next analysis. In particular it is noteworthy that the lateral displacement is relatively small, meaning that during the launch phase the overall spacecraft is not exceeding the dynamic fairing of the launcher. Lastly, the last column refers to the SM related to the yield strength evaluated with FOSY of 1.1, retrieved from [83].

	Lateral	Axial
σ_{VM} [MPa]	57.31	30.24
ε [-]	6.68×10^{-4}	3.61×10^{-4}
u [mm]	0.58	1.68
MS [-]	7.01	14.18

Table 17.2: Results of the multi-nodes analysis under QSL.

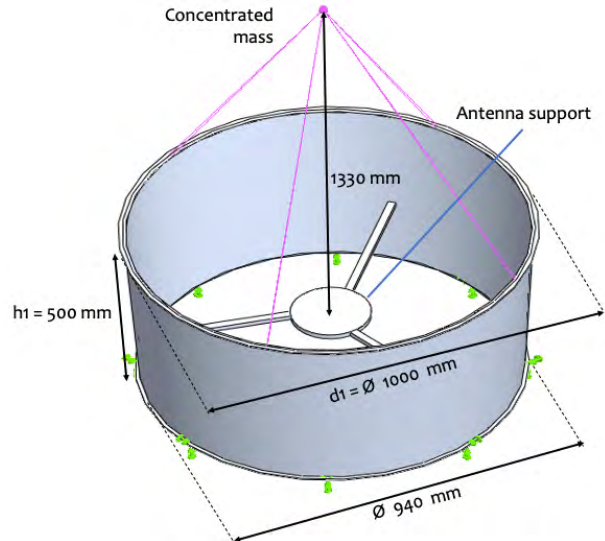


Figure 17.2: Primary structure model.

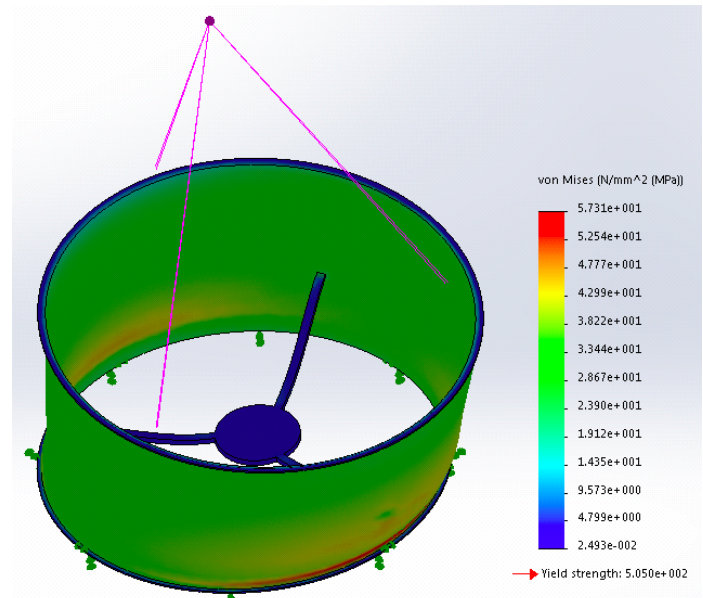


Figure 17.3: Stress field of the primary structure.

Modal Analysis

From the modal analysis, the first mode is found at 48.12 Hz. Hence, the structure is satisfying the design requirement on frequency, therefore no resonance phenomenon will occur.

Buckling Analysis

Firstly, a simplified model has been studied the primary structure considered as a cantilever beam with an hollow circle as section area uniform over the length. Then, the critical strength obtained ($\sigma_{cr} = 141.02 \text{ GPa}$) is higher than the yield strength ($\sigma_{yield} = 505 \text{ MPa}$) meaning that the latter has been considered as the main driver for the design of the structure. But, it could be also understood from the slenderness ratio ($\frac{KL}{\rho} = 2.24$), which is quite small meaning that this kind of structure is prone to fail due to the squashing phenomena instead than buckling. Then a FEA has been performed, the loading condition applied will not reach the critical one since the Buckling Load Factor (BLF) = 13.66 is higher than 1. Hence, the buckling is not predicted.

17.2.3 Entry Capsule

The entry capsule analysis is performed with the following considerations:

- The Skycrane, Skipper and Kowalski have been considered as a unique concentrated mass;
- The reaction force with the cruise stage is applied at the interface $F = 120350 \text{ N}$;
- Capsule fixed to cruise stage interface;
- The loading condition considered is the worst case related to the lateral direction since is the most critical in terms of loads.

For the entry capsule an Aluminium Honeycomb HexWeb CRIII 5052 Hexagonal and as skin material Aluminium 7075-T73 has been selected, its main properties are reported in appendix A.9.1. The reason of choosing sandwich material is because they are rigid panels of minimum weight, aerodynamic smooth surfaces, high fatigue resistance and maintain corrosion protection at elevated temperatures. The degrees of freedom for the sizing for FEA are the truncated cone height h_1 , the truncated cone diameter d_1 and the thicknesses t_{core} and t_{Al} . The results of the sizing are shown in Figure 17.4.

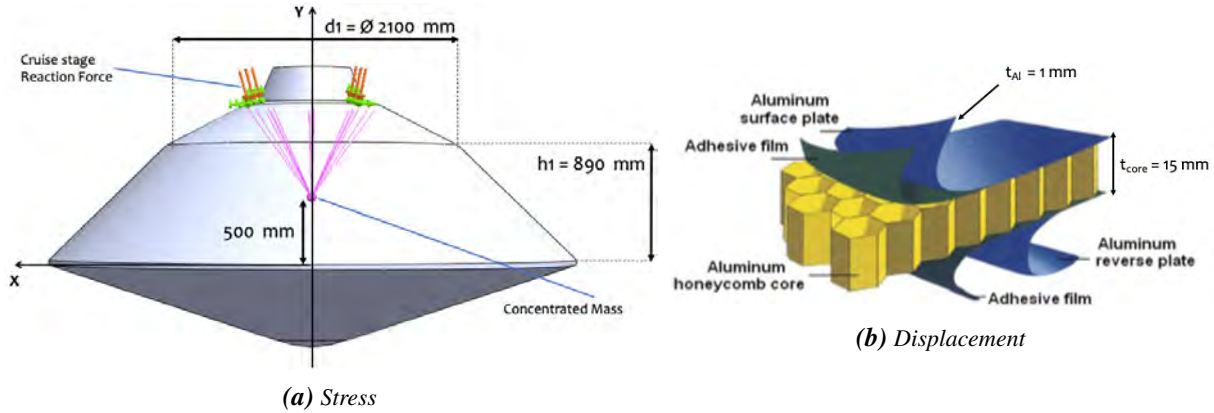


Figure 17.4: Preliminary FEM analysis of the upper arm.

In Table 17.3 are reported the results of the sized structure obtained from the static, dynamic and buckling analysis. Also in this case, from the static analysis the structure under the loading condition remains in the elastic field and has small displacement. Moreover, resonance and buckling will not occur.

Static Analysis				Modal Analysis	Buckling Analysis
$\sigma_{VM} [\text{MPa}]$	$\varepsilon [-]$	$\mathbf{u} [\text{mm}]$	MS [-]	$f_{nat} [\text{Hz}]$	BLF [-]
3.01	2.37×10^{-4}	1.63	37.53	47.25	265.8

Table 17.3: Results of the structural analysis on the entry capsule.

17.3 EDL phase

The high deceleration that acts on the entry capsule during the EDL phase has been considered to verify if the sized structure is a good design. The multi-nodes analysis has been modelled considering the Skycrane, Skipper and Kowalski as a unique concentrated mass. To perform the static analysis, since the capsule is not fixed to anything the inertia relief method is applied. Instead for the buckling analysis the structure has been considered fixed in the top-cone's upper surface. The loading condition is the maximum deceleration 13.6 g, obtained from section 9.3.1, and it acts only along the axial direction. The results are shown in Table 17.4 obtained from the static and buckling analysis. As can be seen, from the static analysis the structure under the loading condition remains in the elastic field and buckling phenomenon will not occur. The strain field are represented in Figure 17.5.

EDL Deceleration	
σ_{VM} [kPa]	1.88
ε [-]	1.26×10^{-7}
BLF [-]	370.22

Table 17.4: Results of the entry capsule under the maximum deceleration arising during the EDL phase.

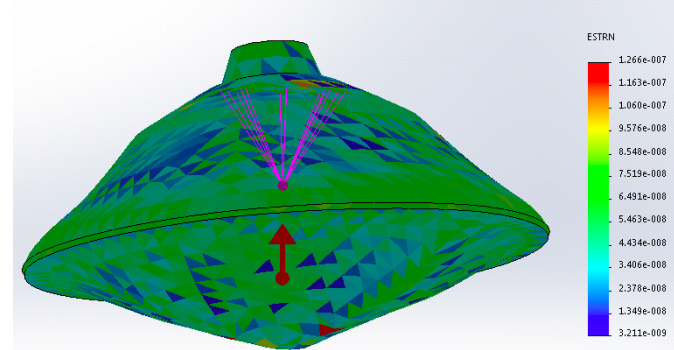


Figure 17.5: Strain field under the maximum deceleration arising during the EDL phase.

17.4 Separations

The various separations, explained in section 16.6, are accounted to verify if the entry capsule could withstand these shock loads with only axial component. In the following are listed the separations considered:

Case I The separation between the cruise stage and entry capsule with a shock load of 32.24 g;

Case II The separation of the heatshield from the backshell with a shock load of 9.26 g.

The multi-nodes results are shown in Table 17.5, based on the same previous model section 17.3. Also in this case the structures can withstand the shock loads since the maximum σ_{WM} is less than the ultimate strength ($\sigma_u = 505$ MPa) and no buckling will occur. In particular the BLF of the Case II is negative meaning that even reversing the direction of the load the buckling will not occur, shown in Figure 17.6.

	Static Analysis		Buckling Analysis
	σ_{VM} [kPa]	ε [-]	BLF [-]
Case I	4.22	3.15×10^{-7}	62.54
Case II	5.01	3.90×10^{-7}	-213.04

Table 17.5: Results for the separation cases.

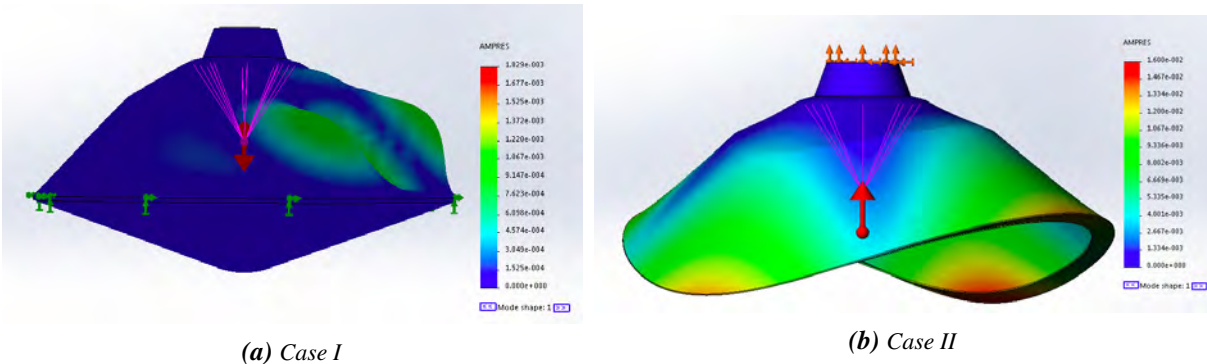


Figure 17.6: Buckling representation for the two cases.

18. Helicopter preliminary design

18.1 Introduction

One of the objective of the MARS-PENGUIN mission is to obtain images of the geysers which are visible just at the beginning of the southern spring. In order to help the rover Skipper to accomplish that goal, it was decided to assist it with an helicopter, Kowalski.

In this chapter a preliminary analysis of the aerial vehicle is conducted. The most relevant aspect analysed is the recharge of batteries with the help of a solar panel since the latitudes and the season in which the helicopter is used can cause some complications. Both for batteries and for solar panel are taken into consideration future developments respect to the ones present in the Mars Helicopter Ingenuity since the MARS-PENGUIN mission will be launched in 2028.

18.2 Power and Energy System

18.2.1 Solar Panel and Batteries

At the MARS-PENGUIN mission latitudes, the elevation of the Sun is low above the horizon, which means that its flux is not sufficient to recharge the batteries of the helicopter. Therefore it was decided to use a vertical solar panel (perpendicular to the ground) attached to the main body, as shown in Figure 18.1. With this configuration, the effective Sun angle will be the zenith angle rather than elevation angle.

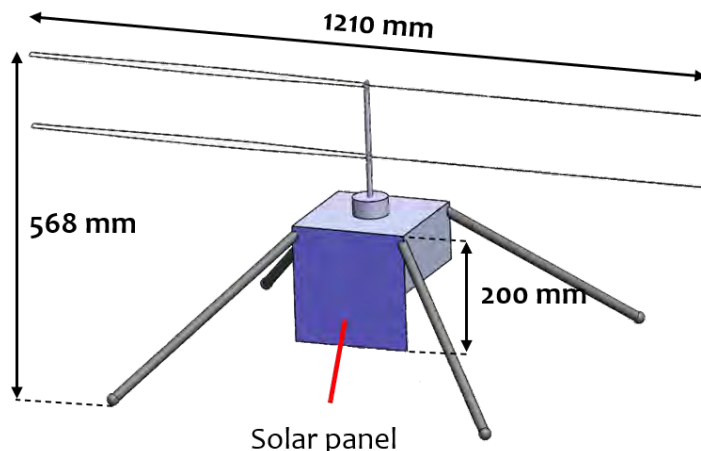


Figure 18.1: The Kowalski helicopter.

For the design of the solar panel is important to take into account also the efficiency. The National Renewable Energy Laboratory(NREL) maintains a chart of the highest confirmed conversion efficiencies for research cells for a range of photovoltaic technologies, plotted from 1976 to the present, from which is possible to suppose that the efficiency of the solar panel used is 37% for the year of the launch.

The Kowalski has 4 Li-Ion batteries with an energy density of 300 Wh/kg, which was supposed knowing the evolution of the batteries through the years. The energy inside them is used to operate the helicopter actuators and avionics during short flights.

18.3 Thermal subsystem

The thermal analysis for the helicopter Kowalsky has been developed starting from a simple three node analysis of the worst hot and cold cases that the aerial vehicle will have to encounter.

The temperature ranges have been highlighted and reported in Table 18.1, from which three nodes have been selected: outside shell, sensors and data processor, batteries .

	Data processor	Battery (Li-ion)	Solar panels	Power unit	Sensors	Shell
Max T [°C]	+50	+45	+130	+50	+50	+90
Min T [°C]	-20	+0	-165	-20	-20	-90

Table 18.1: Temperature ranges for helicopter parts and components

The shell node will be linked to the outside and to the other nodes. The sensors nodes and the batteries node will be linked to each other and to the shell node, but not to the outside. This will mean that the shell will have to withstand the biggest temperature variations, whereas the internal nodes will be protected from the outside conditions, allowing for smaller temperature gradients and variations.

The final architecture found makes use of 2 RHU units. Each of them provides 1 W of heat to the most sensible components of the helicopter. This is paired with a silver paint surface finish: namely Electrodag 503 with $\varepsilon = 0.44$ and $\alpha = 0.37$ which will allow the temperatures to stay within the limits. The degradation of the material has been considered as well, the value of α will increase with time, which will mean the helicopter will heat up more during flight. This factor is mitigated by the fact that flights will be of shorter time spans as the mission goes on, which means the helicopter will not be able to exceed the temperature ranges during flight.

The values of the temperatures of the three nodes are shown in Figure 18.2 and can be seen how they all remain within the given temperature ranges.

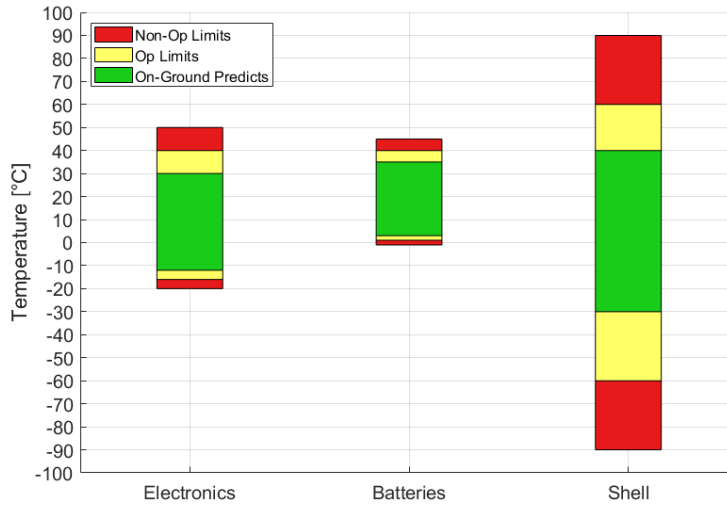


Figure 18.2: Temperatures for the helicopter nodes.

18.4 Communication subsystem

A suitable solution to allow the helicopter communicating with the rover is by means of a lightweight peel-and-stick antenna produced by Octane Wireless (model: AA-350-450). The frequency band of the antenna is 350 to 450 MHz, which is hence suitable for communicating with the Rover's UHF antenna. A near-omnidirectional azimuth radiation pattern is guaranteed, as it can be seen from Figure 18.3.

In correspondence of a 90° off-boresight angle, the RUHF antenna will instead have a gain of 3 dB (see Figure A.13). The main performance parameters are reported in Table 18.2.

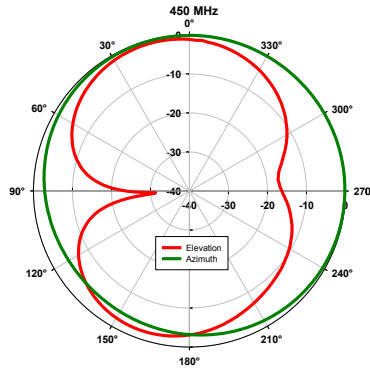


Figure 18.3: Radiation pattern of the helicopter antenna

Input power	8 W
Output power	0.3 W
Amplifier	SSPA
Modulation	BPSK
Link margin	3 dB
Data rate	64 Mbit/s
Range	11.6 km

Table 18.2: Helicopter's communication performance

18.5 Preliminary Design

To start the design, the curve of the solar flux, which arrives at the latitude of the MARS-PENGUIN mission during an entire martian day at the beginning of the southern spring, is found thanks to the MCD software [8]. It is important to state that the flux found corresponds to the diagonal flux and it must be multiplied by the cosine of the elevation of the Sun during the day, which is found with the NASA tool Mars Trek [9]. Doing that, it is possible to find the horizontal flux which impact perpendicularly to the solar panel. The two fluxes are shown in Figure 18.4 and the elevation is shown in Figure 18.5.

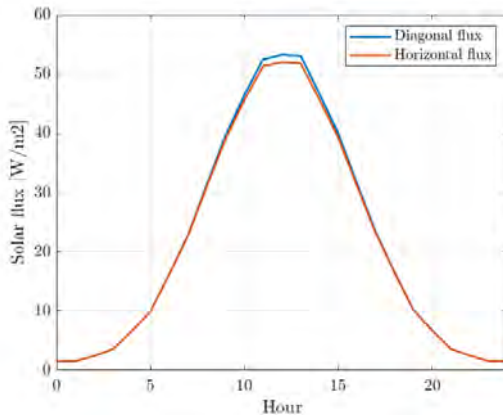


Figure 18.4: Diagonal solar flux and horizontal solar flux arriving at 81°S.

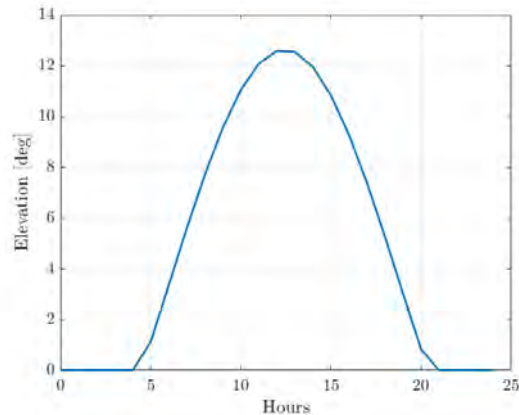


Figure 18.5: Elevation of the Sun at the beginning of the Southern Spring.

To find the total solar energy arriving during the sol, it is computed the area below the curve of the horizontal flux and form that it is calculated the power density of the solar panel, also using the efficiency, which was supposed in subsection 18.2.1.

In order to determine how much big should be the area of the solar panel to recharge the four batteries in one sol, it is necessary to find their amount of power, which is computed using the energy density supposed in subsection 18.2.1, the voltage (4.25 V) and the mass of each battery, assuming it to be 45 g. The value of the area obtained is equal to 0.18 m². Unfortunately a solar panel with such a surface can not be placed vertically attached to the main body of the Kowalski since it would not allow the legs to touch the ground. Because of that, the area of the panel was supposed to be 0.04 m², with which the power produced by the solar panel is 0.31 W.

The consumption of energy is supposed to be due to 2 activities: the flight and the communication with the Skipper. Power for the thermal system is not needed since it is used a RHU, as said in section 18.3. For the flight it assumed that 20% of the power used is at the peak load of 510 W and 80% is at a continuous load of 360 W, instead for telecommunication the power used is 10 W. The evolution of the energy inside the four batteries can be seen in Figure 18.6 for the BoL and in Figure 18.7 for the EoL. The 30% of the BoL is kept as reserve and should be not used if possible.

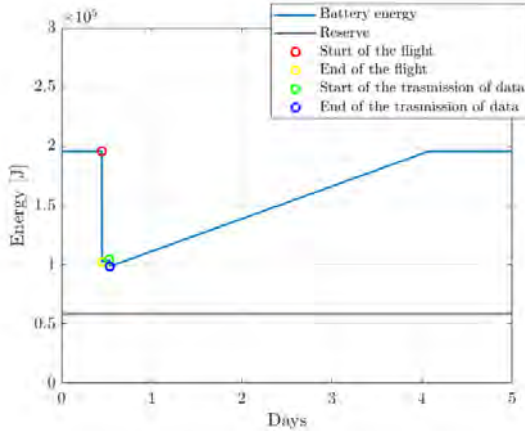


Figure 18.6: Evolution of the energy at the BoL of the batteries.

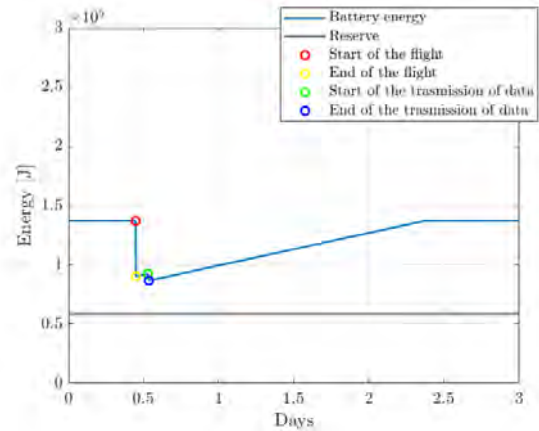


Figure 18.7: Evolution of the energy at the EoL of the batteries.

It is supposed to start the flight at 11 in the morning to not have illuminations problem. The Kowalski can hover or move in every direction for approximately four minutes and then land. It should land with the solar panel facing the Sun to recharge the batteries. After 2 hours the helicopter starts sending information to the rover at 50 Mbps for 10 minutes. The time of flight for the EoL is reduced to 2 minutes in order not to go below the threshold of the reserve. The recharge time varies depending on the energy used for the different activities of the helicopter. The time of flight and the time of transmission of data can be changed according to the requirements. Moreover it is possible to fly or to communicate even if the batteries are not fully recharged, keeping in mind not to consume energy of the reserve. In Figure 18.8, helicopter ConOps are shown.

Further analysis on all the subsystems of the helicopter will be performed.



Figure 18.8: Helicopter ConOps.

19. Project Management

19.1 Introduction

To conclude, in this chapter are reported the final power and mass budgets of the MARS-PENGUIN mission divided by phases, with the margin already included. Then the models to run the tests are discussed and a Risk and Cost analysis is presented. The distribution of the cost during the mission is shown in Figure A.22. In section A.10 are also presented the Gantt chart of the mission and its Work Breakdown Structure and Product Tree.

19.2 Power budget

The power budget of the mission is presented in Figures 19.1 - 19.3. One can notice the elevated Robotics power load at EDL caused by the separation and deployment pyro-devices (evidenced by a star in Figure 19.2). A significant contribution for Skipper is introduced by the drill and locomotion. Skippers total power budget is 370 W including the margin of 12%.



Figure 19.1: Power budget in Cruise.



Figure 19.2: Power budget in EDL.



Figure 19.3: Skipper's Power budget.

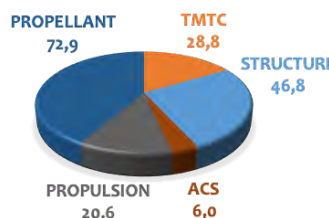
19.3 Mass budget

Based on the analysis performed from all the subsystems a mass budget has been performed for each segment of the mission. The criterion for margins at subsystem level has been reported in the following:

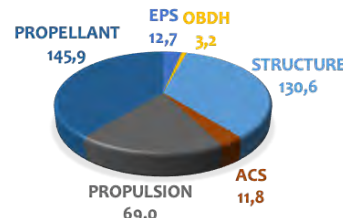
- 20% Margin if the related technology is well known and already space proven;
- 10% Margin if the related technology is not well known and already space proven.

Then 20% margin have been applied to each system, except for the cruise stage since it has been considered as a service module therefore another 20% margin have been applied to the overall system (275.37 kg). Hence, the resulting launch mass is ≈ 1807 kg with an Launch Vehicle Adapter (LVA) of 155 kg. The difference between the launch mass and the maximum P/L mass of the launcher selected, evaluated in section 6.1, is 2743 kg. Hence, the difference is not 20% less than the launcher capability.

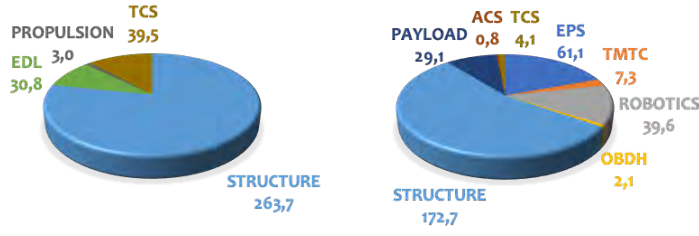
In Figure 19.5 are reported the mass for each segment with margin at subsystem level, instead in Table 19.1 is reported the mass with margin at subsystem and system level.



(a) Cruise Module



(b) Entry Capsule



(c) Sky crane

(d) Skipper

Figure 19.5: Mass division of each subsystem for segment.

Subsystem	Mass w/o Margin [kg]	Margin [kg]	Total Mass [kg]	% of Total [%]
Cruise Module				
ACS	5.4	0.5	6.0	6
Structure	38.8	8	46.8	46
Propulsion	18.7	1.9	20.6	20
TMTC	26.2	2.6	28.8	28
Dry mass	102.2			
Propellant mass			72.9	
Wet mass			175.1	
Entry Capsule				
EDL	28.0	2.8	30.8	9
Structure	219.8	44.0	263.7	78
Propulsion	2.7	0.3	3.0	1
TCS	35.9	3.6	39.5	12
Dry mass	337.0	67.4	404.4	
Skycrane				
ACS	10.8	1.1	11.8	5
EPS	11.5	1.2	12.7	6
OBDH	2.9	0.3	3.2	1
Propulsion	62.7	6.3	69.0	30
Structure	108.8	21.8	130.6	57
Dry mass	227.2			
Propellant mass			145.9	
Wet mass	373.1	45.4	418.5	
Skipper				
ACS	0.7	0.1	0.8	0.2
EPS	55.5	5.6	61.1	19.5
OBDH	1.9	0.2	2.1	0.7
Robotics	33.0	6.6	39.6	12.6
Structure	141.0	31.7	172.7	55.0
TCS	3.4	0.7	4.1	1.3
TMTC	6.6	0.7	7.3	2.3
P/L	29.14			9.3
Dry mass	313.9	62.8	376.6	
Kowalski	1.8	0.4	2.2	

Table 19.1: Division of the mass for each segment.

In the end the variation of the mass margined at system and subsystem level is reported in Figure 19.6 based on the phases of the mission with the timeline.

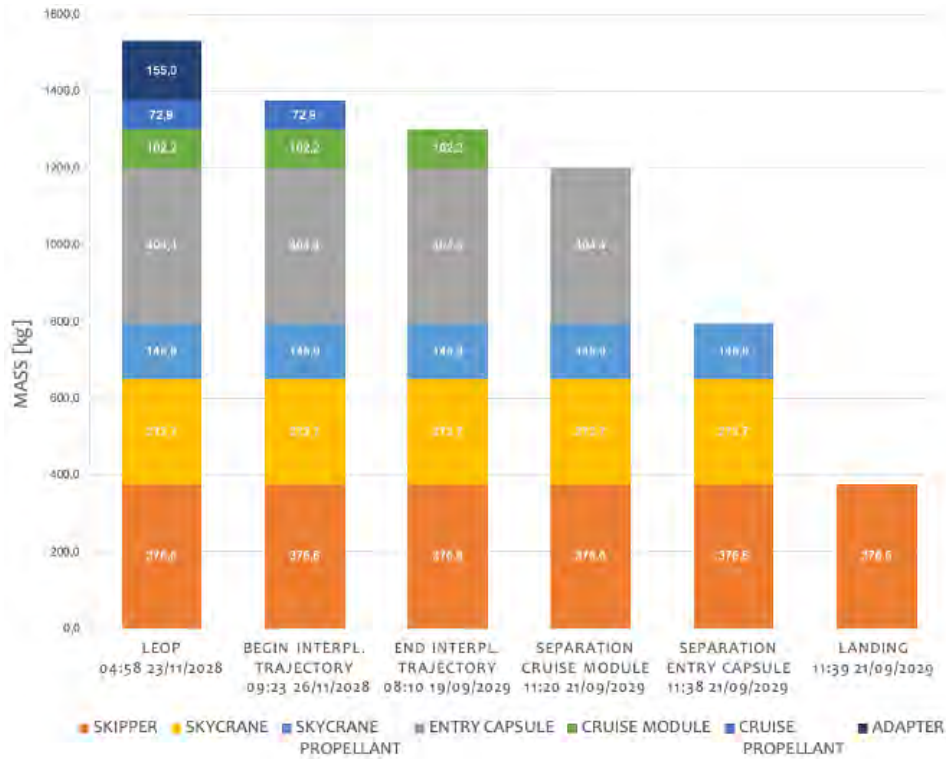


Figure 19.6: Mass variations in relation with the timeline.

19.4 Assembly, Integration, Verification and Test

In this section the AIVT has been analysed. Those operations are supported by different facilities which allow to build and test different components. This process is essential for the accomplishment of the mission since it allows to determine if there are problems in the project and solve them before the launch of the mission. Moreover AIVT is useful to understand the behaviour of the spacecraft during the mission, simulating the possible conditions. The tests are done on different models, even if it brings to an increment of the final cost.

19.4.1 Models and Tests

The model philosophy defines the optimum number and the characteristics of physical models required to achieve confidence in the product verification with the shortest planning and a suitable weighing of costs and risks. It must be defined and frozen in the early phases of the project (A or B).

For this project it has been chosen a prototype philosophy, which is an approach used generally to achieve minimum risk. This choice has been made since the MARS-PENGUIN project can not be recovered or repaired once it is launched and since the requirements of the mission have to be accomplished. A disadvantage of this philosophy is the high cost, since more models are used. On the other hand, the risks are reduced and it is possible to perform parallel activities on different models.

Below in Table 19.2 it is possible to understand which tests have been done with each model.

Model	Physical Properties	Functional & Properties	Humidity	Leak	Pressure	Acceleration	Sinusoidal Vibration	Random Vibration	Acoustic	Shock	Thermal Cycling	EMC/ESD	Life
STM	✓		✓		✓	✓	✓	✓	✓	✓	✓		
EM		✓		✓									✓
QM	✓	✓	✓	✓	✓					✓	✓	✓	
FM	✓	✓		✓	✓			✓	✓	✓	✓	✓	

Table 19.2: Tests done for each model.

The STM, EM and QM models have been used for qualification tests, where it shall be demonstrated that the design, including margins, meets the applicable requirements. Instead the FM model has been used for the acceptance

tests, in which it shall be demonstrated that the product is free of workmanship errors and is ready for subsequent operational use. Also a Development Model has been used in the development areas of new design or where substantial redesign is performed.

Doing tests is not the only way to verify if everything works in the correct way: there is also verification through analysis, in which is performed theoretical or empirical evaluation using techniques agreed with the Customer, **Review-of-design (ROD)**, in which are used approved records or evidence that unambiguously show that the requirement is met, and inspection, in which the verification is done with a visual determination of physical characteristics.

This approach used for equipment tests is not feasible for subsystems. The ones which must be tested are the **TMT**, **EDL** and **TCS** subsystems.

Before the launch, pre-launch tests are performed, which shall verify that no damage or performance degradation of the space vehicle and its constituents has occurred during shipment or handling and mating with the launch vehicle are completed successfully.

19.5 Risk and Cost

In this section, a preliminary analysis of the risk management and of the cost has been done in order to give an idea of the consequences that an unexpected event could happen during the project and of the final cost and how it is divided in each segment.

19.5.1 Risk Management

During the development of a project, it is possible that unforeseen event may occur and, if a recovery plan has not been implemented, it could lead to the end of the mission. Because of that, in every project it is important to prepare a risk analysis in order to know which risks can occur and how to face them.

First of all, the risks must be identified and this could be done with the help of the Risk Database, in which there is an archive of the risks in the previous projects. It provides also information of how to manage those unexpected event.

Then the risk must be evaluated in order to determine the impact that can have on the project schedule. The evaluation has been done using two parameters which are the **Severity Index** and the **Likelihood Index**. The first indicates the risk impact on the performances and the second represents the risk probability. The scores of the two parameters go from 1 to 5 and are defined in section A.10.

Then, with the 2 scores, it is possible to enter in the Risk Matrix, shown in Table 19.3, which gives the Risk Index of the unexpected event. The RI can be divided in 3 areas:

- Green area: it represents a risk which has a low impact on the project
- Yellow area: it represents a risk which has a medium impact on the project
- Red area: it represents a risk which has a high impact on the project

RI	SI				
	1	2	3	4	5
1	1	2	3	4	5
2	2	4	6	8	10
3	3	6	9	12	15
4	4	8	12	16	20
5	5	10	15	20	25

Table 19.3: Risk Matrix

After the evaluation, a risk mitigation plan must be done, in order to bring all the indexes in the Risk Matrix in the green area. This job is tough since could be not easy to find mitigation actions but with the experience acquired in the previous project can be useful to identify potential actions and also team work can be a source of valuable information. Below in Table 19.4, a possible risk for each subsystem in the MARS-PENGUIN project is shown. It is present the description, the RI and the consequences of the unexpected event. Then it is also shown a possible

mitigation action and the RI after the alleviation of the risk. Most of the solutions to reduce the impact on the project correspond to increase the number of tests done, which is possible but it increases the overall cost and the overall duration of the project.

19.5.2 Cost Analysis

In this section, a cost analysis has been performed using the [NASA](#) software Project Cost Estimating Capability, which uses the [Cost Estimating Relationship](#) which is a parametric cost estimating that use sample data set of normalised data of a single product family which are analysed using statistical techniques. This method has some drawbacks and one of them is that the data set is never large enough.

In the [PCEC](#), a preliminary [WBS](#) of the MARS-PENGUIN mission has been inserted and adding the values of the weights of the subsystems and the duration of the phases, it has been possible to estimate a preliminary cost of the project. In the total price are included also the cost of the operations (phase E) and the cost of the launcher. Moreover the cost of the subsystems present in the spacecraft and in the rover Skipper have been found. In [Table 19.5](#) is shown the division of the cost according to the [WBS](#) inserted at the beginning. It can be noticed that the costs of the [RA Soldato](#), of the drill Rico and of the helicopter Kowalski are present but they have been determined from similar components in past missions.

The final cost has been increased of the 10% in order to have reserves which can be used in case of unexpected events.

Risk label	Subsystem	Description	Risk			Risk mitigation	
			LI	SI	RI	Consequences	Action
Miss of the entry point	MA	Major errors in trajectory analysis	1	5	5	The S/C misses the target point. It could either perform a fly-by or hit the planet in another location.	In case of landing to another location the feasibility of the mission could be evaluated
Star tracker failure	ADCS	The attitude information of star tracker is not acceptable	1	1	1	The S/C loses the accurate attitude information	There is considered another star tracker as a backup
Parachute deployment failure	EDL	The motor fails in deploying the parachute	1	5	5	The velocity of the capsule is not reduced enough to have a successful landing	Having an auxiliary parachute deployment system and accurate test of the main deployment system
Engine failure	PS	Failure of more than one of the landing thrusters	1	5	5	Event that could jeopardise the overall mission	Perform more tests
Power amplifier failure	TMT	May be caused by thermal fatigue, excessive vibrations, static electricity stress	2	5	10	Loss of communication capability	Introduce double redundancy of all power amplifiers
Memory/processor corruption	OBDH	Radiation or other events could damage or change the information and elements	3	4	12	The event could cause OBDH failure and jeopardise the overall mission	Introduce OBDH redundancy
Short circuit	EPS	A component could create a short circuit	1	3	3	The event could cause partial EPS failure and damage other components such as sensors or batteries	Implement a short circuit isolation system
Out of bounds temperature	TCS	The temperature of any phase of the mission moves outside of the required temperature boundaries	1	5	5	Loss of the more sensible components such as sensors or batteries	Accurate test of the whole TCS system for each phase of the mission
Drill stuck in the ground	RBT	The drill can get stuck in the ground and cannot be removed	3	5	15	Lack of underground samples for analysis	Accurate test of the drill in different soil and atmospheric conditions
Failed detachment of modules for each segment	STR/CONF	Disruption of the separation mechanisms between each segments	1	5	5	Event that could jeopardise the overall mission	Accurate test during the design phase
Structural failure	STR	Structure of the overall system cannot withstand all environmental conditions which the system will be subjected during its life-cycle	2	5	10	Event that could jeopardise the overall mission	Accurate test during the design phase
Delay of supplier	PM	New supplier does not respect the scheduled delivery	3	4	12	Delay of the whole project, particularly if the delay is in the critical path	Use suppliers which have already been involved in previous projects successfully

Table 19.4: MARS-PENGUIN risk analysis and mitigation action

Element	Cost [M€]
1.0 Project Management	8.89
2.0 System Engineering	38.66
3.0 Safety and Mission Assurance	7.21
4.0 Science/Technology Assurance	11.56
5.0 Payload	183.57
5.01 Payload Management	1.90
5.02 Payload System engineering	8.27
5.03 Payload Product Assurance	1.54
5.04 Rover Skipper	168.24
– Structures	21.76
– Thermal Control	0.76
– EPS	35.24
– ADCS	6.20
– TMTC	18.14
– OBDH	21.15
– RA Soldato	15
– Drill Rico	30
– Helicopter Kowalski	20
5.x Payload I&T	3.62
6.0 Flight System/Spacecraft	212.94
6.01 Flight System PM	4.92
6.02 Flight System System Engineering	21.38
6.03 Flight System Product Assurance	3.99
6.10 Spacecraft	173.28
– Structures & Mechanism	32.51
– Thermal Control	4.55
– Electrical Power & Distribution	31.06
– ADCS	18.43
– Propulsion	5.51
– TMTC	60.07
– OBDH	21.15
6.x Flight System I&T	9.37
7.0 Mission Operation System	138.06
– MOS/GDS Development (Phase B-D)	61.83
– Mission Ops & Data Analysis (Phase E)	76.23
8.0 Launch Vehicle/Services	122.62
9.0 System Integration, Assembly, Test & Checkout	16.95
Total	740.47
Total + 10% of Reserve	814.52

Table 19.5: Division of the total cost of the mission.

20. Conclusion

Designing this mission to the South Pole of Mars has been a challenging but exciting experience, which has required effort and time to be completed.

MARS PENGUIN mission is able to fulfil all the given objectives while providing a very low mass budget and with multiple vehicles interacting and working together.

In particular, high level requirements about departure in late 20s and mission duration of 30 terrestrial months are fulfilled. Also, during the mission lifetime the sampling operations required by the customer will be carried out by a Rover (Skipper) with the support of a small Helicopter (Kowalski). The major concern in the mission design was the uncertain presence of a relay orbiter at the arrival date. Therefore, for this level of design, both MAVEN and MRO have been supposed to serve as a relay, since their end of life is expected to be in the early 30s. MARS-PENGUIN also set the requirements for future Martian orbiters and constellations that could be alternatively used.

The goals to be met for the success of the mission require the implementation of some low TRL technologies, which are expected to be further developed in the upcoming years. The most concerning one is the GNC capabilities for roving, which need to be improved in terms of autonomy and reliability.

To proceed towards phase B there will be some refinement to be performed in the adopted models, such as parachute tumbling in EDL phase. Also, a better characterisation of the customised functions needed for drilling and sampling the peculiar soil at Southern Pole.

Once overcome these criticalities, we are confident that a successful MARS PENGUIN mission will provide significant contributions to the discovery of water resources and eventual extraterrestrial life, paving the road for future Martian settlements.

A. Appendix

A.1 Names selection

The name MARS-PENGUIN, as well as being an acronym for “MARs South Pole ExploratioN and Geysers in-situ INvestigation”, has been chosen in honour of these animals that inhabit the Earth’s south pole, and that now, with our mission, will metaphorically venture to discover the south pole of Mars.

The rover, the helicopter, the drill and the robotic arm of the MARS-PENGUIN mission have been named after the four cool penguins from the movie “Madagascar”, Figure A.1.

Skipper is the leader of the penguins. He devises tactics and gives orders. Calculating, strict, energetic, paranoid, short-tempered and nearly unflappable, Skipper’s raving paranoia and tendency to view even the most ordinary activities as a military operation, combined with his experience in covert ops, has driven him to prepare for nearly any situation, no matter how bizarre or unlikely.

Kowalski acts as the group strategist and gadgeteer. He is a brilliant inventor, but he cannot read (although he does carry around a clipboard upon which he records drawings of their plans). He also tends to over-analyze situations and has created many amazing devices which have put the team in danger.

Rico is the team’s weapons and explosives specialist, who mainly communicates through grunts and squeals, but sometimes he can speak rather normally. Slightly unhinged, Rico swallows useful tools, such as dynamite, and regurgitates them when needed, to the point of regularly regurgitating objects that appear to be too large for him to have swallowed in the first place.

Soldato (italian word for “Private”) is the emotionally sensitive rookie of the group. Though younger and less experienced than the other penguins, he is the most down to earth; Soldato tends to offer simpler, more commonsense solutions in response to Skipper and Kowalski’s complex strategies, often in an understated tone while those strategies are falling apart. He is also a skilled fighter.



Figure A.1: The Penguins of “Madagascar”, in the order from the left side: Soldato, Kowalski, Skipper, Rico.

A.2 Mass statistical estimation

For a preliminary analysis, to define a mass budget, a statistical approach has been implemented for each architecture. The statistical analysis has been performed from current and past missions which were alike to the MARS PENGUIN mission.

In the following has been described the procedure performed to obtain an initial value for the mass of each phase and the overall one. Afterwards the mass breakdown has been reported to show the mass devoted to each subsystem related to each mission phase. The analysis has been based on the architectures obtained from section 4.2 where:

- C - Single Launch, No Orbiter, Rover;
- D - Single Launch, No Orbiter, Hopper.

Dry mass

A regression analysis has been performed by interpolating already existing missions to obtain the dry mass of each phases, shown in Figure A.2. These relate the dry mass with the P/L mass. All the dry mass has been defined starting from its P/L mass that coincide to the wet mass of its subsequent. The launch mass is the sum of the dry mass of the cruise module and the propellant needed to perform the interplanetary trajectory.

Due to the lack of missions with a hopper configuration, its mass has been used together with the rover masses to find the regression rate. Therefore, the dry mass found for the Mars on-ground segment is equal both for the rover and for the hopper, but the safety margin assigned later would not be the same leading to different results.

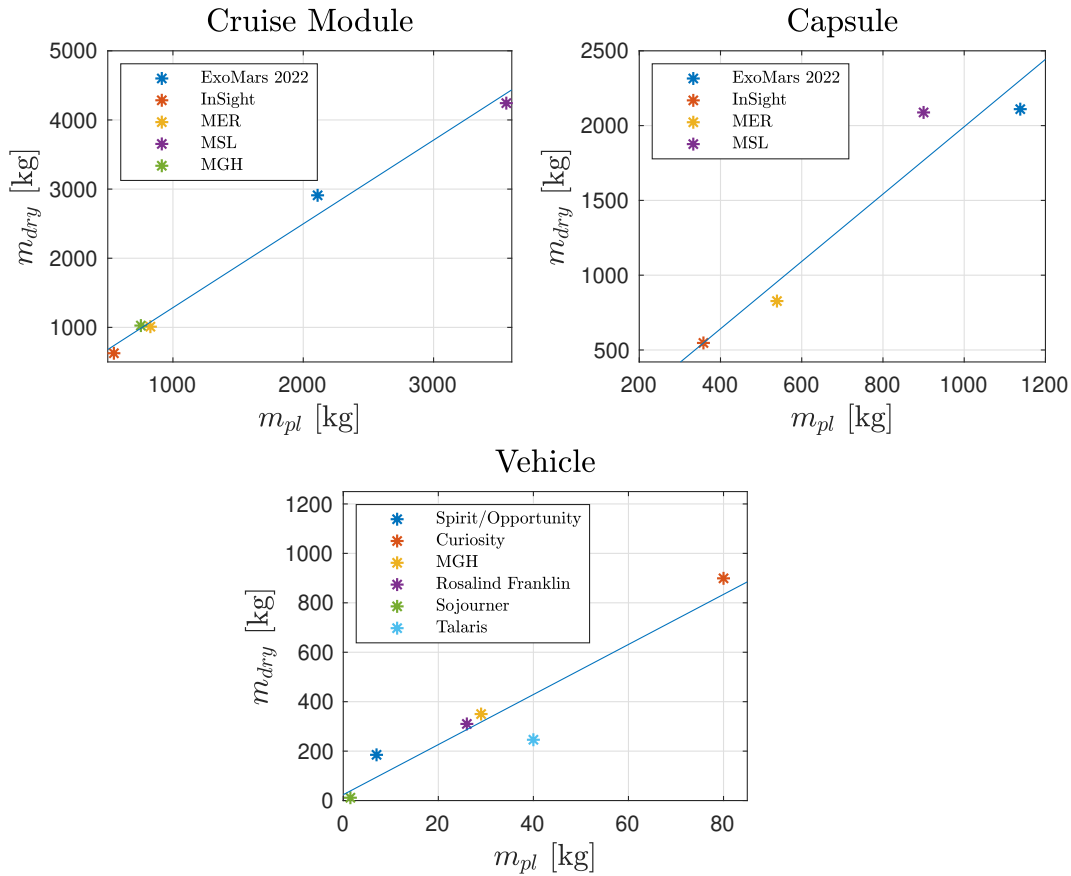


Figure A.2: Regression lines

Wet mass

Since MARS PENGUIN mission shall arrive to Mars, it has been considered as a planetary mission. As a preliminary analysis, for the interplanetary journey it has been considered to use a monopropellant propulsion system. The wet mass has been retrieved from the Tsiolkovsky equation assuming the following values:

- $I_s = 325$ s;
- $\Delta V = 1$ km/s.

The propellant mass during the interplanetary trajectory has been obtained subtracting the dry mass to the wet mass recently found.

Instead the wet mass vehicle of the hopper propellant needed to perform the EDL and the first hop has been already analysed in section 4.2. On the contrary, the rover's EDL has been performed considering the presence of a sky crane since is the heaviest option. Its sky crane has been evaluated based on the known data of the Mars Science Laboratory (MSL).

Mass adapter

The overall system shall be placed inside the launcher with an adapter, the systems that keep the P/L safely attached to their launchers. From the regression rate $m_{adapter} = 0.0755m_{satellite} + 50.252$ retrieved from [54], it is possible to obtain the mass of the adapter knowing the wet mass of the overall system.

Margin

In order to protect the design that has been computed at the preliminary phases, a margin has been applied to each the dry mass determined. In order to evaluate it, the values of the margins are taken from [54]. Since this is still a preliminary analysis, the values have been taken from Conceptual Design Review (CoDR) column and the row has been chosen depending on the dry mass value assumed. For all the architectures the category used to determine the margin is the *next generation S/C* category and the row chosen depends on the dry mass value. Except in the Mars vehicle relative to the hopper the category considered is the *new S/C* because any mission to Mars has had this kind of configuration.

After evaluating all the previous parameters, the total mass has been computed, since it is the sum of the dry mass, margin, propellant mass and the Launch Vehicle Adapter (LVA). The total mass obtained shall be lower than the maximum launchable mass of the launchers examined in order to have a feasible results, this condition is shown in Equation A.1.

$$\text{Dry mass} + \text{Margin} + \text{Propellant} \leq \text{LM} - \text{LVA} \quad (\text{A.1})$$

The previous condition has been satisfied for both the architectures, so the total mass obtained are lower than the launchable mass, that is discussed deeply in section 4.2. In Table A.1 is reported the main results for both architectures.

Architecture	Dry mass [kg]	LVA [kg]	Total mass [kg]
C	1392	207	2281
D	1186	179	1883

Table A.1: Results from the preliminary analysis on the mass.

Phases division

Since the architectures derived does not account for an orbiter, based on the mission phases and timeline analysis ??, three main segments have been identified to perform the overall mission. The configuration considered with their relative phases are listed in the following:

- cruise module from LEOP to separation phases;
- capsule for the Entry, Descent and Landing (EDL);
- vehicle for the ground operations.

Each masses are reported in Table A.2 for the architectures related to the rover and the hopper.

	P/L mass [kg]	Mass [kg]	Margin [kg]	Propellant mass [kg]
Architecture C				
Rover	29.14	323	64	-
Entry Capsule	387	225	45	-
Cruise Module	731	229	45	682
Architecture D				
Hopper	29.14	323	96	221.4
Entry Capsule	419	266	53	-
Cruise Module	540	188	38	518

Table A.2: Division of the masses for the possible architectures.

Comparing the results, the propellant mass on the rover's capsule has not been taken into account since it does not have a propulsive system. Hence it needs an EDL system that at this stage is considered a sky crane since is the heaviest options with a mass of 461 kg, but it will be determined in further analysis. This is taken into account as a contribution in the cruise module's P/L. Instead the hopper's architecture has a propellant mass since to hop needs a propulsive system that has been also used in the EDL phase. Indeed, the amount of propellant for these two modes have been accounted in the hopper propellant mass.

Mass breakdown

By satisfying Equation A.1, it has been possible to proceed with the mass breakdown structure that differs for each segment, as shown in Table A.3.

	EPS [kg]	TMTC [kg]	Structure [kg]	ACS [kg]	TCS [kg]	OBDH [kg]	Propulsion [kg]
Architecture C							
Vehicle	89	18	161	25	54	11	-
Entry Capsule	16	27	111	27	81	8	-
Cruise Module	47	36	104	25	14	8	41
Architecture D							
Vehicle	51	39	101	58	39	23	78
Entry Capsule	13	32	169	-	105	-	-
Cruise Module	38	23	79	20	11	20	34

Table A.3: Mass breakdown for each architectures.

As already said, using the hopper's propulsion for the EDL its capsule is not needed to be an high performance system. So it is supposed not having some subsystem mounted on it.

A.3 ADCS

A.3.1 Disturbances

To find the solar radiation pressure disturbance on the cruise stage, the following formulation is adopted.

$$\bar{F} = -PA(\hat{S}\cdot\hat{N})((1-\rho_s)\hat{S} + (2\rho_s(\hat{S}\cdot\hat{N}) + \frac{2}{3}\rho_d)\hat{N}) \quad (\text{A.2})$$

$$T_{srp} = \bar{r} \times \bar{F} \quad (\text{A.3})$$

in which \bar{S} is the Sun line of sight and \bar{N} is the normal of surface.

The disturbance torques applied on the S/C for a day is shown below.

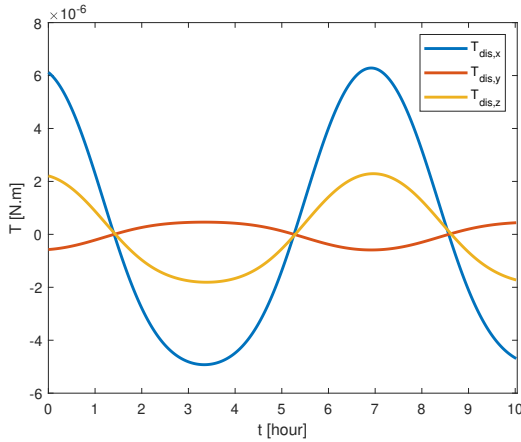


Figure A.3: Disturbance torque applied during few hours

A.3.2 De-tumbling

The behaviour of the S/C during the de-tumbling phase is shown in the following.

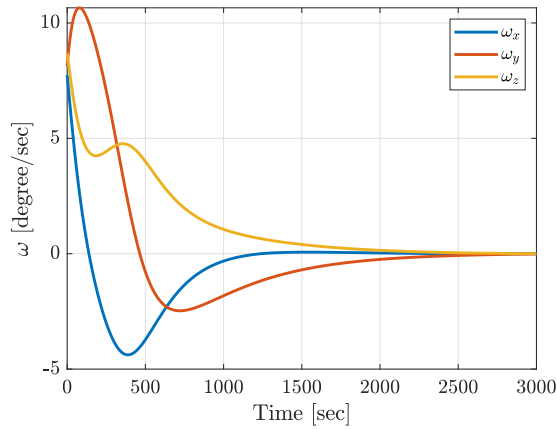


Figure A.4: Angular velocity during the de-tumbling mode

A.4 EDL

A.4.1 Past Missions overview

In Table A.4 are reported the main characteristics of past Mars EDL missions. Some of these values have been used as a starting point for the modelling and also as a crosscheck to verify the quality of the obtained results.

Mission	Viking 1	Viking 2	MPF	MER Spirit	MER Opportunity	Phoenix	MSL Curiosity
Entry velocity [km/s]	4.7	4.7	7.25	5.4	5.5	5.57	5.8
EFPA [deg]	-17	-17	-14.06	-11.49	-11.47	-12.5	-15.2
Ballistic coefficient [kg/m ²]	64	64	63	94	94	70	115
Entry mass [kg]	992	992	584	827	832	600	2800
Entry Attitude Control	3-axis RCS	3-axis RCS	2 RPM passive	2 RPM passive	2 RPM passive	3-axis RCS	3-axis RCS
Lift to Drag ratio	0.18	0.18	0	0	0	0.06	0.22
Heat Shield D [m]	3.5	3.5	2.65	2.65	2.65	2.65	4.5
DGB parachute D [m]	16	16	12.5	14	14	11.5	19.7
Parachute c_D	0.67	0.67	0.4	0.4	0.48	0.67	0.67
Parachute deployment dyn. Pressure [Pa]	350	350	585	725	750	420	750
Parachute deploy Altitude [km]	5.79	5.79	9.4	7.4	7.4	9	10
Touchdown vertical velocity [m/s]	2.4	2.4	12.5	8	5.5	2.4	0.75
Touchdown horizontal velocity [m/s]	<1	<1	<20	11.5	9	<1	<0.5
Landing site MOLA [km]	-3.5	-3.5	-2.5	-1.9	-1.4	-3.5	2

Table A.4: EDL parameters of past missions.

A.4.2 Deceleration profile

In Figure A.5 is reported the deceleration profile of the EDL trajectory where it's possible to see that the peak value reported in subsection 9.3.1 is reached during the entry phase. It is also possible to notice another peak of deceleration due to the effect of the parachute.

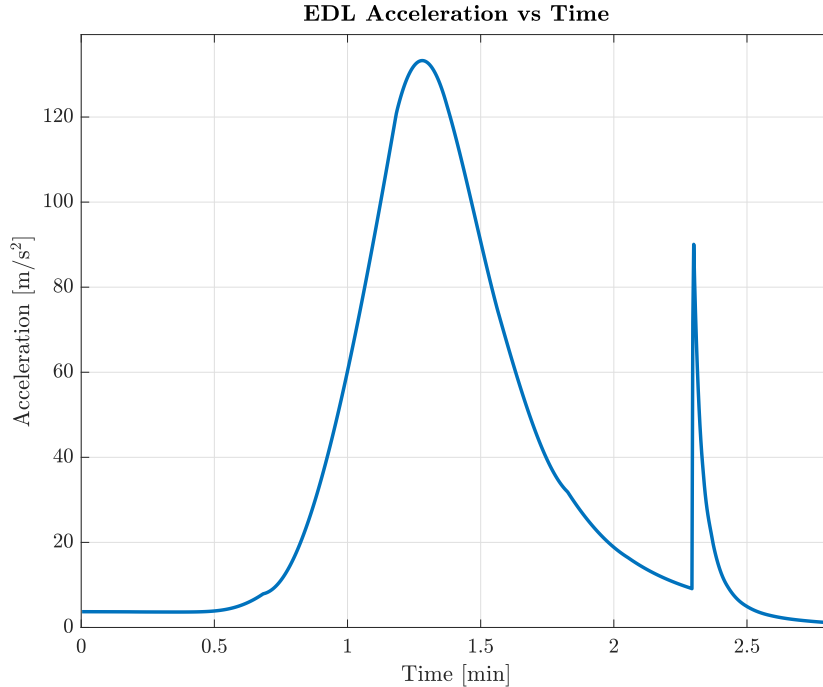


Figure A.5: -12° EFPA deceleration profile

A.4.3 Wind velocity

In Figure A.6 is reported the wind velocity profile at the location and time of the MARS PENGUIN arrival.

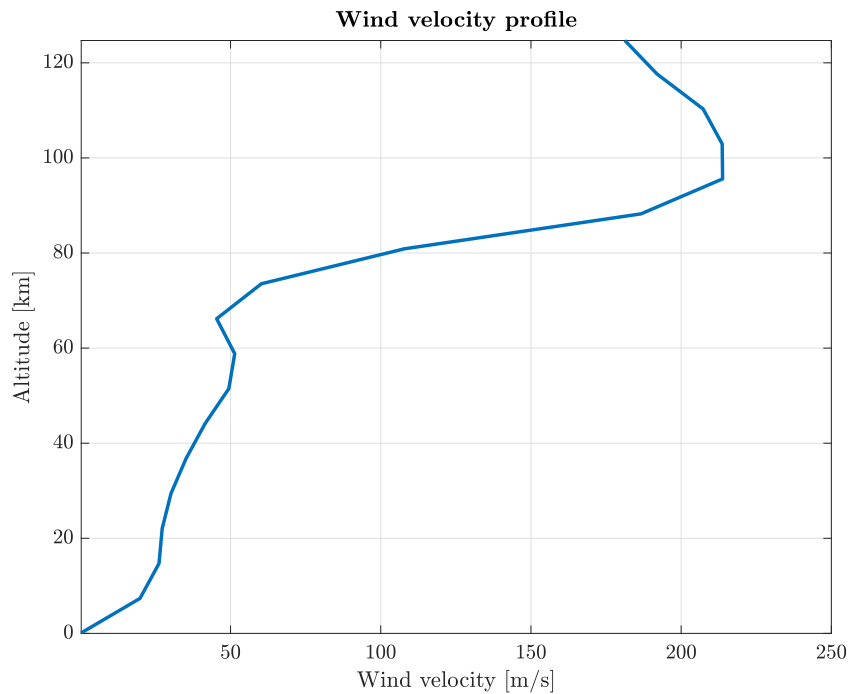


Figure A.6: Wind velocity profile

A.5 Propulsion subsystem architectures

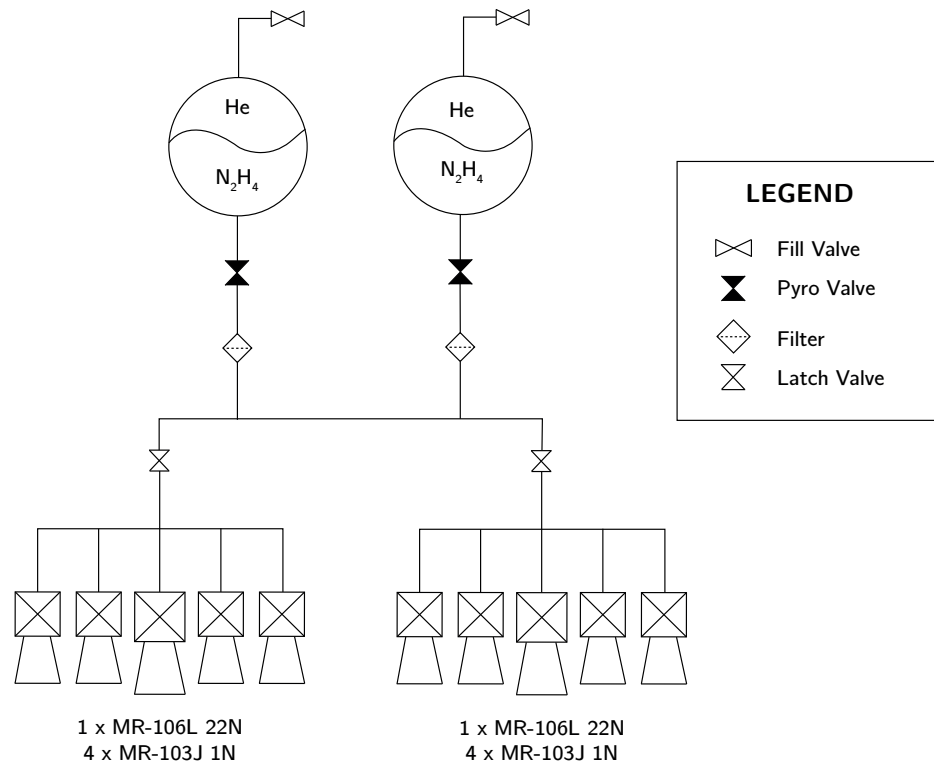


Figure A.7: Cruise propulsion system schematic architecture

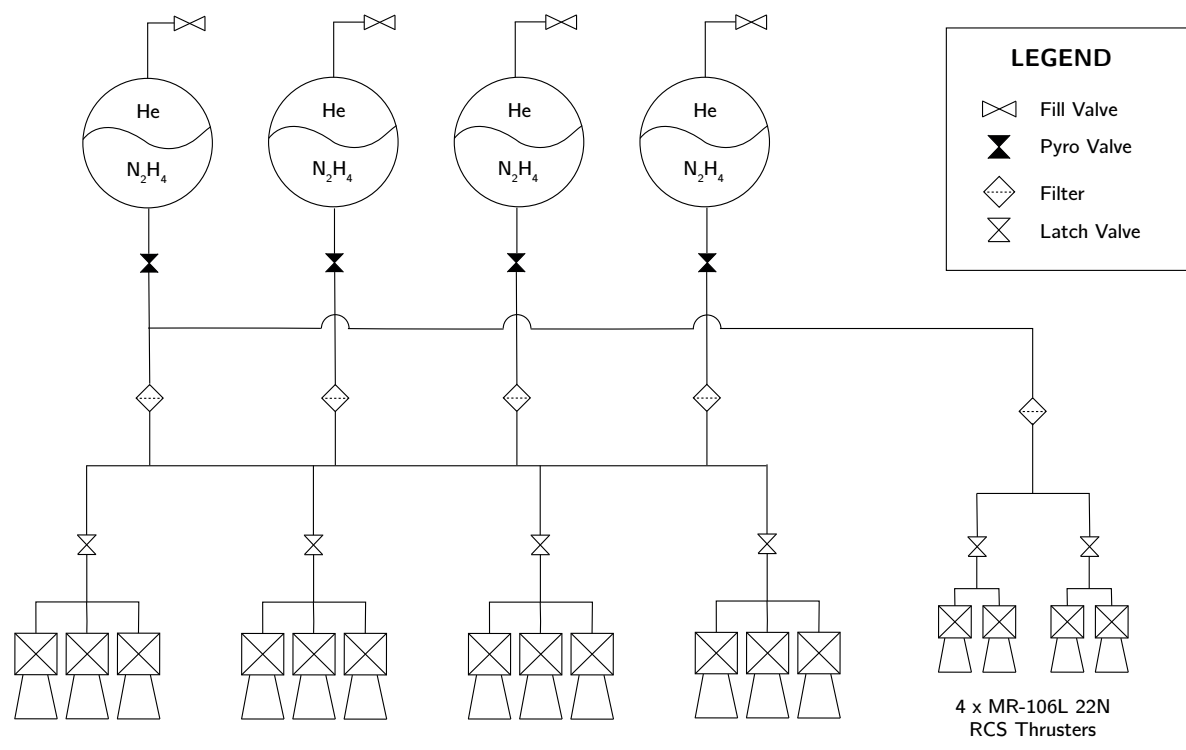


Figure A.8: Landing propulsion system schematic architecture

A.6 TMT**A.6.1 Communication modes**

Modes		Description
COT	Command Transmission mode	Provide guidance and control of the S/C , activate various mission functions or modify the operation of the S/C or its payloads, and counter operational anomalies
STT	Spacecraft Telemetry Transmissions mode	Reports the condition of the S/C systems, its payloads, and provides measured data from S/C instrumentation to a designated Earth station
MTT	Mission Telemetry Transmissions mode	Responsible for the transmission to Earth of scientific and engineering data accumulated through experimentation, active and passive sensing, and computer data generated by S/C and P/L
TRA	Tracking mode	Provide information necessary to determine the location and velocity of the S/C . Necessary also for evaluation of launch and orbit performance, for trajectory corrections, for determining the precise timing for critical manoeuvres and forecasting S/C visibility and antenna pointing angles required by S/C and Earth stations.
OWU	One-Way Unreliable mode	Transmit telemetry from the entry module during EDL , in unreliable mode (i.e. absence of any handshaking protocol). This ensures a continuous data flow, thus preventing data buildups caused by a link dropout.
SAF	Safe mode	Provide low rate telemetry transmission, upon automatic detection of pre-defined off-nominal conditions, that may indicate loss of control or damage to the S/C .

*Table A.5: Communication modes***A.6.2 State of the art & available facilities****Space Segment**

The main characteristics of the currently operating Mars orbiters can be found in [84] and are summarised in Table A.6.

It can be observed that all the orbiters are placed in high-latitude or near-polar orbits and communicate with Earth stations using X-band carriers for the deep space links. Both **Solid-State Power Amplifiers** and **Traveling-Wave Tube Amplifiers** are used for communication with Earth, which never exceed 100 W of output power.

The proximity link makes always use of **UHF** transceivers, typically connected to a quadrifilar helix antenna. In particular, since the launch of MRO, the Electra UHF transceiver has been established as a communication standard for Mars proximity links, both for NASA and ESA missions. Electra features enhanced performance and also new capabilities, relative to prior proximity link radios, among which [85]:

- higher and variable data rates, in all powers of two, up to 128 kb/s for the forward link (space-to-Mars) and up to 2048 kb/s for the return link (Mars-to-space);
- adaptive data rate: the transceiver monitors in real-time the **Signal-to-Noise Ratio (SNR)** and decides whether to increase or decrease the data rate, so as to maximise the data return on a given relay pass;
- frequency agility: capability to operate in a range of carrier frequencies (forward link: 435-450 MHz; return link: 390-405 MHz).

A. Appendix

MARS-PENGUIN

	Mars Odyssey (NASA)	Mars Express (ESA)	MRO (NASA)	MAVEN (NASA)	TGO (ESA)
Launch	2001	2003	2005	2013	2016
Orbit	400×400 km $i = 93^\circ$ SS	330×10530 km $i = 86.9^\circ$ Non SS	255×320 km $i = 93^\circ$ SS	150×6200 km $i = 75^\circ$ Non SS	400×400 km $i = 74^\circ$ Non SS
Deep space link					
Band	X-band	X-band	X-band	X-band	X-band
Power amplifier	15 W SSPA	65 W TWTA	100 W TWTA	100 W SSPA	65 W TWTA
Antenna	1.3 m HGA	1.65 m HGA	3 m HGA	2 m HGA	2.2 m HGA
Proximity link					
Transceiver	CE-505	Melacom	Electra	Electra	Electra
Protocol	CCSDS Proximity-1	CCSDS Proximity-1	CCSDS Proximity-1	CCSDS Proximity-1	CCSDS Proximity-1
Antenna	Quadrifilar helix	2 Patch antennas	Quadrifilar helix	Quadrifilar helix	Quadrifilar helix
Forward link					
Frequency	437.1 Mhz	437.1 Mhz	435-450 MHz	435-450 MHz	437.1 MHz
Data rate	8, 32 kb/s	8 kb/s	8, 32, 128 kb/s	8, 32, 128 kb/s	8, 32, 64 kb/s
Coding	Uncoded	Uncoded	$(7, \frac{1}{2})$ Convolutional	$(7, \frac{1}{2})$ Convolutional	Uncoded
Return link					
Frequency	401.585625	401.585625	390-405 MHz	390-405 MHz	401.585625
Data rate	8, 32, 128, 256 kb/s	2, 4, ..., 128 kb/s	1, 2, 4, ..., 2048 kb/s	1, 2, 4, ..., 2048 kb/s	8, 16, ..., 1024 kb/s
Coding	$(7, \frac{1}{2})$ Convolutional	$(7, \frac{1}{2})$ Convolutional	$(7, \frac{1}{2})$ Convolutional	$(7, \frac{1}{2})$ Convolutional (LDPC)	$(7, \frac{1}{2})$ Convolutional

Table A.6: Key characteristics of the current Mars relay network

Ground segment

Both ESA and NASA own antenna networks characterised by giant parabolic reflectors, aimed at providing uplink/downlink capabilities and S/C tracking⁽¹⁾ for deep space missions. Both networks consist of 3 ground stations, that are about 120° apart in longitude, to provide continuous coverage as Earth rotates.

The main performance characteristics of the ESTRACK's European Deep Space Antenna (DSA) network can be found in an excerpt of the official handbook provided in [86] and are summarised in Table A.7. All three antennas have the same size and are characterised by very similar performance in terms of EIRP, figure of merit (G/T), beamwidth and data rate. The main difference lies in the fact that the oldest station (DSA1) supports S/X-band for both downlink and uplink, while the newer DSA2, DSA3 abandoned S-band in favour of Ka-band. The latter is expected to become in a few years the new deep space communication standard. Indeed, although Ka band is characterised by higher attenuation levels, it allows the transmission/reception at much higher data rates compared to its predecessor (i.e. X-band).

	DSA1 - New Norcia (S,X / S,X)	DSA2 - Cebreros (X / X, Ka)	DSA3 - Malargüe (X, Ka / X, Ka)
Latitude	-31.0482254°	40.4526901°	-35.7760086°
Longitude	116.1914978°	-4.3675499°	-69.3981934°
Altitude [m]	794.095	1550.00	252.2558
Antenna diameter [m]	35	35	35

⁽¹⁾which is carried out by means of Δ -DOR tracking campaigns

Supported frequency bands [MHz]	up: S (2025-2120), X (7145-7235)	up: X (7145-7235)	up: X (7145-7235), Ka (34200-34700)
	down: S (2200-2300), X (8400-8500)	down: X (8400-8500), Ka (31800-32300)	down: X (8400-8500), Ka (31800-32300)
TX beamwidth [deg]	S: 0.3 X: 0.074	X: 0.074	X: 0.074 Ka: NA
RX beamwidth [deg]	S: 0.28 X: 0.064	X: 0.064 Ka: 0.017	X: 0.064 Ka: 0.017
Polarization (same for up/down)	S: RHC, LHC X: RHC, LHC	X: RHC, LHC Ka: RHC, LHC	X: RHC, LHC, linear Ka: RHC, LHC
Modulation schemes	TTCP compliant	TTCP compliant	TTCP compliant
Uplink			
S-band EIRP [dBm]	127.8 (SHPA) 112.1 (SSPA)	-	-
X-band EIRP [dBm]	138 (XHPA) 128 (XLPA)	138 (XHPA) 128 (XLPA) 122 (XSPA)	138 (XHPA) 128 (XLPA) 122 (XSPA)
Ka-band EIRP [dBm]	-	-	131 (KaHPA)
Subcarrier freq. [kHz]	8 or 16	8 or 16	8 or 16
TC data rates [kb/s]	Remnant carrier: 4 SPL mode: 256	Remnant carrier: 4 SPL mode: 256	Remnant carrier: 4 SPL mode: 256
Downlink			
S-band G/T [dB/K]	37.5	-	-
X-band G/T [dB/K]	50.1	50.8 (at 10° elevation)	50.8 (at 10° elevation)
Ka-band G/T [dB/K]	-	55.8 (at 10° elevation)	55.7 (at 10° elevation)
TC data rates [Mb/s]	1.2 (RCD) 8 (SCD) 16 (GMD)	1.2 (RCD) 8 (SCD) 16 (GMD)	1.2 (RCD) 8 (SCD) 16 (GMD)
Supported coding	R-S, Convolutional, Concatenated, Turbo	R-S, Convolutional, Concatenated, Turbo	R-S, Convolutional, Concatenated, Turbo

Table A.7: Performance characteristics of the ESTRACK deep space ground stations

A.6.3 Earth's atmospheric attenuation (ITU models)

The total atmospheric attenuation has been modeled as the combination of 4 main components.

1. Gaseous attenuation due to water vapour and oxygen.

The approximate method valid in the range 1 to 350 GHz and provided in [87] has been implemented. This was done in combination with:

- a model of the mean annual global reference atmosphere given in [88], for estimating the local T and p values
- maps of ρ at Earth surface vs. exceedance probability, that can be found in [89].

2. Attenuation due to rain.

The model employed is valid for frequencies up to 55 GHz and is described in [47]. This was done in

combination with:

- a map of the mean annual rain height, provided in [90]
- a map of the mean annual rainfall rate exceeded for 0.01% of an average year, provided in [91].

Since in our case the exceedance probability considered is $p = 1$ (i.e. 1%), the corresponding attenuation may be extrapolated as

$$A_p = A_{0.01} \left(\frac{p}{0.01} \right)^{[-0.655 + 0.033 \ln(p) - 0.045 \ln(A_{0.01}) - \beta(1-p) \sin \theta]}$$

where

$$\beta = \begin{cases} 0 & \text{if } p \geq 1\% \text{ or } |\phi| \geq 36^\circ \\ -0.005(|\phi| - 36^\circ) & \text{if } p < 1\%, |\phi| < 36^\circ, \theta \geq 25^\circ \\ -0.005(|\phi| - 36^\circ) + 1.8 - 4.25 \sin \theta & \text{otherwise} \end{cases}$$

3. Attenuation due to clouds.

A model based on Rayleigh's approximation has been implemented, which is used in combination with a digital map of the cloud liquid water content [92].

4. Attenuation due to tropospheric scintillation.

The related fading is modeled according to [47].

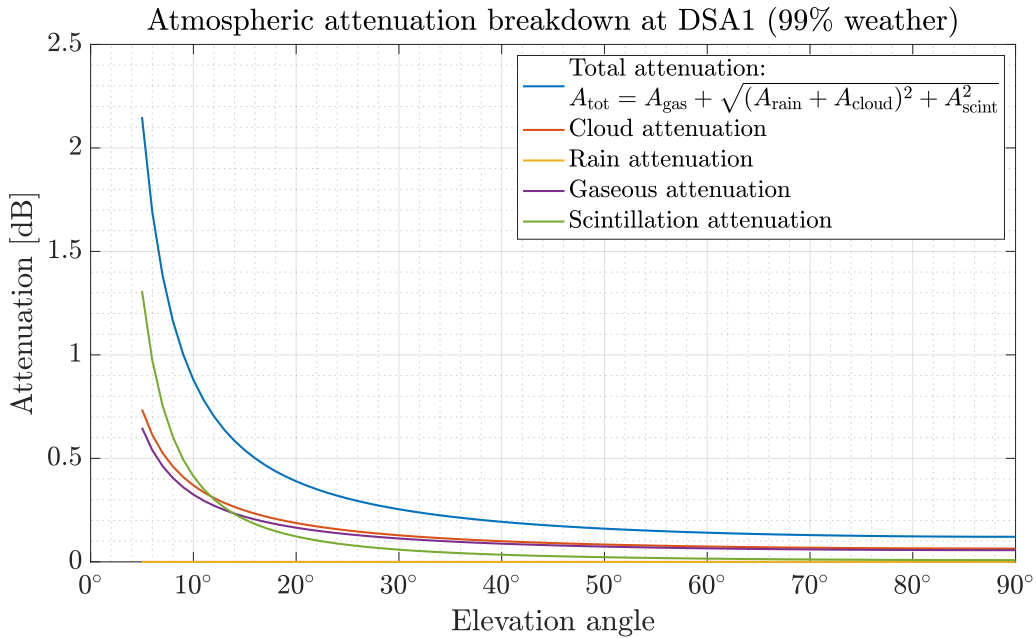


Figure A.9: Atmospheric attenuation components: gaseous, rain, clouds, scintillation

Considering for instance the New Norcia GS, we may compare from Figure A.9 the magnitude of the four attenuation components: in our case, rain attenuation turns out to be negligible. This is thanks to the favourable dry climate of the selected sites, while in equatorial regions the top 1% rain attenuation might be as high as 1.92 dB according to our model.

A.6.4 Safe mode communication

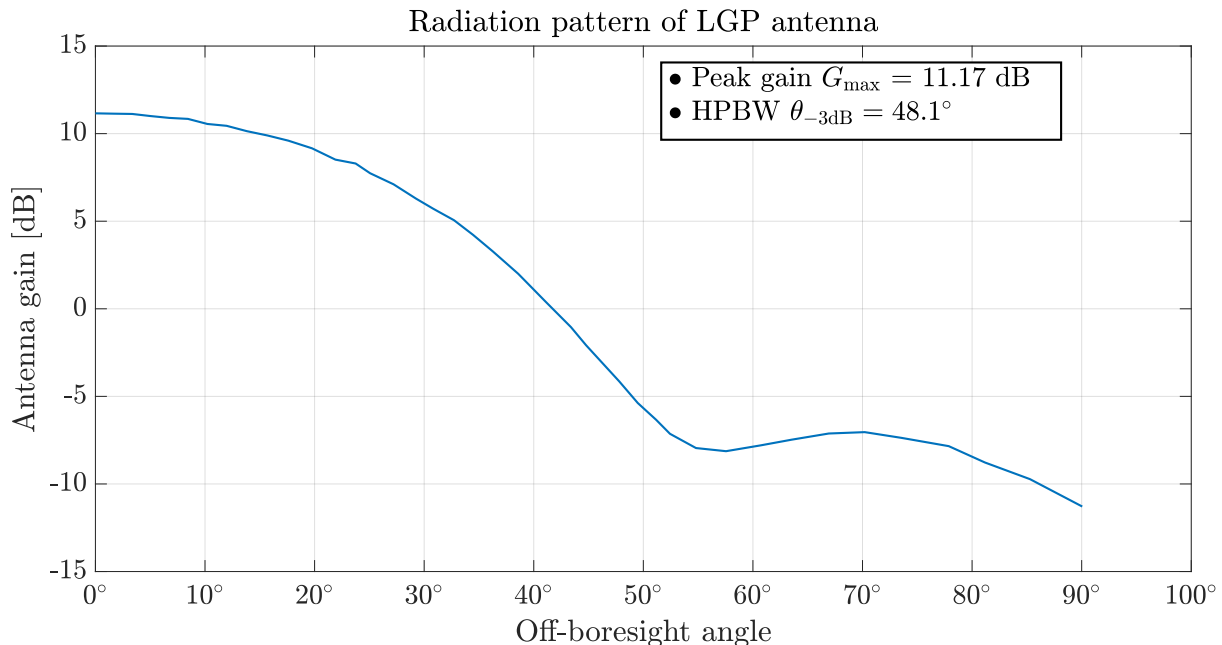


Figure A.10: Radiation pattern of the LGP

A.6.5 EDL

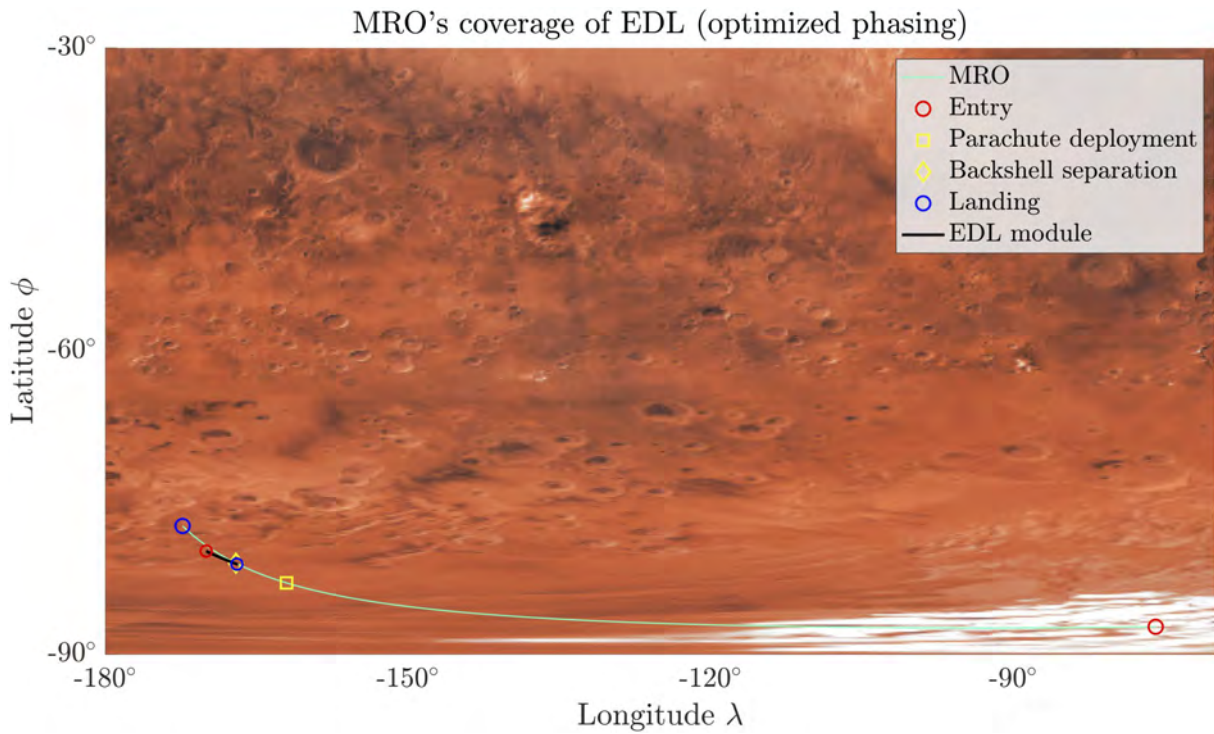
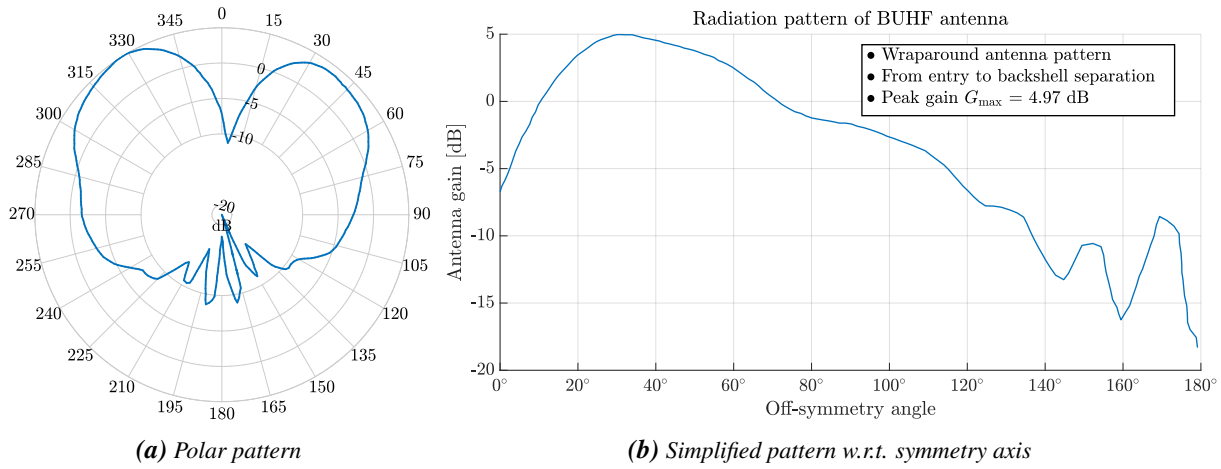
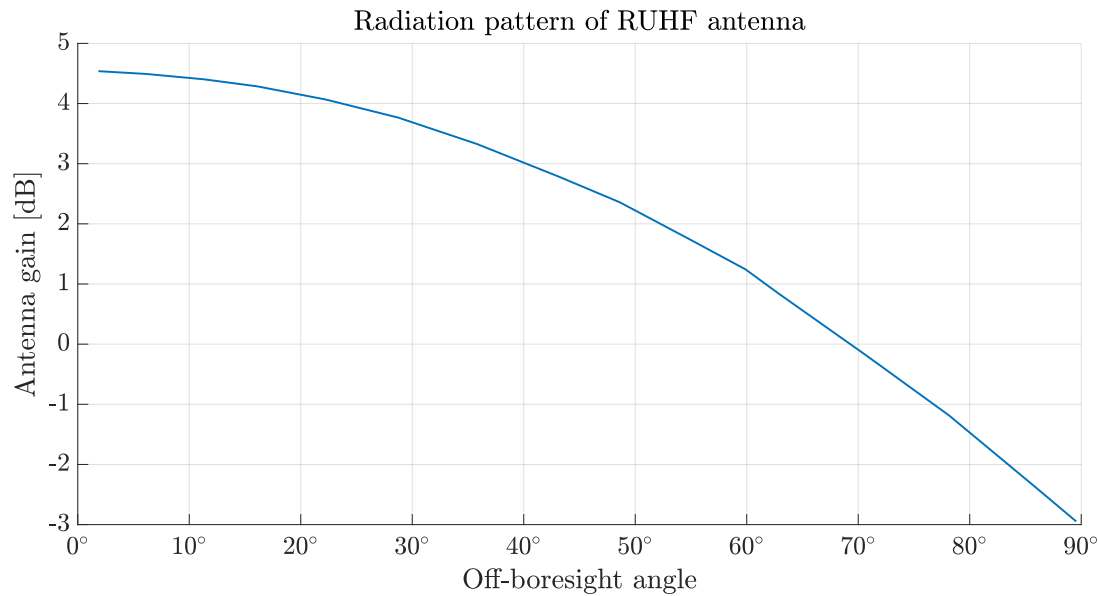


Figure A.11: MRO coverage in correspondence of the optimal phasing

A.6.6 Surface operations

Radiation pattern of BUHF

**Figure A.12:** Radiation pattern of the BUHF antenna**Figure A.13:** RUHF antenna pattern

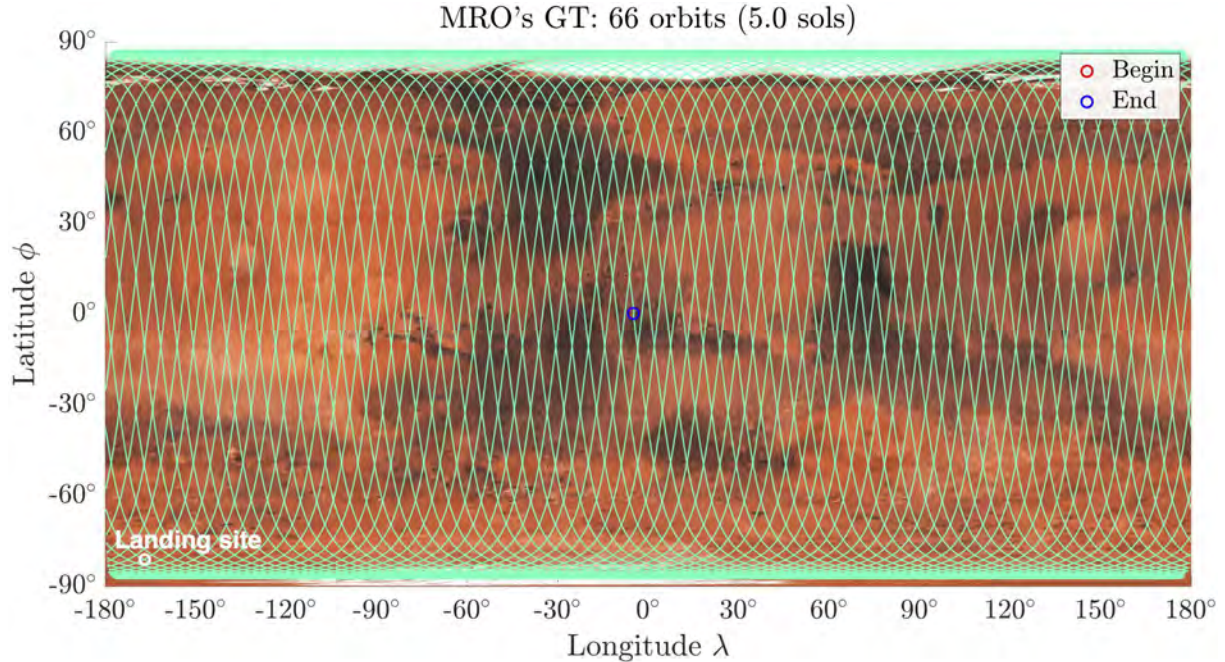


Figure A.14: MRO's ground track over 66 orbits

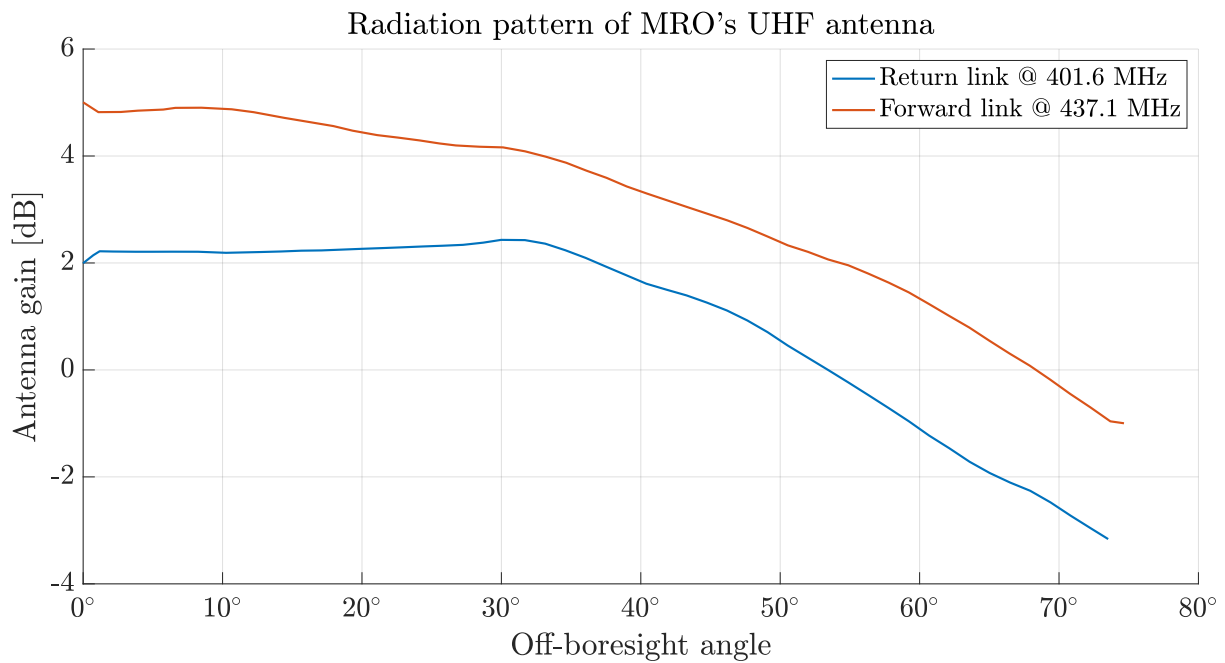


Figure A.15: OUHF radiation pattern

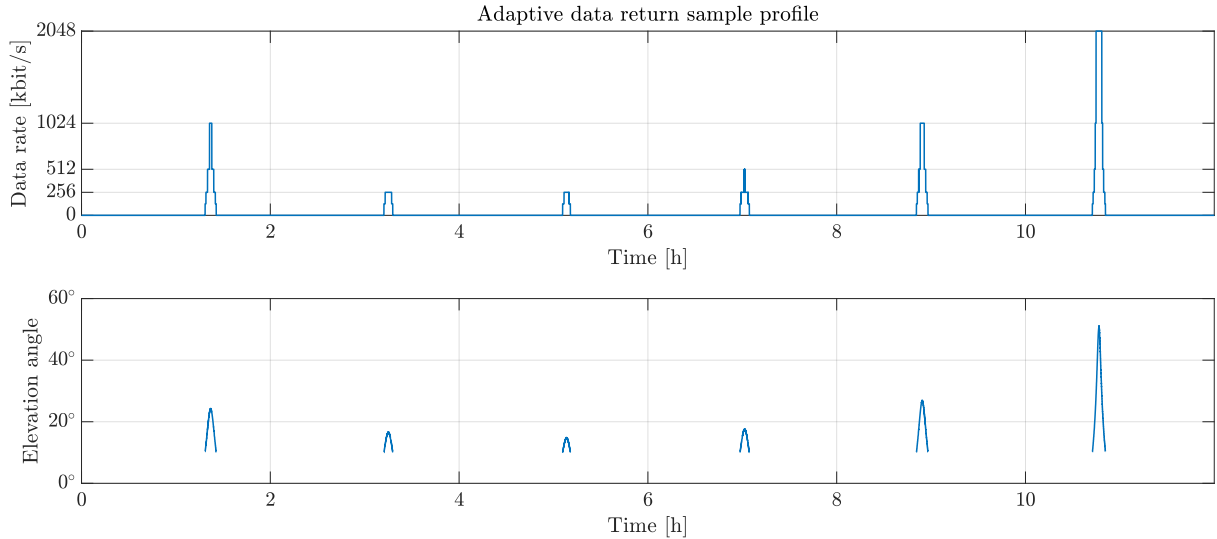


Figure A.16: Data return profile during 6 consecutive orbiter passes

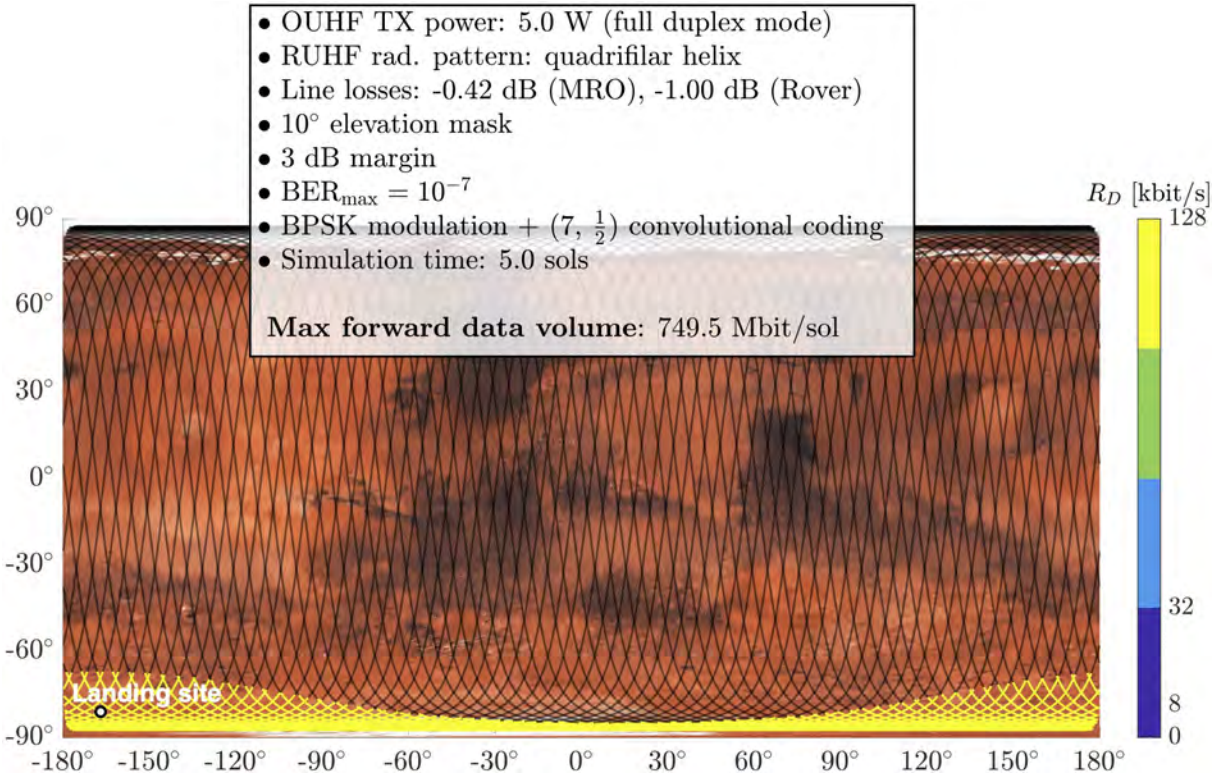


Figure A.17: Forward link performance depending on orbiter pass

The results in Figure A.17 are actually trivial since the maximum data rate of 128 kbit/s is always guaranteed. In addition, the theoretical forward data volume achievable is an order of magnitude larger than the memory allocation onboard MRO, which allows it to store and forward only up to 30 Mbit/sol of data to all landed elements on the Martian surface. Even assuming to exploit the whole single best pass we would end up with a 65.7 Mbit/sol budget.

A.7 Robotics

A.7.1 Skipper Locomotion system

The soil compaction resistance can be described by Equation A.4.

$$R_C = \frac{\left(\frac{3W_w \cos \theta}{\sqrt{d}} \right)^{\frac{2n+2}{2n+1}}}{(3-n)^{\frac{2n+2}{2n+1}} (n+1) (k_c + w k_\phi)^{\frac{1}{2n+1}}} \quad (\text{A.4})$$

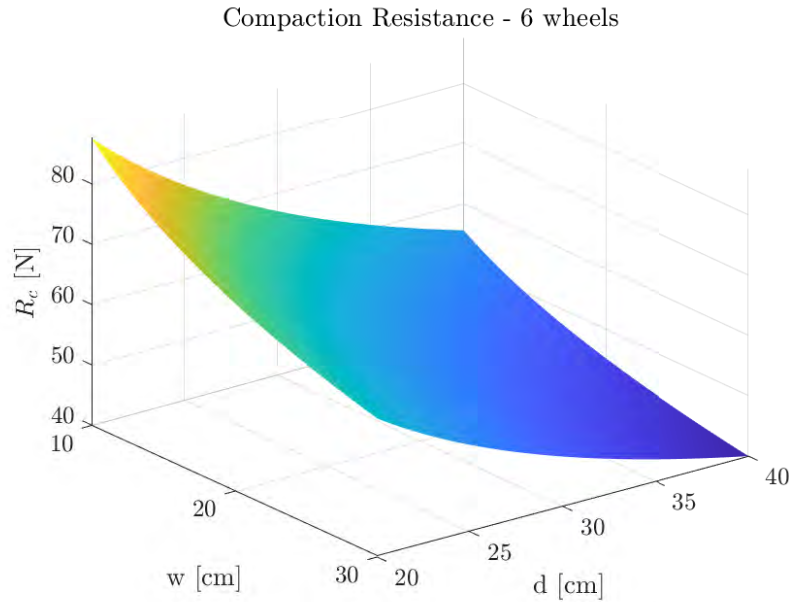


Figure A.18: Compaction Resistance R_c for a 6 rigid wheels configuration as a function of wheel diameter and tire width.

Rolling resistance is the product between the rolling resistance coefficient f_r and the wheel load, Equation A.5. The worst case has been considered using $f_r = 0.4$, typical value for dry sand.

$$R_R = f_r W_w \quad (\text{A.5})$$

Gravitational resistance is computed by means of Equation A.6.

$$R_G = W_w \sin \theta \quad (\text{A.6})$$

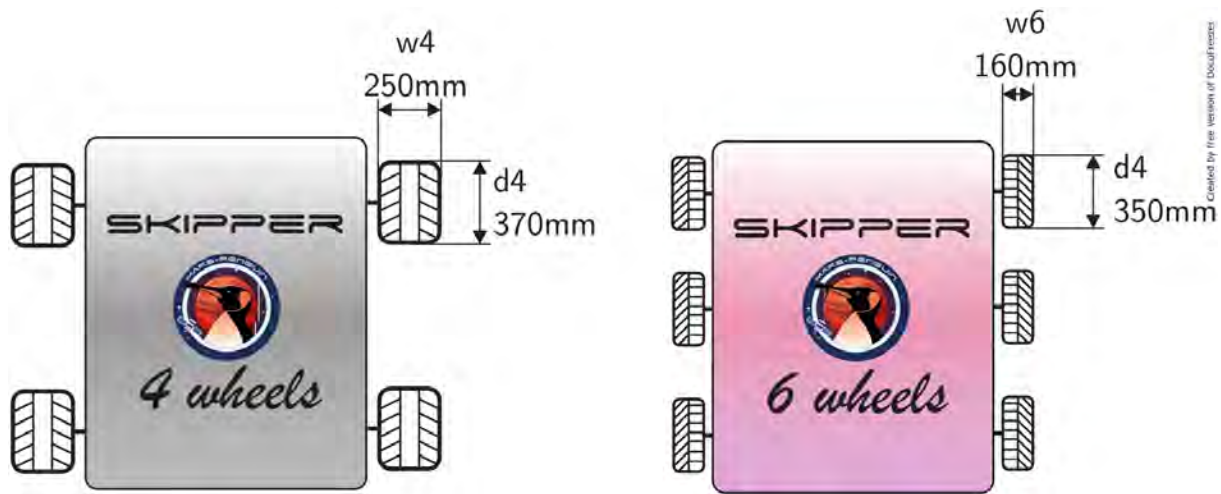


Figure A.19: Skipper configurations with 4 and 6 wheels.

Chassis

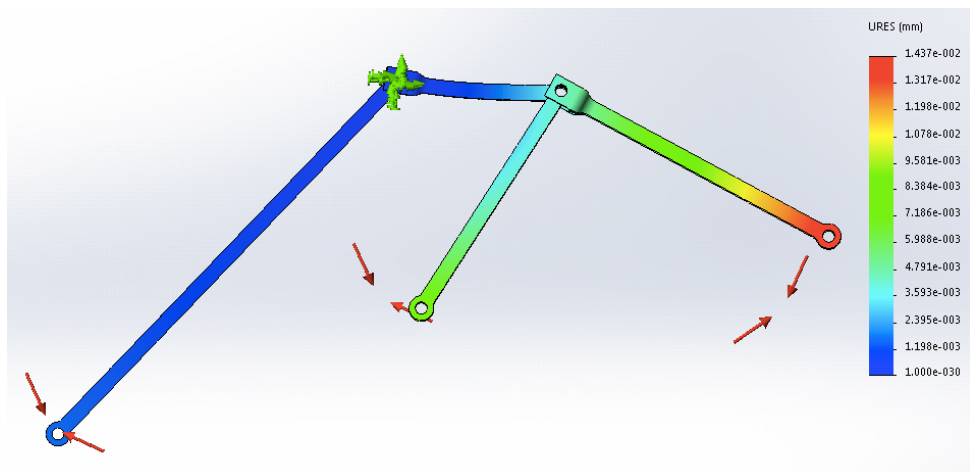


Figure A.20: Displacement field of one side of the rocker-bogie suspension obtained from static analysis.

A.8 Configuration

A.8.1 Bridles Spool Mechanism

In Figure A.21, unroll mechanism for the bridles, that was mentioned in section 16.6, is reported. The four bridles will be rolled up on a spool equipped with a braking system, that will allow the rover to be slowly delivered to the ground from the sky crane.

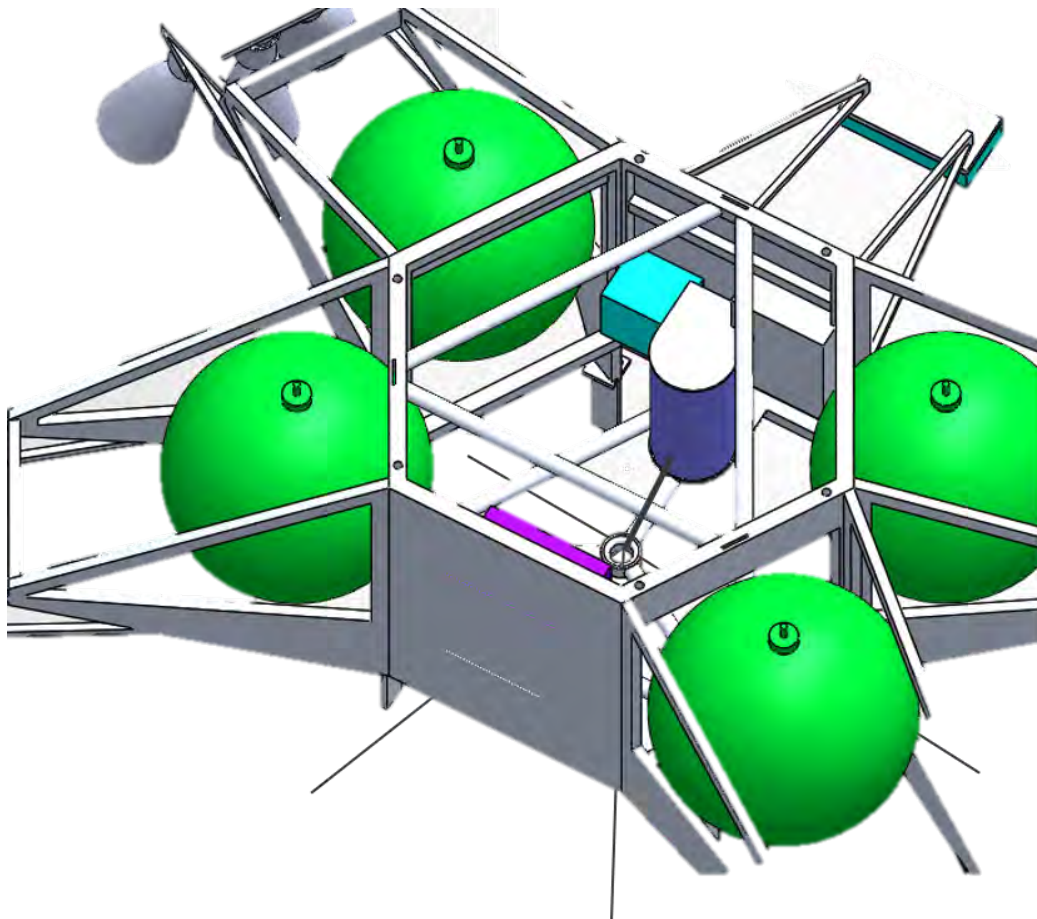


Figure A.21: Bridles unroll mechanism.

A.9 Structure

A.9.1 Materials selected

In Table A.8 are reported the main properties for the two materials used for section 17.2.2 and section 17.2.3.

	Mass Density [kg/m ³]	Modulus of Elasticity [GPa]	Yield Strength [MPa]
Aluminium Alloy (AL7075-T6)	2810	72	505
Aluminium Honeycomb (HexWeb CRIII 5052)	281.5	11.5	435

Table A.8: Properties of the material used for the multinodes analysis.

A.10 Project Management

In Table A.10 and Table A.11 is shown how to give a score to the Severity Index and Likelihood Index, which are combined in order to determine the gravity of the risk, as explained in subsection 19.5.1.

Score	Severity	Cost	Schedule	Technical	Science
5	Catastrophic	Increment of estimated cost results in mission cancellation	Delay results in mission cancellation	Problem leading to malfunction of the whole system	Problem leading to impossibility to obtain scientific data
4	Critical	Critical increment of estimated cost (>10%)	Critical launch delay: 4 years	Problem which has critical effects on some subsystems	Problem leading to critical reduction of scientific data obtained (5%-25% of data obtained)
3	Major	Major increment of estimated cost (<10%)	Major launch delay: 2 years	Problem which has major effects on some subsystems	Problem leading to major reduction of scientific data obtained (25%-65% of data obtained)
2	Significant	Significant increment of estimated cost (<5%)	Significant launch delay: few weeks	Problem which has significant effects on one or more subsystems	Problem leading to significant reduction of scientific data obtained (65%-95% of data obtained)
1	Negligible	Negligible increment of estimated cost (<2%)	Negligible launch delay: few days	Problem which has negligible effects on one of the subsystems performances	Problem leading to negligible reduction of scientific data obtained (95%-99% of data obtained)

Table A.10: Severity Index categorisation.

Score	Likelihood	Likelihood of occurrence
5	Maximum	Certain to occur, will occur one or more times per project
4	High	Will occur frequently, about 1 in 10 projects
3	Medium	Will occur sometimes, about 1 in 100 projects
2	Low	Will seldom occur, about 1 in 1000 projects
1	Minimum	Will almost never occur, 1 of 10 000 or more projects

Table A.11: Likelihood Index categorisation.

In Figure A.22 is presented the S-curve of the cost of the total cost of the MARS-PENGUIN mission, reported in subsection 19.5.2. The curve has been determined using the analytical cost spreading method, which was developed by Wynholds and Skratt and which approximates the experience of actual programs.

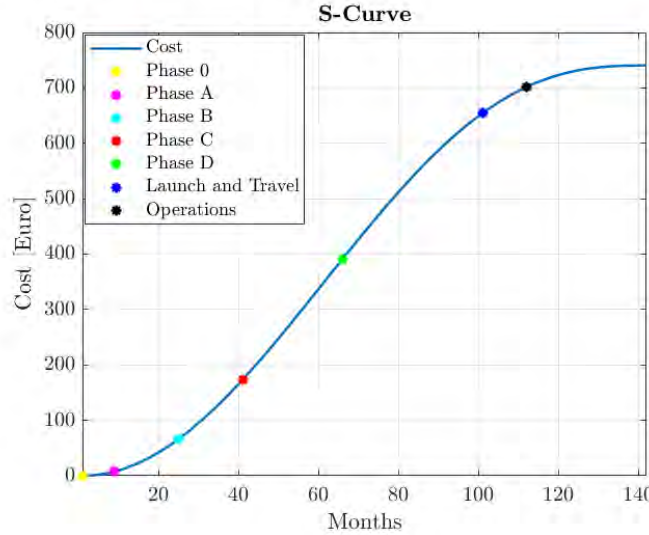


Figure A.22: S-curve of the mission with the beginning of each phase.

The Gantt chart of the MARS-PENGUIN mission is shown in Figure A.23, starting from Phase 0 to Phase F. In the chart are also presented the major reviews performed during the development of the project.

ID	Task Name	Duration	2020	2021	2022	2023	2024	2025	2026	2027	2028	2029	2030	2031	2032
			H2	H1	H2										
1	MARS-PENGUIN PROJECT	4399 d													
2	Phase 0	350 d													
3	MDR	0 d													
4	Phase A	487,13 d													
5	PRR	0 d													
6	Phase B	489 d													
7	B1	125,13 d													
8	SRR	0 d													
9	B2	363,13 d													
10	PDR	0 d													
11	Phase C	762,13 d													
12	CDR	0 d													
13	Phase D	1070,13 d													
14	Integration & Test	823,13 d													
15	QR	0 d													
16	Launch Ops & Checkout	246,13 d													
17	AR	0 d													
18	Phase E	1218 d													
19	Interplanetary Travel	303 d													
20	Operations	915 d													
21	Lake Samples	74 d													
22	Moving to Geysers/Ibernation	588,13 d													
23	Geysers Observation and Samples	253,13 d													
24	Phase F	22 d													

Figure A.23: Gantt chart of the MARS-PENGUIN mission

The Work Breakdown Structure of the MARS-PENGUIN mission is presented in Figure A.24, Figure A.25, Figure A.26, Figure A.27, Figure A.28.

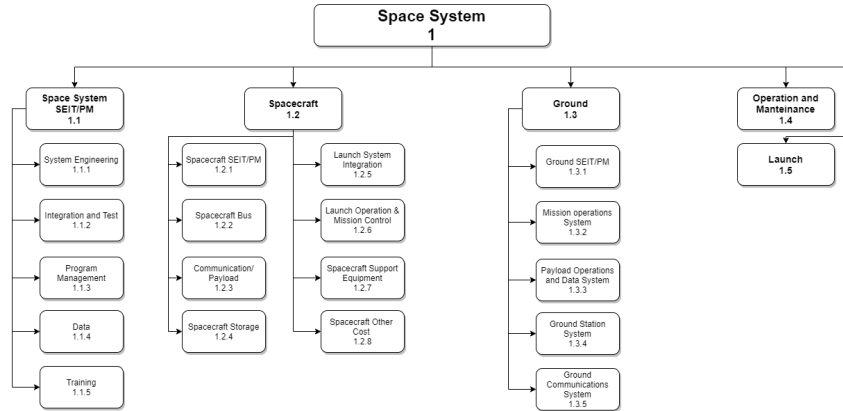


Figure A.24: WBS of the Space System

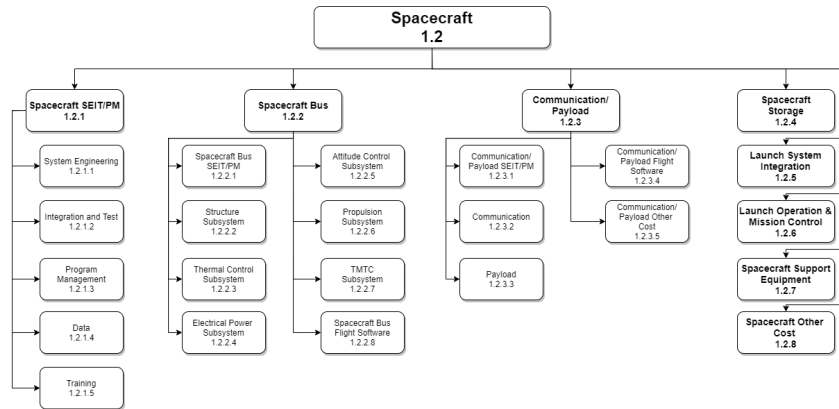


Figure A.25: WBS of the Spacecraft

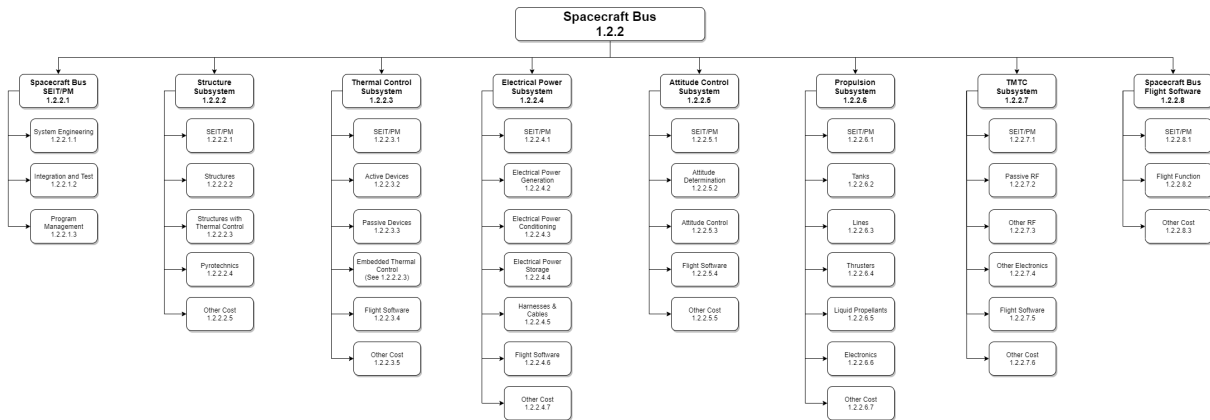


Figure A.26: WBS of the Spacecraft Bus

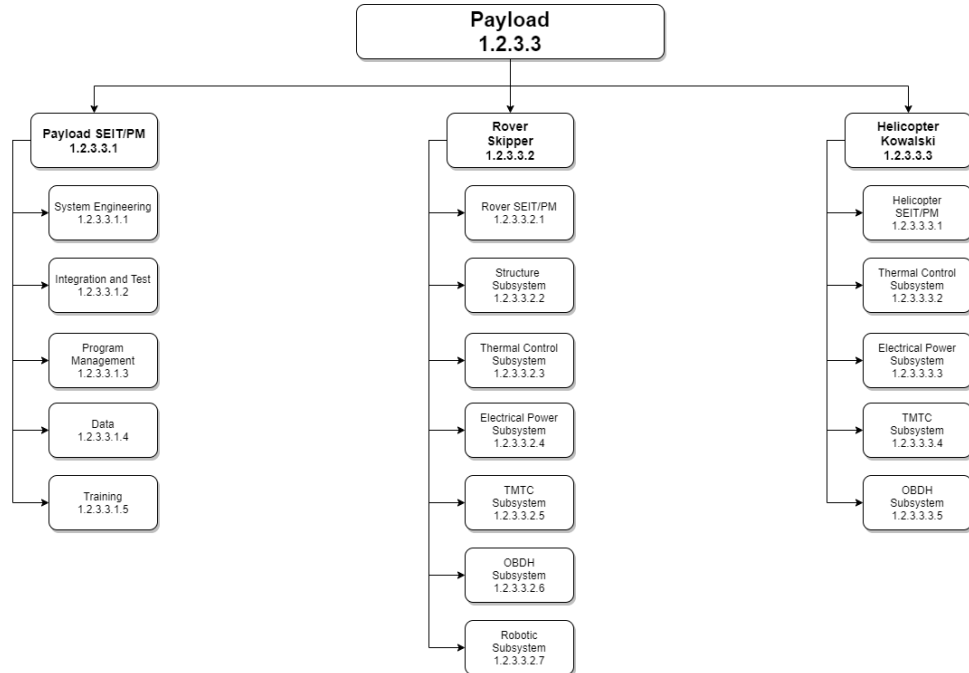


Figure A.27: WBS of the Payload

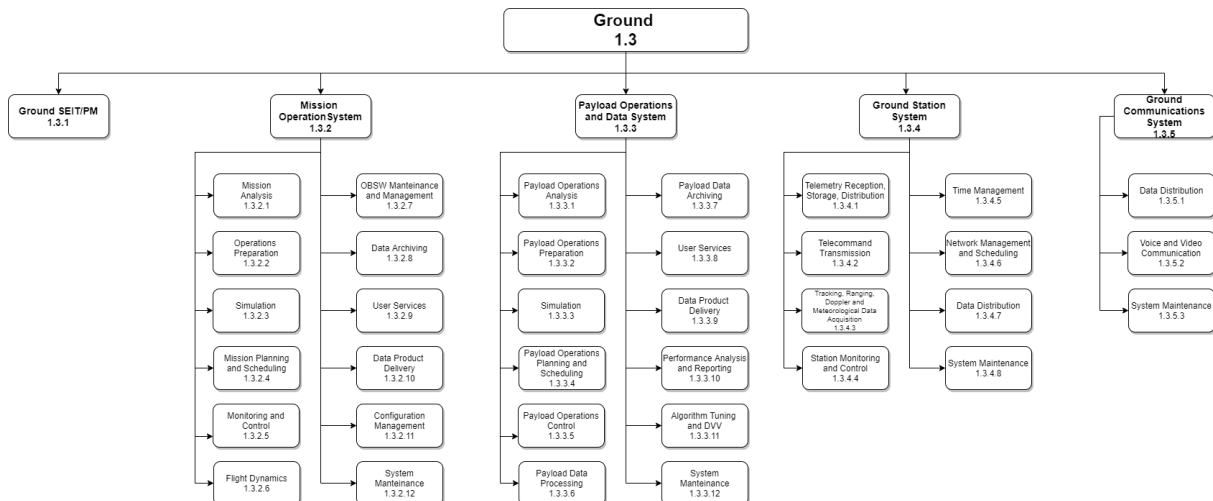


Figure A.28: WBS of the Ground Segment

The Product Tree of the MARS-PENGUIN mission is presented in Figure A.29, Figure A.30, Figure A.31, Figure A.32, Figure A.33.

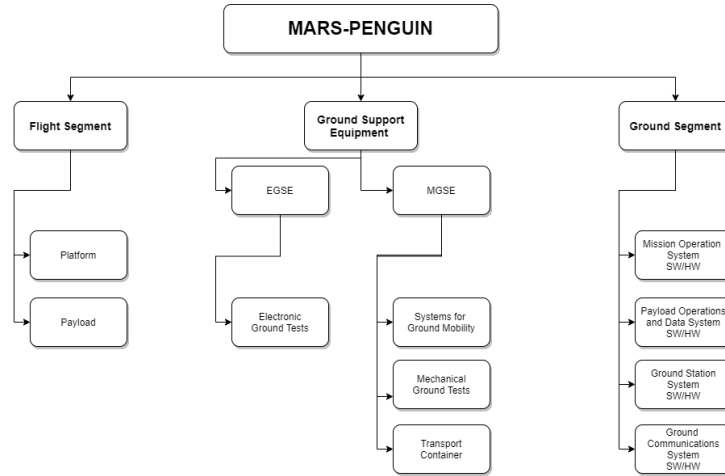


Figure A.29: Product Tree of the mission

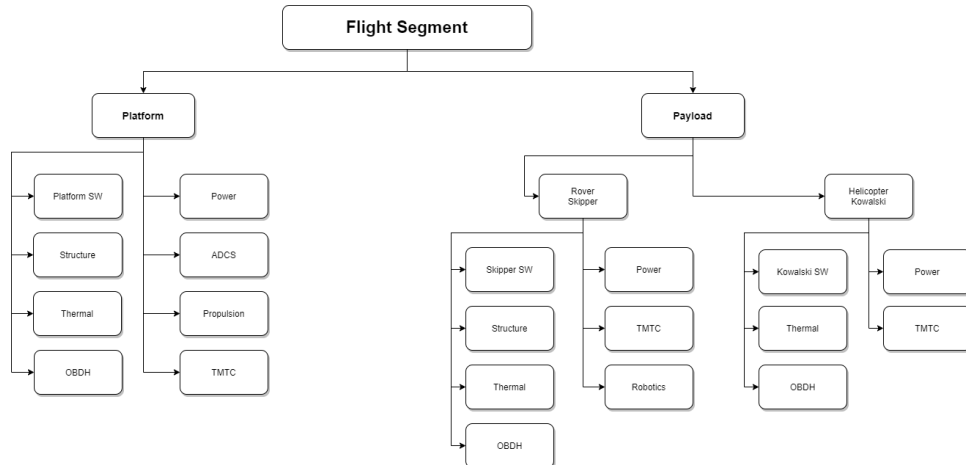


Figure A.30: Product Tree of the Flight Segment

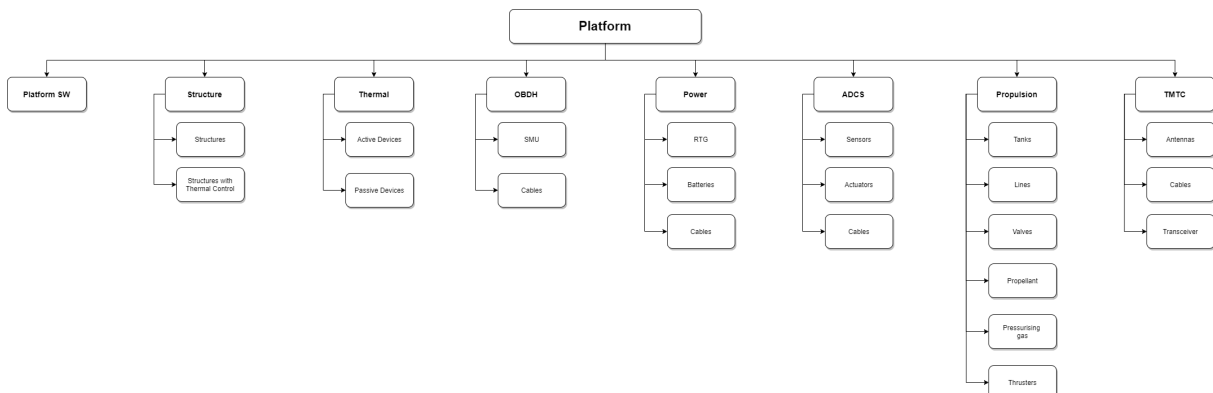
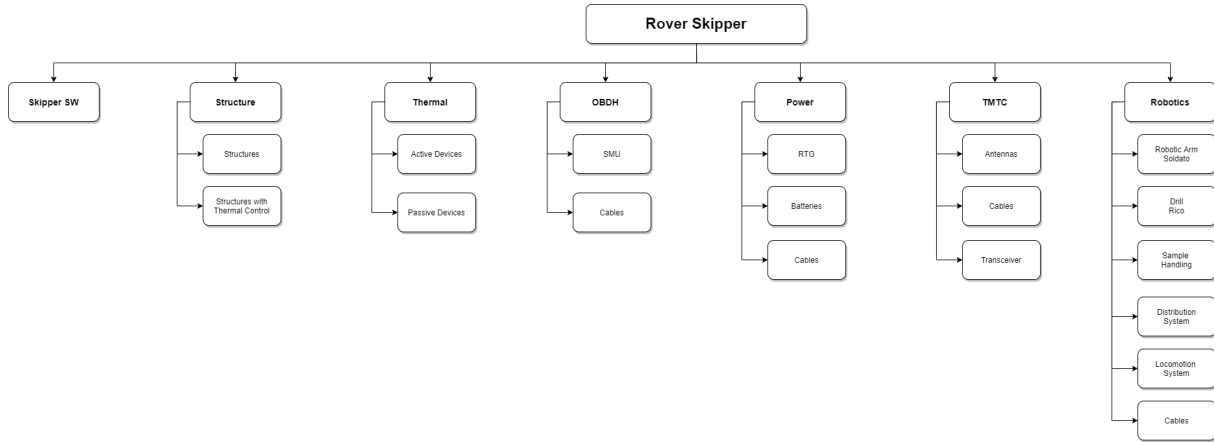
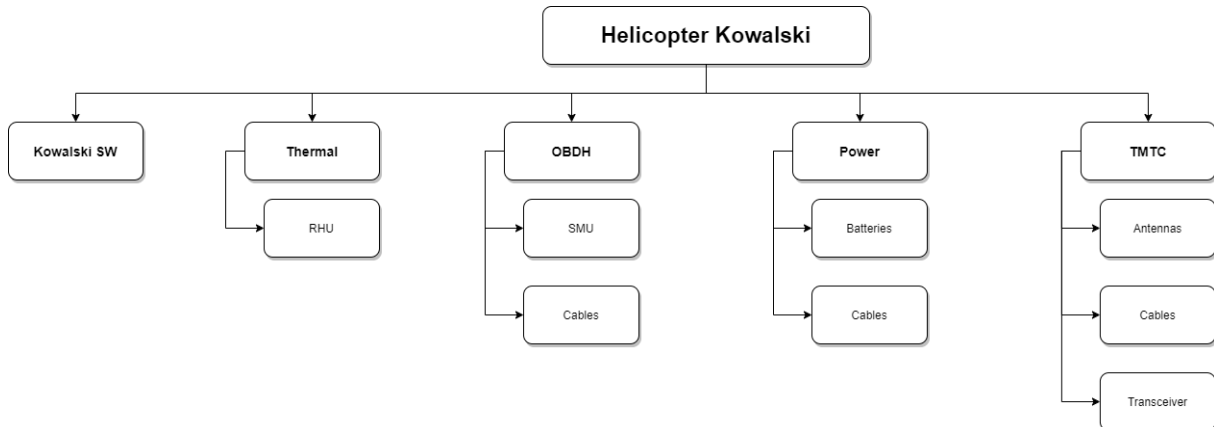


Figure A.31: Product Tree of the Platform

**Figure A.32: Product Tree of the rover Skipper****Figure A.33: Product Tree of the helicopter Kowalski**

References

- [1] Roberto Orosei et al. “Radar evidence of subglacial liquid water on Mars”. In: *Science* 361.6401 (2018), pp. 490–493.
- [2] Philip R Christensen et al. “Mars Global Surveyor Thermal Emission Spectrometer experiment: investigation description and surface science results”. In: *Journal of Geophysical Research: Planets* 106.E10 (2001), pp. 23823–23871.
- [3] Ankit Rohatgi. *WebPlotDigitizer*. Version 4.2. Apr. 26, 2020. URL: <https://automeris.io/WebPlotDigitizer/>.
- [4] Jingyan Hao et al. “Araneiform terrain formation in Angustus Labyrinthus, Mars”. In: *Icarus* 317 (2019), pp. 479–490.
- [5] Antoine Pommerol et al. “Evolution of south seasonal cap during Martian spring: Insights from high-resolution observations by HiRISE and CRISM on Mars Reconnaissance Orbiter”. In: *Journal of Geophysical Research: Planets* 116.E8 (2011).
- [6] Sylvain Piqueux, Shane Byrne, and Mark I. Richardson. “Sublimation of Mars’s southern seasonal CO₂ ice cap and the formation of spiders”. In: *Journal of Geophysical Research: Planets* 108.E8 (2003). DOI: [10.1029/2002JE002007](https://doi.org/10.1029/2002JE002007). URL: <https://agupubs.onlinelibrary.wiley.com/doi/abs/10.1029/2002JE002007>.
- [7] J Hao et al. “Variability of spider spatial configuration at the Martian south pole”. In: *Planetary and Space Science* 185 (2020), p. 104848.
- [8] Ehouarn Millour et al. “The Mars Climate Database (MCD version 5.3).” In: *Geophysical Research Abstracts*. Vol. 21. 2019.
- [9] NASA. *Mars trek*. <https://trek.nasa.gov/mars/>. (Visited on 05/07/2020).
- [10] Oded Aharonson et al. “Depth, distribution, and density of CO₂ deposition on Mars”. In: *Journal of Geophysical Research: Planets* 109.E5 (2004). DOI: [10.1029/2003JE002223](https://doi.org/10.1029/2003JE002223). URL: <https://agupubs.onlinelibrary.wiley.com/doi/abs/10.1029/2003JE002223>.
- [11] David E Smith, Maria T Zuber, and Gregory A Neumann. “Seasonal variations of snow depth on Mars”. In: *Science* 294.5549 (2001), pp. 2141–2146.
- [12] M Alexander. *Mars transportation environment definition document*. National Aeronautics and Space Administration, Marshall Space Flight Center, 2001.
- [13] M Khan and T Yamaguchi. “ExoMars 2018 Mission-Mission Analysis Guidelines”. In: *EXM Reference EXM-G2-TNO-ESC-00003, ESA* (2013).
- [14] Geoffrey Landis, Steven Oleson, and Melissa McGuire. “Design study for a Mars geyser hopper”. In: *50th AIAA aerospace sciences meeting including the new horizons forum and aerospace exposition*. 2012, p. 631.
- [15] Space Studies Board, National Research Council, et al. *Assessment of Mission Size Trade-offs for NASA’s Earth and Space Science Missions*. National Academies Press, 2000.
- [16] Rongjie Liu et al. “Powered-descent trajectory optimization scheme for Mars landing”. In: *Advances in Space Research* 52.11 (2013), pp. 1888–1901.
- [17] Adrien Bouskela et al. “Attitude Control of an Inflatable Sailplane for Mars Exploration”. In: *arXiv preprint arXiv:1902.02083* (2019).
- [18] Adrien Bouskela et al. “Planetary Exploration Using CubeSat Deployed Sailplanes”. In: *arXiv preprint arXiv:1910.03842* (2019).

- [19] NASA. *NASA Armstrong Fact Sheet: Prandtl-D Aircraft*. <https://www.nasa.gov/centers/armstrong/news/FactSheets/FS-106-AFRC.html>. 2016.
- [20] A Noth et al. “SKY-SAILOR Design of an autonomous solar powered martian airplane”. In: *Proceedings of the 8th ESA Workshop on Advanced Space Technologies for Robotics and Automation (ASTRA 2004) ESTEC, Noordwijk, The Netherlands, November 2-4, 2004*. European Space Research and Technology Centre (ESTEC). 2004, F-03.
- [21] Bob Balaram et al. “Mars helicopter technology demonstrator”. In: *2018 AIAA Atmospheric Flight Mechanics Conference*. 2018, p. 0023.
- [22] Wayne R Johnson et al. “Mars Science Helicopter Conceptual Design”. In: (2020).
- [23] Pierpaolo Pergola and Vittorio Cipolla. “Mission architecture for Mars exploration based on small satellites and planetary drones”. In: *International Journal of Intelligent Unmanned Systems* (2016).
- [24] Gerhard Kminek and John D Rummel. “COSPAR’s planetary protection policy”. In: *Space Research Today* 193 (2015), pp. 7–19.
- [25] M Giuliani et al. “Contamination Control Approach for Exomars Mission”. In: *11th ISME International Symposium on Materials in a Space Environment (September 2009)*. 2009.
- [26] Robin Biesbroek. *Lunar and Interplanetary Trajectories*. Springer, 2016.
- [27] *PROTON Launch System Mission Planner’s Guide*. Rev. 6. ariannespace. Dec. 2004.
- [28] *Soyuz User’s Manual*. Issue 2 Rev. 0. ariannespace. Mar. 2012.
- [29] Takuto Ishimatsu, Jeffrey Hoffman, and Olivier de Weck. “Interplanetary Trajectory Analysis for 2020-2040 Mars Missions including Venus Flyby Opportunities”. In: (2009).
- [30] Wanmeng Zhou et al. “Low-Thrust Trajectory Design Using Finite Fourier Series Approximation of Pseudoequinoctial Elements”. In: *International Journal of Aerospace Engineering* 2019 (2019).
- [31] Zhenbing QIU, Huaming QIAN, and Guoqing WANG. “Adaptive robust cubature Kalman filtering for satellite attitude estimation”. In: *Chinese Journal of Aeronautics* 31.4 (2018), pp. 806–819. ISSN: 1000-9361. DOI: <https://doi.org/10.1016/j.cja.2018.01.023>. URL: <http://www.sciencedirect.com/science/article/pii/S1000936118300414>.
- [32] Ahmad Bani Younes and Daniele Mortari. “Derivation of All Attitude Error Governing Equations for Attitude Filtering and Control”. In: *Sensors* 19.21 (2019), p. 4682.
- [33] Bong Wie. *Space Vehicle Dynamics and Control, Revised First Edition*. 2016.
- [34] Nicola Boscolo Fiore. *CubeSat attitude control system in Matlab Simulink*. Mar. 2020. DOI: [10.13140/RG.2.2.20951.83369](https://doi.org/10.13140/RG.2.2.20951.83369).
- [35] Robert M. Manning Robert D. Brown. “Mars exploration entry,descent and landing challenges”. In: *IEEE* (2006).
- [36] Edward C. Wong A. Miguel San Martin Steven W. Lee. “The development of the MSL guidance, navigation and control system for entry, descending and landing”. In: () .
- [37] Juan R. Cruz. “Parachutes for Planetary Entry Systems”. In: () .
- [38] Richard E. Otero and Robert D. Braun. “The Planetary Entry Systems Synthesis Tool: A Conceptual Design and Analysis Tool for EDL Systems”. In: *IEEEAC* 121 (2010).
- [39] Robert Michelltree Behzad Raiszadeh Prasun Desai. “Mars Exploration Rover Heat Shield Recontact Analysis”. In: () .
- [40] <https://www.grc.nasa.gov/WWW/K-12/airplane/atmosrm.htm>. 2020. (Visited on 05/14/2020).

- [41] Eric L. Strauss. “New Ablative Heat Shield Materials for Mars Landers”. In: *SAE Transactions* 75 (), pp. 293–304.
- [42] Malcolm Macdonald and Viorel Badescu. *THE INTERNATIONAL HANDBOOK OF SPACE TECHNOLOGY*. Praxis Publishing, 2014.
- [43] James Roeder Anita Sengupta Richard Kelsch et al. “Supersonic Performance of Disk-Gap-Band Parachutes Constrained to a 0-Degree Trim Angle”. In: *JOURNAL OF SPACECRAFT AND ROCKETS* 46.7 (2009), pp. 293–304.
- [44] Li Shuang and Peng Yuming. “Command Generator Tracker Based Direct Model Reference Adaptive Tracking Guidance for Mars Atmospheric Entry”. In: *Advances in Space Research* (2011).
- [45] http://www-mars.lmd.jussieu.fr/mcd_python/. 2020. (Visited on 05/20/2020).
- [46] Robert S Bokulic and William V Moore. “Near Earth Asteroid Rendezvous (NEAR) spacecraft solar conjunction experiment”. In: *Journal of spacecraft and rockets* 36.1 (1999), pp. 87–91.
- [47] Recommendation (ITU). “Propagation data and prediction methods required for the design of Earth-space telecommunication systems”. In: *ITU-R P.618–13* (2017).
- [48] Celestia STS. <https://celestia-sts.com/ground-station/ttc-processor/>.
- [49] WJ. Larson JR. *Space Mission Analysis and Design*. Microcosm, 1999.
- [50] Jim Taylor. *Deep space communications*. John Wiley & Sons, 2016.
- [51] CCSDS. *TC Synchronization and Channel Coding - Short Blocklength LDPC Codes*. 2017.
- [52] Eun-Young Jung et al. “SIW-based array antennas with sequential feeding for X-band satellite communication”. In: *IEEE transactions on antennas and propagation* 60.8 (2012), pp. 3632–3639.
- [53] Thales Alenia Space. https://www.thalesgroup.com/sites/default/files/database/d7/asset/document/Deep_Space_Secure_Transponders.pdf.
- [54] Charles D Brown. *Elements of spacecraft design*. American Institute of Aeronautics and Astronautics, 2002.
- [55] RUAG Space. <https://www.ruag.com/en/products-services/space/spacecraft/satellite-mechanisms/pointing-and-positioning-mechanisms>.
- [56] Richard P Kornfeld et al. “Entry, descent, and landing communications for the 2007 Phoenix Mars lander”. In: *Journal of Spacecraft and Rockets* 45.3 (2008), pp. 534–547.
- [57] Jim Taylor, Dennis K Lee, and Shervin Shambayati. “Mars Reconnaissance Orbiter”. In: *Deep Space Communications* (2016), p. 193.
- [58] Xudong Bai et al. “Compact design of triple-band circularly polarized quadrifilar helix antennas”. In: *IEEE Antennas and wireless propagation letters* 13 (2014), pp. 380–383.
- [59] L3Harris. https://www2.l3t.com/ce/pdf/data_sheets/L3Harris_SPSH_SPSR_Electra-LiteTransceiver_Final_App.pdf.
- [60] Paula R Brown, Richard E Hodges, and Jacqueline C Chen. “Antennas for Deep Space Applications”. In: *Space Antenna Handbook* (2012), pp. 664–694.
- [61] Róbert Marc, Piotr Węcławski, and Daisy Lachat. “Autonomous Multi-Mode Rover Navigation for Long-Range Planetary Exploration Using Orbital and Locally Perceived Data”. In: Oct. 2018.
- [62] COHAM. *GR-CPCI-GR740 Quad-Core LEON4FT computer*. <https://www.gaisler.com/index.php/products/boards/gr-cpci-gr740>. (Visited on 06/14/2020).
- [63] ISIS. *ISIS On Board Computer*. <https://www.isispace.nl/product/on-board-computer/>. (Visited on 06/29/2020).

- [64] *Stirling Technical Interchange Meeting*. RPS, 2015.
- [65] Loren Jones Gregory A. Carr and Victor Moreno JPL. “Mars Science Laboratory (MSL) Power System Architecture”. In: *10th International Energy Conversion Engineering Conference* (2012).
- [66] Eagle picher. *LP33330 cells dataheet*. <https://www.eaglepicher.com/sites/default/files/LP%2033330%206Ah%20Space%20Cell%200319.pdf>. (Visited on 05/07/2020).
- [67] Mieczyslaw Gregory Bekker. *Introduction to terrain-vehicle systems. part i: The terrain. part ii: The vehicle*. Tech. rep. MICHIGAN UNIV ANN ARBOR, 1969.
- [68] Dimitrios S Apostolopoulos. “Analytical configuration of wheeled robotic locomotion”. In: *The Robotics Institute of Carnegie Mellon University Technical Report CMU-RI-TR-01-08* (2001).
- [69] Liang Ding et al. “Parameter identification for planetary soil based on a decoupled analytical wheel-soil interaction terramechanics model”. In: *2009 IEEE/RSJ International Conference on Intelligent Robots and Systems*. IEEE. 2009, pp. 4122–4127.
- [70] Karl Terzaghi. “Theoretical Soil Mechanics. JohnWiley & Sons”. In: *New York* (1943), pp. 11–15.
- [71] Thomas Brooks, Graham Gold, and Nick Sertic. “Dark rover rocker-bogie optimization design”. In: (2011).
- [72] Nitin Yadav, BalRam Bhardwaj, and Suresh Bhardwaj. “Design analysis of Rocker Bogie Suspension System and Access the possibility to implement in Front Loading Vehicles”. In: *IOSR Journal of Mechanical and Civil Engineering, e-ISSN* (2015), pp. 2278–1684.
- [73] EU. *D2.2 State of the art in Space Automation and Robotics Technologies*. <https://ec.europa.eu/research/participants/documents/downloadPublic?documentIds=080166e5b2166fc7&appId=PPGMS>. 2016.
- [74] J Vago and M Coradini. “EXOMARS–Mars Exploration Programme”. In: *Presentation in Lunar and Planetary Institute Workshop*. 2012.
- [75] M Savoia et al. “PROSPECT: Sampling Tool Approaches for Lunar Icy Regolith”. In: *68th International Astronautical Congress*. 2017.
- [76] Gale Paulsen et al. “The Regolith and Ice Drill for Exploration of New Terrains (TRIDENT); a One-Meter Drill for the Lunar Resource Prospector Mission”. In: *44th Aerospace Mechanisms Symposium*. 2018, p. 13.
- [77] Maria T Zuber et al. “Density of Mars’ south polar layered deposits”. In: *Science* 317.5845 (2007), pp. 1718–1719.
- [78] Robert Bonitz et al. “The phoenix mars lander robotic arm”. In: *2009 IEEE Aerospace conference*. IEEE. 2009, pp. 1–12.
- [79] Richard Fleischner. “Insight instrument deployment arm”. In: *15th European Space Mechanisms and Tribology Symposium*. Vol. 718. 2013.
- [80] Dinesh Prabhu and David Saunders. “On heatshield shapes for Mars entry capsules”. In: *50th AIAA Aerospace Sciences Meeting including the New Horizons Forum and Aerospace Exposition*. 2012, p. 399.
- [81] *Ariane 5 User’s Manual*. Issue 5 Rev. 2. arianespace. Dec. 2016.
- [82] *Payload Flight Equipment Requirements and Guidelines for Safety–Critical Structures*. Rev. C. NASA. Dec. 2002.
- [83] *Space engineering: Structural factors of safety for spaceflight hardware*. ECSS-E-ST-32-10C Rev.1. ECSS. Mar. 2009.

- [84] Charles D Edwards et al. “Relay communications support to the ExoMars Schiaparelli lander”. In: *2017 IEEE Aerospace Conference*. IEEE. 2017, pp. 1–14.
- [85] Charles D Edwards et al. “Relay support for the Mars Science Laboratory mission”. In: *2013 IEEE Aerospace Conference*. IEEE. 2013, pp. 1–14.
- [86] Yves Doat et al. “ESA Tracking Network—A European Asset”. In: *2018 SpaceOps Conference*. 2018, p. 2306.
- [87] Recommendation (ITU). “Attenuation by atmospheric gases”. In: *ITU-R P.676–12* (2019).
- [88] Recommendation (ITU). “Reference standard atmospheres”. In: *ITU-R P.835–6* (2017).
- [89] Recommendation (ITU). “Water vapour: surface density and total columnar content”. In: *ITU-R P.836–6* (2017).
- [90] Recommendation (ITU). “Rain height model for prediction methods”. In: *ITU-R P.839-4* (2013).
- [91] Recommendation (ITU). “Characteristics of precipitation for propagation modelling”. In: *ITU-R P.837-7* (2017).
- [92] Recommendation (ITU). “Attenuation due to clouds and fog”. In: *ITU-R P.840-8* (2019).